Structural-Acoustic Design and Control of an Integrally Actuated Composite Panel

by
Brian S. Bingham

B.S., Mechanical Engineering (1996)
University of Missouri - Rolla

Submitted to the Department of Mechanical Engineering
in Partial Fulfillment of the Requirements for the Degree of
Master of Science

at the
Massachusetts Institute of Technology
September 1998

Signature of Author .....
Brian S. Bingham
Department of Mechanical Engineering
August 14, 1998

Certified by .....
Nesbitt W. Hagood IV
Associate Professor of Aeronautics and Astronautics
Thesis Supervisor

Certified by .....
Mauro J. Atalla
Research Associate

Certified by .....
Ain A. Sonin
Professor of Mechanical Engineering
Departmental Reader

Accepted by .....
Ain A. Sonin
Chairman, Department Graduate Committee
Department of Mechanical Engineering

STRUCTURAL-ACOUSTIC DESIGN AND CONTROL OF AN INTEGRALLY ACTUATED COMPOSITE PANEL

by
BRIAN S. BINGHAM

Submitted to the Department of Mechanical Engineering
on August 14, 1998 in partial fulfillment of the
requirements for the Degree of
Master of Science at the Massachusetts Institute of Technology

ABSTRACT

The need for structural based acoustic control is evident in aircraft, aerospace, and naval systems. A promising approach utilizes active materials to intelligently control the dynamic response of light-weight, modally dense structures supressing the radiated acoustic power. The basic representative structural element of a single panel offers an analytically tractable basis for examining various control methodologies for mitigating the acoustic response. An electro-mechanical Rayleigh-Ritz structural model is combined with an expression of the acoustic power radiated from a retangular panel to yield a fully coupled structural-acoustic model. The insight afforded by this model is used to design the sensor and actuator architecture of the active structure for optimal closed-loop acoustic performance. The manufacturing of a composite panel with eight embedded active fiber composite (AFC) actuators and collocated strain sensors is presented in detail. The geometry of the test article is designed to represent the dynamics of the target applications, and the active elements are embedded in the composite panel to demonstrate the capabilities of the technology. Active control methods are explored through simulations and experiments to compare the applicability to active structural-acoustic control (ASAC). To quantify the comparison, designs based on classical low-authority feedback, optimal feedback, and x-filtered LMS feedforward techniques are presented. The results lend insight into the inherent limitations and advatages of each approach to the problem of broadband control. The investigation is application motivated in that the sensing and piezoelectric actuation occur solely at the structure while the performance is measured in the acoustic field. The conclusions consider the analytically predicted performance along with the corresponding experimental achievment to develop an understanding of the key issues necessary to apply the technology to the active structural-acoustic control of complex systems.

Thesis Supervisor: Nesbitt W. Hagood IV
Title: Associate Professor of Aeronautics and Astronautics

Acknowledgments

First I would like to thank my family who are a constant reminder of what is truly important. Any accomplishments I owe to their unconditional love and support. I would especially like to thank my grandparents for understanding the importance of education.

I would like to thank my advisor, Nesbitt Hagood, for always asking difficult questions and Mauro Atalla for his helpful comments on this work.

I cannot thank the students of AMSL and SSL enough, so I will apologize for only contributing a fraction of the insight I have received.

Finally I would like to thank the administration and technical staff for their indispensable help and guidance.

Contents

List of Figures

List of Tables

Chapter 1

Introduction

Reducing noise levels resulting from mechanical vibrations can increase reliability and user satisfaction while reducing costs and expanding capabilities. Structural-acoustic control attacks this problem by considering how vibrating structures interact with the acoustic medium at the fluid-structure interface. By understanding the dynamics of the structure, the fluid, and the interaction between them, the overall performance of the system can be enhanced. The goal of this work is to present a fundamental analysis of the structural-acoustic system and demonstrate how active materials can be integrated into the structural design to reduce the radiated sound power . To accomplish this a representative structural element is considered and various control methods are implemented in simulation and experiment to quantify the limitations and capabilities of each approach. The analysis presented is meant to be general; it is not the goal to design an optimally performing single panel, but to keep the elements of the problem generic, allowing application of the resulting insight to more complex applications.

1.1 Background

The concept of actively controlling the transmission of sound is not new. Paul Lueg applied for a patent on a device for cancelling a plane wave in a rigid wall waveguide in 1936, [Lueg, 1936]. Using a pressure measurement, a downstream acoustic source, and electronic system connecting the two, Lueg proposed to simply cancel the sensed compression wave with a rarefaction at the acoustic actuator. An overview of the historical development of the active acoustic control is presented in in [Nelson and Elliot, 1992]. Noise cancellation, using acoustic sources and sensors, is generally termed active noise control (ANC). It is shown that multiple sources can be utilized to produce both local quieting and global sound reductions [Elliot et al., 1987], [Nelson et al., 1986]. With the advances in adaptive structures, defined by their ability to beneficially change in response to environmental stimuli, recent work has focused on the coupled structural-acoustic problem, integrating the sensing and

actuation with the structure. The field has become known as active structural acoustic control (ASAC). The advantages of using structural based sensing and actuator technology are clear; it is typically not practice to place secondary sources and error measurements within the acoustic field, and much more attractive to fully integrate the feedback loop and processing within the structure to attain the desired performance. Also, acoustic actuators, typically heavy magnetic coil loudspeakers, add an unacceptable weight to the design. The work in ASAC is moving toward true intelligent structure, with structurally embedded sensing, actuation, and processing. By understanding the physics of the fluid-structure interaction, such a "smart" structure can be used to control the acoustic field without obtrusive microphones and loudspeakers.

Recently there has been much research into applications of adaptive structures to structural-acoustic control. The work can be categorized by the system structure and method of control. Most of the current research has focused on two canonical structures, flat panels and smooth cylinders, which can be analyzed relatively simply to investigate the physics of the structural-acoustic coupling. Work on simple plate structures began with using *ad hoc* feedforward techniques to reduce a single frequency known disturbance with point force or acoustic control inputs, [Fuller et al., 1991] and [Fuller et al., 1992]. More recently system designs that utilize surface sensors to estimate the acoustic radiation and surface mounted piezoelectric elements as control inputs have been implemented [Maillard, 1997]. Most of this work relies on a version of the LMS feedforward control. This control approach can be quite limiting in bandwidth and system architecture in order to maintain convergence and causality of the compensator [Burdisso et al., 1993], but for applications where a known source dominates the disturbance energy, this tonal or narrowband approach is often valid. An example, [Clark and Fuller, 1991], compares the tonal control system using both structural (PVDF) and acoustic (microphone) sensing. For broadband structural actuation, the LMS algorithm must be extended using a representation of the structural model. [Vipperman et al., 1993] presents the x-filtered LMS algorithm which is shown to yield broadband performance on a lightly damped structure.

Sensor design has received a large amount of attention due to its influence on system performance. Structural sensors can be designed or shaped to spatially filter the response, in effect weighting the modes of the structure which radiate efficiently. [Clark and Fuller, 1992] investigates using PVDF strips to observe the *odd-odd* radiating modes, [Johnson and Elliot, 1995] uses a feedforward control based on a *volume velocity sensor*, and [Maillard, 1997] produces an estimate of the farfield radiated power using the coefficients of a digital filter array to selectively weight point surface measurements.

The structural-acoustic control problem is a natural extension of the more mature field of Controlled Structure Technology (CST) which attempts to address the problem of designing high performance structures with a very structured design process [Crawley et al., 1995].

Applying modern feedback control techniques to the canonical structural problems results in generalizations on the tendencies of the optimal solutions [Campbell, 1993], lending insight in to the fundamentals of the controlled structure approach. An analytical analysis of the interior acoustic problem for aircraft is presented in [O'Sullivan, 1998] along with a thorough examination of the motivation for quieting aircraft cabins. Using point force actuation, [Dehandschutter et al., 1997] has experimentally implemented feedback structural control to cancel the radiated acoustic field.

1.2 Motivation

The work in the ASAC thus far has mainly focused on narrowband compensation using simple feedforward techniques. A few applications of feedback structural control for acoustics have begun to appear. Each example in the literature uses a particular architecture making it difficult to compare the results from various sources. This work considers possible compensator designs for a structural system using integrated AFC actuation and structural sensors. By considering the performance of various designs on the same system, under the same experimental conditions, a useful comparison of the performance and limitations is made. This comparative presentation will give insight into the choice of control techniques for more complex systems.

The motivation for this work is application based. In order to convey a feel for the variety of systems and requirements of interest, a few examples are briefly discussed and then used to justify study of a simple panel geometry.

Aircraft Interior Acoustics

Reducing the interior noise levels in aircraft is a very demanding problem due to interior sound pressure levels in excess of 100 dB [Moreland, 1979]. Excessive noise can be unpleasant, but can also cause operator fatigue and mechanical failure. Other interior problems, such as automobiles, locomotives, and civil structures, do not have the same stringent weight requirements inherent to aircraft systems. Typical airframes are constructed by covering a light weight, stiff frame skeleton with a thin, flexible skin, resulting in a lightly damped, highly resonant structure that is very susceptible to disturbances. Weight penalty also restricts the feasibility of passive damping techniques. Lower frequencies demand thicker layers of damping treatments adding more mass to the system. Passive damping techniques satisfying the space and weight requirements are ineffective below 1000-3000 Hz [Leverton and Pollard, 1979], necessitating active control.

Satellite Launch Load Alleviation

With increased demand for satellite launch for both commercial and strategic systems, the reliability and weight reduction of the launch vehicle are critical to the reducing system cost. Currently acoustic launch loads account for over 40% of first day satellite failures [Glaese, 1997]. Severe acoustic loading is a product of both the launch vehicle main engines and the aerodynamic buffeting as the vehicle passes through transonic and maximum dynamic pressure flight. Reducing these extremely high acoustic loads transmitted through the payload shroud has become a topic of significant work, [Glaese, 1997] and [Asari, 1998]. The payload shroud design is a classic example of the tradeoff between reduced cost, calling for a lighter weight structure, and strict acoustic performance, demanding greater transmission loss behavior of the same structure.

Passive damping treatments for this application have not achieved the low-frequency performance requirements. The state of practice is to use acoustic blankets and structural mass-loading of the shroud to mitigate the transmission. The thickness of the treatment must be a significant portion of the wavelength of the disturbance in order to obtain attenuation. Not only does this approach add to the mission weight (cost), but current passive treatments have only been effective for frequencies above 500 Hz [Masters, 1998].

Naval Vessel and Weapon Radiation

Progressive developments of torpedo technology have reduced radiated noise levels considerably. However, the threat has also been improving and the advantage which the US has had in the past has been reduced. To regain the advantage the Navy's current torpedoes will be upgraded by phased prototyping into the next generation weapons. Current work on this retrofitting task focuses on developing conformal coatings around a torpedo which can control radiated noise due to hull vibrations caused by propulsor forcing and external excitation from the turbulent boundary layer.

Composites

In the aircraft and aerospace industries, there is significant pressure to use lighter weight materials to reduce structural mass and thus cost. Increasingly major portions of airframes are manufactured from composite materials due to their high strength to weight ratio. Satellite payload shrouds can also benefit from use of composite materials.

Composite construction allows for the possibility of embedding the sensing and actuation elements of an adaptive structure as an alternative to surface mounting the elements. Active materials, in particular brittle piezoceramics, are particularly vulnerable to environmental damage. Integrating the elements adds robustness to the system, protecting the active materials, and providing a passive load path for a damaged element allowing for

partial survival of actuation capabilities. Also, a fully integrated system is attractive for inclusion into existing structures allowing for a "turn key" solution. Ideally a fully integrated intelligent panel, capable of sensing, processing, and actuation, would be developed for general structural acoustic control applicable to each of the afore mentioned systems. This *smart panel* could be readily applied to many systems without the added complexity of surface mounting elements, establishing connections, and providing external processing. This work moves toward this vision by performing closed loop experiments on a carbon fiber composite panel with structurally integrated sensors and actuators.

1.3 Panel Radiation-A Representative Problem

Due the the widely varied structural systems that require high performance acoustic behavior, this work attempts to approach the problem from a basic level that, while not completely representative of a true system application, will capture a sufficient amount of the system's fundamental physics to guide the design and control of active structural-acoustic systems. The common structural element present in a majority of the previously described systems is a single panel. Most of these systems are engineered with a structural frame consisting of, in the most basic representation, circumferential ribs and longitudinal stringer supports covered with some thin skin material. Specific examples include the Boeing's 747 commercial airliner, Boeing's Chinook-47 military rotor craft, the U.S. submarine fleet, the U.S. Mark-48 torpedo, and most automobiles. At the most basic level the structure of these very different craft are similar due to construction. Depending on the particular application, the interior performance or the radiation performance may be of primary importance, but in either case it is the propagation through this flexible skin which must be mitigated in order to achieve the desired behavior. The representative structural-acoustic system studied here is the single panel. Studying the behavior of this simple structural element will lend insight into the basic approaches and methodologies appropriate for enhanced performance of the specific systems of interest.

The actual design of the experimental testbed is covered in Chapter 4, but the basic approach is to create a system that represents the complex issues in the structural-acoustic problem, but lends itself to a greater degree of understanding and insight than the actual engineering systems. The flat panel is well modeled due the simple geometry as explained in Chapter 2. An accurate physical model allows an understanding of the physics of the problem making it possible to determine what types of strategies and approaches are best suited to address the structural-acoustic control problem. The methodologies developed in order to control the noise radiated from a flat panel will be applicable to the more complex problems that exist in the field, where such accurate modeling and analytical design studies are difficult, if not impossible

1.4 Thesis Outline

A brief sketch of this work is included to give the reader a road map of the analysis and results presented.

Chapter 2-Modeling The structural and acoustic models are developed from the fundamental physical relationships. The Rayleigh-Ritz formulation for a laminated composite plate is presented including the electro-dynamic coupling for representing active structures. The acoustic model is based on the panel radiation problem. A new method of spectrally factoring the harmonic solution allows a state-space representation of the radiating acoustics, the radiation filter, to be appended directly to the structural system. The radiation problem is discussed in detail to relate the physical insight necessary for interpreting the control results which follow. Through an example paralleling the experimental setup, the model is shown to produce a complete state-space description of the system that is ideal for system and control design.

Chapter 3-System Design Design of the experimental panel system, based on the closed-loop acoustic performance, is presented. First, the geometric design of the panel is justified based on the relevant applications. The topology of the control system is discussed in order to emphasize the importance of sensor and actuator architecture on the closed-loop performance of the system. Finally the AFC actuators are placed within the structure based on a simple optimization of the closed loop performance.

Chapter 4-Manufacturing/Experimental Setup To ensure reproducibility, the manufacturing of the test article with embedded AFC actuation and strain sensors is detailed. The canonical experimental procedure for measuring the farfield radiated power is explained to set a standard for closed-loop comparisons and the experimental setup and equipment are listed. Limited experimental results are presented to verify the setup and illustrate the correlation with the design model.

Chapter 5-Structural-Acoustic Control Presenting the basic theoretical development of the control designs is necessary for understanding the experimental implementation. Classical feedback, linear optimal feedback, and adaptive feedforward methods are introduced and the limitations and capabilities of each are discussed. Examples are presented based on the structural-acoustic model of the experimental setup. These examples illustrate the concepts and set performance benchmarks for the implementations.

Chapter 6-Experimental Results To compare the capabilities and limitations of the proposed control methods, each is implemented and a standard experiment is performed to determine the closed-loop performance, reduction in radiated sound power,

under consistent conditions. Direct comparisons are made with the predicted behavior from Chapter 5 to highlight the insight of analytical results and the challenges of implementation.

Chapter 7-Conclusions The final comparison of the compensation techniques is presented in its most succinct form along with suggested avenues for future investigation.

Chapter 2

Structural-Acoustic Modeling

Modeling is simply a mathematical description of a physical process. Once codified it can be used to quantify the dynamic response of the system. Purely structural models consider the behavior of the system *in vacuo*, neglecting the interaction with the surrounding medium. Considering the fluid-structure interaction, structural-acoustic models capture the physics of the structure, the fluid, and the interaction between the two. There are a multitude of approaches to such problems, depending upon the goal of the analysis. The following will explain the modeling methods chosen to solve the structural-acoustic problem at hand, why the approach was applied, and how it was implemented. The method is sketched by including only the pertinent resulting statements, but all the excellent references are included at each step in the development. As an example, the model formulation for the experimental setup under consideration, a flat rectangular panel, is presented as an illustration of the approach.

2.1 Structural Model

Structural dynamics is an expansive field. There are many approaches available to representing a structure in motion. The engineer must choose which method is appropriate for the type of analysis undertaken. For the particular system under consideration here, a thin flat panel, a closed form solution to the governing partial differential equation exists. Foresight into the acoustic coupling analysis indicates that the desired form of the vibration model is a time-domain state-space representation.

2.1.1 Plate Equation

The place to begin the analysis of a vibrating plate is with the fundamental equation of motion. The detailed development of the plate equations is included in many textbooks such as [Jones, 1975], and an excellent survey is supplied by [Leissa, 1969]. Only a brief

treatment of the assumptions and results are included here. For thin, uniform thickness, plates composed of linear elastic materials we tacitly assume a state of plane stress. The Kirchoff assumption dictates that all planes perpendicular to the centerline remain normal, and the displacements are assumed small compared to the thickness of the panel. Finally all rotary inertia terms are neglected. Under these restrictions the balance of forces along with the constituent relations yields the canonical plate equation for the out of plane displacement $w(x, y, t)$.

$$D\nabla^4 w + \rho h \frac{\partial^2 w}{\partial t^2} = 0 \tag{2.1}$$

$$D \equiv \frac{Eh^3}{12(1-\nu^2)}$$

$$\nabla^4 = \frac{\partial^4}{\partial x^4} + 2\frac{\partial^4}{\partial x^2 \partial y^2} + \frac{\partial^4}{\partial y^4}$$

For the simple case of a homogeneous isotropic panel the governing equation of motion is Equation (2.1), where ρ is the material density, E is the isotropic stiffness, h is the constant plate thickness, and ν is Poisson's ratio. This simple expression of the governing relation is a fourth order wave equation. Using the appropriate boundary conditions, and assuming a temporally harmonic solution, the resulting eigenvalue problem must be solved to determine the characteristic functions (eigenfunction basis) and natural frequencies (eigenvalues). Homogeneous solutions for two particular boundary cases will be important in quantifying the structural-acoustic coupling of a vibrating panel: the infinite plate and the simply-supported plate.

The boundary conditions for an infinite panel are implicitly defined by assuming no reflection at the boundary. This can be realized by assuming a temporally and spatially harmonic solution to Equation (2.1)[1] in two dimensions, i.e., $w(x, y, t) = Ae^{(\imath(\omega t - k_x x - k_y y))}$. This solution represents only an outwardly traveling wave, satisfying the radiation condition by construction. Substitution into the wave equation immediately yields the relation between the temporal frequency (ω) and the structural wave number (k_b), where c_b is the bending wave phase speed.

$$\text{Dispersion Relation} \qquad k_b^2 = k_x^2 + k_y^2 = \omega\left(\sqrt{\frac{\rho h}{D}}\right) \Rightarrow k_b \propto \sqrt{\omega} \tag{2.2}$$

$$k_b \equiv \frac{\omega}{c_b}$$

This relation is known as the dispersion relationship[2], and implies that the bending wave

[1] The convention for complex notation should be explicitly defined. The dependence on time is specifically noted as the positive exponential function $e^{\imath\omega t}$. From this the typical wave solution is of the form $e^{\imath(\omega t \pm kx)}$ where the sign of the wave number determines the direction of propagation

[2] This relation should be contrasted with the similar relationship for second order wave equations (e.g., infinite axial vibration of bars or acoustic waves) where the wave number is *linearly* related to the frequency, and the wave speed is therefore constant with frequency.

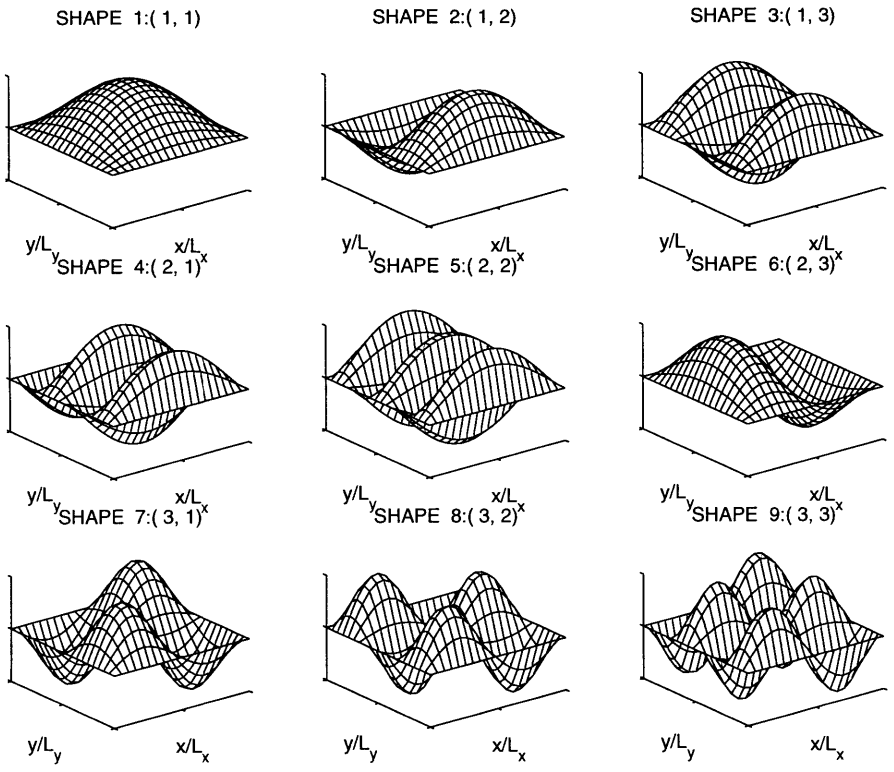

Figure 2.1: First Nine Mode Shapes of a Simply-Supported Uniform Panel

speed ($c_b \equiv \omega/k_b$) is dependent on the frequency of vibration. This result will become very important for understanding the physically coupling mechanisms to the surrounding fluid.

For the simply supported boundary conditions, out of plane deflections and reaction moment are set to zero along the plate boundary[3]. To solve the partial differential equation (2.1), the solution is assumed to be temporally harmonic, and the spatial dependence is assumed separable[4]. The resulting eigenvalue problem is satisfied exactly by an infinite summation of panel modes, as illustrated in Figure 2.1, operating at the corresponding eigenfrequencies.

$$w(x,y,t) = e^{i\omega t} \sum_{p=1}^{\infty} \sum_{q=1}^{\infty} A_{(p,q)} \Psi_{(p,q)}(x,y)$$

$$\Psi_{(p,q)}(x,y) = sin\left(\frac{p\pi x}{L_x}\right) sin\left(\frac{q\pi y}{L_y}\right)$$

$$\omega_{(p,q)} = \left(\frac{\pi^4 D}{\rho h a^4}\right)^{1/2} [p^2 + q^2 \frac{L_x}{L_y}]$$

Where L_x and L_y are the rectangular panel dimensions and a is the characteristic dimension of the panel, i.e., $a = \sqrt{L_x^2 + L_y^2}$. Each of these eigenfunctions or modes is designated by

[3] i.e., $w(x,y,t) = 0 = \frac{d^2}{dx^2} w(x,y,t) = 0$ along the boundaries.

[4] $w(x,y,t) = X(x)Y(y)e^{i\omega t}$.

the number of half-wavelengths in the x and y directions using the indices (p, q). These simple mode shapes will be used as assumed modes for the Rayleigh-Ritz model that is explained in the following.

For other combinations of boundary conditions the eigenvalue problem becomes more cumbersome, but numeric solutions for almost any scenario can be found in [Blevins, 1979]. Once these fundamental solutions are obtained, the general solution can be expressed as an infinite summation of the eigenfunctions or mode shapes. For all but the simplest forcing functions, this wave solution becomes prohibitively cumbersome and we must use approximate methods (e.g., assumed modes, finite elements, Galerkin, etc. [Craig, 1981]) to solve the governing equations.

2.1.2 Energy Methods/Rayleigh Ritz Model

Vibrating structures are continuous systems. For any real structure deviating from the canonical beam, plate, and shell geometries, a closed form solution to the continuous formulation is not tractable, so the system must be discretized into a finite degree of freedom representation yielding an approximate solution. For the panel problem, such a closed form solution does exist, but in order to capture the response to arbitrary forcing functions (the inhomogeneous solution to the partial differential equation) a discrete model is needed. These types of models most often take the form of finite element or assumed modes models. The contrast between the two can be put most simply by the fact that finite elements assume simple deflection shape functions over small elements that make up the global structure, while assumed modes models assume deformation shapes over the entire structure. The technique for solving both types of formulations utilizes the principle of least action to derive the equilibrium equations. Because of the simple closed-form eigenfunctions for a vibrating plate, the assumed modes modeling method is a natural choice. This section briefly outlines the basic method and the following sections describe the particularities to implementing the technique for a composite laminate panel with embedded actuation and sensing elements.

Principle of Least Action

The principle of least action is a very powerful fundamental approach to mechanics that can be applied to a great variety of problems. One of Richard Feynman's best lectures illustrates the elegance of this theory [Feynman, 1989]. Applying the principle to problems in dynamics is explained in [Crandall, 1968] where the following statement of Hamilton's principle is found.

An admissible motion of a dynamic system between specified configurations at t_1 and t_2 is a natural motion if, and only if, the variation indicator

$$V.I. = \int_{t_1}^{t_2} (\delta\mathcal{L} + \sum_i f_i \cdot \delta R_i) dt \tag{2.3}$$

vanishes for arbitrary variations.

The Lagrangian $\mathcal{L}$ accounts for all the stored energy in the system and can be expressed as the difference between the kinetic complementary-energy (T^*) and the potential energy (V). The summation of Equation (2.3) expresses the energy contribution from the externally applied forces (f_i), where δR_i is the corresponding virtual displacements.

$$\mathcal{L} = T^* - V$$

The power of this approach is that, as long as all the energy in the system is accounted for, the principle of least action yields the equations of motion for the system. The solution to this problem can be determined using some simple results from calculus of variations.

For electro-mechanical systems, five terms are typically included in the Lagrangian. While above statement of Hamilton's principle is very generic, a more specific expression, particular to electro-mechanically coupled adaptive structures, is presented in [Hagood et al., 1990] and [Rodgers, 1995]. For brevity this analysis begins with a statement of Hamilton's principle- the variations of each of the contributing energies.

$$\int_{t_1}^{t_2} \left[\left(\int_V \rho \dot{\mathbf{u}}^{\mathbf{T}} \delta\dot{\mathbf{u}} \, dV \right) - \left(\int_V \delta\mathbf{S}^T \mathbf{T} \, dV \right) + \left(\int_V \delta\mathbf{E}^T \mathbf{D} \, dV \right) + \left(\int_{A_s} \delta\mathbf{u}^T \mathbf{f} \, dA_s \right) - \left(\delta\phi^T \mathbf{q} \right) \right] dt = 0 \tag{2.4}$$

Where ρ is the material density, $\mathbf{u}, \dot{\mathbf{u}}$ are vectors representing the particle displacement and velocity respectively, $\mathbf{S}$ and $\mathbf{T}$ are the second order mechanical strain and stress tensors respectively[5], $\mathbf{E}$ and $\mathbf{D}$ are the first order electrical field and displacement tensors respectively, $\mathbf{f}$ expresses the externally applied mechanical forcing function, and $\mathbf{q}$ expresses externally applied charge.

Using an assumed modes model, often termed a Rayleigh-Ritz model, the spatial and temporal variables are separated by assuming shape functions for each. The only constraint on the choice of shape functions is that they satisfy the geometric boundary conditions. For the simply-supported example this is equivalent to restricting the shape functions to be zero along the boundary (the geometric condition), but without requiring moment, which is proportional to the second derivative, (the natural condition) be zero. However, the choice of basis functions greatly influences the accuracy and convergence of the solution. For

[5]The second order tensor notation for stress and strain is explained in detail in [Fung, 1977].

situations that approach the ideal, use of the corresponding analytic eigenfunctions from the eigenvalue analysis results in an exact solution for a finite number of included modes. Where the conditions are more real than ideal, it is often useful to use an arbitrary basis of orthogonal shape functions that requires including more shape functions to converge, but is capable of representing arbitrary mode shapes. An orghogonal basis can represent arbitrary shapes including normal modes. These assumed modes for deflection shapes, $\psi_\eta(\mathbf{x})$, and voltage potential shapes, $\psi_\nu(\mathbf{x})$, are expressed in vector notation.

$$\mathbf{u}(\mathbf{x},t) = \sum_{i=1}^{N} (\psi_\eta(\mathbf{x}))_i \, \eta_i(t) = \psi_\eta(\mathbf{x})\eta(t) \tag{2.5}$$
$$\phi(\mathbf{x},t) = \sum_{j=1}^{M} (\psi_\nu(\mathbf{x}))_j \nu_j(t) = \psi_\nu(\mathbf{x})\nu(t)$$

Equation (2.5) is a general statement of the assumed modes, which transforms the equation in the global system coordinates, represented by the vector $\mathbf{x}$, to an equation in terms of general, or shape coordinates, represented by the displacement column vector η, where the length of η is equivalent to the the number of assumed modes allowed in the system. For systems such as plates, where the exact eigenvalues are known, this discretization of the continuous problem simply truncates the infinite sum solution to the partial differential equation.

In order to develop this analysis, each of the terms in the variational principle, will be dealt with separately and then collected to form the equilibrium equations. The goal of the analysis is to express each of the energy terms as a function of the generalized electrical and mechanical coordinates.

Kinetic Mechanical Energy: $\int_V \rho \dot{\mathbf{u}}^{\mathbf{T}} \delta\dot{\mathbf{u}} \, dV$

Simply applying the separation of variables indicated by the Ritz assumed modes in Equation (2.5) allows variation in kinetic energy to be expressed in the generalized coordinates as,

$$\delta K = \int_V \delta\dot{\eta}^T \psi_\eta^T \rho \psi_\eta \dot{\eta} \, dV$$

To eliminate the time derivative of the variation, the expression is integrated in time, by parts, and the stationarity of the end points is used to yield[6],

$$\delta K = \delta\eta^T \left(- \int_V \phi_\eta^T \rho \phi_\eta dV \right) \ddot{\eta} :$$

[6]Ex. $\int_{t1}^{t2} \delta\dot{u}^T \dot{u} \, dt = [\delta u^T \dot{u}]_{t1}^{t2} - \int_{t1}^{t2} \delta u^T \ddot{u} \, dt$. Since, $\delta u(t1) = \delta u(t2) = 0$, the first term vanishes leaving $\int_{t1}^{t2} \delta u^T \ddot{u} \, dt$

Mechanical Potential Energy (Passive): $\int_V \delta \mathbf{S}^T \mathbf{T}\, dV$

To relate the strains and stresses to the displacements both the constitutive material properties and the kinematic strain-displacement relations must be derived. Classical Laminated Plate Theory (CLPT) is a standard method for analyzing these relationships. For composite structures, [Jones, 1975] illustrates how the lamina properties (kinematics and constitutive relations) are combined to determine the laminate properties.

First the constitutive relations are utilized to relate the stress and strain for lamina materials. Starting the analysis with the canonical plane stress[7] assumption, the constitutive relations can immediately be expressed.

$$\begin{bmatrix} T_1 \\ T_2 \\ T_6 \end{bmatrix} = \begin{bmatrix} c_{11}^E & c_{12}^E & 0 \\ c_{12}^E & c_{22}^E & 0 \\ 0 & 0 & c_{66}^E \end{bmatrix} \begin{bmatrix} S_1 \\ S_2 \\ S_6 \end{bmatrix} \tag{2.6}$$

For electro-mechanically coupled systems the constitutive relationships must be extended. The analogs to the mechanical states of stress (T_i) and strain(S_i) in the electrical domain are electrical displacement (D_j) and electric field (E_j)[8] respectively. The coupling between these domains is embodied the 'd' constants. For laminate plates the field is assumed to be appreciable only in the out-of-plane direction (3), i.e. $E_1 = E_2 = 0$[9]. Lastly the relation between electric displacement and field is expressed for a dielectric material through the effective dielectric permitivity, and the fully coupled constitutive relations can be expressed as[10]

$$\begin{bmatrix} D_3 \\ S_1 \\ S_2 \\ S_6 \end{bmatrix} = \begin{bmatrix} \varepsilon^T & d_{31} & d_{32} & 0 \\ d_{31} & s_{11}^E & s_{12}^E & 0 \\ d_{32} & s_{12}^E & s_{22}^E & 0 \\ 0 & 0 & 0 & s_{66}^E \end{bmatrix} \begin{bmatrix} E_3 \\ T_1 \\ T_2 \\ T_6 \end{bmatrix} \Rightarrow \begin{bmatrix} D_3 \\ T_1 \\ T_2 \\ T_6 \end{bmatrix} = \begin{bmatrix} \varepsilon^S & e_{31} & e_{32} & 0 \\ e_{31} & c_{11}^E & c_{12}^E & 0 \\ e_{32} & c_{12}^E & c_{22}^E & 0 \\ 0 & 0 & 0 & c_{66}^E \end{bmatrix} \begin{bmatrix} E_3 \\ S_1 \\ S_2 \\ S_6 \end{bmatrix}$$

$$\begin{bmatrix} \mathbf{D} \\ \mathbf{T} \end{bmatrix} = \begin{bmatrix} \varepsilon^S & \mathbf{e} \\ -\mathbf{e}' & \mathbf{c}^E \end{bmatrix} \begin{bmatrix} \mathbf{E} \\ \mathbf{S} \end{bmatrix} \tag{2.7}$$

[7] Generalized Hooke's law relates stress and strain by $\sigma_i = C_{i,j}\epsilon_j$ $i, j = 1, \ldots, 6$, which has 36 independent stiffness constants! Requiring that the energy be univalued guarantees that $C_{i,j}$ must be symmetric, reducing the number of independent constants to 21. Assuming orthotropic materials, where the material properties are symmetric about three mutually orthogonal planes, further reduces this number to 9. Finally the stresses in the 1-2 plane ($\sigma_1\, \sigma_2\, \sigma_6$) are assumed to dominate, and the remaining terms in the stain-stress relationship are neglected. Inverting this 3x3 compliance matrix yields the plane stress constitutive relations.

[8] It should be noted that there are six components of stress and strain (2^{nd} order tensor) i=1, ... ,6, while only three components of electrical displacement and field (first order tensor) j=1, ... ,3. For a complete explanation of the tensor notation see [Fung, 1977].

[9] For AFC's the properties can be used as if the applied field was in the out-of-plane direction

[10] Note that for Equation (2.7) the ^{T} indicates a property at a constant state of stress, while the $'$ indicates a transpose operation.

where the piezoelectric induced stress constants, e-constants, are

$$\mathbf{e} = \begin{bmatrix} e_{31} & e_{32} & 0 \end{bmatrix} = \begin{bmatrix} c_{11}^E & c_{12}^E & 0 \\ c_{12}^E & c_{22}^E & 0 \\ 0 & 0 & c_{66}^E \end{bmatrix} \begin{bmatrix} d_{31} \\ d_{32} \\ 0 \end{bmatrix}$$

Material properties are given in the local frame (1-2-3 coordinates) and must be rotated to the global frame (x-y-z coordinates) in order to assemble the global properties. The basic operation is explained in [Jones, 1975] for passive materials and extended to include the electrical terms in [Rodgers, 1995]. From mechanics of materials we can transform the stresses,

$$\begin{bmatrix} T_x \\ T_y \\ T_{xy} \end{bmatrix} = \begin{bmatrix} c^2 & s^2 & -2sc \\ s^2 & c^2 & 2sc \\ sc & -sc & c^2 - s^2 \end{bmatrix} \begin{bmatrix} T_1 \\ T_2 \\ T_{12} \end{bmatrix} \Rightarrow \mathbf{T}_{global} = [R_T]\mathbf{T}_{local}$$

$$c = cos(\theta) \;\; s = sin(\theta)$$

For strain the transformation is slightly different,

$$\begin{bmatrix} S_x \\ S_y \\ S_{xy} \end{bmatrix} = \begin{bmatrix} c^2 & s^2 & -sc \\ s^2 & c^2 & sc \\ 2sc & -2sc & c^2 - s^2 \end{bmatrix} \begin{bmatrix} S_1 \\ S_2 \\ S_{12} \end{bmatrix} \Rightarrow \mathbf{S}_{global} = [R_S]\mathbf{S}_{local}$$

In both cases θ denotes the angle *from* the x-axis *to* the 1-axis.

The electrical terms are unaffected as $D_{global} = D_{local}$ and $E_{global} = E_{local}$. By directly substituting these relations and a bit of algebra the resulting equation for rotating the material properties to the global frame is given.

$$\begin{bmatrix} D_g \\ T_g \end{bmatrix} = \begin{bmatrix} D_l \\ R_T T_l \end{bmatrix} = \begin{bmatrix} \varepsilon^S & e \\ -R_T e' & R_T c^E \end{bmatrix} \begin{bmatrix} E_l \\ S_l \end{bmatrix} = \begin{bmatrix} \varepsilon^S & e R_S^{-1} \\ -R_T e' & R_T c^E R_S^{-1} \end{bmatrix} \begin{bmatrix} E_g \\ S_g \end{bmatrix}$$

The resulting global material properties are defined in terms of the local properties and a simple transformation.

$$\varepsilon_g^S = \varepsilon_l^S \;\; \mathbf{e}_g = \mathbf{e}_l \, R_S^{-1} \;\; c_g^E = R_T \, c_l^E \, R_S^{-1}$$

Next the strain-displacement kinematics must be established in order to express the mechanical terms in the energy expression as a function of displacement. The standard thin plate assumptions are explained in the development of the general plate partial differential equation (2.1). Additionally the bonding between the lamina is assumed to be non-shear-deformable, allowing only continuous displacement at the lamina interface. The first step is to express the strains at a given location, (x, y, z), as a function of the mid-plane strain

at the centerline (S_i^0) and the mid-plane curvatures (κ_i).

$$\begin{bmatrix} S_1 \\ S_2 \\ S_3 \end{bmatrix} = \begin{bmatrix} S_1^0 \\ S_2^0 \\ S_3^0 \end{bmatrix} + z \begin{bmatrix} \kappa_1 \\ \kappa_2 \\ \kappa_3 \end{bmatrix} \tag{2.8}$$

The reason for Equation (2.8) is that the mid-plane strains and curvatures can be simply expressed as a function of the centerline displacement vector $\mathbf{u} = [u^0\ v^0\ w^0]^T$ by using the differential operator defined by [Crawley and Lazarus, 1989], $\mathbf{L}_u$.

$$\begin{bmatrix} S_1^0 \\ S_2^0 \\ S_3^0 \\ \kappa_1 \\ \kappa_2 \\ \kappa_3 \end{bmatrix} = \begin{bmatrix} \frac{\partial}{\partial x} & 0 & 0 \\ 0 & \frac{\partial}{\partial y} & 0 \\ \frac{\partial}{\partial y} & \frac{\partial}{\partial x} & 0 \\ 0 & 0 & -\frac{\partial^2}{\partial x^2} \\ 0 & 0 & -\frac{\partial^2}{\partial y^2} \\ 0 & 0 & -2\frac{\partial^2}{\partial x \partial y} \end{bmatrix} \begin{bmatrix} u^0 \\ v^0 \\ w^0 \end{bmatrix} \Rightarrow \begin{bmatrix} \mathbf{S}^0 \\ \kappa \end{bmatrix} = \mathbf{L}_u \mathbf{u} \tag{2.9}$$

Using these relationships and a bit of matrix algebra[11] the resulting contribution to the variation in mechanical potential energy can be expressed as a function of the generalized coordinates.

$$\delta U_{passive}^M = \delta\eta^T \left[\int_{A_s} (\mathbf{L}_u \psi_\eta)^T \begin{bmatrix} \mathbf{A} & \mathbf{B} \\ \mathbf{B} & \mathbf{D} \end{bmatrix} (\mathbf{L}_u \psi_\eta)\, dA_s \right] \eta \tag{2.10}$$

The matrix [**A B** ; **B D**] is the standard CLPT stiffness matrix for extension (**A**), bending (**D**), and coupling (**B**), and the terms can be expressed as a summation over the n laminate plies,

$$\mathbf{A} = \sum_{i=1}^{n} c^E [z_i - z_{i-1}]$$

$$\mathbf{B} = \frac{1}{2} \sum_{i=1}^{n} c^E [z_i^2 - z_{i-1}^2]$$

$$\mathbf{D} = \frac{1}{3} \sum_{i=1}^{n} c^E [z_i^3 - z_{i-1}^3]$$

Mechanical Potential Energy (Active): $\int_V \delta \mathbf{S}^T \mathbf{T}\, dV$

From the constitutive relations, it is evident that the electric field contributes to the strain through the induced stress coefficients (e-constants), i.e., $\mathbf{T} = \mathbf{c}^E\mathbf{S} - \mathbf{e}^T\mathbf{E}$. Recalling that the applied field is restricted to contain only a single out-of-plane component, substituting

[11] $\int_V \delta U^M dV = \int_V \delta S^T T dV = \int_V \delta S^T c^E S dV$, where $S = [I\ zI][S^0 \kappa]^T = [I\ zI] L_u u$ with $I \equiv$ the identity matrix, thus $\int_V \delta U^M dV = \int_V u L_u^T [I\ zI]^T c^E [I\ zI] L_u u\, dV$, and assuming constant lamina properties we can integrate through the thickness and sum over n plies, $\int_{A_s} u L_u^T \sum_{i=1}^n \int_t [I\ zI]^T c^E [I\ zI] dz\, L_u u dA_s$

potential shapes, ψ_ν, and the strain-displacement relations yields an expression for the mechanical potential energy contributed by the active elements, where I represents the identity matrix.

$$\delta U^M_{active} = \int_V \delta \mathbf{S}^T \mathbf{T} = -\int_V \delta\eta^T \psi_\eta^T L_u^T \begin{bmatrix} I \\ zI \end{bmatrix} \mathbf{e}^T \mathbf{E}\, dV. \tag{2.11}$$

A differential operator can be used to relate the electric field and potential. For a uniform field only in the out-of-plane direction, the operator is a simple first derivative.

$$E_3 = -\frac{\partial}{\partial z}\phi(z) = L_\phi \phi(z)$$

Substituting this relation into Equation (2.11) yields an expression for the electro-mechanical coupling.

$$\delta U^M_{active} = \int_V \delta \mathbf{S}^T \mathbf{T} = \delta\eta^T \left[-\int_V \delta\psi_\eta^T L_u^T \begin{bmatrix} I \\ zI \end{bmatrix} \mathbf{e}^T L_\phi \psi_\nu dV \right] \nu$$

Electrical Potential Energy (Passive): $\int_V \delta \mathbf{E}^T \mathbf{D}\, dV$

The electrodynamic coupling is again evident from the constitutive relations. The electrical displacement ($\mathbf{D}$) is expressed as a function of electric field ($\mathbf{E}$) and stress ($\mathbf{S}$), i.e., $\mathbf{D} = \varepsilon^S \mathbf{E} + \mathbf{eS}$. The first term is considered the passive contribution and the second term illustrates the coupling and is termed the active contribution.

For the passive contribution, direct substitution of the constitutive relationship in Equation (2.7) and the assumed potential shapes yields the expression,

$$\delta U^E_{passive} = \int_V \delta \mathbf{E}^T \varepsilon^S \mathbf{E}\, dV = \delta\nu^T \left[\int_V [L_\phi \psi_\nu]^T \varepsilon^S [L_\phi \psi_\nu] dV \right] \nu$$

For most cases, with monolithic or composite active elements, the potential shape function is linear, and the generalized voltages coincide with the electrode voltage. Under these conditions the electric field is related to the applied voltage by a constant ($\frac{1}{t}$).

Electrical Potential Energy (Active): $\int_V \delta \mathbf{E}^T \mathbf{D}\, dV$

To include the coupling between the mechanical strain and electrical displacement a simple substitution of the already developed constitutive relations,

$$\delta \mathbf{E} = L_\phi \psi_\nu\, \delta\nu$$
$$\mathbf{S} = \begin{bmatrix} I & zI \end{bmatrix} \mathbf{L}_u \psi_\eta \eta$$

where I is the identity matrix, yields the expression for the active component of the electrical potential energy.

$$\delta U^E_{active} = \int_V \delta \mathbf{E}^T \mathbf{e}\mathbf{S} dV = \delta\nu^T \left[\int_V (L_\phi \psi_{nu})^T \mathbf{e} \begin{bmatrix} I & zI \end{bmatrix} (\mathbf{L}_u \psi_\eta) dV \right] \eta$$

Work Terms: $\int_{A_s} \delta \mathbf{u}^T \mathbf{f} dA_s$ and $\delta \phi^T \mathbf{q}$

The variations in electrical and mechanical work can be expressed in the generalized coordinates by simply substituting the assumed modes transformation.

$$\delta W^M = \delta \eta^T \left[\int_{A_s} \psi_\eta^T \mathbf{f} \, dA_s \right]$$
$$\delta W^E = \delta \nu^T \phi_\nu^T \mathbf{q}$$

This accounts for the energy of externally applied forces and charges.

Equilibrium Equations

Finally returning to the original expression of Hamilton's principle, Equation (2.4), and substituting the expressions for the energy terms in generalized coordinates,

$$\int_{t_1}^{t_2} \delta\eta^T \left[-\left(\int_V \phi_\eta^T \rho \phi_\eta \, dV \right) \ddot{\eta} - \left(\int_{A_s} (\mathbf{L}_u \psi_\eta)^T \begin{bmatrix} \mathbf{A} & \mathbf{B} \\ \mathbf{B} & \mathbf{D} \end{bmatrix} (\mathbf{L}_u \psi_\eta) \, dA_s \right) \eta \right.$$
$$\left. + \left(\int_V (\mathbf{L}_u \psi_\eta)^T \begin{bmatrix} I \\ zI \end{bmatrix} \mathbf{e}^T L_\phi \psi_\nu \, dV \right) \nu + \left(\int_{A_s} \psi_\eta^T \mathbf{f} \, dA_s \right) \right] \tag{2.12}$$
$$+\delta\nu^T \left[\left(\int_V (L_\phi \psi_{nu})^T \mathbf{e} \begin{bmatrix} I & zI \end{bmatrix} (\mathbf{L}_u \psi_\eta) dV \right) \eta + \left(\int_V (L_\phi \psi_\nu)^T \varepsilon^S (L_\phi \psi_\nu) \, dV \right) \nu - \phi_\nu^T \mathbf{q} \right] dt = 0$$

Allowing for arbitrary variation in both generalized coordinates ($\delta\eta$ and $\delta\nu$), this expression yields the standard coupled electro-dynamic equations of motion [Hagood et al., 1990].

$$\text{Actuator Equation} \quad \mathbf{M}\ddot{\eta} + \mathbf{K}\eta = \mathbf{B}_f \mathbf{f} + \Theta\nu \tag{2.13}$$
$$\text{Sensor Equation} \quad \Theta^T \eta + \mathbf{C}\nu = \mathbf{B}_q \mathbf{q} \tag{2.14}$$

This matrix equation is the governing equation for this finite-degree-of-freedom system in terms of the generalized shape coordinate coordinates. The unforced (homogeneous) equation is a simple eigenvalue problem. Solving for the eigenvalues and the eigenvectors yields the natural frequencies of the system and the associated mode shapes. The modes are a linear combination of the assumed shapes, so again it is emphasized that for systems with known mode shapes, the included shape function should yield exact solutions for the resonant frequencies.

The eigenvalue problem is the discrete analog to the continuous, partial differential equation eigenvalue problem from the wave equation for the plate. The methods developed for vector spaces can be applied to both problems, where the former is considered in the usual n-dimensional vector space, and a functional vector space is considered in the latter [Wornell, 1997]. The associated properties of the solutions are directly analogous if formulated in this manner. By assuming a temporally harmonic solution, $\eta(t) = \eta e^{i\omega t}$

the homogeneous equation is recognized as the eigenvalue problem, $K\eta = \lambda M\eta$, where the eigenvalues are the the square of the natural frequencies, $\lambda = \omega^2$. It can be shown that for dynamic systems the matrix $M^{-1}K$ is positive definite, real, and symmetric. From linear algebra, [Strang, 1986], the undamped eigenvalues are positive and real, and the eigenvectors (Q) are orthogonal. This important result allows the mass and stiffness matrices to be transformed into modal coordinates, ξ, by decoupling the individual modes using the diagonalization guaranteed by this orthogonal basis.

$$\begin{aligned} [Q]^T[M][Q]\{\ddot{\xi}\} + [Q]^T[K][Q]\{\xi\} &= [Q]^T[B_f]\{f\} + [Q]^T[\Theta]\{\nu\} \\ M_m\ddot{\xi} + K_m\xi = B_{fm}f + \Theta_m\nu, \text{ with} \quad \{\eta\} &= [Q]\{\xi\} \end{aligned} \tag{2.15}$$

The modal mass and stiffness matrices (M_m and K_m) in Equation (2.15) are diagonal matrices. From this formulation it is simple to assemble the state-space representation of the actuator equation by using the modal displacements, ξ, and the modal velocities, $\dot{\xi}$, as the states.

$$\begin{aligned} \begin{pmatrix} \dot{\xi} \\ \ddot{\xi} \end{pmatrix} &= \begin{bmatrix} 0 & I \\ M_m^{-1}K_m & 2\zeta\sqrt{M_m^{-1}K_m} \end{bmatrix} \begin{pmatrix} \xi \\ \dot{\xi} \end{pmatrix} + \begin{bmatrix} 0 & 0 \\ M_m^{-1}B_f m & M_m^{-1}\Theta_m \end{bmatrix} \begin{pmatrix} f \\ \nu \end{pmatrix} \\ \mathbf{u}(x,y) &= \begin{bmatrix} \psi_\eta(x,y)Q & 0 \end{bmatrix} \begin{pmatrix} \xi \\ \dot{\xi} \end{pmatrix} \end{aligned} \tag{2.16}$$

Here the output equation has been written to yield the displacement vector at a coordinate point (x, y) by recalling the shape and modal transformations. Viscous damping is typically assumed to acceptably represent losses in the lightly damped, linear systems. Damping is included by assuming values for the modal damping coefficients, ζ_i[12].

Implementation

As with any modeling, task the theory is the portion easily explained and generally stated, but the actual implementation can be just as demanding a task. To assemble this model, the shape functions must first be established, and then numeric integration must be performed to solve for the matrix parameters in the actuator and sensor equations, Equation (2.14). The previous expressions are general for any chosen shape function which satisfies the geometric boundary conditions of the problem. The consummate favorite reference for mode shape expressions is [Blevins, 1979]. The area integrals in Hamilton's principle, Equation (2.12), are evaluated using a standard Gaussian integration technique developed in [Burden and Faires, 1989]. This Rayleigh-Ritz model for classical laminated plates is illustrated through an example included in the later portion of this chapter.

[12]Viscous damping is a specific type of the more general proportional or Rayleigh damping generally expressed as $[C] = \alpha[M] + \beta[K]$ for any coefficients α and β.

2.2 Acoustic Model

One goal of this work is to create simple model of acoustic response to a vibrating structure that is useful for system and control design. This model relates the acoustic performance of the system to the disturbance and control inputs, typically mechanical forces, electrical actuation, and pressure sources. This section explains the consideration of the structural-acoustic interaction for the panel radiation problem. The main assumption is that the surrounding medium is a *light fluid.* That is, the structure is considered to vibrate *in vacuo* and the induced acoustic pressures and velocities are found based on the representation of the structural motion as a radiation source. For acoustic applications in air, this assumption is normally valid. When the structure under consideration is in a heavier medium, e.g., water, the resulting loading on the structure by the fluid cannot be ignored.

Beginning with the typical assumptions for the second order acoustic wave equation, the radiation problem is formulated and the simplification for simple geometries is illustrated. Based on a general formulation of the acoustic radiation problem, a simple expression for the harmonic radiation from a flat plate is derived - the *Rayleigh integral.* From this relation, the farfield radiated power can be expressed as a function of the panel vibrations. This harmonic representation is then transformed to the time domain, i.e., a state-space model, by fitting the numerical results with a Laplace domain transfer function and spectrally factoring the expression into a simple radiation filter that maps the modal velocity outputs of the structural model to the radiated acoustic power which is subsequently utilized as the figure of merit in the structural-acoustic control design.

2.2.1 Radiation from a Flat Panel - Rayleigh Integral

Due to the simple geometry, the acoustic radiation from flat panels can be elegantly solved, which is a rare result for structural acoustic problems. This problem is treated in most textbooks on the interaction between sound and structures, [Fahy, 1985], [Norton, 1989], and [Junger and Feit, 1972]. The development here is greatly simplified, but necessary in order to understand the application, and restrictions, of this type of analysis.

The analysis begins with the standard acoustic wave equation.

$$\nabla^2\psi - \frac{1}{c^2}\frac{\partial^2}{\partial t^2}\psi = 0 \tag{2.17}$$

Equation (2.17) is derived from the constitutive relation, continuity conditions, and equilibrium equations based on the basic assumptions of linear inviscid acoustic perturbations. Each of the variables of concern, particle velocity ($\mathbf{U}$), acoustic pressure (p), and velocity potential (ψ), must satisfy this equation which is written in terms of the velocity potential. The phase speed of sound propagation in the medium is (c)[13], and ∇^2 is the Laplacian

[13]Typically $c = \sqrt{\frac{B}{\rho}}$, where B is the bulk modulus of the fluid and ρ is the density.

operator in the appropriate coordinate frame.[14] A complete derivation, with all the appropriate assumptions and restrictions, is developed in [Norton, 1989]. Typically a temporally harmonic solution is assumed, which is analogous to taking a Fourier transform, $\psi(\mathbf{x},t) = \Psi(\mathbf{x})e^{i\omega t}$. For radiation, the Helmholtz equation for a point source at $\mathbf{r}_o$ the solution at the observation point $\mathbf{r}$ must be satisfied.

$$(\nabla^2 + k^2)G(\mathbf{r},\mathbf{r}_o) = \delta(\mathbf{r}-\mathbf{r}_o), \text{where } k \equiv \frac{\omega}{c} \tag{2.18}$$

This equation is satisfied by the *Green's function*, $G(\mathbf{r},\mathbf{r}_o)$, where $\delta()$ denotes the Dirac delta function representing a point source, and k is the acoustic wave number. For outward traveling waves from a small source ($ka \ll 1$, where a is the characteristic source dimension), the Green's function is simply expressed as [Pierce, 1981],

$$G(\mathbf{r},\mathbf{r}_o) = \frac{1}{4\pi|\mathbf{r}-\mathbf{r}_o|}e^{-ik|\mathbf{r}-\mathbf{r}_o|} \tag{2.19}$$

Expression (2.19) represents an outward spherical wave with amplitude that linearly decays with distance. To solve the inhomogeneous Helmholtz Equation (2.18) we multiply by the pressure at $\mathbf{r}$ and integrate the entire expression over a conveniently defined volume.

$$\iiint_V p(\mathbf{r})(\nabla^2 + k^2)G(\mathbf{r},\mathbf{r}_o)dV = \iiint_V p(\mathbf{r})\delta(\mathbf{r}-\mathbf{r}_o)dV = p(\mathbf{r})$$

The last expression makes use of the sifting property of the impulse function. To eliminate the wave number, the spatial derivative of the pressure is substituted, i.e., $\nabla^2 p(\mathbf{r}) = -k^2 p(\mathbf{r})$.

$$\iiint_V p(\mathbf{r})\nabla^2 G(\mathbf{r},\mathbf{r}_o) - G(\mathbf{r},\mathbf{r}_o)\nabla^2 p(\mathbf{r})dV == p(\mathbf{r})$$

It is noted that this particular form of the radiation expression in the same form as Gauss' divergence theorem [O'Neil, 1995],

$$\iiint_V f\nabla^2 g - g\nabla^2 f \, dV = \iint_S (f\nabla g - g\nabla f)\cdot N \, dS$$

Directly applying this theorem yields the expression for the radiated pressure in terms of the surface integral about the boundary of the integration volume.

$$\iint_S (p(\mathbf{r})\nabla G(\mathbf{r},\mathbf{r}_o) - G(\mathbf{r},\mathbf{r}_o)\nabla p(\mathbf{r}))\cdot N \, dS$$

The relation between pressure and velocity, $\nabla p(\mathbf{r}) = i\omega\rho\mathbf{U}$, is substituted and the normal components of the quantities are retained, leaving the general expression for the radiated pressure at the point r.

$$\text{Kirchoff} - \text{Helmhotz Eqn. } p(\mathbf{r}) = \iint_S \left(p(\mathbf{r}_s)\frac{\partial}{\partial n}G(\mathbf{r},\mathbf{r}_s) + i\omega\rho v_n(\mathbf{r}_s)G(\mathbf{r},\mathbf{r}_s) \right) dS \tag{2.20}$$

[14] E.g., in rectangular coordinates $\nabla^2 = [\frac{\partial^2}{\partial x^2} + \frac{\partial^2}{\partial y^2} + \frac{\partial^2}{\partial z^2}]$.

Where v_n is the normal component of the particle velocity vector $\mathbf{U}$. This equation warrants consideration. For flat plate problems the integration region is chosen to be the half space on the radiating side of the panel. For radiating bodies the Green's function disappears as $r \to \infty$ leaving just the integration over a single plane containing the vibrating plate. Where the pressure and normal velocity are known at this boundary surface, this formulation yields a solution for the pressure in the entire acoustic field. At the plane containing the panel, the fluid-structure interface, the velocity in the fluid is prescribed by the structural vibration. Additionally the normal derivative of the general Green's function for an infinitesimal source goes to zero eliminating the first term of Equation (2.20). Substituting the Green's function and considering the method of images which allows for the pressure doubling at a rigid boundary, the Rayleigh integral [Rayleigh, 1945] results.

$$\text{Rayleigh Integral} \qquad p(\mathbf{r}) = \frac{i\omega\rho}{2\pi} \iint_S \frac{v_n(\mathbf{r}_s) e^{-ik|\mathbf{r}-\mathbf{r}_s|}}{|\mathbf{r}-\mathbf{r}_s|} \, dS \tag{2.21}$$

The development of this equation is included here for completeness. In the literature there are many discrepancies as to the basic assumptions necessary to derive this equation, how it may be applied, and the form of the equation. For two dimensional geometries Equation (2.21) is very general. Restrictions on the application of the Rayleigh integral only arise when farfield simplifications are introduced to allow analytic manipulations. This integral expression can be interpreted as an infinite summation of contributions from infinitesimal point sources on the structures surface which superimpose to yield the pressure at the observation point.

2.2.2 Radiation Filter

Rayleigh Integral for Panel Modes in the Farfield

From the discussion of the wave solution for a thin plate, the exact mode shapes for a panel with simply supported boundary conditions are given in Equation (2.3) as two superimposed sine functions. Considering the out-of-plane velocity as a summation of modal contributions allows for the solution of the Rayleigh integral to be expressed in terms of these modal contributions. To evaluate this integral analytically, the farfield assumption is made with respect to the evaluation of ($\overline{R} = |\mathbf{r} - \mathbf{r}_s|$). The distance $\overline{R}$ is present in two terms in the Rayleigh integral 2.21 and different approximations are made for each term in order to simplify the expression. For the term in the denominator, the spreading loss, the simple assumption that the observation distance is much greater[15] than the characteristic dimension of the structure ($\mathbf{r} \gg \mathbf{r}_o$) allows for the approximation, $\overline{R} \approx r$. The exponential term must be approximated more accurately because the phase relationship is critical to the validity of the integration. In addition to the spatial restriction, the wavelength must

[15]Typically the $\gg$ expression is meant to express a multiplicative factor of 3 or more [Bies, 1988]

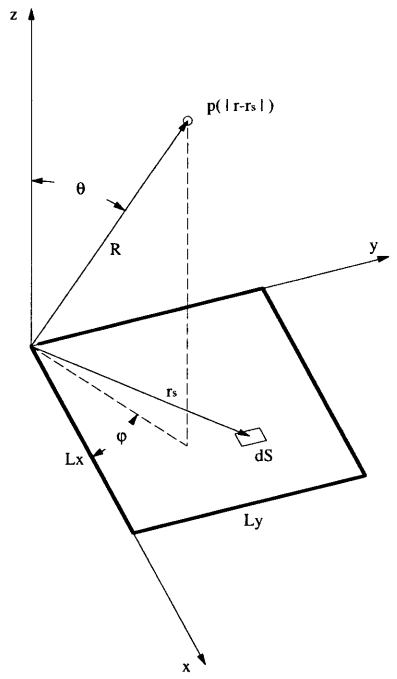

Figure 2.2: Coordinate convention for Rayleigh integral equation

be sufficiently long ($ka \ll 1 \Rightarrow \lambda \gg 2\pi a$), where a is the characteristic dimension of the panel[16]. Linearizing the exact expression about $r = r$, $\phi = \theta = 0$ yields the approximation.

$$\begin{aligned} \overline{R} &= \sqrt{(rsin(\theta)cos(\phi) - x)^2 + (rsin(\theta)sin(\phi) - x)^2 + (rcos(\theta))^2} \\ &\approx r - xsin(\theta)cos(\phi) - ysin(\theta)sin(\phi) \end{aligned} \tag{2.22}$$

This allows for the r dependence to be removed from the integrand. This approximation limits the following analysis to solutions for the farfield pressure at low frequencies. As a guideline, one might consider a square panel with characteristic dimension $a = 0.3m$, coupled to the surrounding air ($c_{air} \approx 343m/s$). The spatial restriction is satisfied for $r > 3a \approx 1m$, were the frequency condition requires that $\omega \ll \frac{c}{a} = 1143\ Hz$ (or $\lambda \gg 2\pi a = \frac{3\pi}{5} \approx 1.9m$).

With these restrictions, the farfield Rayleigh integral, expresses the pressure as a sum of modal contributions.

$$p(\mathbf{r}) = \frac{i\omega\rho}{2\pi}\frac{e^{-\imath kr}}{r}\sum_p\sum_q \dot{\eta}_{(p,q)} \left[\int_0^{L_x}\int_0^{L_y} sin(\frac{p\pi x}{L_x})sin(\frac{q\pi y}{L_y})e^{ik(xsin(\theta)cos(\phi)+xsin(\theta)sin(\phi))}\right] dxdy$$

This expression can be evaluated exactly, through integration by parts, to determine the con-

[16]Consider the approximation along the z axis, $\theta = 0$. The error in the approximation is greatest at $x = L_x$, $y = L_y$ and takes the form $e^{-\imath k\sqrt{r^2+L_x^2+L_y^2}} \approx e^{-\imath kr}$. Since $\sqrt{r^2 + L_x^2 + L_y^2} < r + \sqrt{L_x^2 + L_y^2}$, the error in the approximation is bounded by $e^{\sqrt{L_x^2+L_y^2}}$. The condition for small error is that this term approach unity, or equivalently $k(L_x^2 + L_y^2) = ka \ll 1$

tribution of each panel mode to the farfield pressure. This was first proposed in [Wallace, 1972].

$$p(r,\theta,\phi,\omega,t) = \frac{i\omega\rho L_x L_y}{2\pi^3}\sum_p\sum_q\left[\dot{\eta}_{(p,q)}\frac{1}{pq}\left[\frac{(-1)^p e^{-i\alpha}-1}{(\frac{\alpha}{p\pi})^2-1}\right]\left[\frac{(-1)^q e^{-i\beta}-1}{(\frac{\beta}{q\pi})^2-1}\right]\right]\frac{e^{(i\omega t-kr)}}{r}$$
$$\alpha = kL_x sin(\theta)cos(\phi) \tag{2.23}$$
$$\beta = kL_y sin(\theta)sin(\phi)$$

Farfield Radiated Power

From the expression of the farfield pressure in terms of the modal velocities, the radiated power is related directly to the vibration of the structure [Baumann et al., 1992]. The double summation in Equation (2.23) can be represented more cleanly in vector notation as an inner product of two vectors of length n, where n is the number of modes (p,q) considered in the analysis.

$$p(r,\theta,\phi,\omega,t) = i\left(\frac{\omega\rho L_x L_y}{2\pi^3}\right)\left[\{\dot{\eta}\}^T\{m\}\right]\frac{e^{(i\omega t-kr)}}{r} \tag{2.24}$$
$$\mathbf{m} = \frac{1}{pq}\left[\frac{(-1)^p e^{-i\alpha}-1}{(\frac{\alpha}{p\pi})^2-1}\right]\left[\frac{(-1)^q e^{-i\beta}-1}{(\frac{\beta}{q\pi})^2-1}\right]$$

It should be explicitly noted here that two separate indices are critical to understanding the relations between the structural mode shapes and the radiated power. The (p,q) indices are used to designate particular mode shapes by the number of half wavelengths in the x and y directions respectively. Considering the vector $\mathbf{m}$, it becomes tedious to have two indices for a single vector, and when considering the coupling between to modes the sequential numbering of the included modes must be used. To designate this index i (or j) will be used. For example, the first element $(i=1)$ in the vector $\mathbf{m}$ corresponds to the $(p,q)=(1,1)$ mode, the second $(i=2)$ to the $(p,q)=(2,1)$ mode, etc.

The acoustic intensity is defined as the time averaged energy density through a unit area [Norton, 1989].

$$I = \frac{1}{T}\int_0^T pvdt = \frac{1}{2}\mathcal{R}[pv^*] = \frac{1}{2}\frac{[pp^*]}{\rho c} \tag{2.25}$$

The second expression in Equation (2.25)[17] considers the pressure (p) and velocity (v) as temporally harmonic functions[18], and the third uses the characteristic impedance for a spherical wave, ρc. The radiated acoustic power is simply the integral of the intensity over a hemisphere. From Equations (2.24) and (2.25) the radiated farfield acoustic power, Π, is expressed as a vector product.

$$\Pi = \frac{k^2(\rho c)(L_x L_y)^2}{8\pi^6}\int_0^{2\pi}\int_0^{\pi/2}\left[\dot{\eta}^H m m^H \dot{\eta}\right]sin(\theta)d\theta d\phi$$

[17] $\mathcal{R}[x]$ denotes the real portion of the complex variable x.

[18] Complex notation is a convenient *representation* of harmonic signals, but physical quantity (i.e., what is measured) is the real value at any instant in time and space. The time average of real signals is simply

Where the $()^H$ operator is the hermitian, or the conjugate-transpose. Finally, noting the modal velocities are independent of the integration, a radiation matrix is defined ($M(\omega)$), and the radiated power can be expressed a simple function of this matrix and the modal velocities.

$$M(\omega) = \frac{k^2(\rho c)(L_x L_y)^2}{8\pi^6} \int_0^{2\pi} \int_0^{\pi/2} [mm^H] sin(\theta) d\theta d\phi \tag{2.26}$$

$$\Pi = \left[\dot{\eta}^H M(\omega) \dot{\eta}\right] \tag{2.27}$$

This radiation matrix is built upon the harmonic solution of the farfield Rayleigh integral. In order to realize the structural-acoustic coupling, this expression must be transformed to the time-domain, i.e., state-space. The state-space representation is also much more amenable to control design techniques, the final utility of this model. The first step toward time domain is to numerically calculate $M(\omega_i)$ for a set of frequency values and then use least squares curve fitting techniques to fit the resulting functions with rational transfer functions in the Laplace domain. It is useful to incorporate some of the *a priori* knowledge of the shape of these functions when deciding the form of the polynomial representations. This will be discussed further in the example and interpretation which follows.

Spectral Factorization

Spectral factorization is typically encountered in problems associated with stochastic processes. As will be shown, spectral factorization consists of separating a frequency domain power spectral density expression in to two expressions, one with poles and zeros in the only left half-plane and one with poles and zeros only in the right half-plane. This technique is necessary to separate the Laplace domain realization of the radiation matrix, Equation (2.27), into a stable and unstable system. This allows for consideration of just the stable system where the output of this system is shown to express the radiated power of the system. The factored system, $G(s)$, has modal velocity inputs and an output vector which yields the radiated power.

$$M(s) \Rightarrow \tilde{G}(s)G(s), \text{ where } \tilde{G}(s) \equiv G(-s)^T$$

$$\Pi = \left[\dot{\eta}^T \tilde{G}(s)\right] [G(s)\dot{\eta}] = \left[z^T z\right] \tag{2.28}$$

expressed using complex notation. The derivation is simply:

$$\begin{aligned} < \alpha(t)\beta(t) > &= \frac{1}{T}\int_0^T \mathcal{R}[Ae^{\imath wt}] \cdot \mathcal{R}[Be^{\imath wt}] dt, \text{ where } T = \frac{2\pi}{\omega} \\ &= \frac{1}{T}\int_0^T \mathcal{R}[(a+ib)e^{\imath wt}] \cdot \mathcal{R}[(c+id)e^{\imath wt}] dt \\ &= \frac{1}{T}\int_0^T (acos(\omega t) - bsin(\omega t))(ccos(\omega t) - dsin(\omega t)) dt \\ &= \frac{1}{2}(ac+bd) = \frac{1}{2}[AB^*] \end{aligned}$$

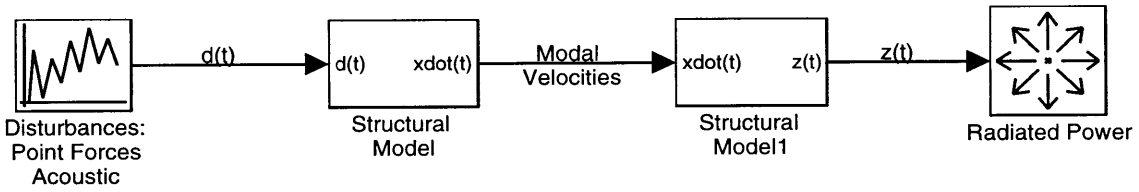

Figure 2.3: One directional coupling of structural-acoustic model

As background information, the basis for generic spectral factorization is discussed from the stochastic processes point of view [Wornell, 1997]. Spectral factorization plays a large part in forming the causal Wiener filter which is a least-square optimal estimator of some random process $x(t)$ from observations of another random process $y(t)$. Without proof, solution for the causal Weiner filter is presented.

$$H(s) = [S_{yy}^{+}(s)]^{-1} \left[\frac{S_{xy}(s)}{S_{yy}^{+}(-s)} \right]_{+} \tag{2.29}$$

were the power spectral density of the random process $y(t)$, denoted $S_{yy}(s)$ is factored into causal and non-causal portions respectively, $S_{yy} = S_{yy}^{+} S_{yy}^{-}$. The properties of power spectrums make this process fairly simple for rational representations. It will be shown that these same techniques lend some necessary insight into the factorization of the radiation filter. The construction of the radiation matrix indicated that it is very similar to the power density spectrum of a random process, sharing many of the convenient properties exploited in the spectral factorization. Again without proof the following properties of power spectral densities are stated [Wornell, 1997].

- Symmetry $\Rightarrow S_{yy}(s) = S_{yy}(-s)$
- Real-valued on $s = j\omega \Rightarrow S_{yy}(j\omega) = S_{yy}^{*}(-j\omega)$
- From both the above $S_{yy}(j\omega) = S_{yy}^{*}(j\omega)$

The symmetry condition infers that the pole zero pattern is symmetric about the $j\omega$ axis. This symmetry allows for a simple factorization when considering a spectral density represented by rational polynomials. The causal spectral factor $S_{yy}^{+}(s)$ is simply the left half plane poles and zeros of $S_{yy}(s)$, and the non-causal factor is the right half plane poles and zeros. In the following example the rational, s-domain fit of the radiation matrix will be factored in a completely analogous manner.

Appended Structural-Acoustic Model

The radiation matrix is expressed as the *radiation filter*, $G(s)$, in Equation (2.28) which expresses the power as a function of the shape velocities used in developing the Rayleigh-Ritz model. Equation (2.16) shows the state-space vibration model expression with modal

velocity states. The output of this system can be configured as the shape velocities, which allows the system to be appended with the radiation filter dynamics in order to capture the coupled behavior of the system in a single state-space model. Figure 2.3 illustrates this process pictorially.

Care must be taken in distinguishing the assumed shape functions (η) coordinates from the modal coordinates (ξ), which are linear combinations of the assumed modes expressed by the eigenvector linear transform.

2.3 Plane-Wave Acoustic Disturbance

The base assumption in the preceding development is the light fluid does not load the vibrating structure, allowing for a simplified approach. The alternative, when fluid loading is not negligible, is to consider the fully coupled problem often addressed for interior acoustic models. Applications are often aimed at mitigating the transmission of sound through a thin flexible partition. This problem is addressed by considering the representation of an acoustic disturbance, exciting the mechanical system, which in turn radiates acoustic energy. The

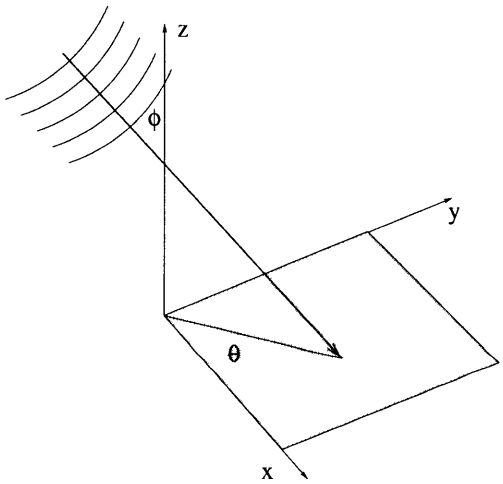

Figure 2.4: Incident Acoustic Plane Wave Disturbance

disturbance model considers an acoustic *plane wave* impinging the panel from an arbitrary direction. The development follows the analysis in [Fahy, 1985] for a baffled plate. The panel responds to the total acoustic field present at the interaction surface, which is a sum of the blocked pressure, due to the incident acoustic disturbance, and the radiated field due to panel motion. The latter term can be evaluated by considering a standard wave number transform which decomposes vibration of the finite panel into infinite spatial wave components in the same manner that a function in time can be represented, using a Fourier transform, as a function of contributing temporal frequencies. The impedance function of infinite waves is used to determine the radiated, near-field pressure, and the inverse

transform yields an expression for the radiated field as a function of the modal velocity contributions. The surface pressure is thus represented by two terms, the first a pressure due to the modal velocity and the second due to the incident pressure wave.

$$p_f = p_1(\dot{\eta}) + p_2(P_i)$$

Because the first term is a function of the modal velocity it effects the viscous damping of the system. Since the damping in the structure is an assumed or identified quantity, this term can be safely neglected from the formulation without consequence.

With this assumption the pressure disturbance can be quantified by simply considering the blocked pressure from the incident plane wave. Consider an impingent acoustic wave described by the wave number k, the complex amplitude P_i, and the direction of propagation with relation to the panel described by ϕ and θ as shown in Figure 2.4. The one dimensional acoustic wave is doubled due to the reflection of the hard boundary, and projected onto the flat panel. In keeping with the approach derived for the Rayleigh-Ritz model, the product of the pressure with each shape function ($\Psi_\eta(x,y)$) is integrated over the panel area to express the generalized force in the shape function generalized coordinates.

$$F_m = 2P_i \int_0^{L_x} \int_0^{L_y} \Psi_\eta(x,y) e^{-k[sin(\phi)cos(\theta)x - sin(\phi)sin(\theta)y]} dx\, dy \tag{2.30}$$

Equation (2.30) shows that this disturbance will be a function of the acoustic frequency by the dependence on the wave number of the incoming wave. The influence of a particular incident wave on a particular mode of vibration will vary with the frequency of excitation. This dependence is not present for the normal plane wave which is simply the area integral of each mode. For this special case where $\phi = 0$, a normal plane wave can only excite volumetric modes of the system, i.e., non-volumetric modes, by definition, have mode shapes with integrate to zero. This type of acoustic disturbance is seen to be fundamentally different from the mechanical disturbances (point forces, active elements, etc.) in that the disturbance only excites the modes which radiate efficiently. An example of the difference between disturbance types is included in the later discussion on actuator placement.

2.4 Modeling Example - Composite Test Panel

The implementation of this model is shown to converge to the exact solution for simple panel structures and the model is experimentally verified in the results which follow. To communicate the implementation of this approach, an example is explained in detail. For consistency, this example is the model of the experimental design detailed in later chapters. The 12x10.3" quasi-isotropic laminate model is solved assuming nine simply supported shape functions and integrating using twelve point two dimensional Gaussian quadrature. The model represents the response of an integrated composite structure to three inputs:

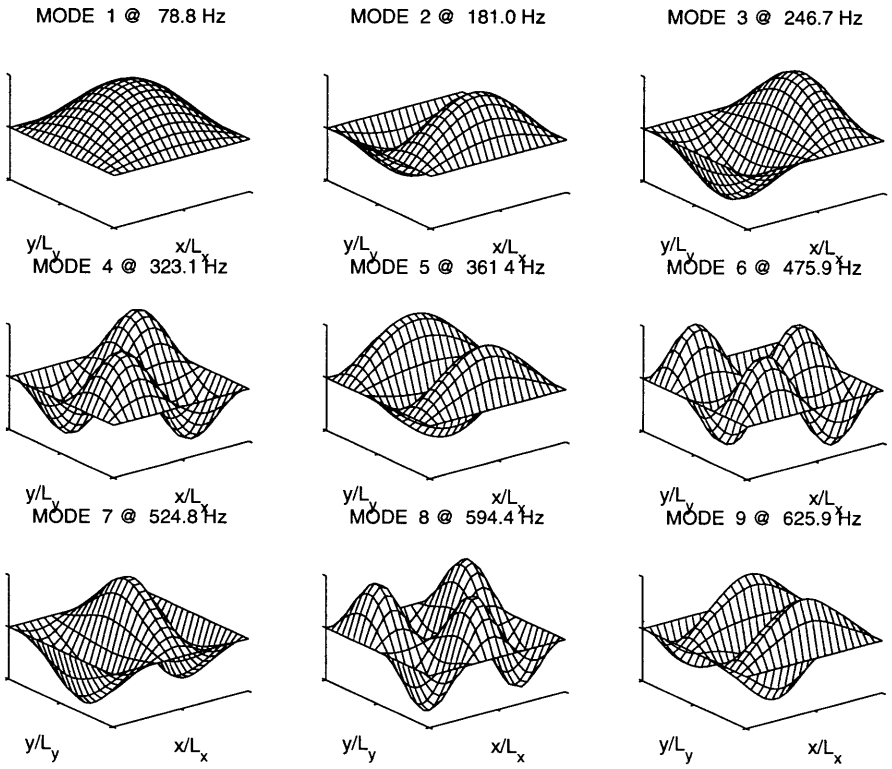

Figure 2.5: First Nine Mode Shapes for a Simply Supported Composite Panel with Embedded Active Fiber Composites

point forces, four symmetric AFC actuators, and an incident plane wave normal to the surface. The three input, 18 state, state-space structural model which results can be arranged with a variety of outputs. The matrix eigenvalue problem results in the mode shapes and natural frequencies shown in Figure 2.5. The eigenvectors represent the relative contribution of each assumed mode to these natural shapes. By comparison with the assumed shape function in Figure 2.1, the composite layup is observed to behave in a similar manner to the isotropic panel for which the modes are exact. The added mass and stiffness of the embedded active elements add a degree of inhomogeneity to the structure and the fiber composite lamina are not isotropic, causing the modes to differ slightly from the assumed shapes.

The acoustic model is independent of the particular dynamics of the panel and can be formulated with just information on the assumed modes for the solution. As long as the motion of the structure can be accurately described using these simply supported panel modes, the radiation filter that is appended to the Rayleigh-Ritz model shall determine the farfield radiated power.

Calculation of the terms of the radiation matrix $M(\omega)$ is a computationally intensive task. The closed-form solution to the Rayleigh integral for the panel mode identified by the

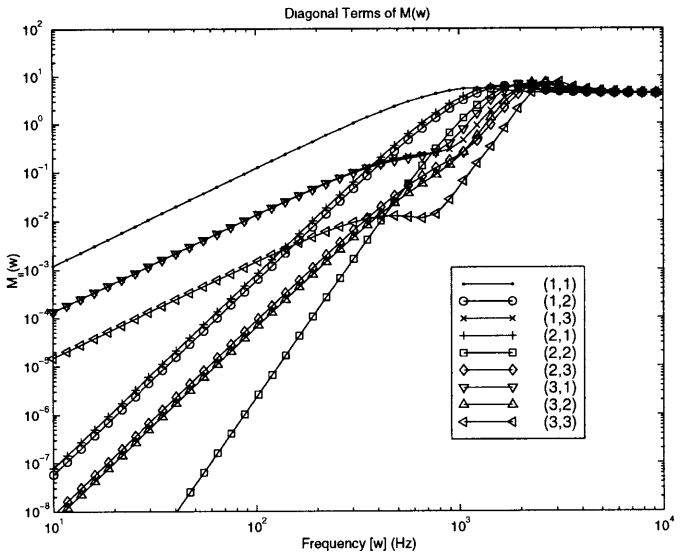

Figure 2.6: Diagonal Terms of the Radiation Matrix, $M(\omega)$.

indices (p, q), Equation (2.24), allows for a direct solution of the vector $\mathbf{m}$ dependent on the three variables θ, ϕ, and ω. At each harmonic frequency, ω, Equation (2.26) is numerically integrated using Gaussian quadrature. This two dimensional integration is performed over a range of values for the harmonic frequency yielding a set of matrices, $M(\omega_i)$, defining the relationship between the modal velocities and radiated power as a function of frequency, Equation (2.27). Figure 2.6 shows the diagonal terms of these matrices as a function of the acoustic frequency. The integration is done using 40 point 2-D Gaussian quadrature integration over a hemisphere for 50 frequency values. The legend in the figure refers to the mode shapes, as indexed by (p, q), represented by each trace. This should not be confused with the (i, j) indices which refer to the locations of elements within the nxn matrices, $M(\omega_i)$[19]. The interpretation of this result is very important to the understanding of the panel radiation problem. For now just the self-radiation terms, represented by the diagonal terms of the $M(\omega)$ matrices will be considered, and the significance of the coupling, off-diagonal, terms will be treated next. A non-dimensionalization of the radiation matrix is accomplished by defining the *radiation efficiency.*

> *Radiation Efficiency* - σ: For any described velocity profile, the radiation efficiency is defined as the ratio of the radiated power of the panel with the prescribed vibration profile to the vibration of a rigid piston operating with the same temporally and spatially averaged velocity.

Relying on the far-field assumption, the power can be calculated in closed form for the

[19]For example the mode shape (3,3) maps to the (9,9) location in the radiation matrix, i.e., corresponds to the 9^{th} mode.

radiation from rigid piston [Norton, 1989].

$$\Pi_{piston} = \frac{1}{2}\rho c A_s V_n^2 = \rho c A_s < |V_n^2| >$$

Where $< |\cdot| >$ denotes the time average of the uniform normal velocity and A_s is the surface area of the piston. From the expression for the power radiated by the vibrating panel, the assumed shape functions, and complex analysis, the power radiated by a single panel mode (p, q) can be expressed in terms of the averaged velocity.

$$\begin{aligned} < |V_n^2| >_{(p,q)} &= \frac{1}{T}\int_0^T \int_0^{L_x} \int_0^{L_y} \mathcal{R}\left[\dot{\eta} e^{i\omega t} \sin\left(\frac{p\pi}{L_x}\right) \sin\left(\frac{q\pi}{L_y}\right)\right]^2 dx\, dy\, dt \\ &= \frac{1}{8}\dot{\eta}^2 \end{aligned}$$

The radiation efficiency of a single mode shape can then be expressed as a function of the corresponding diagonal term in the radiation matrix.

$$\sigma_i = \frac{\Pi_{panelshape(i)}}{\Pi_{piston}} = \frac{8}{\rho c L_x L_y} M_{(i,i)}(\omega) \tag{2.31}$$

The conclusion here is that the radiation efficiency, treated in most acoustic texts as a means for studying radiation from the flexural waves of a panel, can be determined by a constant scaling of the radiation matrix. To further generalize this analysis, the frequency dependence of the modal efficiencies is normalized by the *critical frequency.* The critical frequency corresponds to the matching of the acoustic wave number and flexural wave number. In the analysis of an infinite plate, the impedance of the traveling wave drops to zero at the critical frequency, indicating infinite radiation [Norton, 1989]. Conceptually, this occurs due to the coincidence of the wavelengths of the acoustic perturbations and the flexural wave. The relationship changes with frequency due to the dispersive nature of the solution to the fourth order plate wave equation[20]. To consider the critical frequency of an individual mode of a panel, the structural wave number comes directly from the mode shape, $(k_p \equiv \sqrt{\left(\frac{p\pi}{L_x}\right)^2 + \left(\frac{q\pi}{L_y}\right)^2})$. Normalizing the acoustic wave number $(k \equiv \omega/c)$ by the structural wave number illustrates the behavior for finite structures where the radiation efficiency asymptotes to unity.

The low-frequency region of the radiation efficiencies plotted in Figure 2.7 indicates how well each of the mode shapes radiates sound power. The conclusion is well known, the modes with an odd number of half wave lengths radiate most effectively. This is intuitively verified by considering the volume velocity of each of the mode shapes. For even modes, the net volume displaced is zero, while for odd modes there is a positive displacement of fluid,

[20]The eigenvalues of the plate wave equation show that the wave number is proportional to the *square root* of the frequency. On the other hand the second order wave equation for the acoustic medium yields a linear relation between wave number and frequency, so that at only one frequency will the wavenumbers (and hence wavelengths) be equivalent.

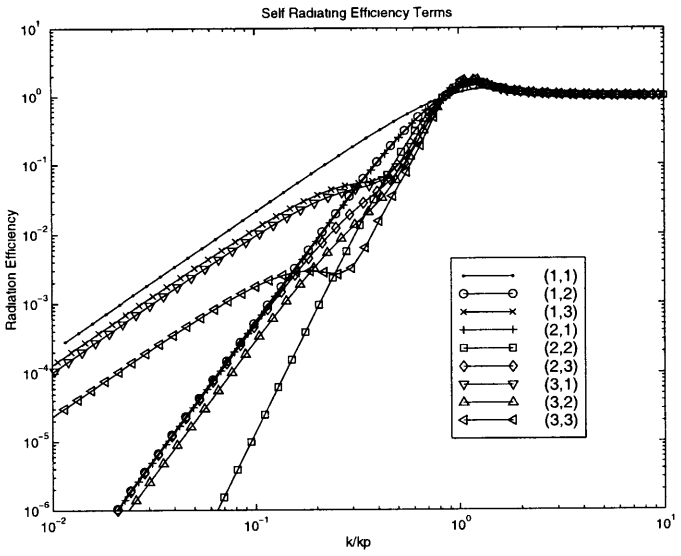

Figure 2.7: The radiation efficiency (σ) for the modes of a simply supported panel

causing acoustic transmission. Care must be taken to recall the assumptions made in this development. The far-field ($r \ll a$) consideration is not restrictive, because conservation of energy demands that energy in the far-field also be present in the near field, but the low frequency restriction ($ka \ll 1$) indicates that this analysis is only accurate below the critical frequency. For this example, the structural resonances are well below that critical frequency, making the error negligible, but it shown that the high frequency asymptote is correct as the radiation efficiency approaches unity. The panel radiating with a certain shape function performs like a rigid piston as the wave lengths become small compared to the panel dimensions.

The numerical solution to the harmonic Rayleigh integral yields a matrix ($M(\omega_i)$) at each frequency of excitation. When taken collectively for a set of frequencies, each term represents a vector in the frequency domain characterizing the frequency response of the radiation filter. Each term is fit with a Laplace domain transfer function. By construction, the individual terms in the matrix system ($M_{i,j}(s)$) must have pole/zero symmetry about the $j\omega$ axis, be real valued, and have equivalent numerator and denominator order to capture the high frequency asymptote.

$$M_{(i,i)}(s) = \frac{(s^2 - a_1^2)(s^2 - a_2^2)\dots(s^2 - a_n^2)}{(s^2 - b_1^2)(s^2 - b_2^2)\dots(s^2 - b_n^2)} \tag{2.32}$$

For each term (i,i)a set of parameters (a's adn b's) describes the transfer function. Each term is fit by optimizing these parameters of the transfer function model in Equation (2.32). The order of the model used is adaptively chosen based on a simple least-square approximation of the low-frequency slope, thus minimizing the number of degrees of freedom necessary

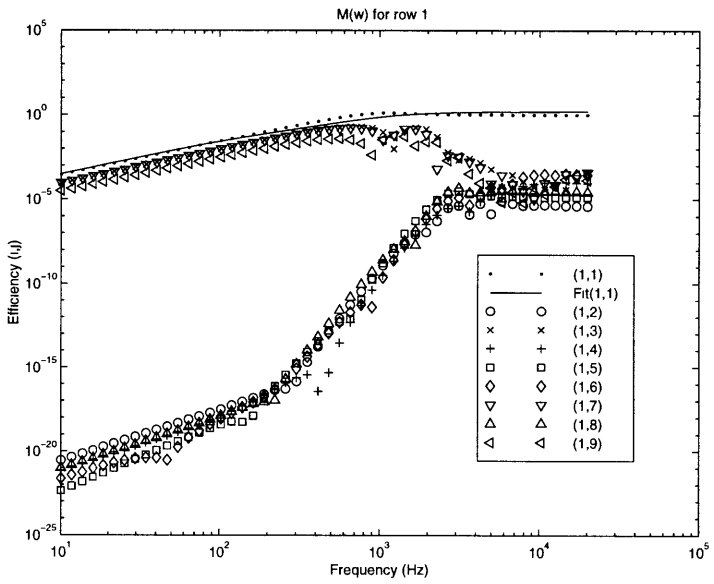

Figure 2.8: Terms of the First Row of the $M(\omega)$ Matrices Along with the Least Squares Fit of the (1,1) term

to achieve an accurate representation. Figure 2.8 illustrates this process by showing the terms of the first row of the matrix for all frequency values. The indices in this and the following figures refer to the i, j terms of the matrices and should not be confused with the (p, q) indices describing the assumed panel modes. From the relative magnitudes of the terms, it is clear that the coupling (off-diagonal) terms can not be neglected in the formulation. This row of the matrix illustrates that the (1,3), (1,7), and (1,9) terms are significant. These terms in the matrix map to coupling between the odd-odd modes of vibration. Similarly, by examining the rows and columns of the matrices, the significant coupling terms can be identified. For this nine mode example the following panel modes were found to exhibit significant coupling

$$(1,1) \leftrightarrow (1,3) \leftrightarrow (3,1) \leftrightarrow (3,3)$$
$$(1,2) \leftrightarrow (3,2)$$
$$(2,1) \leftrightarrow (2,3)$$
$$(2,2) : \text{No Coupling}$$

The spectral factorization of the multiple-input, multiple-output system is a challenge. If the off-diagonal coupling terms are neglected the system decouples and the factorization can be done directly by utilizing the pole/zero symmetry of the model to split the transfer function into right and left plane poles and zeros. However, it has been shown, from the above discussion and in [Snyder and Tanaka, 1995], that these terms cannot be disregarded without compromising the accuracy of the solution.

Three main methods are suggested for the spectral factorization of the full system, $M(s)$. A direct approach is taken using a method derived in [Francis, 1987]. Francis develops a factorization algorithm for state-space systems with few restrictions. This process, while theoretically straight forward, is difficult to implement. The algorithm demands the solution of a standard algebraic Riccati equation that experience shows can be numerically unstable. Solutions were possible for a few cases where the coupling between modes (off-diagonal terms in M(s)) was ignored, but in general the solution failed due to the eigenvalues of the associated Hamiltonian matrix which approached the jw-axis. Another method has been developed in [Overschee et al., 1997], particularly for power spectral factorizations. The method is again algorithmic, and relies on subspace techniques to derive a factorization.

The method which was most successful in this analysis is also the simplest. It is suggested in [Baumann et al., 1992], that the individual matrices may be factored, using Cholesky decomposition, and then the spectral factors ($G(s)$) could be realized directly in the Laplace domain in order to approximate $M(s) = \tilde{G}(s)G(s)$. Each matrix, $M(\omega_i)$, is factored using an eigenvalue decomposition[21]. From the eigenvalue solution at each frequency point, M can be factored into a new set of matrices $G(\omega_i)$. This is equivalent to taking the matrix square root of each data point.

$$M(\omega_i) = V\Lambda V^T = G^T(\omega_i)G(\omega_i), \text{ where } G(\omega_i) = \sqrt{\Lambda}V^T \tag{2.33}$$

For the example followed here, all 50 matrices are factored using Equation (2.33). The eigenvectors are sorted and normalized so that the diagonals of V are the maximum values for each eigenvector and positive. This makes physical sense because the natural modes of vibration are similar to the *radiation modes* explained by [Johnson and Elliot, 1995]. This step can be thought of as decomposing the radiation into such radiation modes at each acoustic frequency. Since these roughly correspond to vibration modes, each eigenvector is dominated by one entry indicating the contributing mode. If this step is not included, the difficulties recounted in [Dehandschutter et al., 1997] are encountered, i.e., an *a priori* parameterization is difficult to discern. By consistently ordering the eigenvectors in this manner, the cross-coupling between modes (resulting from the off-diagonal terms of the radiation matrix) is reduced, thus reducing the order of the realization required to capture the behavior.

The matrices $G(\omega_i)$ represent a multi-input, multi-output, system in the frequency domain. In order to model this system, the characteristics already discussed are used to arrive at a simple, low order model, capable of representing the system. A frequency domain, nonlinear, least-squares fitting method is used to match the parameters of the model with

[21] From construction $M(\omega)$ is guaranteed positive-definite and real-valued; therefore the decomposition $M_i = V\Lambda V^T$ will exist, the eigenvalues are real and positive, and the eigenvectors are real.

numeric solution for the radiation matrix at each frequency. The optimization utilizes a logarithmic frequency-domain cost function that is found to work well for structural systems with large amplitude variations [Jacques, 1994]. From direct factorization (separating the right and left half-plane poles and zeros) of the model used for the $M(s)$ terms, a stable causal model for fitting the $G(s)$ terms is shown.

$$G_{(i,j)}(s) = K * \frac{(s-a_1)(s-a_2)\dots(s-a_n)}{(s-b_1)(s-b_2)\dots(s-b_n)} \tag{2.34}$$

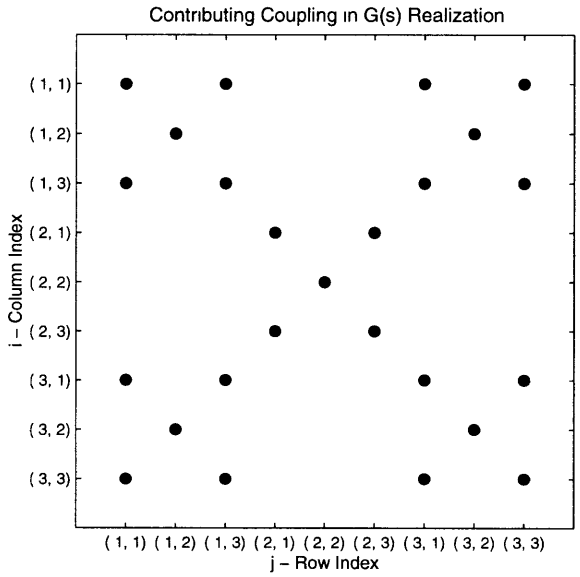

Figure 2.9: Representation of Coupling Terms in the $G(s)$ System

For each term in the radiation matrix, the algorithm automatically determines whether the individual term is significant[22] and selects the order of the system, n, to satisfactorily represent the low-frequency slope of the numeric solution. Figure 2.9 illustrates the significant coupling terms identified in the decomposed matrices, $G(\omega_i)$. The coupling between particular mode shapes, as indicated by the axes on the figure, shows the same intuitive relation explained in terms of the $M(\omega_i)$ solution, i.e., the coupling of like modes tends to be significant when calculating the radiated power - odd modes couple with odd modes and even modes couple with even modes.

As an example of the fitting procedure, Figure 2.10 shows the significant elements from the eigenvalue decomposition, $G(\omega_i)$, and the corresponding Laplace domain systems used to fit the radiation response. Similar plots showing the fitting results corresponding to each row of the radiation matrix are included in Appendix A. The high frequency points in the

[22]The tolerance of 1% was implemented by determining the 2-norm for each term of G over the frequency range was approximated yielding a single nxn matrix. Significant terms were identified by normalizing this matrix and neglecting terms less than the prescribed tolerance.

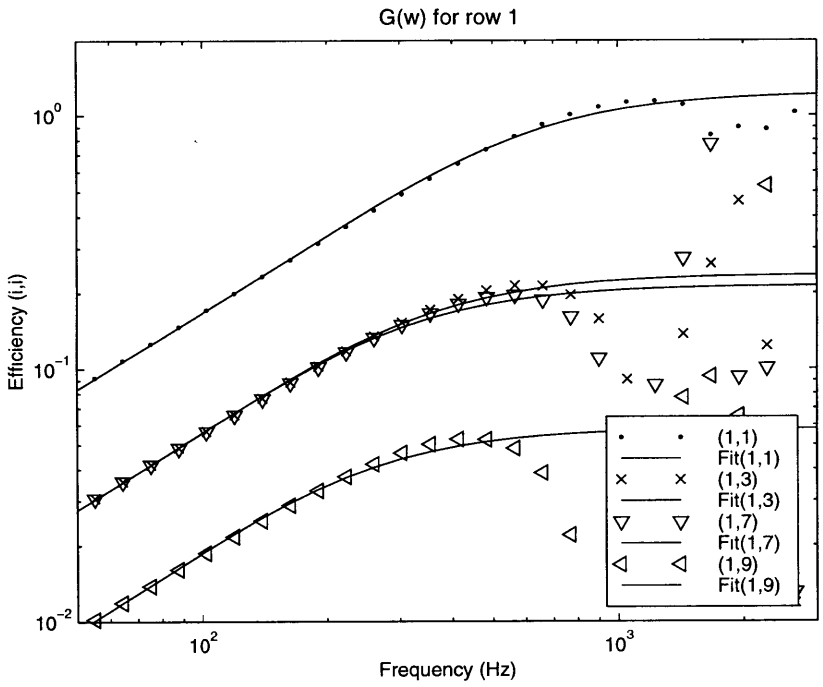

Figure 2.10: Realization of $G(s)$ Systems Corresponding to the First Row of the $G(\omega_i)$ Solution

data are not considered in the fitting in order to capture the correct asymptotic properties and the low frequency slope. This is justified in two ways: first the resonant response of the particular modes are found to be well below the corresponding critical frequency and, as the frequency approaches the critical/coincident frequency, the farfield assumptions are invalidated as the acoustic wavelength approaches the characteristic length of the panel.

To verify the least-squares fitting and spectral factorization algorithms, the acoustic radiated power predicted by the *radiation filter* $G(s)$ is directly compared to the same solution from the harmonic solution for the individual matrices, $M(\omega_i)$. A simple test is performed using the fully coupled structural-acoustic model. For this example recall that the nine mode vibration system contains 18 states corresponding to the shape velocities and displacements. The state-space equations are assembled such that the input to the system is an off-center active fiber composite actuator that can be shown to excite all the modes of the structure[23]. The output of this system is simply the 9 shape displacements, η. It should also be noted that a modal damping ratio of $\zeta = 1\%$ was used in this example. In Figure 2.11 three methods of realizing the harmonic solution for the radiated power as a time-domain state space model are compared. A benchmark for comparison is set by first calculating the frequency response of the structural system with modal velocity

[23]This excitation serves as the disturbance source in the later control examples and experimental implementation.

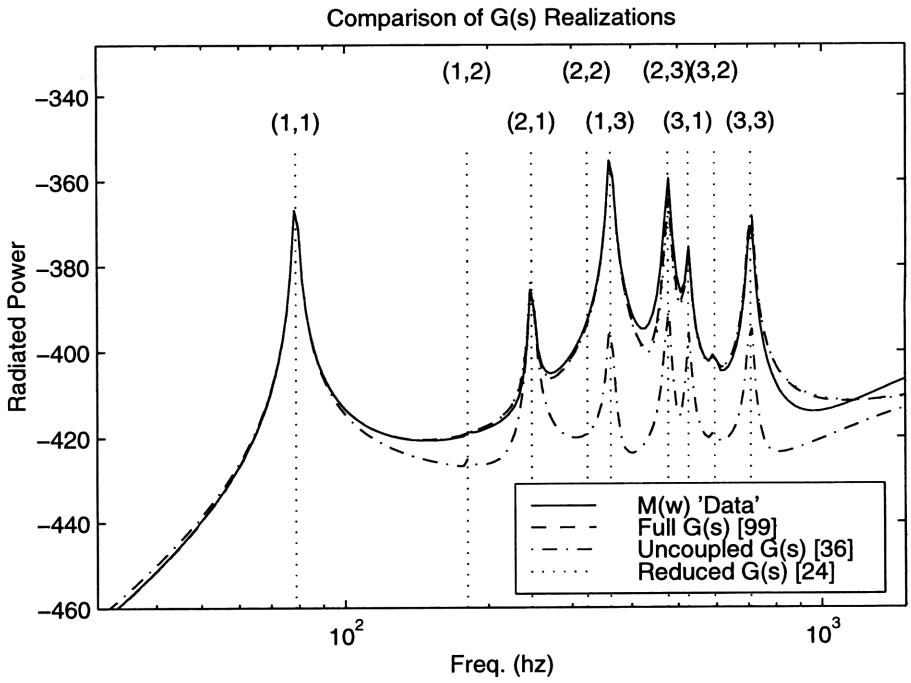

Figure 2.11: Comparison of Realizations of the G(s) Radiation Filter

output ($z(\omega)$). The power spectral density (PSD) of the radiated power can be calculated directly from the numerical solutions ($M(\omega_i)$) by taking the general inner product ($PSD = z^T M z$) at each frequency point. This is shown by the trace labeled [M(w) 'Data'] in the figure. The validity of the eigenvalue decomposition method and frequency-domain fitting algorithm is ascertained by calculating the frequency response of the coupled structural-acoustic system using the full, 99 state, radiation filter. This trace, labeled [Full G(s)] shows almost exact correlation. To emphasize the importance of including the coupling effect in the formulation, a 36 state radiation filter just using the diagonal, or uncoupled, terms of the filter as illustrated by the trace labeled [Uncoupled G(s)]. Neglecting this phenomenon results in a large underestimation of the radiation by the higher modes of the structure. Finally a reduced balanced realization ([Zhou et al., 1995]) is presented in the form of a 24 state, fully coupled radiation filter. Comparison of this trace, labeled [Reduced G(s)] shows that it produces the same power spectrum as the full system with a much lower order model. This lower order realization results in a lower-order compensator in the following examples and implementation. Reduced order compensators offer practical advantages for implementation. The size of the system introduces increasing computational load which reduces the available bandwidth. To implement compensators with high frequency content, the size of the filter must be sufficiently small to satisfy these hardware constraints.

2.5 Summary

A general development of the structural-acoustic model used for control and design is presented in detail to give insights that will be indispensable for the system design and control to follow. The Rayleigh-Ritz formulation for a classical laminated plate is presented in full as is the derivation of the expression for the radiated power from the simple, exact solution for the simply-supported eigenfunctions. The acoustic model quantifies the intuitive notion of radiation efficiency of the mode shapes of the panel. The final result is a coupled structural-acoustic model mapping the various inputs to the farfield radiated power. This state-space representation will be shown to be essential to the modern control design, allowing the tools of structural control to be utilized for acoustic control.

Chapter 3

Design for Structural-Acoustic Control

This chapter presents the design of the experimental test article, a composite panel with embedded sensing and actuation, used to evaluate the closed-loop performance of various structural-acoustic control methods. First the experimental geometry is presented as a design compromise between application relevancy and experimental practicality. The sensor-actuator architecture is examined with the goal of selecting a configuration that will provide the best controlled performance.

The choice of sensors and actuators for a controlled structure greatly impacts the final performance. As discussed in the introduction, Chapter 1, space, weight, and performance requirements motivate using structural sensing and actuation to mitigate radiated acoustic power, generally termed active structural-acoustic control (ASAC). By combining the sensor-actuator insights developed within the controlled structures field with an understanding of the physics of the fluid-structure interaction, the appropriate architecture for ASAC was chosen to yield the best performance.

The scope of this analysis is narrowed by the consideration of a single type of actuator. This work focuses on the capabilities of active fiber composite (AFC) actuators for structural-acoustic control. Piezoelectric elements operate as strain inducing actuators without inertial reaction, and can therefore satisfy system requirements that are unattainable using inertial actuation (e.g., shakers or point force transducers). For example, the space inside a torpedo hull is not sufficient to incorporate reacting actuators. Application to aircraft cabin noise are severely weight restricted. The added mass of shaker or loudspeaker actuators is often too costly to implement. This chapter focuses on two design issues, what type of sensors will be best suited for the subsequent control design, and where to place the actuator and sensor elements. The two problems will be treated separately.

3.1 Panel Experiment Design

As explained in Chapter 1, a single panel is used in this work as a representative structure to capture the relevant physics of the structural-acoustic control problem while remaining simple enough to allow a thorough analytical investigation. As a representative structure, the design of this experiment does not attempt to represent a single application. Instead it intends to be a reasonable compromise, incorporating a sense of the widely varied applications which stand to benefit from active structural-acoustic control (ASAC) and the inherent restrictions of experimental implementation. In order to arrive at a design that accomplishes this, the target applications are considered to determine the range of geometric and dynamic parameters that exist, thus allowing the application to drive the design of the experimental article.

Application Dynamics

Three target structures were identified for this work in the introduction: aircraft interiors, satellite launch shrouds, and naval weapons. A brief listing of the elementary dynamics of each is explored in order to provide a bit of background and to justify the experiments performed.

The basic airframe design can be considered as a supporting frame covered with a thin skin. This design allows for a decoupled analysis of each panel defined by the ribs and stringers which provide structural as well as computational boundaries. A single panel structure is representative of the first-order dynamics of such a system and serves as a starting point for understanding the structural-control of aircraft interiors. To design a panel that will capture the issues inherent to the problem, the actual airframe design of a few aircraft are considered.

	DC-9‡	**DC-10†**	**Boeing 747†**	**Boeing Chinook47‡**	**Experiment**
Stringer Spacing(cm)	23	20.3	24.13	0.31-0.76	30.5
Frame Spacing(cm)	48	50.8	55.9	51-100	26.3
Aspect Ratio	2.08	2.50	2.32	1.31-1.65	1.16
Skin Thickness(cm)	0.16	0.18	0.18	0.05-0.1	0.159
Typical Radius(cm)	165	301	325	Flat	Flat

Table 3.1: Panel Geometry for Various Aircraft[1]

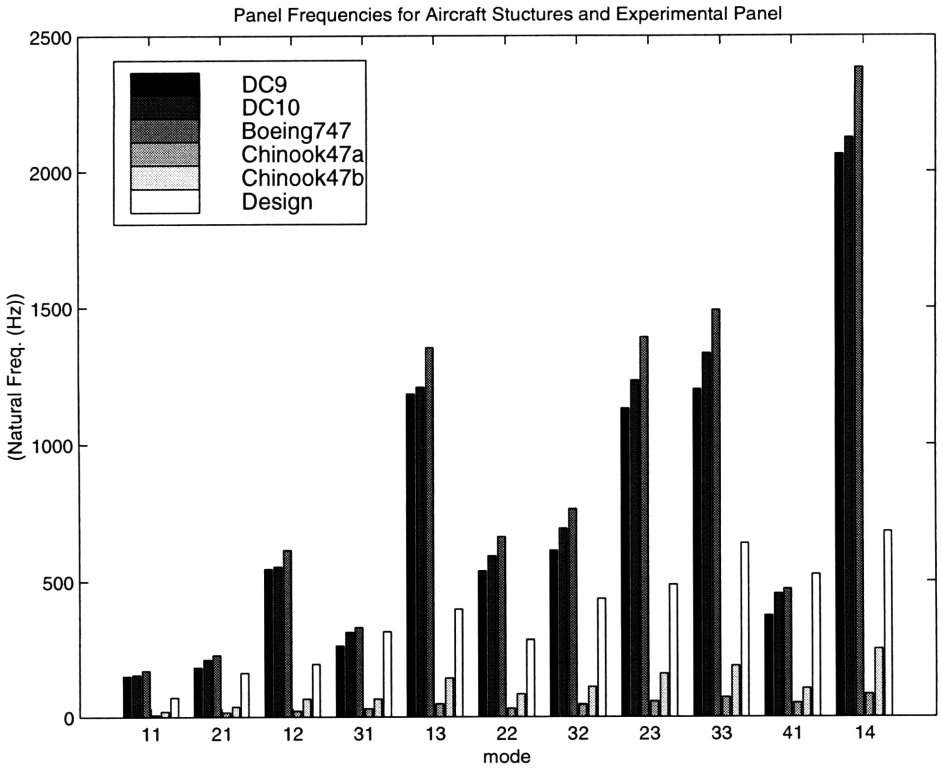

Figure 3.1: Comparison of Panel Frequencies for Aircraft Structures

Assuming the riveted or spot welded skin attachment provides a boundary condition similar to a pinned case, as simple analysis is performed to get an idea of the panel mode frequencies for these structures and compared with the experimental implementation of this thesis. Figure 3.1 compares the dynamics of these examples. In general it can be seen that this experiment exhibits resonant frequencies lower than the curved panels of typical cylindrical airframes, but higher than the Boeing Chinook helicopter example with flat fuselage surfaces. This analysis gives an indication that the resonant behavior of the experiment in relation to the the aircraft interior application and shows that the modal dynamics are within the range of the target applications.

The payload shroud on a satellite launch vehicle cannot be analyzed as simply. For a 16.7-Ft diameter aluminum isogrid Titan IV payload shroud the external acoustic spectrum peaks between 100 and 200 Hz with significant levels from 30 Hz to 3500 Hz [Masters, 1998]. This gives an empirical indication of the frequency range of interest for this application. Work at Boeing on the Sea Launch program performed simple closed-loop experiments to simulate the launch shroud with a large, 10-Ft square, flat panel with a first resonant mode near 25 Hz [Morris, 1998]. While the first panel mode of the experimental testbed for this thesis is considerably higher, near 80 Hz, it is within the range of the targeted dynamics of

[1]†- [Niu, 1988] ‡- [Fripp et al., 1997]

the application.

In reaction to motivation to retrofit the existing naval torpedo cache with a noise reduction system, work at the Naval Undersea Warfare Center (NUWC) has experimentally investigated the radiation from a Mark 48 torpedo section. A 10" diameter tube was used as an approximation of a vehicle hull and found to radiate significantly when operating at a 688 Hz resonant mode [McDowell, 1998].

Experimental Dynamics

The previous discussion is included to provide an indication of the dynamic frequency range of interest, both for the structural disturbance and the acoustic performance. The conclusion is that the dynamics of concern vary from sub-audible frequencies on the order of 10 Hz up through 1 kHz where passive treatments become a more efficient option. Certain practical constraints on the panel geometry must also be addressed. Specifically it is desirable for the panel to be manufactured from a standard cure procedure which is setup to produce 12x14" composite plates [Lagace, 1988]. Also the characteristic length of the panel must be sufficiently small to allow for farfield measurements within the existing anechoic facilities, i.e., $R \ll a$ and $ka \ll 1$, were R is the measurement distance, a is the characteristic dimension, and k is the acoustic wave number. Finally the aspect ratio of the panel is chosen to yield a degree of modal separation in the bandwidth of concern, allowing for simpler experimental identification of constituent modes. The final design used for this work and described in detail later in the chapter has dimensions of 12x10.3" to satisfy these requirements. The nominal bandwidth of the structure begins with the first resonance near 80 Hz with at least nine resonant modes below 1 kHz, allowing for acceptable modal density to simulate the difficulties of high bandwidth structural-acoustic control.

No panel can truly represent completely the dynamics of the full structural-acoustic control problem, but to understand the problem we must start with a simple structure that can be accurately modeled and experimentally tested. The actual design of this experiment is still unique, and by understanding that the goal is not to create a methodology for controlling a panel, but to use the insight of this representative problem as a step toward implementation of structural based acoustic control, a reasonable compromise is made.

3.2 System Topology - Sensor Choice

The topology of a controlled structure defines the relationships between the inputs (disturbances: d(s) and control: u(s) signals) and the outputs (performance: z(s) and measurement: y(s) sensors). Much research has gone into quantifying the fundamental relationships that pervade. A few definitions supplied by [Fleming, 1990] and [Campbell, 1993] lend a framework considering these relations.

Type The type of sensor or actuator is defined by the spatial distribution and impedance.

Dual A sensor/actuator pair is termed dual if the sensor and actuator are both of the same type.

Analogous Outputs or inputs are defined as analogs if there exists an explicit expression of the relations: $z(s) = \phi_{zy}(s)y(s)$ or $d(s) = \phi_{du}(s)u(s)$ respectively.

Collocated A sensor/actuator pair is termed collocated if they are the dual and have the same spatial location, i.e., collocation implies duality.

This quantification of the system architecture lends insight into the behavior of the closed-loop structure. The behavior of the compensator and thus the closed-loop performance is investigated by [Campbell, 1993] for possible combinations of these topologies. [Fleming, 1990] illustrates how these relations translate to the placement of the zeros of the SISO transfer functions and thus the control performance.

For the control designs explained in Chapter 5, the results are based on a special topology that has been shown to have beneficial properties. Collocated, dual sensor/actuator pairs are known to produce a *positive real*[2] transfer function with an alternating pole zero pattern. The benefits for this simple architecture are explained briefly in the control design explanation of this thesis and extensively in [MacMartin, 1990]. This result is very important for local, low authority, control designs because it guarantees the *hyperstability* of theoretical rate feedback yielding infinite robustness. The benefits of such collocation and duality for optimal control designs is generalized for structural applications in [Campbell, 1993].

Arguably the most important characteristic of a sensor/actuator pair is the *roll-off*. Any control implementation must address the unmodeled or mis-modeled high frequency dynamics. Considering the stability of the compensator in terms of typically frequency domain design concepts, one method of doing this is to reduce the loop gain with increasing frequency. Low loop gain indicates a gain stabilized control loop (i.e., the loop will be stable independent of the phase characteristics). To lower the loop gain the designer must introduce dynamics into the compensator. This roll-off filter is typically realized by introducing real or complex poles into the compensator. The trade-off is that these dynamics introduce inherent phase loss which tends to destabilize the design, i.e., reducing the original gain margin. Ideally the system design would take this into account, selecting a sensor-actuator architecture that has inherent roll-off. By examining the fundamental physical relationships during the system design step, the control design step can be greatly simplified.

[2] A Laplace-domain function is termed positive real if, $G(s) \geq 0$ for all (s). For input/output transfer functions this is observed as phase bounded by $\pm 90°$ for all frequencies

To quantify the trade-offs between different types of sensor/actuator pairs, a simple analysis is presented to illuminate the fundamental comparisons. Considering only collocated pairs, the basic relationship between the control input and sensor output can be defined by the *dereverberated transfer function.* As explained by [MacMartin, 1990], the dereverberated transfer function describes the fundamental physical properties of a sensor/actuator pair independent of the particular structure boundaries. It also defines the bandwidth of the controller, or the *regions of control* defined by the controlled structures technology paradigm [Crawley et al., 1995]. The dereverberated transfer function can be evaluated in three ways: considering the infinite wave model, cepstum analysis, or applying critical damping to the reverberant model. The former method is most intuitive since for collocated pairs it essentially ignores the reflected energy from the boundaries considering only the local impedance relationship between the sensor/actuator power pair. The next section includes a single example of the wave model for illustration, followed by a summary of similar results for a variety of candidate pairs.

Wave Model of Dereverberated Transfer Functions

The following analysis is based on the governing equation of a one-dimensional beam, but the resulting insight is shown, through illustration, to be fundamental to the sensor/actuator relationships. The key steps in the development are highlighted, but a more comprehensive account of the solution can be found in [Fahy, 1985]. The wave equation for a Bernoulli-Euler beam is expressed as a fourth order partial differential equation. A closed form solution is found by assuming a general wave solution in spatial and temporal coordinates.

$$Dw^{IV}(x,t) + \ddot{w}(x,t) = f(x,t), \text{ where, } D = \frac{EI}{m}$$
$$w(x,t) = Ae^{-i\omega t \pm kx}$$

The non-reflecting, infinite boundary allows the solution to include only the outward traveling wave (the positive k term). Substitution yields the *dispersion relation* between the temporal frequency and the spatial wave number.

$$\begin{aligned} k &= \pm \sqrt{\omega}\,(D^{1/4}) \\ &\quad \pm i\sqrt{\omega}\,(D^{1/4}) \end{aligned}$$

Considering a point force at location $x = 0$ on an infinitely long beam, the boundary conditions are implicitly defined to match the reaction force and to preserve slope continuity across the boundary. Solving for the displacement due to application of the point force F_o, the dereverberated transfer function for point force to displacement is expressed.

$$\frac{w(0,t)}{F_o} = \frac{1}{k^3}\frac{\sqrt{2}}{EI}e^{-i(\omega t + \pi/4)}$$

To condense the result, the dependence on the material properties can be removed, explicitly highlighting the frequency dependence of the relationship.

$$\frac{w}{F} \propto \frac{1}{k^3} = \frac{1}{\omega^{3/2}} \tag{3.1}$$

This simple relationship indicates the slope of the dereverberated transfer function. Typically represented through Bode plots in the frequency domain, this particular relation yields a logarithmic slope of -30 decibels per decade. A general analysis of a host of typical sensor and actuator pairs is presented in [McCain, 1995]. These results follow directly from this simple example by recalling the fundamental differential relationships from mechanics of materials. Again, the dependence on the material properties can be ignored so that the physical insight is clear.

Slope $\theta = w' = kw$

Differential Slope [3] $\Delta\theta = w'' = k^2 w$

Moment $M_o \propto \frac{d^2w}{dx^2} \propto \frac{1}{k} F_o$

Couple Moment $m_o \propto \frac{dM}{dx} \propto F_o$

To consider the distributed action of piezoelectric sensors and actuators, the actuation can be considered as an applied couple moment and the sensor output as a differential slope or equivalently a strain signal [Crawley and Lazarus, 1989]. These simplified relations allow the dereverberated slope to be calculated for a variety of canonical sensor and actuator pairs. The dispersion relation is used to express each in terms of the temporal frequency of excitation. Recalling that the hyperstability guarantee is associated with rate feedback compensation, the results are presented in Table 3.2 for *power pairs* which exhibit this positive real properties.

		RATE OUTPUTS		
		Velocity	Slope Rate	Strain Rate
INPUTS	Point Force	$\propto 1/\sqrt{\omega}$ (-10dB/dec.)	$\propto 1$ (0dB/dec.)	$\propto \sqrt{\omega}$ (10dB/dec.)
	Point Moment	$\propto 1$ (0dB/dec.)	$\propto \sqrt{\omega}$ (10dB/dec.)	$\propto \omega$ (20dB/dec.)
	Couple Moment	$\propto 1$ (0dB/dec.)	$\propto \sqrt{\omega}$ (10dB/dec.)	$\propto \omega$ (20dB/dec.)

Table 3.2: Slope (Amplitude vs Frequency) of Dereverberated Response of Sensor/Actuator Pairs

[3] This relation is also valid for strain, i.e., $\epsilon \propto w''$.

Obviously, the slopes in Table 3.2 do not account for the resonant modes caused by finite structures which operate in standing, rather than traveling, waves. The dereverberated relations for collocated, dual sensor/actuator pairs occupy the diagonal elements in the table. This solution gives an indication of the inherent roll-off characteristics of particular power pairs. As will be shown in the following control analysis, the more 'natural' roll-off, the greater degree of stability robustness guaranteed for local control techniques. For pairs with roll-up (negative roll-off) the response actually increases with increased frequency indicating that any non ideal behavior would have sufficient gain to destabilize the system.

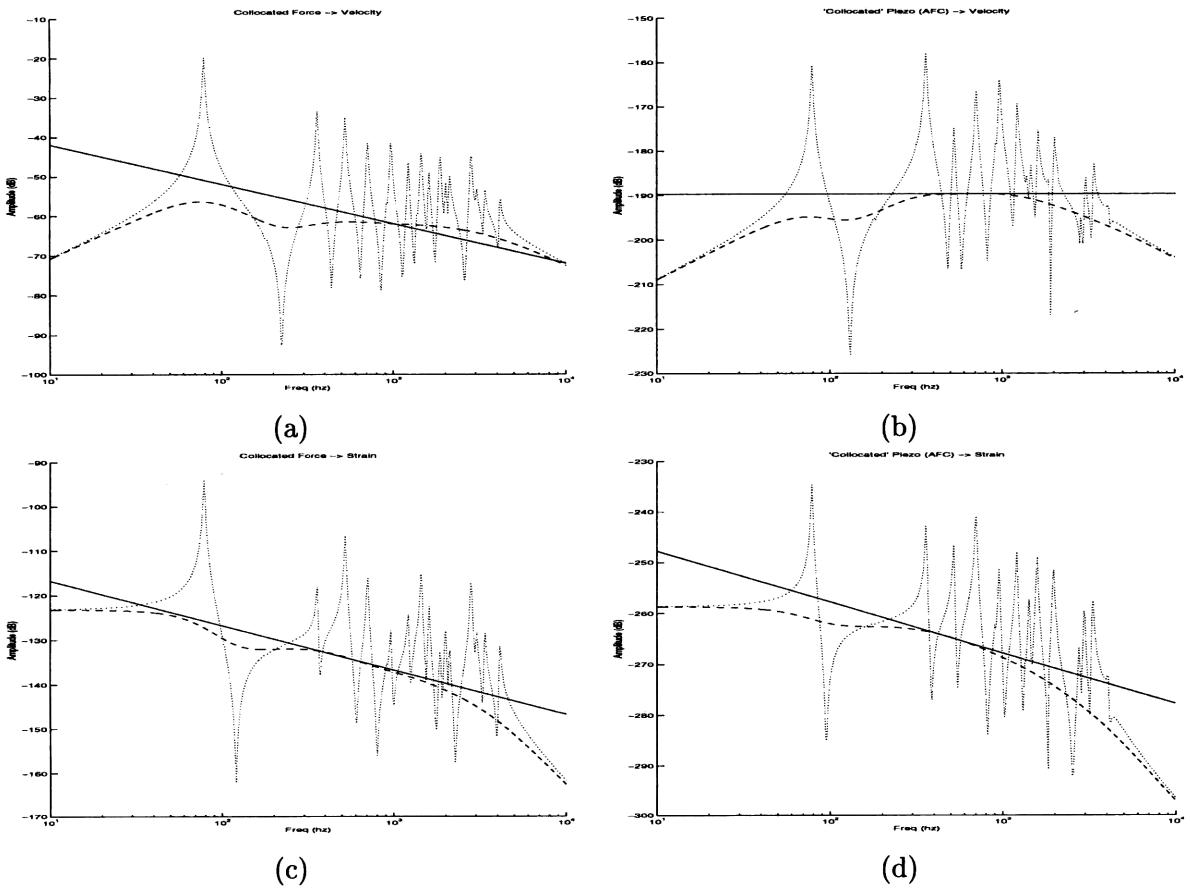

Figure 3.2: Comparison of Dereverberated Wave Model and Rayleigh Ritz Model for Sensor/Actuator Pairs: a) Force/Velocity, b) AFC/Velocity, c) Force/Strain, and d) AFC/Strain

Figure 3.2 illustrates these relationships. Three traces are shown for each sensor/actuator pair. The solid line indicates the dereverberated slope from the beam wave model summarized in Table 3.2. The dotted line indicates the lightly damped ($\zeta = 1\%$) resonant response of the Rayleigh-Ritz model for the experimental panel design. The same model is used to produce the dashed line, but the critical damping ($\zeta = 70.7\%$) is specified. These com-

parison show how the wave model for an infinite beam can be used to investigate the fundamental sensor/actuator relationships for more complicated structures. Although the wave model derivation is for a beam, the slopes of Table 3.2 are shown to accurately represent the behavior of the sensor/actuator pairs for the vibrating panel. This simple solution yields insight into the roll-off characteristics of particular architectures.

From Table 3.2, only the point force/velocity pair exhibits high frequency roll-off. Structural based control applications require implementation of non-reacting actuators, typically active materials. For piezoelectric actuation, the dereverberated transfer function does not roll-off for any of these sensor types. For the associated collocated, dual pair (for example and AFC actuator and a strain gage or PVDF film sensor) the roll-up is most severe at 20dB per decade.

The system designer is faced with a decision that will greatly influence the closed-loop performance of the system. To utilize the hyperstability predictions, a similar distributed strain sensor, the dual pair, must be used. The implicit hazard of such a design is that the amplitude of the response increases with frequency. The limitations of the models used to derive these results must be considered as the high frequency behavior is increasingly uncertain. These errors will destabilize the control design because of the high gain of the loop transfer function, requiring the designer to add dynamics to the compensator to roll-off the amplitude. These added dynamics must gain stabilize high frequency dynamics without effecting the phase margin of the closely spaced lower modes, a task that is difficult, if not impossible, for modally dense structures.

The alternative is to select a non-collocated sensor, such as a point velocity measurement. For a distributed piezoelectric actuator and a point sensor, the transfer function is bounded by $\pm$ 90°and the pole-zero-pole pattern remains unchanged up to a threshold frequency. This frequency limit corresponds to a point in the response were the shape of the dominant mode of the structure a node line that falls between the sensor location and the boundary of the actuator. Thus the pair is considered 'collocated' up for a particular bandwidth. For the system considered in this thesis, an accelerometer signal is integrated to provide a point velocity sensor. This configuration is observed to maintain the properties of a collocated pair through the bandwidth of concern, and the compensator design is rolled-off to gain stabilize the system at a frequency below the point where the phase is no longer indicative of a positive real plant. The analytic and experimental examples which follow illustrate the difficulty in realizing these theoretical guarantees.

For this work accelerometers were used as the control sensor rather than the embedded strain gages. This choice is made for a few reasons. First, the dereverberated slope of the AFC/velocity pair is flat, while the AFC/strain rate pair has a positive slope. For classical and optimal designs the compensator must roll-off and remain stable. This behavior is easier to accomplish by starting with an the AFC/velocity pair. Also, as illustrated in the

plots of Appendix C], the accelerometer sensor signal has much less noise than the strain gage sensors. For rate feedback designs, the accelerometer signal can be integrated quite easily, while differentiation of the strain signal will introduce even more noise. Based on these analytical and practical considerations, the acceleration measurement was chosen for compensation, but the strain gages were still incorporated into the structure to demonstrate the technology and for future investigations.

3.3 Active Fiber Composites (AFC) for Structural-Acoustic Actuation

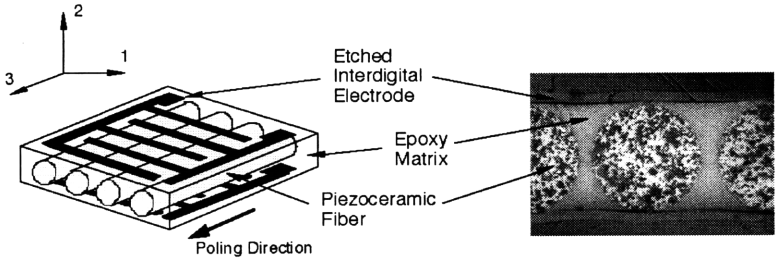

Figure 3.3: AFC Geometry and Components

This work concentrates on the application of a new active material technology for structural-acoustic control. Active fiber composites have been extensively studied for potential benefits as structural actuators and sensors [Bent, 1997], [Bent and Hagood, 1996], [Rodgers et al., 1996], and [Rodgers, 1995]. The composite structure of AFC elements and the interdigitated electrode pattern introduce significant advantages over traditional monolithic applications of piezoceramic materials.

Primary Longitudinal Mode Actuation The purpose of interdigitated electrode pattern shown in Figure 3.3 is to produce electric field primarily in the fiber direction. The strain in the plane of the actuator is due to the much larger d_{33} coupling constant. This is contrasted with monolithic actuation where electric field is applied in the transverse (out-of-plane) direction to induce in-plane strain through the secondary actuation characterized by the d_{31} coupling constant. For example consider bulk PZT-5H where typical values for the d constants are $d_{33} = 593\,(10^{-12}m/V)$ and $d_{31} = -274\,(10^{-12}m/V)$ for a factor of two increase in strain for a given applied field [Mattiat et al., 1971]

Anisotropic Actuation By using the longitudinal mode of actuation, AFC actuators induce a directional strain, a capability not available with monolithic actuators. For example, planar actuation of a standard MIDE[4] AFC is quantified by the two piezo-

[4]MIDE Technology Corporation - Cambridge, MA

electric constants $d_{33} = 115x10^{-12}\, m/V$ and $d_{31} = -50x10^{-12}\, m/V$. The large difference between these constants indicates the strain is mainly in the fiber direction, while a monolithic actuator is defined by the equivalent transverse mode coupling constants $d_{31} = d_{32}$. This capability is key for applications demanding tailored actuation.

Structural Integration Due to the composite construction, AFC's are well suited for structural integration. The entire device is enclosed by the outer Kapton plies containing the electrode materials and electrically isolating the high voltage signals from the host structure.

Conformability Another advantage of the fiber/epoxy system is the conformablility of the actuator for application to complex surfaces. Bulk piezoceramics are far too brittle to conform to such surfaces, and manufacturing of shaped elements is expensive and particular to only a single application

Damage Survival Encapsulating the active material fibers in an epoxy matrix adds a degree of damage robustness by providing a load bearing path in the event of fiber damage. The effect of fiber damage on actuator performance is studied in [Pizzochero, 1997].

Work continues on developing the AFC technology for wide application use. Much of the work is focused on designing a manufacturing process that will eliminate the state-of-practice hand layup methods and increase the reliability/repeatability of the final product. For the experiments chronicled in later chapters of this thesis, standard AFC actuators, as shown in Figure 3.4 are supplied by MIDE for integration into the composite host. The actuator shown has dimensions of 6x2" and is split into two 3x2" elements.

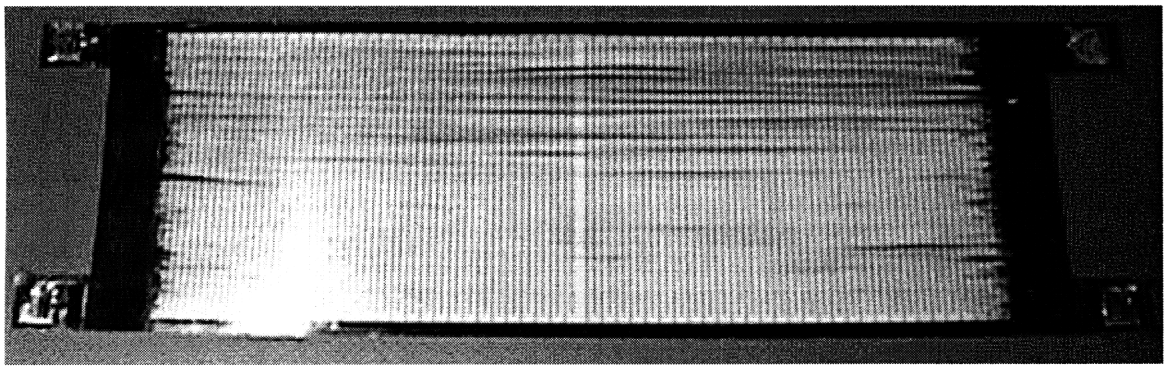

Figure 3.4: Standard MIDE AFC Actuator Pack

3.4 AFC Actuator Placement

In the field of active structures the emphasis is on the synergetic combination of design and control. To effectively produce a high performance structure, the design must leverage

the foresight into the control system to maximize the closed-loop performance. This work is meant to be a generic exploration into the structural-acoustic control problem through consideration of a basic problem, i.e., the goal is not to produce the optimal panel design, which would be of little practical use, but to consider the panel as a structure representative of more complex application. The actuator and sensor placement problem is well studied in the literature of active structures, and the difficulty of the problem has been addressed with powerful optimization methods in order to maximize the performance. The goal of this section is to discuss the tradeoff between an 'optimal' solution, which is computationally intensive, and a 'suboptimal' design which utilizes the structural-acoustic insight to maximize the performance using a constrained search space for the placement problem.

Conceptually, the problem of optimally choosing a design parameter is a straight forward process of defining a *cost function* to represent the desired performance and choosing an appropriate optimization algorithm to minimize this cost. The richness of the field is a product of the wide variety of implementations that are possible using a wide variety of algorithms, each with advantages and disadvantages. The type of *parameter space* considered for the design, either finite placement locations or continuous variation, categorizes the approach at a basic level. [Anderson, 1993] provides and excellent survey of the combinatorial placement problem arising from optimally designing large space structures. Essentially the designer is faced with placing N elements over a space including N_p possible locations[5]. The computational size of this problem prevents direct search algorithms. Aggregation algorithms, which sequentially place each element, are contrasted with random search algorithms (or exchange methods), which operate similar to steepest descent continuous schemes considering the multidimensional gradient at each iteration. At each sequential step the optimization is highly non-linear, demanding robust numeric techniques. Two studied alternatives are simulated annealing, where non improving solutions are accepted with a decreasing rate, and genetic algorithms, utilizing a evolutionary approach where successive interactions are mutated stochastically, in order to escape the local minima that tend to trap less robust schemes in suboptimal solutions.

The continuous version of the placement problem demands a different set of techniques to approximate the minimums of the parameter space. Most schemes typically use some sort of gradient method, such as steepest descent or quasi-Newton iteration, to search for the minima. For convex optimization problems, particularly quadratic cost functions, this approach quickly determines optimal solutions. The difficulty with this approach is that the initial guess becomes critical for convergence to global minima where the cost function is a highly irregular containing many localized minima. Such techniques are applied to the structural-acoustic problem by [Clark and Fuller, 1992] where the design parameters define

[5]The reference gives the illustrative example of a placing 5 elements in 200 possible locations leading to $\binom{N_p}{N} = \frac{N_p!}{N!(N_p-N)!} \approx 2.5(10^9)$ possible combinations!

both the piezoelectric actuator and polyvinylidene fluoride (PVDF) sensor locations. This consideration decouples the two problems doing a single dimensional optimization for each parameter.

Cost Function

The design problem at hand is how to choose the locations of structural actuator elements[6] to achieve the best acoustic performance. This first step of specifying the performance cost function guides the result - the optimization is only as good as its cost function. Some measure of system performance must be quantified in order to define the cost function. The goal is to arrive at a design that has the largest reduction in radiated acoustic energy. To represent this figure of merit, the cost function is defined as the reduction in root mean square (RMS) acoustic radiation due to compensation using linear quadratic regulator (LQR) control gains. Optimal control is used to calculate the cost because this allows the desired acoustic performance to be directly included in the control design, resulting in an optimal solution. The full linear quadratic Gaussian (LQG) optimal control problem is explained in a later chapter, but a subset of this analysis is repeated for completeness.

$$\begin{aligned} J_{LQR} &= \lim_{\tau\to\infty} \frac{1}{\tau} \int_0^\tau \left(x^T(t) Q x(t) + u^T R u \right) \, \mathrm{d}t \\ &= \lim_{\tau\to\infty} \frac{1}{\tau} \int_0^\tau \left(x^T(t) (C_z^T C_z) x(t) + \rho u^T u \right) \, \mathrm{d}t \end{aligned} \tag{3.2}$$

The scalar cost is an expression of the trade-off between the state cost ($x^T Q x$) and the control cost ($u^T R u$). The power of the optimal control solution is derived from the statement of the cost function in Equation (5.3). The second expression explicitly shows the state cost ($z(t) = C_z x(t)$) as an output of the state-space system, and assumes a scalar weighting can be applied to each control channel (ρ). The LQR problem assumes *full state feedback*, which effectively allows the compensator perfect knowledge of the system. This assumption is rarely true for engineering applications, hence the necessity of including a state estimator in the dynamics of the LQG controller. The unrealistic LQR solution is used to compare potential actuator locations because it represents the asymptotic limit of the achievable performance of the LQG implementation. The optimal feedback control is defined by the LQR gain matrix, K, which is shown to be the unique solution to the control algebraic Ricatti equation (CARE), Equation (3.3)).

$$\begin{aligned} \text{CARE} \qquad & X A + A^T X + Q + X B_u R^{-1} B_u^T X = 0 \\ & u = -K\, x = (R^{-1} B_u^T X)\, x \end{aligned} \tag{3.3}$$

The quadratic cost for this simplified version of the LQR problem is defined by the state cost ($\mathbf{z}^T \mathbf{z}$) and the control cost ($\rho \mathbf{u}^T \mathbf{u}$). The convenience of the previously developed

[6]The AFC actuators supplied by MIDE are completely described in Chapter 4.

structural-acoustic model formulation becomes evident here as the quadratic state cost is simply the radiated power found by the inner product of the radiation filter output vector. The control cost are considered to be uniform on each channel, allowing the scalar value of ρ to determine the compensator bandwidth. The elegance of this simple solution for linear systems with such a quadratic cost is that the optimal control signal is simply a linear combination of the states, expressed compactly by the gain matrix. For systems modeled with stochastic, white noise, disturbances, the optimal regulator solution is independent of the physics of the disturbance, a property known as *certainty equivalence* [Bertsekas, 1995]. This result is intuitively pleasing, since if the disturbance is truly random, the control can do little more than assume it to be absent[7].

Even though the control gain matrix is independent of the disturbance source, the resulting performance is a function of the type of disturbance. Considering the response of the linear state-space system to the unit intensity white noise disturbance entering through the input matrix B_w, the resulting state covariance matrix, Σ_{xx}, can be found from solving a Lyapunov equation.

$$\begin{aligned} \text{Open} - \text{Loop} \quad & A^T\Sigma_{xx} + \Sigma_{xx}A + B_wB_w^T = 0 \\ \text{Closed} - \text{Loop} \quad & (A - B_uK)^T\Sigma_{xx} + \Sigma_{xx}(A - B_uK) + B_wB_w^T = 0 \end{aligned}$$

The covariance of the output and control gains can be found directly from the state-space equations and the full state feedback. The RMS state and control costs can be found using a bit of stochastic linear system theory (see Chapter 5 for a more explanation).

$$\begin{aligned} \text{State Cost} \quad & (RMS_{performance})^2 = trace(\Sigma_{zz}) = trace(C_z\Sigma_{xx}C_z^T) \\ \text{Control Cost} \quad & (RMS_{control})^2 = trace(\Sigma_{uu}) = trace(K\Sigma_{xx}K^T) \end{aligned}$$

To compare the resulting performance for placing an element at any particular position, it is insufficient to directly compare just the state performance for constant values of the control weighting parameter ρ. The LQR solution seeks an optimal trade off between state and control cost, not a fixed bound on control. Normalizing the RMS reduction in sound power by the control energy, or RMS control effort, results in a performance function that accurately reflects the relative performance at each candidate location.

$$J_{placement}(x, y, \rho) = \frac{\Pi_{OpenLoop} - \Pi_{ClosedLoop}}{\Pi_{Control}} = \frac{\Delta\Pi_{LQR}}{\Pi_{Control}} \tag{3.4}$$

An example of this performance metric, for a subsection of the panel model is shown in Figure 3.5. The normalized closed-loop acoustic performance is calculated at each (x, y)

[7]When the disturbance can be characterized by its power spectral density, the dynamics of the disturbance model can be appended to the state-space plant. The pre-whitening technique transforms the problem back to a system with white noise input, again with certainty equivalence.

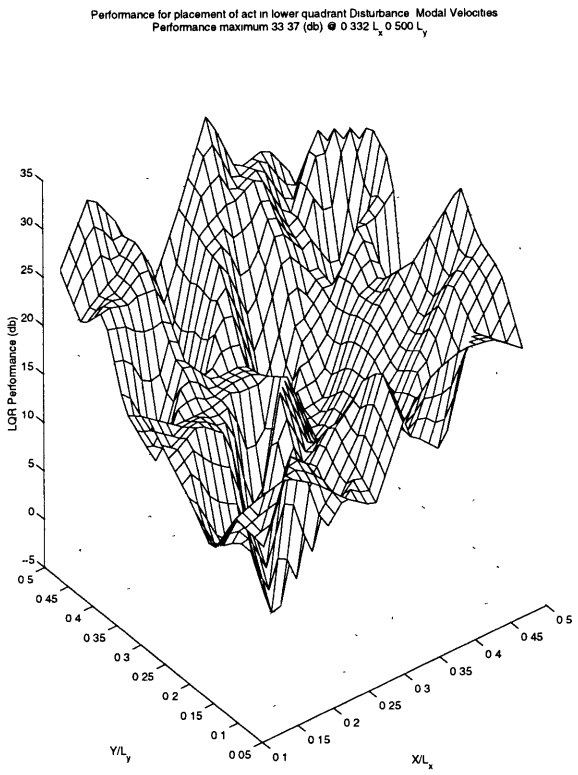

Figure 3.5: Performance Surface for Placing a Single AFC Pair with Point Force Disturbance

coordinate over the the lower left quadrant of the panel. Only a single quadrant is shown due to the computational effort required to exhaustively search the surface. The *performance surface* is highly irregular, containing many local minimum and maximum points indicating the necessity for a highly robust numerical scheme to find the global optimal solution. Standard continuous gradient methods can only hope to converge to a global maximum with a highly accurate initial guess.

Very Finite Placement - Average Disturbance

From the previous analysis, two challenges must be addressed in order to place the AFC elements effectively. First is the complexity of this combinatorial placement problem with a highly irregular performance surface as previously shown. The physical constraints of manufacturing of the composite add even more complexity to the general problem. This is addressed by assuming a few discrete placement location, effectively reducing the parameter space to a point were a *direct search* can be carried out over the entire space. The second challenge is how to quantify a general disturbance. This work strives to maintain a level of ubiquity by not relying on a single particular application for the design parameters; therefore, the disturbance used in the performance calculation and subsequent optimization must be a compromise of each possibility. By averaging the performance metric for four

possibilities enables the metric to capture the aggregate performance of the system.

The final placement algorithm is conceptually simple, but computationally challenging. The search space includes nine possible locations where the centers of the AFC actuators are placed at the anti-nodes of the odd-odd[8] panel modes of vibration. The strain energy for the odd-odd modes is largest at these locations of high curvature, indicating that strain actuation at these points will have high authority over the volumetric radiating modes. Additionally two orientation possibilities, (0° and 90°), were included, resulting in eighteen possible configurations for the first placement step. Each actuator is assumed to be embedded in the same ply location, as far from the neutral axis as possible. The design does not utilize multiple ply locations because stacking elements in multiple layers only serves to increase the authority of the actuators without effecting the fundamental input/output behavior. The test article contains multiple actuators to investigate how distributed actuation will effect performance, so the design includes multiple, spatially separated, actuator locations.

Beginning with just the passive panel layup, a single AFC symmetric pair is placed at each of the possible locations. For each location the full Ritz model, the closed-loop response, and the normalized performance is computed. Resolving the full Ritz model, M, K, and Θ matrices, rather than just the electro-magnetic coupling of the Θ matrix, accounts for the changes in mass and stiffness and well as the actuation differences[9]. Simply identifying the maximum yields the optimal solution for this placement. Once an element is placed, the same process is done for each successive element. The previously placed AFC pairs are considered stationary in each successive search and the full multiple input LQR problem is solved to analyze the performance. The final result of this approach is the experimental design shown in Figure 3.7. The corresponding sequential performance gain is illustrated by Figure 3.6. The bar graph shows the increased performance with each sequentially added actuator pair. The final design includes four AFC pairs. Each AFC exhibits unique properties, i.e., d-constants, which could be easily included the placement process, but it is assumed to have little influence on the outcome. Elements with the decreasing authority are placed at the sequential locations during manufacturing.

3.5 Summary

This chapter presents the architecture for the composite active panel designed and built to investigate active structural-acoustic control (ASAC). The design intent is not to completely

[8] A mode shape is referred to as 'odd-odd' if the shape consists of an odd number of half wavelengths in both the x and y directions, hence odd-odd modes are the most volumetric.

[9] It should be noted that the natural frequencies were found to shift only slightly as the AFC elements where placed about the panel, bringing to question the need for the additional computational load of recalculating the full model at each iteration

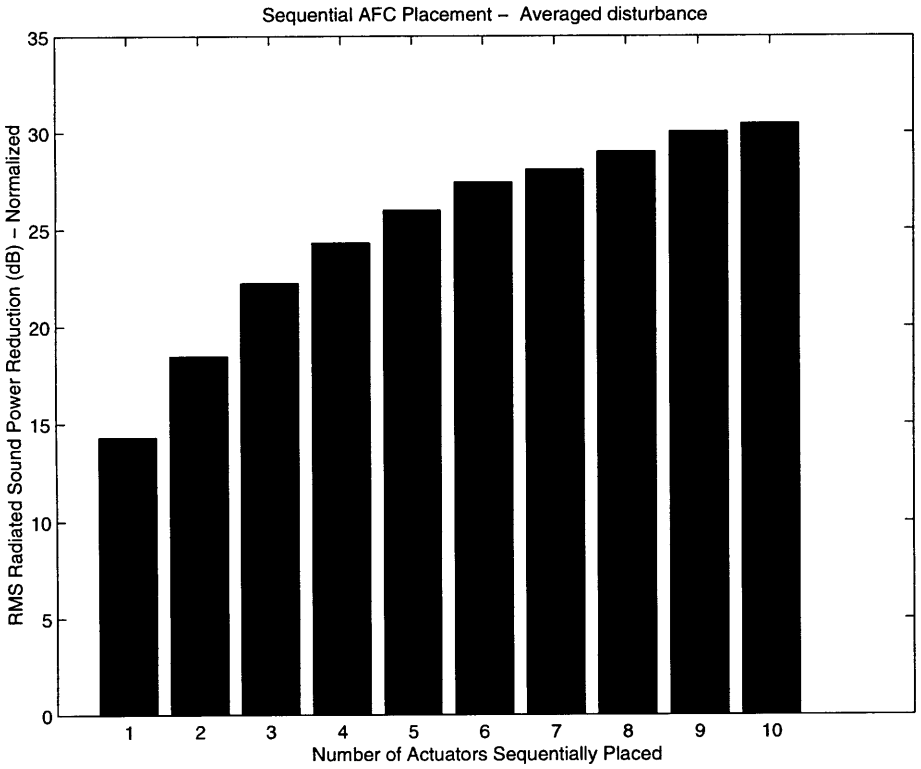

Figure 3.6: Increasing Acoustic Performance with Sequentially Place Actuator Pairs

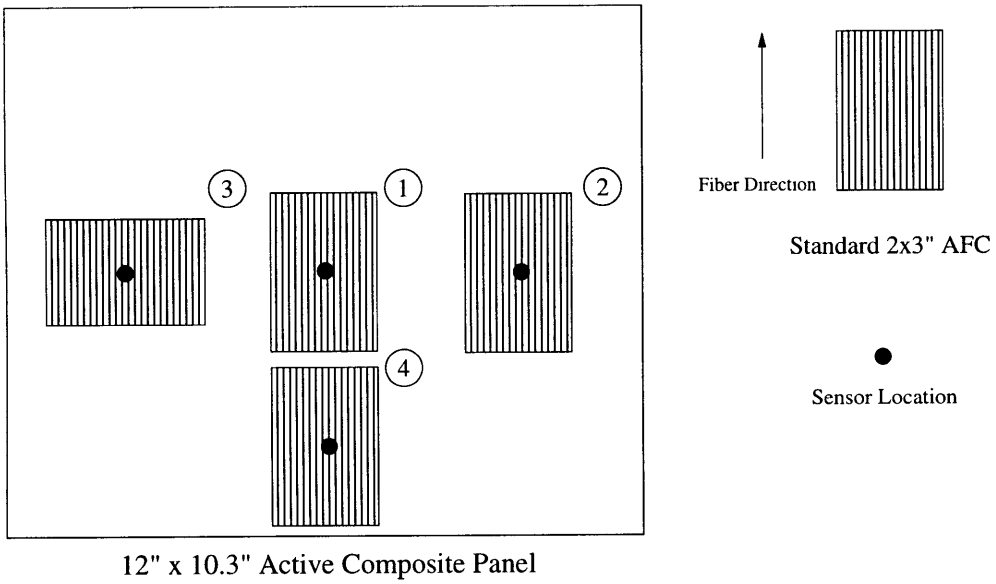

Figure 3.7: Result of Actuator Placement for Four Sequentially Placed AFC Pairs in Composite Panel

optimize the design of this one panel, but to treat it as a representative structure and consider the choices available for active structural design for control.

The sensors, point velocity measurements obtained by integrating the acceleration signals, are chosen to be spatially collocated, but are not dual. The advantages of this topology, for local and high authority control, will become more evident in the following control design investigations.

To place the actuators, a compromise is presented as a sufficient solution for design of the structural-acoustic control system. The parameter space is shown to be highly nonuniform, requiring sophisticated robust techniques for accurate optimization. An alternative approach is taken by defining a very small search space resulting in a optimization problem that can be carried out directly. This suboptimal approach yields simple and effective solution.

The resulting design, represented in the analytical examples to follow, and manufactured for the experimental implementation, is depicted graphically in Figure 3.7.

The symmetric actuators are placed in order to exert the maximum closed-loop structural-acoustic performance based on a sequential placement scheme. The sensor locations are chosen to exploit the advantages of collocation for classical and optimal control techniques. Both strain gages and accelerometers are placed at these specified locations to investigate the dynamic behavior, however the dereverberated transfer function analysis indicates that acceleration signals will be better suited for implementation of low authority control techniques. The numbering shown in Figure 3.7 is used throughout the work to reference the particular actuators and sensors.

Chapter 4

Composite Manufacturing and Experimental Setup

This chapter describes the experimental setup used to explore the possibilities of active structural-acoustic control (ASAC). Manufacturing of the composite panel structure, with embedded sensing and actuation, is chronicled and the experimental setup is detailed for completeness. Also an outline of the standard dynamic testing procedure is outlined to provide the consistency necessary to make comparative conclusions on the results of the experiments which follow.

4.1 Composite Panel Manufacturing

The manufacturing process for the composite panel with embedded actuation and sensing in recorded here. The basic construction is based on the standard *net resin* cure for graphite fiber composites as outlined in the course notes [Lagace, 1988].

Laminate Layup

The basic structure of the laminate is derived from a *quasi-isotropic* layup, that is one in which the extensional stiffness is equivalent in all direction and there is no bend-twist coupling. The absence of mechanical coupling is indicated by the off diagonal blocks, B, being zero in the composite stiffness matrix, $[AB;BD]$ [Jones, 1975]. There are many quasi-isotropic layups; the simplest being a three-ply [-60/0/60] layup. For this experiment an eight ply symmetric layup denoted by $[0/\pm 45/90]_s$ of graphite/epoxy [1] is used as the nominal passive layup. This type of 'black aluminum' is typical of applications which benefit from the increased stiffness and strength to weight ratio of composites structures.

[1] AS4/3501-6, 32% resin, from Hercules Inc., Wilmington, DE

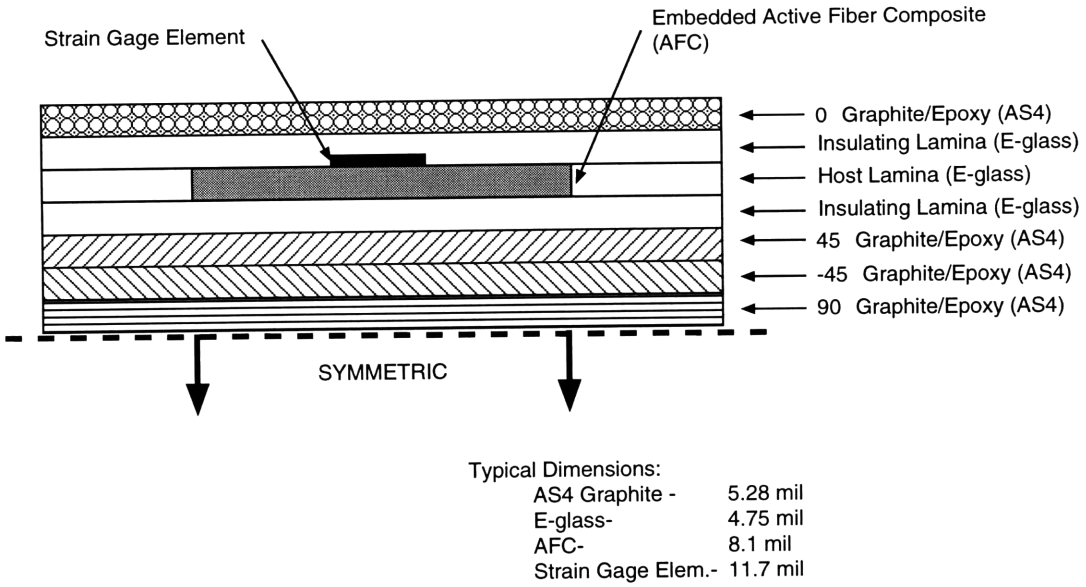

Figure 4.1: Layup Cross-Section of Composite Panel

The quasi-isotropic graphite/epoxy passive layup was modified to include the embedded active components as shown in Figure 4.1. Three issues are important in for incorporating structural sensors and actuators into laminate structures: isolation, shielding, and connections. The active fiber composites[2] (AFC's) require very large driving potentials, demanding that the power leads be well insulated from the surrounding conductive graphite plies. The strain gage sensors[3] are very sensitive to electro-magnetic field disturbances, such as the high electrical fields from the AFC's, and require proper shielding in order to accurately measure strain. Finally each of the elements must be robustly connected when assembling the prepreg laminate in order survive the harsh environment of a composite cure (e.g., 350°F and 85 psi).

To accommodate the embedded sensors and actuators and provide a measure of electrical isolation, three e-glass[4] host plies where incorporated into the layup for each active ply. E-glass is an isotropic, non-conductive, woven prepreg of approximately the same thickness as the AFC elements. A ply the full size of the panel was included both above and below the two active layers while material was removed from the middle layer of e-glass in order to incorporate the AFC's with minimal thickness discontinuities. The full layup is illustrated by the typical cross-section shown in Figure 4.1. The constitutive properties for the three materials used in this layup, graphite/epoxy, e-glass, and AFC, are included in Appendix B for reference. The nominal AFC properties supplied by the manufacturer are listed in the appendix along with the properties of individual elements measured prior to

[2]Standard 2"x3" AFC from MIDE; Cambridge, MA
[3]0/90°T-Rosettes from Measurements Group - CEA-06-062UT-120
[4]450-1/2 glass fabric with F155 resin system - Hexcel Corporation; Pleasanton, CA

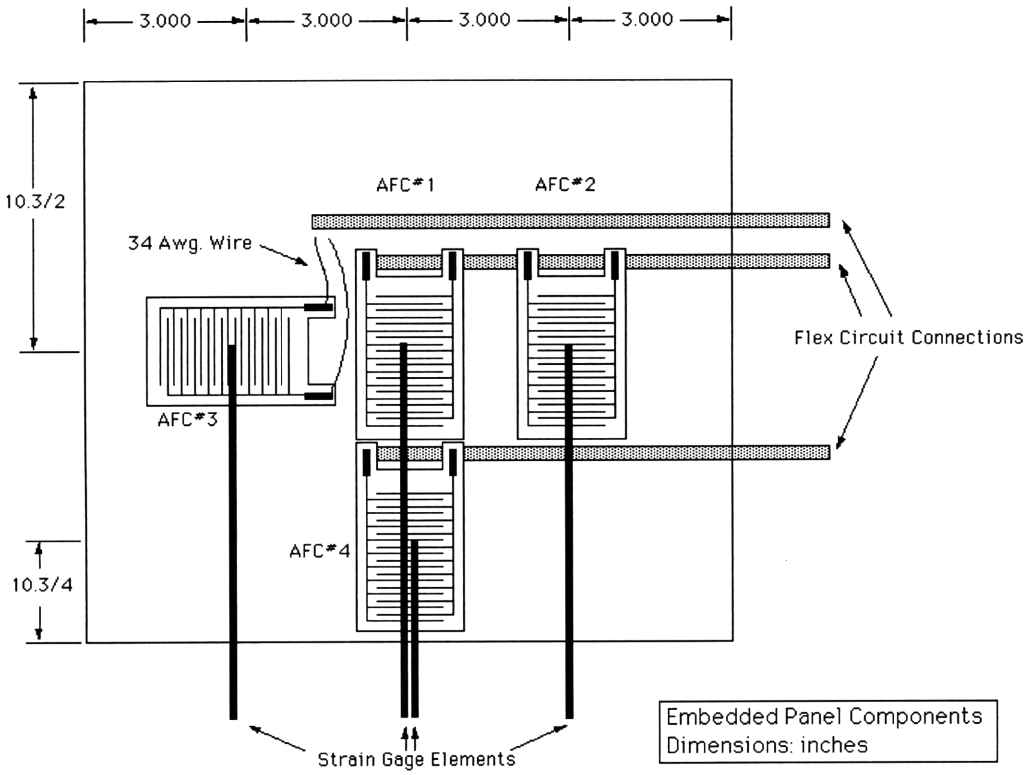

Figure 4.2: Layout of Components Embedded in the Composite Panel

incorporation into the structure.

The layout of the AFC elements was determined by optimizing the closed-loop performance of the system in Chapter 3. The final placement is illustrated in Figure 4.2. Each of the actuator pairs is placed symmetrically about the neutral axis at the particular locations. The actuators are labeled with the same convention from Chapter 3 The strain gage elements will be explained shortly and are placed in the approximate center of each actuator. The flex circuit connections are made by placing the leads in the e-glass host ply after soldering the AFC leads to the exposed conductor pads on the flex circuit.

Manufacturing Process

Preparation of the sensor and actuator elements was necessary prior to assembling the prepreg laminate. After the physical properties of the individual actuators are measured, the AFC's were attached to straight flexible circuits[5]. The flex circuits are encapsulated copper conductors used to supply power to the AFC elements. The thin flat construction introduces minimal discontinuities in the laminate. The conductive material was exposed by abrading the Kapton coating allowing the AFC leads to be directly connected to the flex circuit without exposing any conductive surfaces. The AFC's were tested a final time

[5]Flex circuits - Allflex Packaging Products; Ambler, PA

to ensure the connections were intact and then cleaned using TrichloroEthylene to remove any materials which might degrade the bond quality.

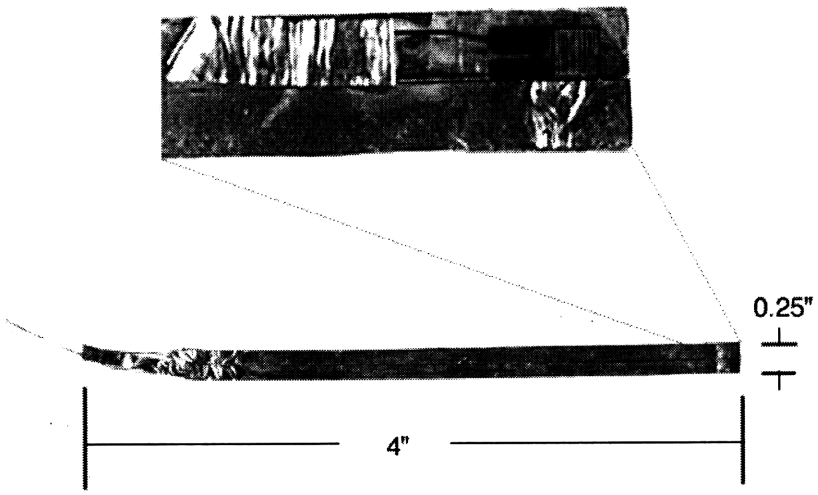

Figure 4.3: Shielded Strain Gage for Composite Integration

From previous experience, mounting foil strain gages directly to the interdigitated electrodes of the AFC elements is not acceptable. The high electrical field from the AFC interdigitated electrodes induce noise in the metallic gages that prevents measurement of the strain signal. To alleviate this difficulty, each gage rosette was encapsulated in thin (0.001") copper ribbon electrically shielding the gage and leads from the high electric field. The process consisted of sandwiching the gage and attached leads between copper ribbon strips using structural epoxy[6]. Figure 4.3 shows an example of one of these sensor packages which was incorporated into the structure. Once cured these elements were tested for connectivity and cleaned in order to be incorporated in the composite.

The embedded elements were incorporated into the standard prepreg cure. Each lamina ply was cut from the appropriate prepreg rolls to manufacture a 12x14" composite panel. The sequence shown in Figures 4.4 and 4.5 illustrates the embedding procedure for one active ply. The outer most 0°graphite fiber ply is placed first followed by a full layer of e-glass for electrical insulation. The strain gage elements are incorporated, as shown in Figure 4.4, at locations coinciding with the center points of the AFC actuator elements. Next the host e-glass ply is added, as shown in Figure 4.5a, with material removed to accommodate the added thickness of the elements. The AFC elements and the flex circuit connections are placed into the host ply as shown in Figure 4.5b and another full layer of insulating e-glass is added. From here the structural ± 45 and 90°lamina are added to

[6]Shell EPON 828 resin with EPI-CURE 3223 curing agent

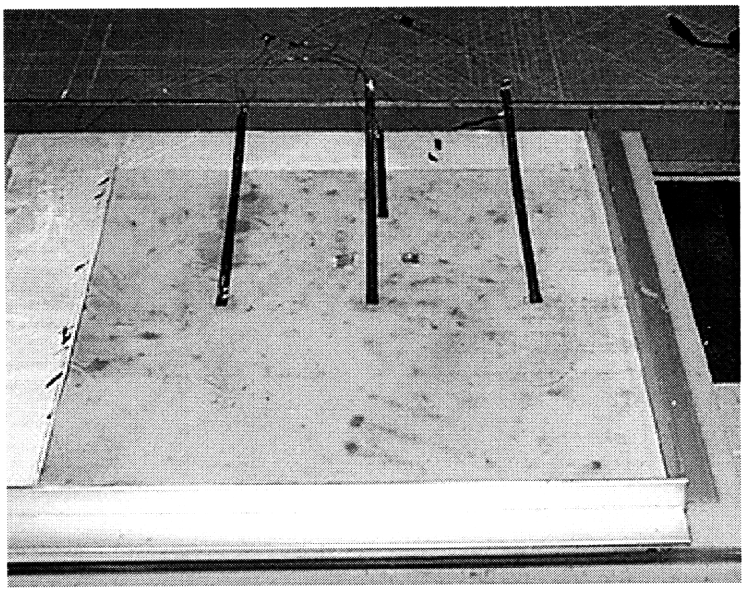

Figure 4.4: Embedded Strain Gage Elements in Host Lamina

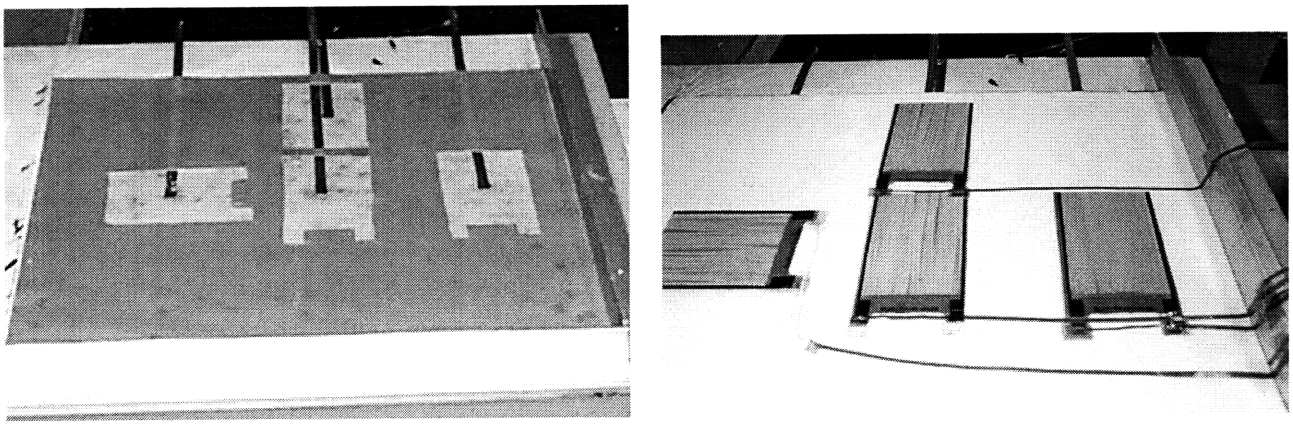

(a) (b)

Figure 4.5: a) E-Glass Host Ply for AFC Actuators b) Embedding Actuators and Flex Circuit Connections in Prepreg Assembly

complete one symmetric half of the panel. The process is repeated in reverse, with the exception of the strain gage elements, to compete the prepreg assembly.

Once the prepreg laminate was assembled, including the two active plies and the sensors, preparation for a standard composite cure was done in the Technology Laboratory for Advanced Composites (TELAC) facilities. The particular steps involved in the net resin cure procedure are detailed in [Lagace, 1988]. Maintaining the integrity of the external connections, the flex circuits and 34 AWG strain gage wires, was the only additional step. From past experiences, the liquification of the epoxy during the cure and capillary action along the connector surfaces can cause the epoxy to encapsulate the external wiring, destroying

the external connecting surfaces. Guaranteed non-porous Teflon (GNPT) tape enclosing the external wiring alleviated this problem. The wiring was placed between layers of the two layer cork dam surrounding the panel in order to minimize the low curvature bending that occurs when the a vacuum is applied to the laminate. The entire assembly was cured in the TELAC autoclave as shown in Figure 4.6. The standard cure for the graphite/epoxy

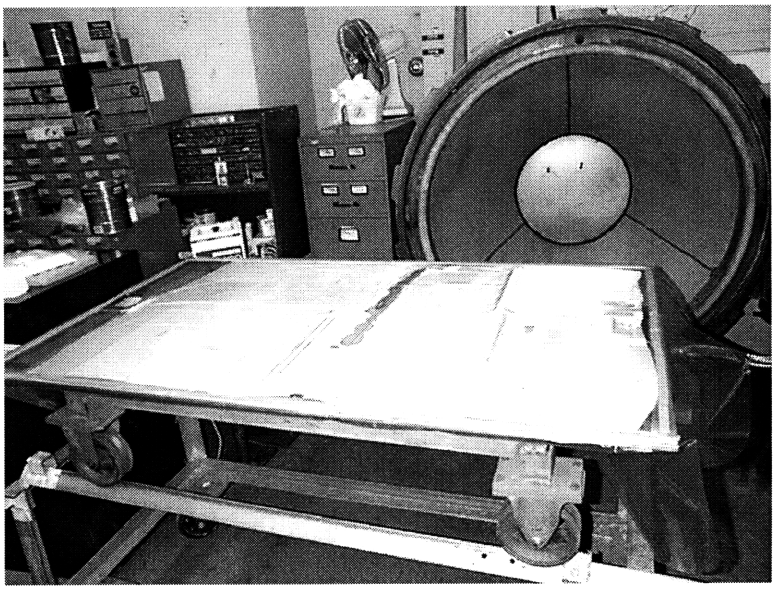

Figure 4.6: Composite Panel Prepared for Cure Process

system consists of a pre-cure at 240°F for one hour, followed by 350°F cure cycle for two hours. During the cure process, an 85 psi environment is maintained in the autoclave while a vacuum of 29" Hg is applied to the laminate. It is possible to cure at lower pressures, but for this experiment, the standard cure was used without incident. It should also be mentioned the e-glass in the laminate actually cures at a temperature of 250°F, but through conversation with the manufacturer, the elevated temperature cure was determined to be acceptable .

Typically an eight hour post-cure at 350°F completes the cure cycle to guarantee full curing of the laminate. In previous experiments this step was not included due to time constraints, but when manufacturing the panel chronicled here, this step was included. Visual inspection prior to the post-cure indicated a good bonding, but after the post-cure procedure, large delaminations occurred between the AFC Kapton electrode surfaces and the e-glass host plies. The e-glass and graphite plies actually separated from the AFC elements producing 'bubbles' protruding 1-2 mm above the panel surface and as large as the 2x3" actuators. Drilling, by hand, small holes in the outer two layers of composite and using a hypodermic syringe to inject structural epoxy[7] repaired the delaminations. Figure 4.7

[7]Shell EPON 828 resin with EPI-CURE 3223 curing agent

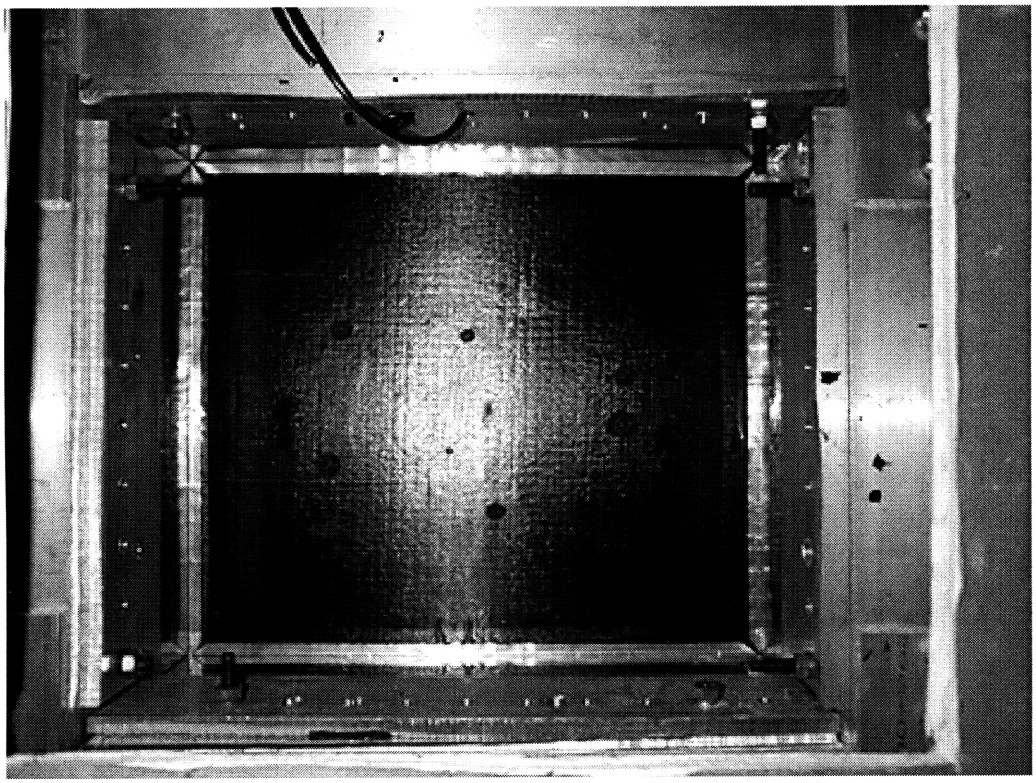

Figure 4.7: Rear View of the Active Composite Panel Mounted in Anechoic Chamber

shows the rear view, from outside the anechoic chamber, of the composite panel mounted in the rigid frame. The small botches on the surface indicate where epoxy was inserted to bond the passive pays to the AFC electrode surfaces. This difficulty was definitely disconcerting, but had little effect on the resulting accuracy of the dynamic model.

4.2 Dynamic Testing

For completeness the testing apparatus is fully documented, including the anechoic facilities, the mounting structure within the chamber, and the testing hardware and software. The importance of the boundary conditions is emphasized and the method used here is verified through experimental analysis. The challenges of the high voltage requirement of the AFC actuators is discussed and the characteristics of the amplification system is described. The testing hardware and software, including the real-time control computer and data acquisition equipment, are detailed.

4.2.1 Testing Facilities

Anechoic Chamber

Experimental measurements of the radiating acoustic field require some type of anechoic facilities to absorb the radiating energy, preventing reflection and resonant acoustic behavior. The design of AMSL's anechoic chamber[8] was driven by the physics of the interior aircraft noise control problem. The unique perforated metal cone wall treatment allows for use of a more shallow cone design, maximizing the internal space of the chamber while maintaining a low frequency cutoff of at least 120 Hz. Qualification testing illustrated that no significant reflection was present above 100 Hz, and that acoustic measurements could be made within approximately 6" of the wall surface. Testing of the facility was done in accordance with the American National Standard, Section S12.35-1990.

Panel Mounting

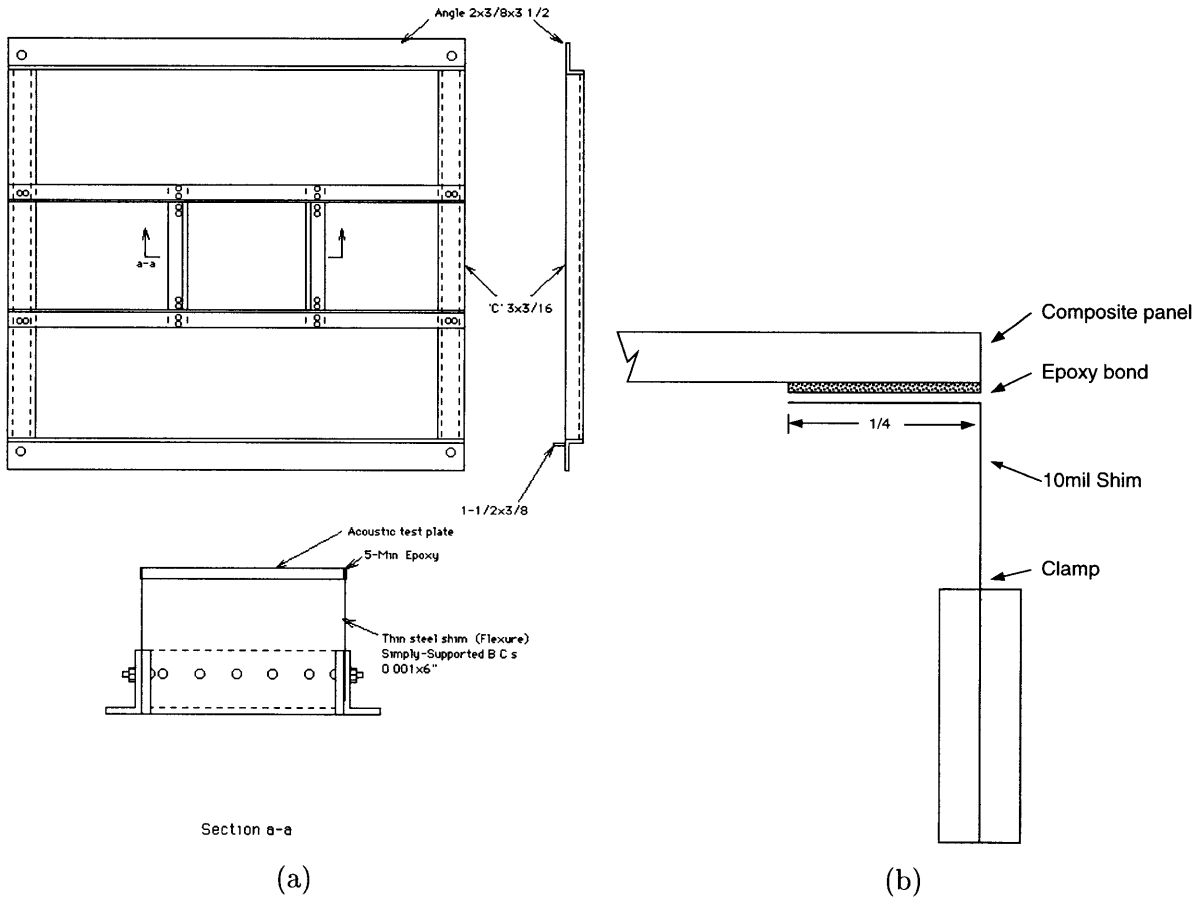

Figure 4.8: a) Frame for Mounting Panel Structure b) Schematic of Boundary Conditions

[8]The anechoic facilities were supplied by Industrial Acoustics Co; Bronx, NY and assembled by Viking Enterprises

One wall of the anechoic facility has a removable section. Removing the surface treatment and a section of the wall opens a four foot square to the laboratory. A steel frame was manufactured to be securely fastened to the wall in order to house the transmission experiments as shown in Figure 4.8. The square frame is made of steel channel sections and is used to attach the aluminum 2x3" L-sections for mounting the test article. To approximate the simply supported boundary conditions, thin shim steel flexures are used to attach the panel to the rigid frame. A 1/4" fold is made in the shim in order to bond the shim to the composite panel using structural epoxy[9]. Through experimental verification this method is shown to approximate the computationally attractive simply-supported boundary conditions due to the low torsional stiffness parallel to the boundary and high displacement stiffness out of plane.

4.2.2 Acoustic Baffle Design

To perform valid acoustic measurements a baffle was constructed in the plane of the panel, extending to the edges of the anechoic chamber opening. This serves two purposes- it serves to block the transmission of sound from the external environment, while separating the influence of the two radiating sides of the panel. One might recall the solution to the inhomogeneous Helmholtz Equation 2.18 which required knowledge of the surface velocity in the entire plane, thus the canonical *infinite baffle* radiation problem. The reference [Bies, 1988] gives a lucid account of the fundamentals of the transmission analysis. The results can be summarized with a few simple relations.

To discuss the baffle design, a conceptual presentation of the panel transmission problem is undertaken. The definition of transmission ratio illustrates the metric for considering how a partition blocks the flow of acoustic energy.

$$TL \equiv -10log_{10}\frac{transmitted\,energy}{incident\,energy}\,(dB)$$

The transmission of a simply supported panel can be described by considering a few discrete frequency ranges defined by the first resonant, $f_{1,1}$, and critical, f_c, frequencies of the panel.

$$f_{1,1} = \frac{\pi}{2}\sqrt{\frac{B}{m}\left[\frac{1}{L_x^2}\frac{1}{L_y^2}\right]}$$

$$f_c = \frac{c^2}{2\pi}\sqrt{\frac{m}{B}}$$

Figure 4.9 illustrates the fundamental properties of the transmission loss for the defined frequency regions.

1. At low frequencies, the transmission loss is controlled by the panel's bending stiffness, $B = EI/(1-\nu^2)$. The stiffer the panel, the less induced vibration and hence acoustic transmission.

[9]Shell EPON 828 resin with EPI-CURE 3223 curing agent

2. Above the first natural frequency, the loss is proportional to the mass of the panel increasing with frequency at 6dB per octave up to the critical frequency.

3. At the critical frequency the acoustic wavelengths match the structural wavelengths, allowing perfect coupling between the vibration and transmitted energies.

4. Above the critical frequency the damping controlled portion of the transmission loss increases with a 9dB per decade slope.

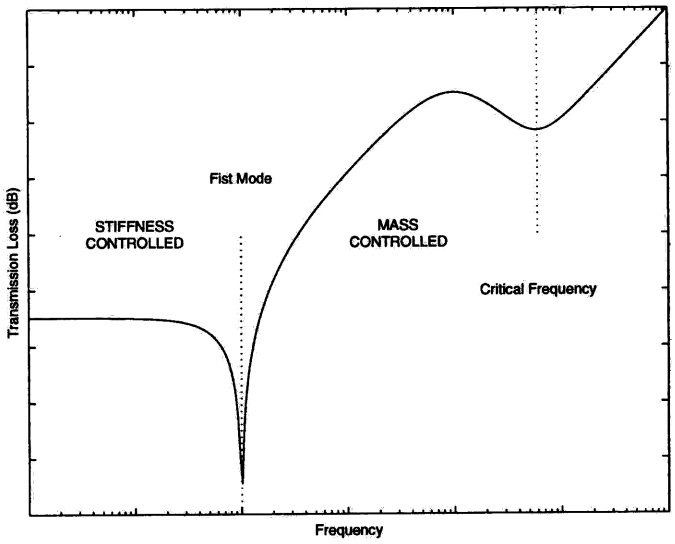

Figure 4.9: Frequency Regions of Panel Transmission Loss

The question in designing a partition to minimize the transmission is whether to add stiffness or mass. Added stiffness increases the first natural frequency and thus the stiffness controlled region of the transmission loss curve, but reduces the coincident frequency and the mass controlled region of the curve. On the other hand, a high mass, low stiffness partition may have a first resonant mode well below the audible range and a very high critical frequency resulting in a mass controlled transmission loss. This discussion serves as a simple explanation of what is contained in the empirical data tables of many handbooks and acoustic references. Essentially the observation is that for low frequency attenuation, the partition should be massive and compliant in order to utilize the mass controlled region of the transmission loss spectrum.

The resulting baffle design illustrated in Figure 4.10 consists of three layers of 1/4" sheet rock mounted in the wall of the anechoic facility. The individual layers are constructed to fit closely with the chamber wall and the composite test article to reduce transmission. The first layer is mounted flush with the panel surface, while the second layer is placed up against the rigid frame. A third layer is included farther behind the panel. The back of

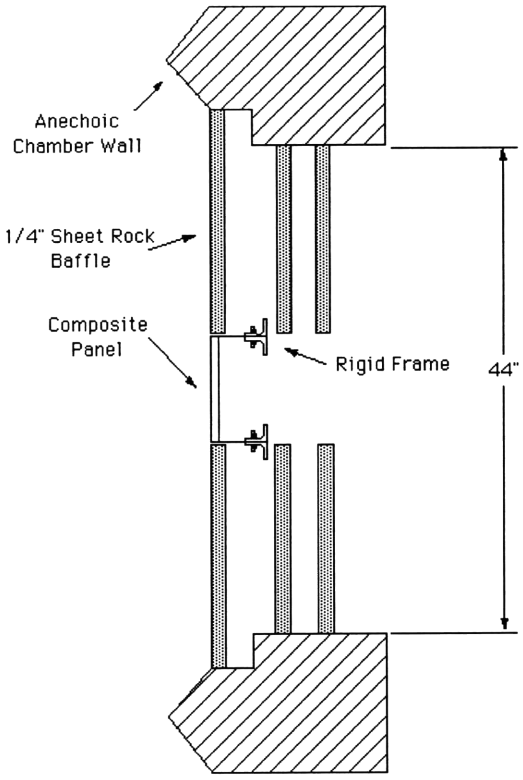

Figure 4.10: Acoustic Baffle Design

the panel is open to the outside environment to allow acoustic actuation of the panel and reduce the mass loading observed when the rear volume is enclosed.

The experimental setup is shown in Figure 4.11 from inside the anechoic facility. The sheet rock baffle is shown to fit tightly within the opening in the chamber wall with the microphone traverse pivoting about the centerline of the panel. In Figure 4.12 the surface mounted accelerometers are more clearly visible along with the leads and the flex circuit connections supplying power to the integrated AFC elements.

4.2.3 Testing Equipment

This section includes a complete listing of the dynamic measurement and control equipment used in the later experimental portions of this work.

Accelerometers: ENDEVCO Model 2222C miniature piezoelectric accelerometers are surface mounted (wax) to the panel at the center locations for the AFC actuator elements. All four accelerometers are left attached during testing for consistency. Their small size (0.5 grams) is observed to have a negligible effect on the dynamics of the system. The frequency response specification indicate accurate amplitude response (within 1dB) from 1 to 10,000 Hz. Each 2721B charge amplifiers is set to a sensitivity of 100mV per g of acceleration.

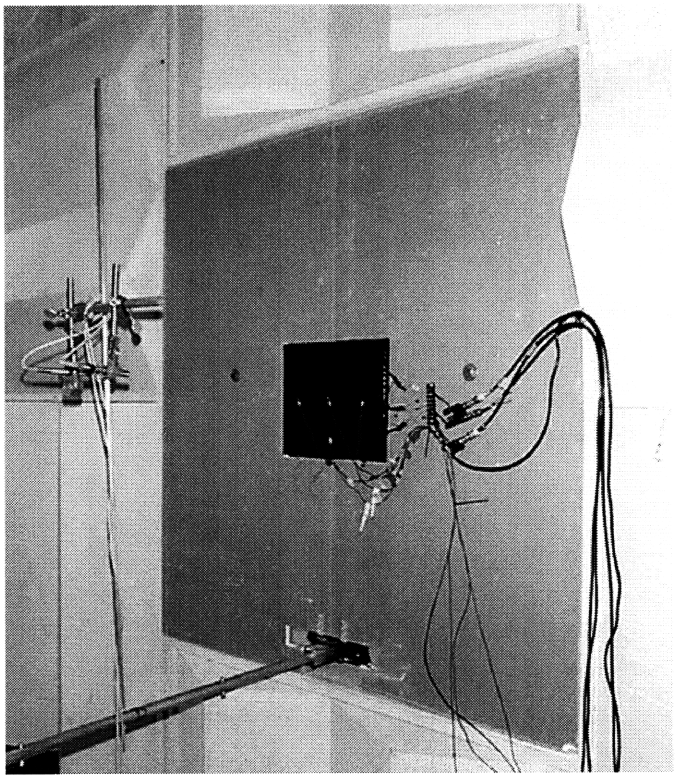

Figure 4.11: Baffled Composite Panel in Anechoic Chamber with Microphone Traverse

Microphones: Bruel and Kjaer 1/2" condensor microphones, type 4165, with type 2669 preamplifiers and 5935L voltage supply. The microphones are verified to have a flat frequency response from approximately 10 to 10,000 Hz.

Strain Gages/Conditioners: Measurements Group CEA-06-062UT-120 strain gages are embedded in the structure and the 1/4 bridge connections are made using the ??? conditioner.

Amplifiers: For system characterization and control the input signal is amplified in two stages. The first stage is accomplished using Yorkville AudioPro 3400 amplifiers modified to have a flat frequency response across a broad frequency range ($\approx$ DC-20kHz). While the amplifiers are capable of delivering 1200 Watts of power to an 8Ω load impedance, the absolute maximum voltage attainable is 240 V peak. The maximum open circuit voltage gain is measured to be approximately 60 V/V. AFC's require a much higher voltage for operation, typically on the order of kilovolts, while introducing a capacitive load ($Z = \frac{1}{j\omega C}$). Step up transformers are used to increase the output voltage by a factor of 25:1. The capacitive load of approximately 1.5nF per AFC actuator in conjunction with the inductance of the transformer causes a R-L-C resonance. Experimentally this resonant peak and associated phase loss is found to

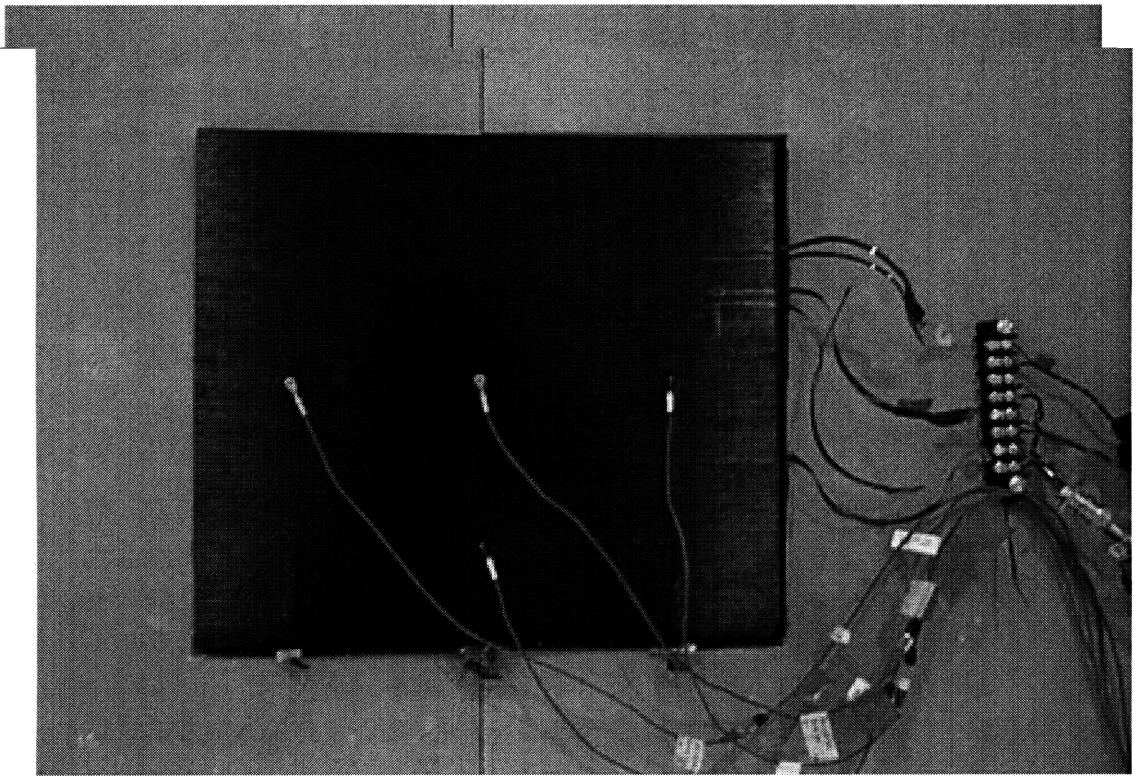

Figure 4.12: Front View of Baffled Composite Panel

be beyond the dynamic range of concern for these experiments.

Anti-Aliasing Filters: Four digitally programmable analog filters were used to condition the sensor signal prior upstream of the digital compensator. For the input/output characterization, these filters were included in the signal path in order to account for any destabilizing phase delays introduced. The modules are supplied by Frequency Devices, model number 824L8L5. The corner frequency of these four-pole, low-pass, Bessel filters is set within the range of 200 to 51,200 Hz using a simple DIP switch. While the Bessel filter does not have the sharpest corner, it does exhibit less phase perturbations near the corner frequency.

Shaker: Bruel and Kjaer Type 4810 mini-shaker.

Force Transducer: PCB Piezoelectroncis, Inc force transducer, model 208-A02 with a charge amplifier model 484B.

Spectrum Analyzer: A SigLab 20-42 spectrum analyzer from dspTechnology, Inc. was used to acquire the frequency response functions used to characterize the system for both open and closed-loop operation.

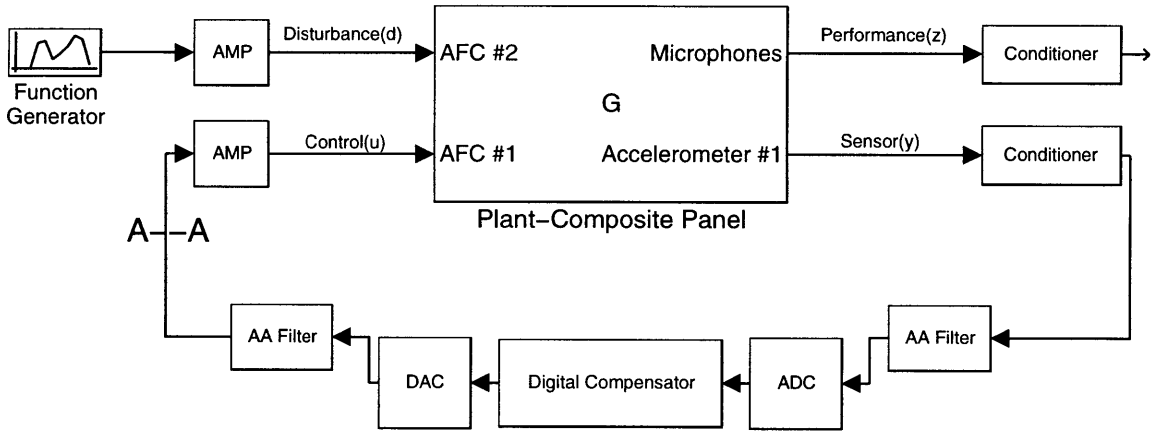

Figure 4.13: Block Diagram of Canonical Experiment

Digital Controller: Dynamic compensator designs are realized using dSPACE digital signal processing (DSP) hardware and software. The dedicated DSP processor is a TMS320C40 - 60 MHz chip on a model DS1003-512 processor board. A local high speed bus connects this with the input an output boards. The DS2003 analog to digital converter (ADC) uses two parallel converters to simultaneously sample up to 32 channels with 16-bit resolution. Each converter can sample at a speed of 5μs, thus for each input pair 5μs of sampling time is required. Each of the 32 channels of the digital to analog converter (DAC) operates in parallel with a period of 10μs with 14-bit resolution. The companion software allows for C-code generation and down loading directly from SIMULINK block diagram models of the compensator system. Two interfacing programs, COCKPIT and TRACE, are used to adjust parameters in the simulation and examine internal signals of the compensator in real-time allowing rapid prototyping of potential designs.

4.3 Standard Experimental Procedure

For consistency a standard experimental procedure is outlined which allows direct comparisons of open-loop input-output behavior as well as the closed-loop control performance presented in the Chapter 6. Care is taken to describe this procedure in order to highlight some of the subtleties of implementations not often discussed.

Canonical Experiment

To characterize the structural system the input-output behavior must be quantified, most often by measuring transfer functions between the various inputs and outputs. In the setup described by Figure 4.13, the open-loop behavior is first measured. In order to

Freq. Range (Hz)	Disturbance Level (Volts RMS)
0-200	250
200-1,000	100
1,000-5,000	50

Table 4.1: Standard Transfer Function Measurement

increase the frequency resolution three transfer functions were measured for each signal path. The disturbance level was varied in order to maximize the coherence in both the sensor (accelerometer) and performance (microphone) measures[10].

When measuring the control signal path two critical elements must be included. By breaking the loop at the section A-A shown in Figure 4.13, and setting the digital compensator to have unity gain at the standard sampling period of $1.5(10^{-4})s$ (6.66 kHz), the phase delay of the computation and the anti-aliasing filters is included in the open-loop data. Simply taking the open-loop transfer function without this hardware in the loop causes unaccounted phase-delay to be added to the control loop, potentially destabilizing the design. This was verified many time experimentally.

The second issue that is easily overlooked is quantization error in the digital/analog conversion process (the ADC and DAC elements). Since the dSPACE hardware has a fixed input range of +/-10 Volts, the gain in the loop must be spread in such a way that the signal at the location of conversion be a significant portion of the full-range, hence the amplifier included on the sensor signal in Figure 4.13.

Acoustic Radiated Power Measurement

The figure of merit for the acoustic control considered in this work is total radiated sound power. Experimental measurement of this quantity requires a few assumptions and is subject to restrictions which will be presented in brief.

Generally, to measure power requires both a force (pressure) and velocity measurement at a single point. Knowledge of the point impedance, the relation between force and velocity, allows power to be calculated from just one of these quantities. The acoustic pressure is an experimentally accessible quantity, while the velocity is not; therefore, to derive the radiated power from pressure knowledge demands that the measurements be taken at a location where the acoustic impedance is known. In the farfield the acoustic impedance is known to be the *characteristic impedance*, $Z = \rho c$, the product of the density and speed of

[10]It was observed that a small input resulted in coherence near 1.0 for the acceleration measurement because the linearity of the system is based on the small deflection assumption, while the coherence of the acoustic measurement was limited by the high noise floor which demanded a large input signal

sound of the medium. The farfield is defined by three criteria [Bies, 1988]. Each is evaluated for this particular experiment[11].

$\mathbf{r \gg \lambda/2\pi}$: This restriction requires that the measurement point be a significant portion of the longest wavelength in the band of interest. Farfield measurements at 70 Hz must be taken at least 0.78m from the source.

$\mathbf{r \gg a}$: This simply demands the observation be made at a distance exceeding the characteristic dimension of the source. For this panel that is approximately 0.305m.

$\mathbf{r \gg \frac{\pi l^2}{2\lambda}}$: This restriction relates the respective size of the source with the acoustic wavelength. For compact sources the farfield behavior is geometrically near to the source, even for high frequencies. For this example a 1,000 Hz pressure measurement can be considered to be farfield at distances greater that 0.436m

From the above, the farfield for the bandwidth of consideration starts at a distance of 0.78 meters from the panel surface. Unfortunately this criteria could not be satisfied in implementation. The anechoic facilities used for these experiments must serve two functions. First the non-reflecting wall surfaces allow for measurement of radiating energy by absorbing the majority of the incident energy. Second the massive walls must block transmission of the exterior environmental noise from corrupting the interior acoustic noise measurements. From the previous discussion on the acoustic partitions, it can be ascertained that to block low frequency signals requires exceedingly thick and massive walls. The excessive low frequency background noise present in the anechoic chamber demanded that the pressure measurement be taken close enough that the radiation from the panel could be discerned from the background noise[12].

To satisfy this tradeoff between signal to noise ratio and validity of the farfield assumption, all the recorded acoustic measurements presented are taken at a radius of $R \approx 22'' \approx 0.56m$. Despite the fact that these measurements are not in the true farfield, as discussed in [Bies, 1988] they are within the *geometric near field* were power can still be accurately approximated from pressure measurements. This is possible because the pressure and velocity are still in phase or the impedance is still real valued in this area. Interestingly the pressure measurements cannot be used to make such and approximation in the *hydrodynamic near field* where this is not the case.

Using the mid-plane microphone traverse, pressure measurements were made at discrete points on a constant radius half-circle at angles varying between -90 and 90 degrees. From these measurements the acoustic directivity at individual frequencies can be measured. Appendix D gives a few examples of the directivity measurements.

[11] For acoustic frequencies between 70 and 1,000 Hz the corresponding wavelengths vary between 4.9 and 0.343 m, and for this experiment the characteristic length (l) is taken to be $\approx$ 1ft=0.305m

[12] Recall that the pressure decays at a rate of $1/R$ in the farfield and the sound power at a rate of $1/R^2$

From pressure measurements in the mid-plane arc, the farfield radiated acoustic power can be approximated. From the spectral analysis of the microphone output signal, the power spectral density of the pressure signal ($Spp(j\omega)$) can be combined with with the characteristic impedance to yield the acoustic intensity, the power per unit area. Numeric integration of these intensity measurements over the half-space yields the radiated power. For the discrete measurements taken on the mid-plane in these experiments this integration is done by a simple weighted summation of the spectrums using the differential azimuthal angle ($\Delta\theta_i$).

$$\Pi(j\omega) = \int_s I(j\omega) dA_s = \sum_{i=0}^{N} \frac{Spp_i(j\omega)}{\rho c} (2r^2 \Delta\theta_i) \; (Watts) \tag{4.1}$$

Typically dynamic measurements are made in the form of transfer functions which describe the output normalized by the input. In the following the radiated power is normalized by the input as well as by taking transfer functions of acoustic output normalized by disturbance input.

4.4 Experimental Verification

To verify the experimental setup, the results from simple dynamic experiments are presented. Transfer functions are utilized to quantify the input/output relationships. The inputs include: point forces applied through a mini-shaker, embedded AFC elements, and incident acoustic disturbances, while the measured outputs include four collocated, surface mounted accelerometers and eight collocated embedded strain gages (pairs at 0° and 90°). A set of transfer function measurements is included in Appendix C to illustrate the behavior of the structure and the instrumentation. For the sake of validation, two transfer functions are compared in detail. These two inputs are taken to be the control and disturbance signals respectively. From Figures 4.14 and 4.15 the analytic Ritz model is shown to correlate very well with the measured data. This provides experimental verification of the model. Specifically the correlation lends confidence in the method of approximating the simply-supported boundary conditions. Not only are the pole locations in close proximity, but also the placement of the zeros is accurately represented. Table 4.4 quantifies the correlation by using a system identification method, FORSE[13], to approximate the experimental modal properties. The table indicates that the model captures most of the eigenmodes. The even modes are not observable from the centered accelerometer, and are thus not represented in the system identification.

[13]The FORSE system identification is explained thoroughly in Chapter 6.

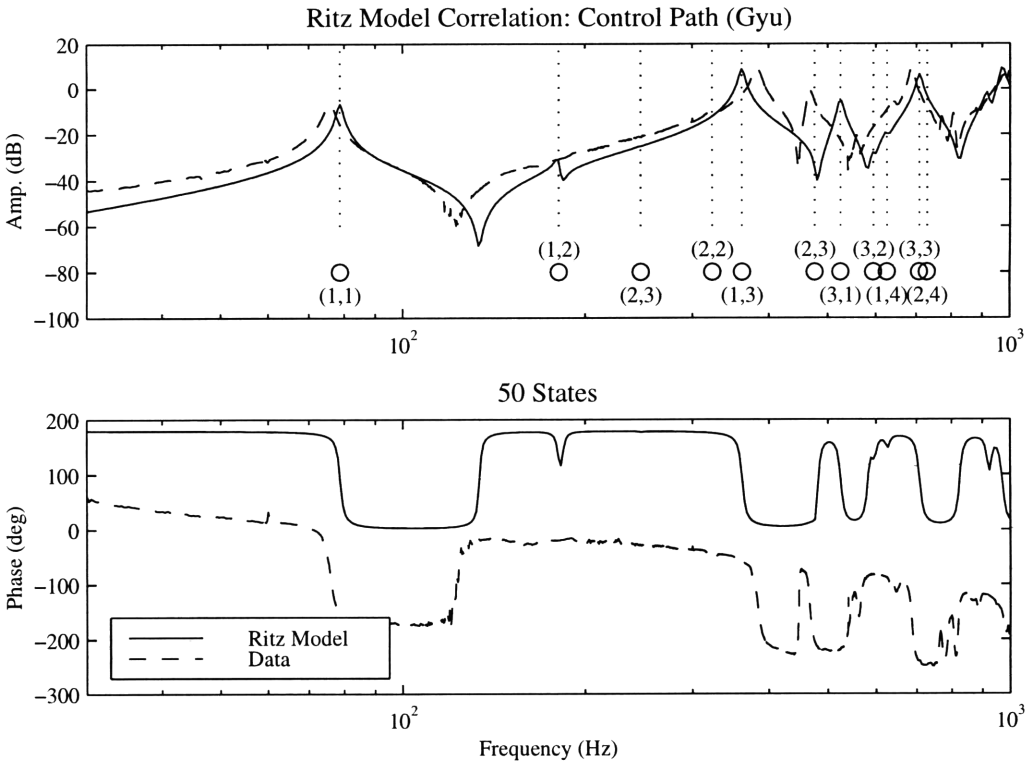

Figure 4.14: Correlation Between Ritz Model and Data for AFC #1 to Accelerometer #1 Transfer Function

4.5 Summary

From the work described in this chapter, an experimental testbed is manufactured which captures the structural-acoustic behavior of the representative panel structure. The manufacturing of the composite panel with embedded sensing and actuation is chronicled along with the dynamic characterization of the inputs and outputs of the system. Probably most importantly, the structural modeling is verified experimentally and vice-versa. The result is an experimental setup which is simple enough to glean insight into the fundamental dynamics through the use of an accurate simple model, while capturing the inherent complexity of a structural-acoustic system.

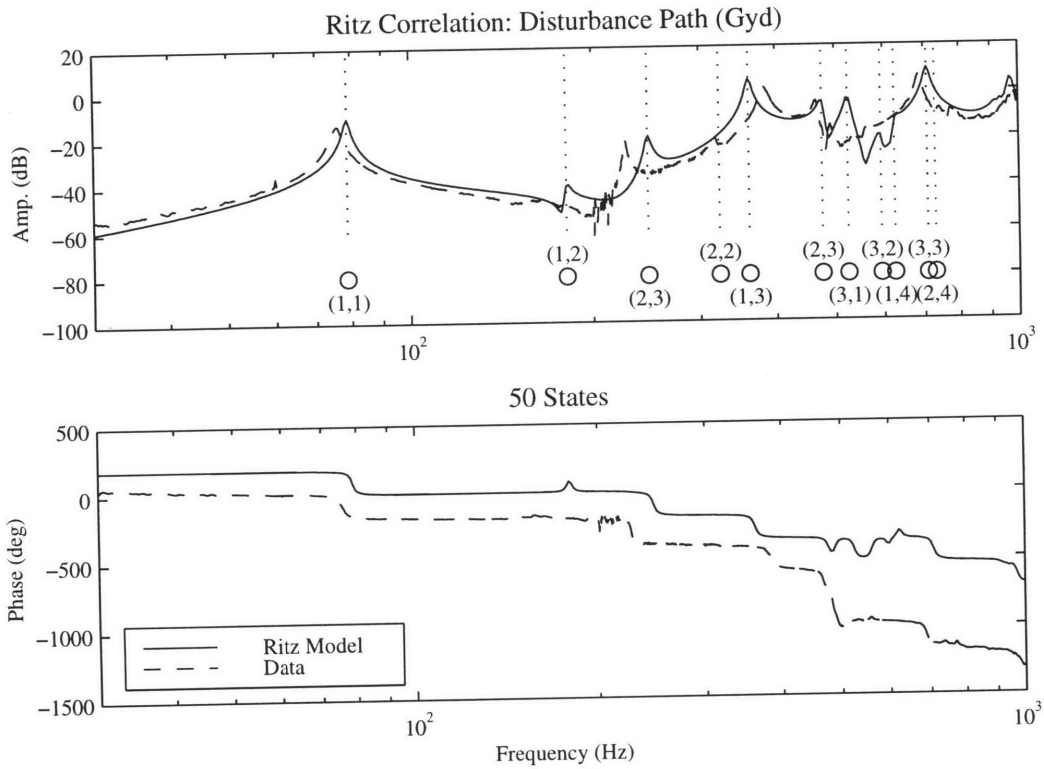

Figure 4.15: Correlation Between Ritz Model and Data for AFC #2 to Accelerometer #1 Transfer Function

Ritz		MODE	FORSE	
ω_i	ζ_i	SHAPE	ω_i	ζ_i
78.8	0.0100	(1,1)	75.7	0.0125
181.1	0.0100	(2,1)		
246.7	0.0100	(1,2)	226.6	0.0064
323.1	0.0100	(2,2)		
361.4	0.0100	(1,3)	382.9	0.0159
475.9	0.0100	(2,3)		
524.8	0.0100	(3,1)	466.8	0.0081
594.9	0.0100	(3,2)		
625.9	0.0100	(1,4)		
707.7	0.0100	(3,3)	687.0	0.0112
728.8	0.0100	(2,4)	706.6	0.4566
918.1	0.0100	(3,4)		
937.6	0.0100	(4,1)		
970.6	0.0100	(1,5)	976.3	0.0236
1003.4	0.0100	(4,2)	1160.1	0.0826

Table 4.2: Correlation Between Ritz and FORSE Modal Parameters

Chapter 5

Vibration and Acoustic Control

Lightweight flexible structures must meet increasingly stringent dynamic performance requirements. The field of high performance structural design has reached such a level of maturity that a general methodology has been developed to approach the overall design synthesis. Controlled Structures Technology (CST) brings together all the tools developed for the various facets of design of such structures and sets forth a cohesive paradigm in which to view these problems [Crawley et al., 1995].

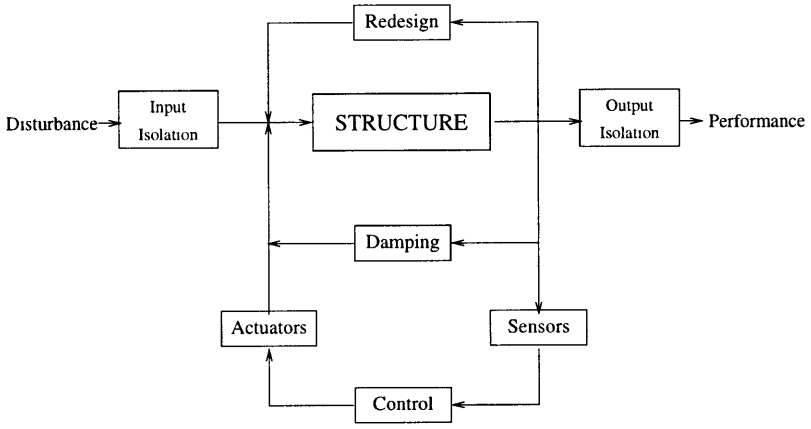

Figure 5.1: Controlled Structure Technology (CST) Diagram

The approach is succinctly described by Figure 5.1. Each of the tasks depicted consists of a complete field of study, but it is the goal of CST to use all these fields together to produce a structure which meets the performance goals while minimizing the associated costs. This thesis fits within this paradigm by presenting the basic analysis of structural control to mitigate acoustic radiation. Delineating the capabilities and limitations of this approach enables the system designer to make informed decisions between active and passive technologies and between competing approaches to the active control problem. The CST methodology focuses on considering the entire problem, so that each design choice will

enhance the final closed-loop performance.

In this chapter the background on three control techniques, as applied to the structural-acoustic control problem, will be presented: classical feedback control, optimal feedback control, and adaptive feedforward control. The capabilities and limitations of each method are illustrated by first presenting the theoretical basis of the compensation technique. Examples based on the structural acoustic model of Chapter 2 are also included to highlight the results for the particular active structural-acoustic panel control.

5.1 Basic Problem Statement

Canonical System

Before beginning it is beneficial to present a common framework of notation to allow comparison of control methods. In general, the structural control problem can be represented with the very simple structure shown in 5.2. The canonical components of a controlled structural problem are:

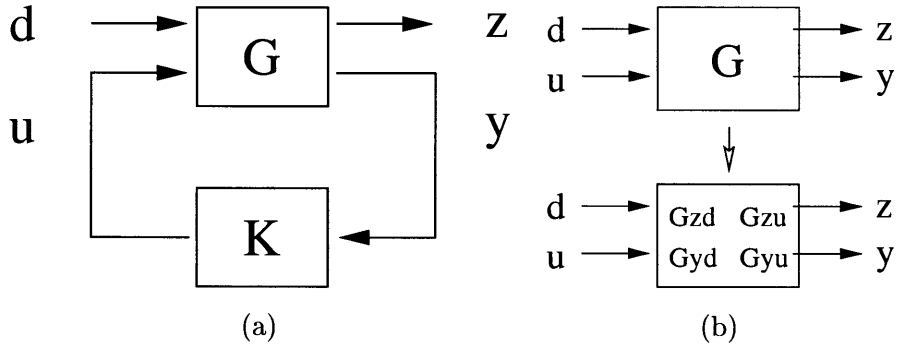

Figure 5.2: a) Generalized *modern paradigm* for control, b) Signal Paths of the Open-Loop Plant

P: Structural plant;

K: Compensator;

d: Disturbance inputs;

u: Control inputs;

z: Performance outputs; and

y: Sensor outputs.

This general paradigm is well developed in the control literature [Levine, 1996]. The structural-acoustic control problem simply lumps the acoustic coupling into the general

structural model. While this standard representation assumes a feedback structure, the defining parameters will be consistent with the feedforward presentation.

Intuition about the canonical problem results from considering the closed-loop performance response to process noise (disturbance d) and sensor noise (v)[1].

$$Z(s) = \frac{G}{1+GK}D(s) + \frac{GK}{1+GK}V(s) = S(s)D(s) + C(s)V(s)$$

The two transfer functions can, $S(s)$ and $C(s)$, are typically referred to the *sensitivity* and *complimentary* responses respectively. The goal of the regulation problem is to minimize influence of the two disturbance sources on the performance. Control design is always a compromising process. The two noise sources simultaneously demand that the *loop gain* response (GK) be maximized, reducing the sensitivity response to process noise, and minimized, reducing the complimentary response to sensor noise or model uncertainty. A solution to this dilemma results from considering the disturbance as containing relatively low frequency components and the sensor noise as representing the uncertainty in the system response at high frequencies. The loop gain transfer function is designed, in general, to have finite bandwidth (where the loop gain transfer function (GK) crosses the unit gain (0 dB) location). Below this frequency the design achieves disturbance rejection while remaining insensitive to the errors at frequencies above this bandwidth.

Model control methods are typically founded on linear, time-invariant, state-space models representing the plant and the compensator. A canonical example relates input vector (u) to the output vector (y) using the internal state vector (x).

$$\begin{aligned} \dot{x}(t) &= Ax(t) + Bu(t) \\ y(t) &= Cx(t) + Du(t) \end{aligned} \tag{5.1}$$

Structural-Acoustic Example

To explore the possibilities for structural-acoustic control, this thesis extends the results of much work done on structural control. The challenges of active structural control are described well in [MacMartin and Hall, 1992]

> Active control of lightly damped, modally dense structures is difficult do to the parametric uncertainty that is inherent in any model of such a structure. The first few modes of the structure can usually be modeled with sufficient accuracy for many state-space control design techniques. However, it may be necessary to have some control authority over many more modes of the structure.

Equivalently three statements are made concerning the fundamental limiting factors of structural control:

[1]The sensor noise is used by the control designer to model the multiplicative error in the system, which can include spillover or un-modeled dynamics.

- Structures are inherently lightly damped, causing large variations in gain and phase of the resulting input-output relationships;
- Structures are modally dense;
- Structures are difficult to accurately model and experimentally verify consistently at high frequencies.

To illustrate the theoretical results presented for each control concept, simulations performed on the coupled structural-acoustic model presented in Chapter 2. For consistency and comparison, a basic single input, single output (SISO) architecture is used for each case. The example is defined in terms of the parameters of the canonical system structure of Figure 5.2.

P: The two input, two output structural-acoustic Ritz model;

K: Three basic compensator designs: classical, optimal, and adaptive;

d: The disturbance enters through a secondary AFC actuator placed at $(L_x/6, L_y/2)$ - AFC #2 from the placement problem of Chapter 3 (see Figure /reff:placediag);

u: Control is achieved using the centrally located AFC pair - AFC #1 (see Figure /reff:placediag);

z: The performance metric is the farfield radiate acoustic power, the output of the radiation filter model; and

y: A collocated accelerometer is used as the feedback and error sensor;

The example parallels the experimental results presented in Chapter 6.

Performance Evaluation

To compare control designs it is necessary to specify a consistent performance metric. In applications, engineering judgment must be used when selecting a performance metric. Many designs have optimized the wrong criteria, and despite being 'good' design the result does not achieve the necessary performance.

From a control perspective the structural-acoustic problem is one of disturbance rejection. The disturbance input is considered to be a white noise stochastic process with unit impulse auto covariance, $\Phi(\tau)$. Taking the Fourier transform of this expression yields the autospectrum, $\Psi(\omega)$, which is unity for all frequencies indicating that the disturbance has infinite energy. For stationary, ergodic processes this is expressed simply [Papoulis, 1965].

$$\Phi(\tau) \equiv E[d(t)d^T(t+\tau)] = \delta(\tau)$$
$$\mathcal{F}[\delta(\tau)] = \Psi(\omega) = 1$$

From linear system theory, the covariance of the state vector, Σ_{xx}, satisfies a Lyapunov equation in response to such a random disturbance. Directly from the state-space equations (5.1) the covariance matrix of the performance (Σ_{zz}) and the control (Σ_{uu}) can be determined.

$$AX + XA^T + BB^T = 0$$
$$\Sigma_{xx} \equiv E[xx^T] = X$$
$$\Sigma_{zz} \equiv E[zz^T] = E[Cx(Cx)^T] = CXC^T$$
$$\Sigma_{uu} \equiv E[uu^T] = E[Kx(Kx)^T] = KXK^T$$

From the covariance matrices, the root mean square (RMS) value of the vector (z) can be easily determined from the definition.

$$(RMS(z))^2 = \lim_{T\to\infty} \frac{1}{T} \int_0^T z^T(t)z(t)\,dt = trace(E[zz^T]) = trace(\Sigma_{zz})$$

This yields a simple way to determine the RMS response of the performance variable assuming disturbance components at *all* frequencies.

To consider the response over a limited bandwidth, and eventually to evaluate the performance from experimental data, the RMS response is evaluated directly from the frequency response, $z(\omega_i)$, using Parseval's Theorem.

$$(RMS(z))^2 = \frac{1}{2\pi} \int_0^\infty z^T(\omega)z(\omega)\,d\omega \approx \sum_i z^T(\omega_i)z(\omega_i)\Delta\omega_i$$

Typically the *RMS reduction* will quantify the performance of a control system. This is simply the difference in the open-loop and closed-loop RMS performance in decibels.

$$\text{RMS Reduction} = 20 * \log\left(\frac{RMS_{open-loop}}{RMS_{closed-loop}}\right)$$

Disturbances

The possible disturbance sources are as varied as the possible applications. For the examples considered here, it is desired to choose a disturbance which represents as many of these possibilities as reasonable. Three possible disturbances, a point force, an AFC actuator, and an incident acoustic wave, are compared in Figure 5.3. Each bar represents the normalized modal contribution, or terms in the forcing matrix of the Rayleigh-Ritz model, indicating which vibration modes are influenced the most. The location of the point force was chosen to have good modal control/observability, thus it influences each of the modes. The AFC is located in the center of the panel with fibers along the y-direction, thus the high controllability of the (1,3) and (3,3) modes with high strain energy (curvature) in the fiber direction. The plane wave acts analogously to the modal radiation in that it excites

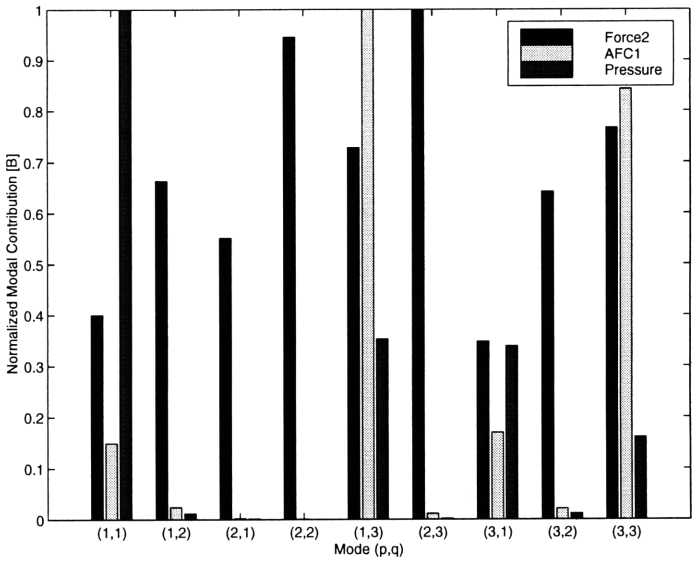

Figure 5.3: Three possible disturbances: Point Force (Forse2), Central AFC (AFC1), and Plane Pressure Wave (Pressure)

the acoustically radiating volumetric modes. Each of these disturbances excites a different modal profile. This observability consideration must be taken into account when simulating control designs and generalizing the results for application.

5.2 Classical Control

Simplicity of implementation and robustness to modeling errors make classical techniques attractive. Two types of classical feedback methods give very elegant results for structural control: rate feedback (RF) and positive position feedback (PPF). Considering these basic methods, gives the control designer insight into the physical challenges of structural control. Here the basics of the theoretical results are discussed with examples from the already developed structural-acoustic model.

The simplicity of these techniques comes at a cost. Design is performed with just knowledge of the control to sensor open-loop dynamics. While this simplifies the design, because no real model is necessary for controller design, the compensator does not take into account the information about the disturbance source or the performance function. Note the example presented here considers the Ritz model of the dynamic response of the central AFC control actuator and a collocated acceleration measurement sensor.

5.2.1 Rate Feedback

Rate feedback control is a very general term for a proportional compensator that directly feeds a rate sensor signal, such as velocity or strain rate, back to the control actuator. Many convenient relationships can be exploited in structural control when rate feedback is explored on systems with collocated and dual, sensors and actuators as described at length in [Campbell, 1993]. The fundamental relationships for this type of architecture is developed from infinite wave model results presented in Chapter 3. The following statements are repeated concerning the sensor/actuator transfer function, $G_{yu}(s)$.

1. The plant is positive real, that is the phase is bounded by $\pm 90°$;

2. The poles and zeros alternate with increasing frequency (P-Z-P pattern).

For non-dual pairs it is still possible to be 'collocated' as defined by the pole-zeros structure which we will see, guarantees theoretical robustness of rate feedback designs. A transfer function is considered 'collocated' for this analysis up to the frequency where the above statements fail. For the particular case of interest here, the actuator is a distributed active fiber composite (AFC), and the sensor is modeled as a point acceleration measurement. From the standing wave consideration of simple substructures, this pair retains collocated behavior up to a frequency where the significant modes have an anti-node line falling between the edge of the actuator boundary and the point sensing location. At higher frequencies the input-output transfer function drops below -90 degrees, and the P-Z-P pattern in interrupted by a *missing zero.* This result can bound the capabilities of rate feedback control

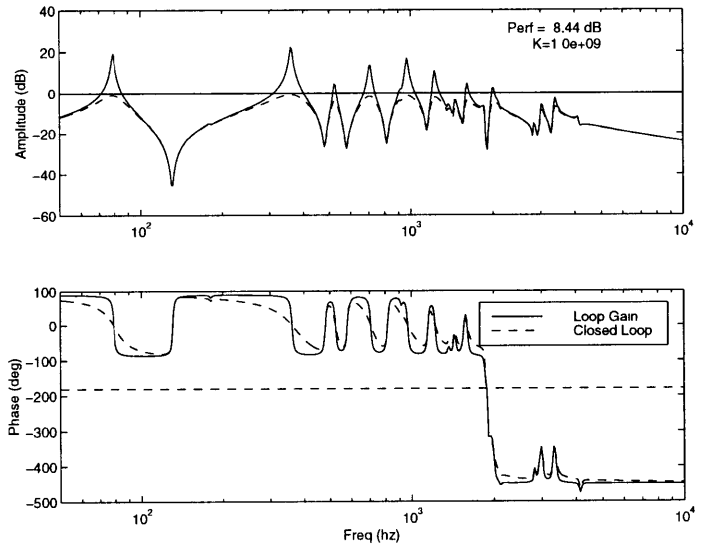

Figure 5.4: Theoretical Performance of Rate Feedback for Panel Vibration

The consequence of the above statements for rate feedback is what has been termed *hyperstability.* In Figure 5.4, the compensator is just a proportional gain (k) on the velocity sensor, thus the loop-gain transfer function ($G_{yu}K$) is simply a scaled version of the open-loop. For this example the control is the applied voltage to the centrally located AFC patch and the sensor is the velocity at the geometric center of the panel[2]. This model contains the first 49 modes of vibration which give a theoretical model of the composite structure up to 4.1 kHz. It is important to note that the transfer function stays collocated, in the sense that the phase remains bounded and the alternating pole-zero structure is preserved, up through 2 kHz where the phase drops indicating a missing zero. From classical frequency domain design techniques it is evident that while the transfer function stays collocated, the phase margin for this design is guaranteed to be at least 90° and there is infinite gain margin because the phase never crosses over the 180° bound.

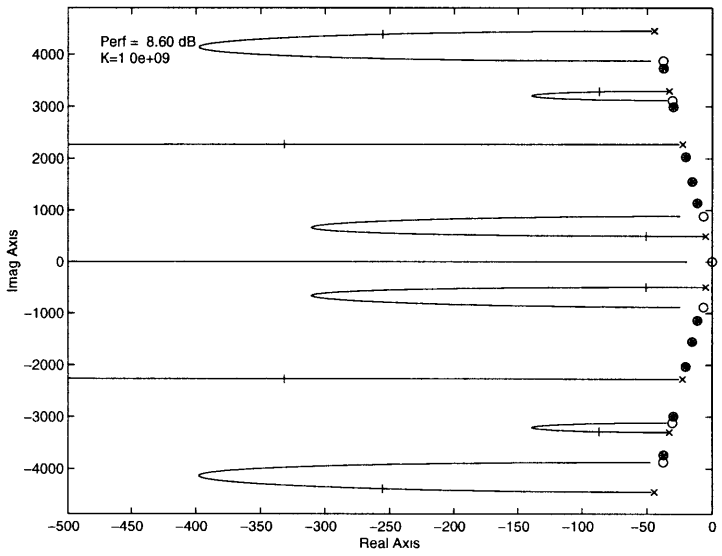

Figure 5.5: Theoretical Root Locus for Rate Feedback (o: open-loop zeros, x: open-loop poles, and +: closed-loop poles)

The root locus plot in Figure 5.5 shows how the closed loop poles migrate farther into the left half plane as the compensator gain is increased indicating an increase in the damping ratio of the resonant poles. The control-displacement system also exhibits this property, but placing the zero at the origin (differentiating) *pulls* the root locus into the right half plane. As the poles migrate along the root locus with increasing gain, the level of damping is increased until an optimal value is achieve, at which point pole begins to migrate back toward $j\omega$ decreasing the damping and increasing the eigenfrequency or actively stiffening

[2]It is assumed that an acceleration measurement (accelerometer signal) can be integrated exactly to yield velocity.

the structure. This illustrates perfectly why this method of control is often termed *active damping*

A bit of realism must be introduced to temper these theoretical results. The consequence of implementation is that the control designer must deal with limitations on sensor and actuator dynamics as well as unmodeled dynamics of the structure. In anticipation of the experimental implementation described in Chapter 6, the rate feedback must be *rolled-off* at high frequencies due to both of these considerations. Recalling the actuator-sensor relationships developed earlier, it will become clear that choosing controller pairs with *natural* magnitude roll-off, while maintaining the collocated rate feedback phase bound will be beneficial[3]

For this example, the model is assumed to accurately represent the system up to about 1 kHz. To design a compensator robust to these errors, the loop must be gain stabilized above this frequency. Dynamics are introduced in the compensator to decrease the loop gain at higher frequencies. For a single pole roll-off filter the compensator takes the form,

$$K(s) = k\left[\frac{\omega_{ro}}{s+\omega_{ro}}\right]$$

where the cutoff frequency ω_{ro} is selected in order to balance performance and robustness,

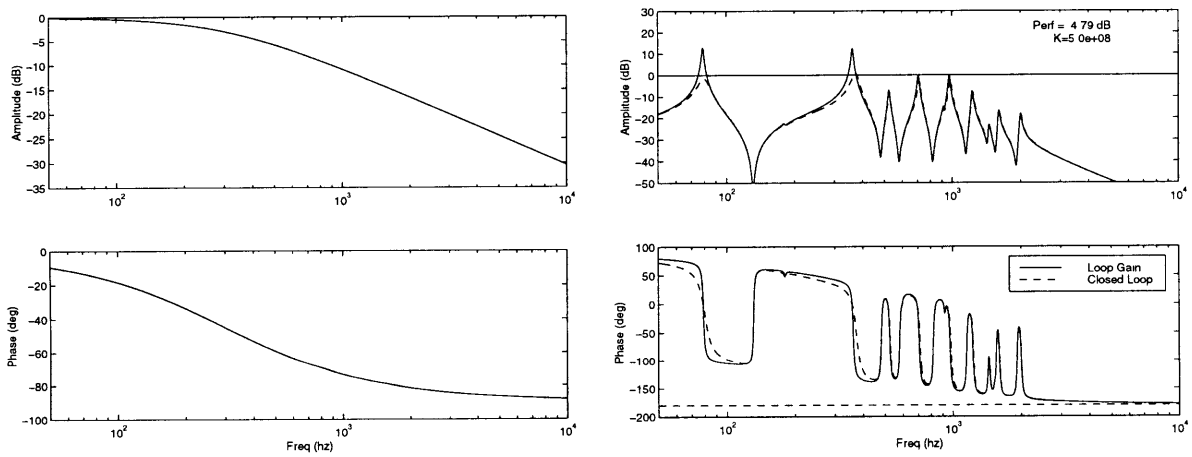

(a) (b)

Figure 5.6: Rate feedback (RF) with single pole roll-off at 350 Hz: (a) - Compensator K(s), (b) - Loop Gain and Closed Loop

the dynamic tension of all control designs. The inevitable consequence of introducing this roll-off is associated the phase lag. This example illustrates the fundamental problem of attempting to roll-off the magnitude of modally dense structures. For this example, the

[3]This has been the 'holy-grail' of many research topics in structural control, that is, finding structural control pairs with roll-off *and* collocation

single pole roll-off is placed at 350 Hz in order to reduce the loop gain of the resonant peaks above 1 kHz and robustify the compensator. The associated phase lag of 90° reduces the guaranteed phase margin to zero, as the high frequency phase is now bounded by $0/-180°$. If the gain was increased to a point where these higher modes exceeded the 0 dB level, the phase margin would be reduced to zero. To further illustrate this behavior the root locus

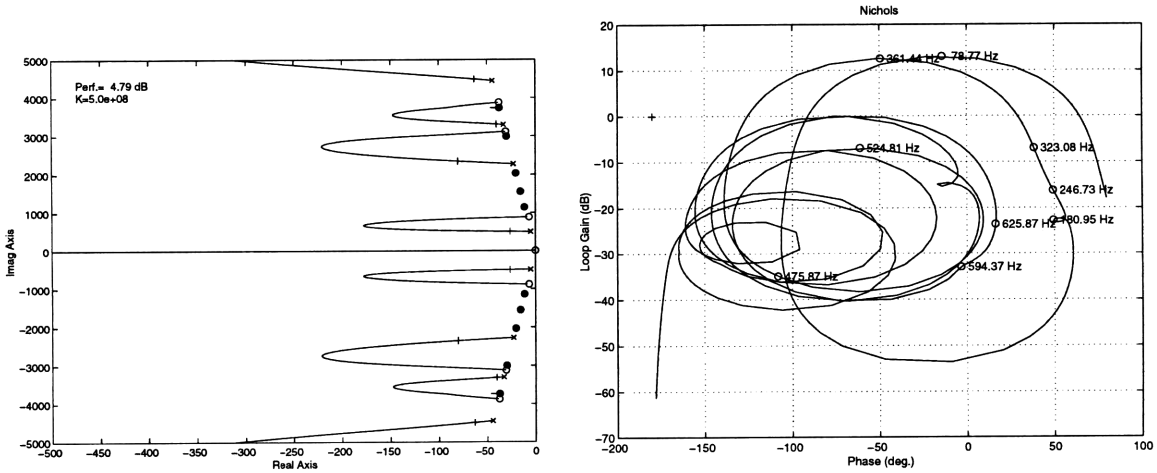

(a) (b)

Figure 5.7: RF with single pole roll-off: (a) - Root locus (b) - Nichols

and Nichols plots of the loop gain transfer function are displayed in Figure 5.7. Direct comparison of the root locus with Figure 5.5 where the roll-off is not included illustrates the diminished performance of this robust design. The traces of the close-loop poles do not extend as far to the right indicating a tighter limit on the achievable damping. The Nichols plot is another method of visualizing the stability of the loop gain. Each mode is represented by an additional loop in the plot and the roll-off filter is shown to gain stabilize the higher modes by lowering the gain below 0 dB at higher frequencies.

Another option to address this consideration is to use complex or resonant poles to introduce the desired roll-off. The advantage, recalling the rules for bode plotting, is that the high frequency slope is steeper and the phase transition (from 0 to 180°) takes place over a narrower frequency range. This compensator is more capable of introducing roll-off between closely spaced resonant modes without destabilizing the system.

As more considerations of implementation are included, this design ceases to be simple and takes into account more characteristics of the particular plant. The motivation of this local control technique is to provide a simple technique that performs robustly with a degree of independence from the actual structural model; however, implementation often demands that dynamics specific to a particular structure (such as notch filters) be included. How well these theoretical results transfer to experiment will be completely addressed in Chapter 6.

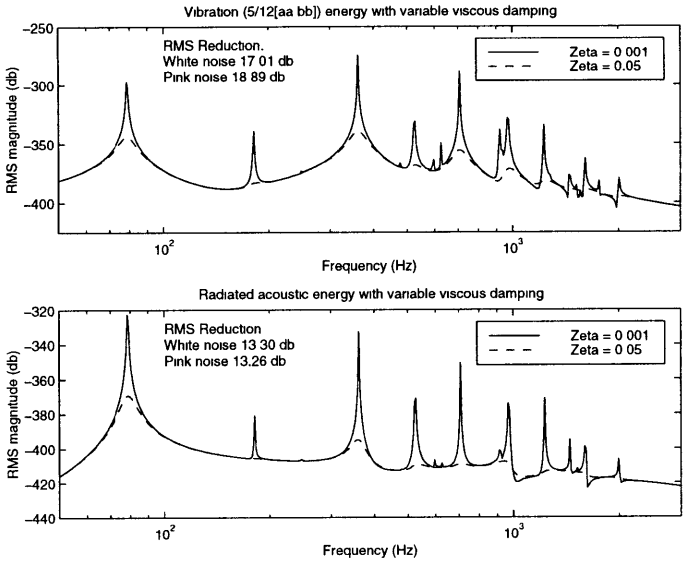

Figure 5.8: Vibration and Acoustic Performance with Added Damping

So far, rate feedback has shown to reduce the vibration of structural element robustly and with few complications. It is fairly obvious that this reduced vibration energy will translate into reduced acoustic radiation. The RMS performance is calculated for the example model with two different assumed values for the modal viscous damping ratio (ζ) to illustrate this. In Figure 5.8 the RMS vibration is plotted from the frequency response of the 25 mode model. The performance, quantified by the RMS reduction from $\zeta = 0.001$ to $\zeta = 0.05$ conditions, is directly analogous to active damping using rate feedback. For this case the disturbance is considered to enter through the AFC control actuator. The calculation is performed as explained above for the theoretical white noise disturbance and for the band-limited frequency response (indicated by the "pink noise" performance label in figure). This analysis verifies the intuitive notion that by actively damping the resonant response of the structure, the acoustic radiation is also reduced.

5.2.2 Positive Position Feedback

Another approach that has proven useful for the control of resonant structural problems is *Positive Position Feedback* (PPF). The features of PPF often cited are similar to those of local rate feedback. The controller is again very simple, robust to modeling errors and spillover effects, and fairly independent of the dynamics of the structure [Fanson and Caughey, 1987].

To continue to gain an intuitive notion of the operation of this control method, it is cast here as a variant on the rate feedback design. As shown in Figure 5.9, the canonical PPF control design for a structural plant with position as the output is simply a proportional gain and a resonant two pole filter. This is equated to the second representation, where

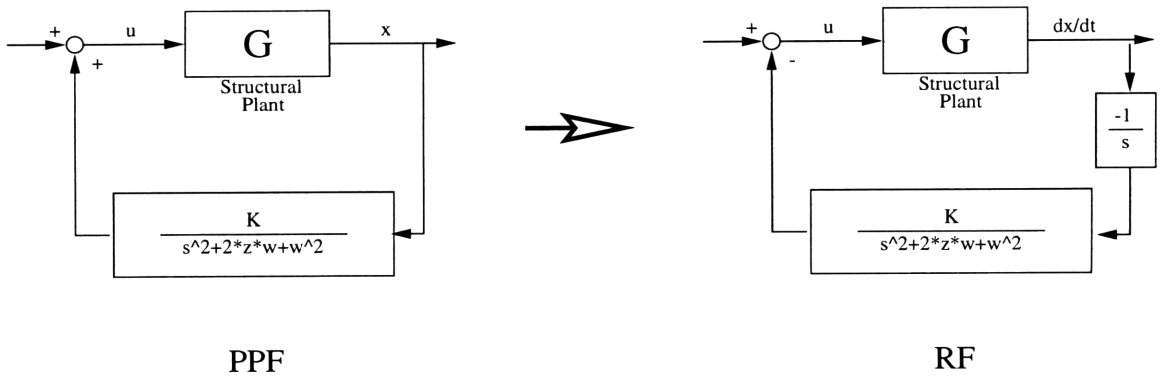

Figure 5.9: Equivalent Realizations of Positive Position Feedback

the plant has velocity output and the feedback is *negative*, by adding an integrator (pole at zero) and reflecting the negative sign into the compensator gain. From the previous discussion on the desirable features of rate feedback, we can now interpret PPF by directly comparing its operation with that of the rate feedback design.

Typically, for reasons that will become evident, the resonant frequency of the compensator is matched to that of a particular resonant mode of the structure. The other design parameter is the damping ratio (ζ) for the complex compensator pole pair. From Figure

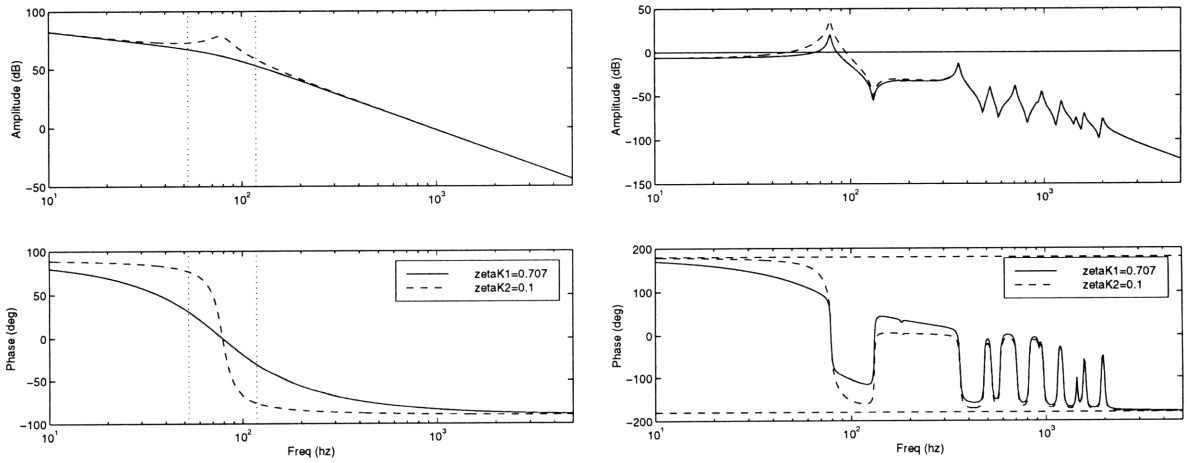

Figure 5.10: For two PPF compensator damping ratios: (a) - Compensator dynamics K(s), (b) - Loop gain G(s)K(s)

5.10 the interpretation of PPF as a filtered rate feedback method can be shown by three frequency regions in the compensation. The frequency response of the compensator in plot a) is in terms of negative feedback of the velocity signal for direct interpretation in terms of rate feedback designs.

- Below the resonant frequency of the compensator the phase of the compensator is

90°indicating negative feedback of an acceleration signal which effectively softens the structural response.

- Near the resonant frequency, the phase of the the compensator quickly passes through 0°, indicating simple rate feedback at the resonant frequency. The damping ratio of the compensator dictates the width of this phase transition, hence the bandwidth of the active damping region.
- Above the resonant frequency, the phase is 90°, indicating negative feedback of the position signal which tends stiffening the response.

For this analytical example, the modal frequencies are known exactly. This SISO example uses the first resonant frequency for the compensator and two values for the damping ratio. From the closed loop response it is evident that decreasing the damping, in an effort to

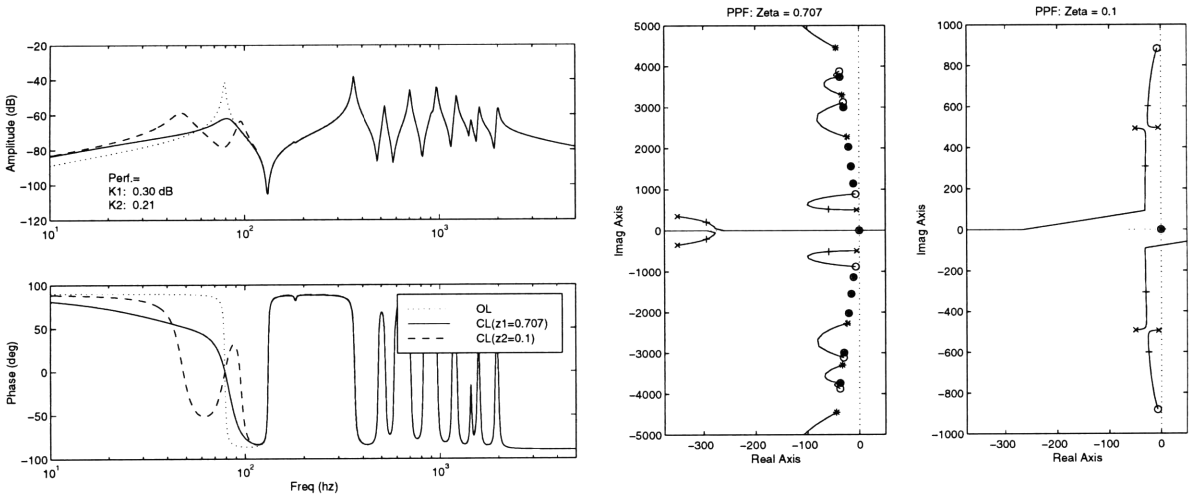

(a) (b)

Figure 5.11: For two compensator damping values: (a) - Closed loop performance (b) - Root locus

maximize the gain of the rate feedback portion of the compensator bandwidth, causes the phase transition to be constricted in frequency to a point where the mode of concern is actually 'split'. From the root-locus plots in Figure 5.11, this splitting of the first mode can be directly observed. Since the compensator poles are at the same frequency as the first mode of the structure, as the compensator damping is decreased the compensator poles migrate toward the open loop poles of the system. The behavior illustrated in the second root-locus shows how decreasing the ratio from 0.707 to 0.1 will cause two modes to appear near the original frequency with little damping. This is manifested in the RMS performance metric as the performance is reduced despite the fact that the gain at the resonant frequency is increased.

Intuitively PPF for a single mode can be thought of as a very localized rate feedback controller. The three pole roll-off (-60dB/decade) beyond the resonant frequency robustifies the system by gain stabilizing all the modes beyond the mode of concern. This narrowband performance of the PPF methodology is both an advantage and a disadvantage. The method is certainly more robust, but the trade off is that a quite accurate modal frequency must be available and that the control only adds damping to the mode of concern.

To apply the method to multiple modes, it is possible to sequentially close PPF loops for each mode of concern. Here a simple example of sequentially closing the PPF control loop targeting the first mode, and then closing a loop targeting the second mode is presented. The two compensators are developed independently as shown in Figure 5.12. The difficulty

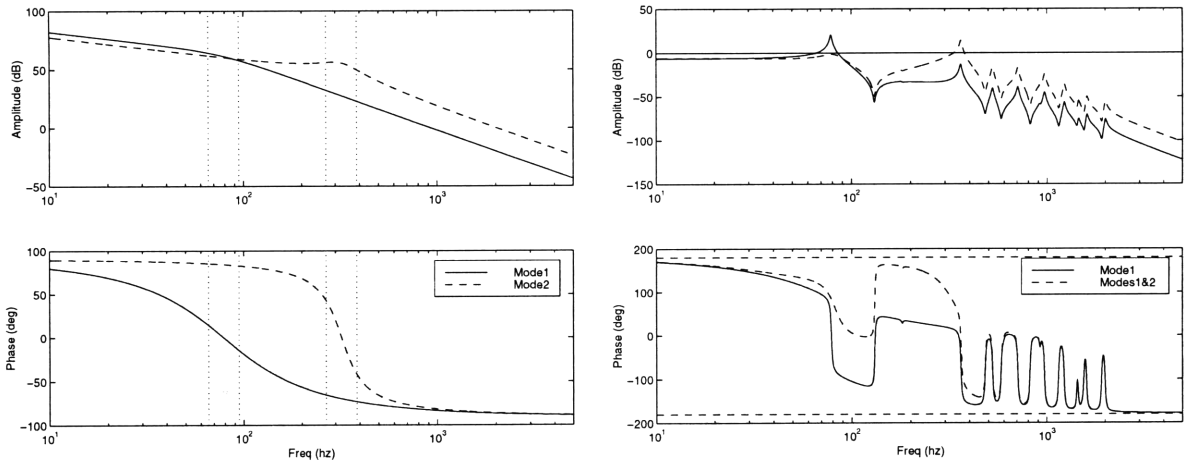

Figure 5.12: a) Independent PPF compensators b) Sequential Loop Gain

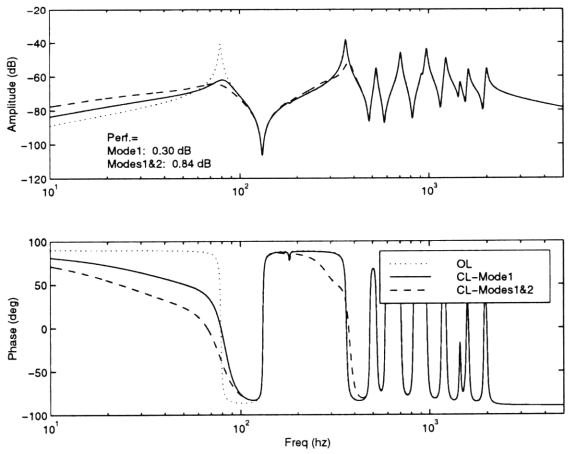

Figure 5.13: Closed loop performance for sequentially closing two PPF loops

in attempting to control two modes with PPF control is that the fourth mode[4], must be used with sufficient gain to force the loop gain above unity. In order to do this without adding much flexibility to the low frequency range (that is keeping the low frequency loop gain below unity), a lightly damped ($\zeta = 0.2$) pole pair must be used in the second mode compensator. While this method does show that more than a single mode can be controlled using PPF, the eigenfrequency of each target mode must be accurately known, and three more states are added to the compensator model. For more than a few modes this defeats the intent of developing simple local control methods.

5.3 Linear Optimal Control

Many excellent references give all the details of optimal control theory for a wide variety of applications: [Bertsekas, 1995], [Levine, 1996], [Lublin et al., 1996], and [Zhou et al., 1995]. This section will present just the essential background necessary to make the results that follow comprehensible, and a simple example to illustrate the benefits and pitfalls of these powerful theories as applied to the very specific structural-acoustic control problem. By design, the application of optimal control techniques is simplified through the radiation filter formulation explained earlier. The advantage of this approach is that by expressing the radiated power as the output of the coupled state-space structural control model, the performance metric can be directly incorporated into the compensator design. This is contrasted by the classical techniques previously discussed, and the feedforward methods to follow, which are designed to reduced the sensor signal. For the active structural-acoustic control (ASAC) presented here, this sensor is integrated with the structure, thus mitigating the sensor response does not directly address the performance goal.

Basic Optimal Control Problem

In order to set the framework for later discussions, a detailed framework for discussing the design, solution, and implementation of the basic optimal control problem is presented here. This *modern paradigm* is explained thoroughly in the excellent reference [Lublin et al., 1996], which completely details the practical properties of $\mathcal{H}_2$ and $\mathcal{H}_\infty$ control design. The theory extends from the Liner Quadratic Regulator problem (LQR), where the *cost function* is expressed as a quadratic function of the linear system. The solution to the regulator problem is combined with the powerful estimation result for linear state-space systems, the Kalman filter, to yield an optimal control scheme based on the limited information in the system sensors. The difference between the $\mathcal{H}_2$ and $\mathcal{H}_\infty$ control designs originates from the specification of the cost. The $\mathcal{H}_2$ design seeks a minimization of the $\mathcal{H}_2$

[4]This appears as the second observable mode in the transfer function

norm[5] which minimizes the RMS frequency response over the entire bandwidth, while the $\mathcal{H}_\infty$ problem minimizes the $\mathcal{H}_\infty$ norm[6], which minimizes the peak of the frequency response. The solution for the former comes from a constrained linear optimization step using calculus of variations and the latter results from a game theory min-max consideration. This theory is well developed and only the results are considered here.

For notation the detailing of this canonical system framework is repeated. The open-loop, linear, time-invariant system is succinctly represented by,

$$\begin{pmatrix} \dot{x}(t) \\ z(t) \\ y(t) \end{pmatrix} = \begin{bmatrix} A & B_w & B_u \\ C_z & 0 & D_{zu} \\ C_y & D_{yw} & D_{yu} \end{bmatrix} \begin{pmatrix} x(t) \\ w(t) \\ u(t) \end{pmatrix} \tag{5.2}$$

$$w(t) = \begin{pmatrix} d(t) \\ n(t) \end{pmatrix} \quad z(t) = \begin{pmatrix} z_x(t) \\ z_u(t) \end{pmatrix}$$

with the following basic assumptions.

1. Feed through from noise to performance (D_{zw}) is zero.
2. $\begin{bmatrix} A & B_u \end{bmatrix}$ is stabilizable[7] and $\begin{bmatrix} A \\ C_y \end{bmatrix}$ is detectable[8].
3. $\begin{bmatrix} A & B_w \end{bmatrix}$ is stabilizable and $\begin{bmatrix} A \\ C_z \end{bmatrix}$ is detectable.
4. $\begin{bmatrix} B_w \\ D_{yw} \end{bmatrix} \begin{bmatrix} B_w^T & D_{yw}^T \end{bmatrix} \equiv \begin{bmatrix} V_{xx} & V_{xy} \\ V_{xy}^T & V_{yy} \end{bmatrix} \geq {}^{9}0$ with $V_{yy} > {}^{10}0$.
5. $\begin{bmatrix} C_z^T \\ D_{zu}^T \end{bmatrix} \begin{bmatrix} C_z & D_{zu} \end{bmatrix} \equiv \begin{bmatrix} R_{xx} & R_{xu} \\ R_{xu}^T & R_{uu} \end{bmatrix} \geq 0$ with $R_{uu} > 0$.

Here the general noise vector, $w(t)$, includes both the process noise, $d(t)$, and the sensor noise, $n(t)$, while the generalized performance, $z(t)$, includes the state penalty, $z_x(t)$, and the control penalty, $z_u(t)$, allowing the cost function for each formulation to be expressed as simply,

$$J_2 = \lim_{\tau \to \infty} \frac{1}{\tau} \int_0^\tau z^T(t) z(t)\, \mathrm{d}t = E[z^T(t) z(t)] \tag{5.3}$$

---

[5] $||G||_2 \equiv \left(\frac{1}{2\pi} \int_{-\infty}^{\infty} trace[G(j\omega) G^*(j\omega)] d\omega \right)^{1/2}$, which can be equated to the sum of the areas under the singular value curves or the RMS value of the output of the system $G(s)$.

[6] $||G||_\infty \equiv sup_\omega \sigma_{max}[G(j\omega)]$

[7] All unstable states are reachable from B_u, while all unreachable states are stable.

[8] All unstable states are observable from C_y, while all unobservable states are stable.

[9] Positive semidefinite

[10] Positive definite

The essence of the LQG design is to minimize the quadratic cost of Equation (5.3). Optimal control theory, [Lublin et al., 1996], shows that this is done by direct feedback of the state vector. The LQR gain matrix relating the optimal control to the state vector is found to satisfy an algebraic Ricatti equation. Since the internal states of the system are not all available, an estimator must be implemented to estimate the states of the system based on the sensor measurements. The Kalman filter is introduced to minimize the square estimation error. The dynamic estimator takes the form of a state-space system with the same dynamics of the original plant, where the input is the error between the sensor measurement ($y(t)$) and the estimated system output ($\hat{y}(t) = C_y\hat{x}(t)$ based on the estimated state vector ($\hat{x}(t)$). The dynamic Kalman filter estimator equations are simply expressed.

$$\begin{aligned} \dot{\hat{x}}(t) &= A\hat{x}(t) + H[y(t) - C_y\hat{x}(t)] \\ \hat{y}(t) &= C_y\hat{x}(t) \end{aligned}$$

The Kalman filter gain (H) is calculated from the solution to an algebraic Ricatti equation similar to that of the LQR problem. From the LQR gain matrix, the system dynamics, and the Kalman gain matrix, the dynamic LQG compensator is fully defined. The details of the solution are clearly presented in [Lublin et al., 1996].

This notation is completely general, and can be manipulated to include a wide variety of problems. For many problems, a few simplifying assumptions can be made to gain a bit of intuition about the problem statement and identify the important design parameters. For many problems the following assumptions hold:

1. No feed through terms in the structural plant model.
2. No cross penalty on state and control in the LQR problem
3. Uncorrelated process and sensor noise
4. Equivalent control penalty on each control input (ρ-scalar)
5. Equivalent sensor noise on each sensor (μ-scalar)

For the $\mathcal{H}_2$ version of the control design, this reduces the quadratic cost function statement for the LQR problem to,

$$J_2 = \lim_{\tau\to\infty} \frac{1}{\tau} \int_0^\tau \left(x^T(t)N^TNx(t) + \rho u^T(t)u(t)\right)\, \mathrm{d}t \tag{5.4}$$

Similarly, the Kalman filter minimizes the square estimation error, and again the solution takes the form of an analogous Ricatti equation [Zhou et al., 1995]. This formulation highlights a few design parameters the control designer uses to specify the performance/robustness trade off of a particular LQG design.

N: Output matrix specifying the state weighting, $z_x = Nx$

ρ: Control penalty specifying the amount of control authority, and hence the bandwidth of the controller.

μ: Sensor noise strength specifying the quality of the estimation done by the Kalman filter.

Optimal Control for Structures

Using the simplifying assumption listed above a few asymptotic properties of the LQR and LQG controlled systems can be derived [Athans, 1997]. Using these limits of performance, a set of simple rules has been developed designing LQG compensators for structural control, [Campbell, 1993]. For analogous, dual, collocated input and output pairs, as described in Chapter 3, the results can be summarized by the following for the case where the sensor noise is assumed to be small ($\mu \to 0$).

Low-Gain: As $\rho \to \infty$ the LQG design reduces to rate feedback on the dominant mode in the disturbance response, actively damping the structure.

High-Gain: As $\rho \to 0$ the LQG design reduces to position feedback, actively stiffening the structure.

These asymptotes guide an intuitive design approach to select the control weight (ρ) which dictates the desired bandwidth. The bandwidth of a particular controller design, defined by the gain crossover frequency of the dereverberated loop gain transfer function, defines the two conflicting frequency regions for control: low frequency performance and high frequency robustness. From these results a set of 'Neo-classical' design rules are developed in [Campbell, 1993] in order to balance the optimality of the LQ solution with the intuition of classical techniques.

Optimal Control for Acoustic Radiation

The structural-acoustic model developed in Chapter 2 expresses the coupling of the farfield radiated power to the modal velocities for a simply supported plate through a spectrally factored radiation filter. This coupling can be compared to the frequency weighted $\mathcal{H}_2$ and $\mathcal{H}_\infty$ problems explained in [Gupta, 1980] and [Lublin et al., 1996]. By specifying the response of weighting functions, the compensator design can be tailored to account for frequency dependent cost statements. For example, a function can be used to add frequency dependence to the control cost parameter (ρ) such that the cost is low in the region of where the dynamics are particularly offensive, causing higher compensator gain in this bandwidth. The dynamics of these weighting filters is then lumped into the dynamics of the nominal plant, transforming the design process to a selection of scalar (or vector)

design parameters, typically ρ and μ. Weighting functions representing the control cost, state cost, sensor noise, and process noise can be tailored by the control designer to influence the compensator design. Typically only one or two of these options are used since each adds order to the system, thus the compensator, and the effect of the weighting functions can be redundant. For example consider the approach to using weighting functions to roll-off the high frequency gain of a design. The same effect can be obtained by either adding a weighting function on the state-cost with decreasing amplitude or defining an control weighting with increasing amplitude. Each is sufficient and using both adds needlessly to the order of the system.

The acoustic radiation model of Chapter 2 is directly analogous to such a frequency weighting function. The structural state-space model is formulated with a modal velocity vector output. The *radiation filter*, $G(s)$, is appended to this system to map the modal velocities to the radiated power. This is a specific, physically based, frequency weighting function which in effect simply weights the structural output based on knowledge of the acoustic coupling. This approach is illustrated in the following example and will be referred to as the radiation filter linear quadratic Gaussian design (RF-LQG).

Design Example - RF-LQG

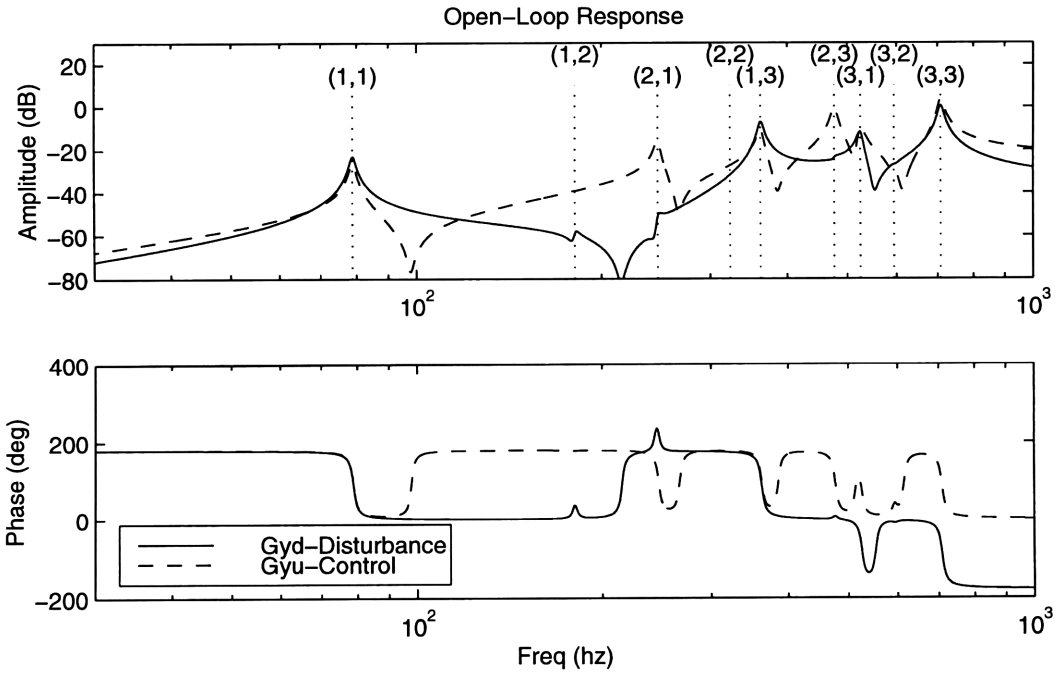

Figure 5.14: Open-Loop Frequency Responses for Design of Optimal Controllers

First the open-loop frequency response of the system is presented in Figure 5.14. The architecture of the system is consistent with the previous examples as described in Section 5.1; the

disturbance enters the system through a secondary AFC actuator placed at $(L_x/6, L_y/2)$, the control is achieved using the centrally located AFC pair, and the structural sensor is taken to be an accelerometer collocated with the center of the control actuator. One subtle but influential difference is the sensor location for this example is slightly offset from the exact center of the panel (1mm in both the x and y directions) to correlate with the experimentally observed response. This slight perturbation is necessary due to the inexact location of the sensor and the finite size of the device. A true point measurement in the exact center is thus unattainable in practice. The importance of this is illustrated by the observiblility of the modes with even components, i.e., the (2,1) and (2,3) modes are clearly present in the sensor response to the disturbance input. The ramifications of this will be explained as the loop is closed.

The dynamics of this example follow directly from the structural-acoustic model of Chapter 2. Appending the 9 mode, 18 state structural model with the 24 state radiation filter results in a 42 state structural-acoustic model with disturbance and control inputs, and sensor and performance outputs. To illustrate how this approach fits directly into general optimal control framework of Equation (5.2), the coupled model is developed explicitly starting with the independent vibration and radiation models. The state-space structural model is given as,

$$\begin{pmatrix} \dot{x}(t) \\ \dot{\eta}(t) \\ y(t) \end{pmatrix} = \begin{bmatrix} A & B_d & B_u \\ C_{\dot{\eta}} & 0 & 0 \\ C_y & D_{yd} & D_{yu} \end{bmatrix} \begin{pmatrix} x(t) \\ d(t) \\ u(t) \end{pmatrix} \tag{5.5}$$

$$x = \begin{pmatrix} \eta(t) \\ \dot{\eta}(t) \end{pmatrix}$$

The output equation is assembled so that the modal velocity vector, $\dot{\eta}$, is included in the output. The radiation filter has its own dynamics mapping the modal velocity vector to the radiated power, $\Pi(t)$.

$$\begin{pmatrix} \dot{x}_{rad}(t) \\ z_{rad}(t) \end{pmatrix} = \begin{bmatrix} A_{rad} & B_{rad} \\ C_{rad} & D_{rad} \end{bmatrix} \begin{pmatrix} x_{rad}(t) \\ \dot{\eta}(t) \end{pmatrix} \tag{5.6}$$

$$\Pi(t) = z_{rad}^T(t)\, z_{rad}(t) \tag{5.7}$$

By appending the state-space formulations of Equation (5.5) and Equation (5.6),

$$\begin{pmatrix} \dot{x}(t) \\ \dot{x}_{rad}(t) \\ z_{rad}(t) \\ y(t) \end{pmatrix} = \begin{bmatrix} A & 0 & B_d & B_u \\ B_{rad}C_{\dot{\eta}} & A_{rad} & 0 & 0 \\ D_{rad}C_{\dot{\eta}} & C_{rad} & 0 & 0 \\ C_y & 0 & D_{yd} & D_{yu} \end{bmatrix} \begin{pmatrix} x(t) \\ x_{rad}(t) \\ d(t) \\ u(t) \end{pmatrix}$$

The general definitions of noise, $w(t)$, combines the influence of sensor, $n(t)$, and process noise, $d(t)$, while the general performance, $z(t)$, expresses both the state, $z_x(t)$, and control

cost $z_u(t)$. This condensed notation parallels the canonical format of Equation (5.2).

$$\begin{pmatrix} \dot{x}(t) \\ \dot{x}_{rad}(t) \\ z_{rad}(t) \\ z_u(t) \\ y(t) \end{pmatrix} = \begin{bmatrix} A & 0 & B_d & 0 & B_u \\ B_{rad}C_{\dot{\eta}} & A_{rad} & 0 & 0 & 0 \\ D_{rad}C_{\dot{\eta}} & C_{rad} & 0 & 0 & 0 \\ 0 & 0 & 0 & 0 & \rho \\ C_y & 0 & D_{yd} & \mu & D_{yu} \end{bmatrix} \begin{pmatrix} x(t) \\ x_{rad}(t) \\ d(t) \\ n(t) \\ u(t) \end{pmatrix} \tag{5.8}$$

$$w(t) = \begin{pmatrix} d(t) \\ n(t) \end{pmatrix} \quad z(t) = \begin{pmatrix} z_{rad}(t) \\ z_u(t) \end{pmatrix}$$

The typical assumptions of the preceding development are utilized and the final form of the acoustic cost function reflects the optimal balance between control effort and radiated power.

$$J_2 = \lim_{\tau\to\infty} \frac{1}{\tau} \int_0^\tau z^T(t)z(t)\,\mathrm{d}t = \lim_{\tau\to\infty} \frac{1}{\tau} \int_0^\tau \left[\Pi(t) + \rho u^T(t)u(t)\right]\,\mathrm{d}t \tag{5.9}$$

Once the problem is posed in this framework, all the tools to arrive at an optimal solution are available. For this example only two design parameters are left to specify the compensator. The variance (strength) of the sensor noise is quantified by the parameter μ. It is difficult to connect the value of this parameter to the actual sensor noise, thus it is typically set to a 'low' value assuming reasonable estimation. A value of 0.001 was found to give reasonable results. The control cost specification, ρ, is used to trade off the conflicting design objectives of performance and robustness. As the parameter is lowered the design achieves more performance at the cost of stability robustness. For implementation robustness allows for the unavoidable uncertainty in the model.

To choose a reasonable design, the stability robustness was qualified by the *phase margin* and *gain margin* of the loop gain transfer function. The performance is reflected by the decibel reduction in acoustic power over the bandwidth of concern[11]. Figure 5.15 shows the results of varying the design parameter and the corresponding stability and performance metrics. The design value of $\rho = 0.0011$ is chosen because of the local increase in gain margin at this location shown by the vertical hash. The resulting design yields a 5.67 dB reduction in radiated acoustic power over the open loop case and achieves a gain and phase margin of 3.04 dB and 10.68°respectively.

Figure 5.16 serves to visualize the design. The 42 state compensator is shown in plot (a) along with the open-loop eigenfrequencies. Plot (b) illustrates the gain and phase margin bounds through the loop gain frequency response. Comparing this response to the previously presented classical designs illustrates the intuition of the asymptotic relationships for optimal structural control. At the resonance locations which have gain larger than the

[11]This performance is calculated directly from the frequency response over the bandwidth from 30-1000 Hz to be consistent with the experimental results to follow.

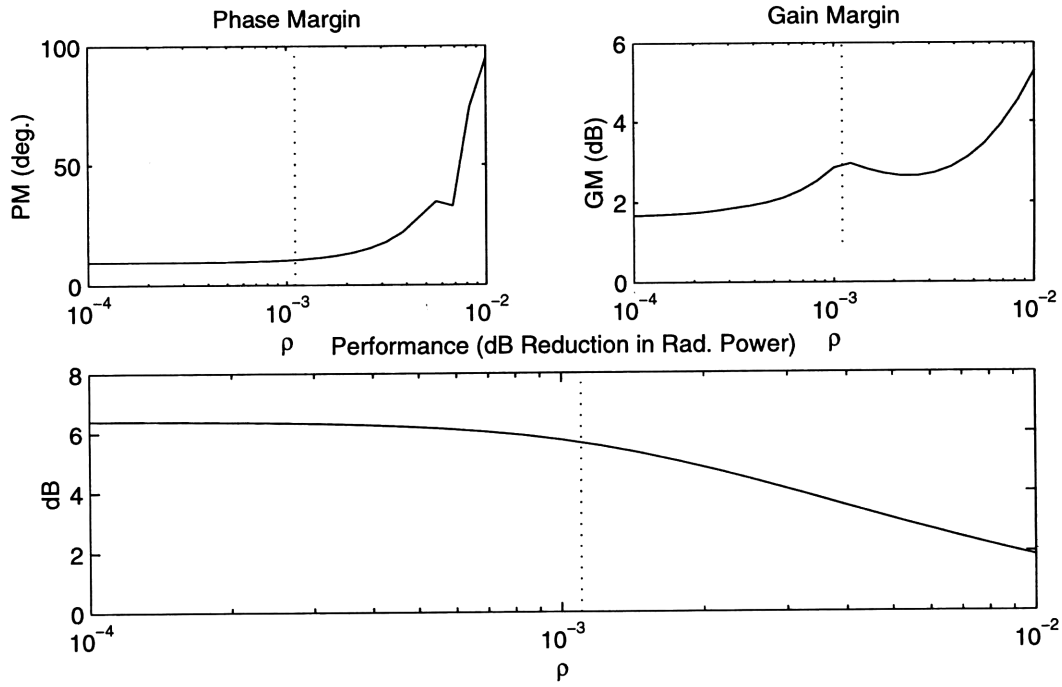

Figure 5.15: Robustness/Performance Trade-off for RF-LQG Designs

critical 0 dB level, the phase is observed to be 0°. This is the same behavior observed in the rate feedback designs, verifying the expected asymptotic low-gain LQG behavior – adding damping to structural modes. These same relationships are also illustrated in the Nichols plot of the loop gain response, plot (c). Again comparison with the classical design results shows that the compensator is actively damping the modes of concern. The small gain and phase margins are highlighted by the proximity of the trace to the critical point.

Finally, Figure 5.17 shows the achieved acoustic performance of the RF-LQG design. It is obvious that the radiation filter has targeted the compensator on the modes which radiate efficiently, particularly the odd modes of vibration. The design effectively damps the (1,1), (1,3), (3,1), and (3,3) modes, but does not have a noticeable effect on the even modes, (1,2) and (2,3). To explain this we return to the open-loop response of Figure 5.14. By moving the sensing location slightly off center, the disturbance effect on these even modes is illustrated by the resonant peaks at frequencies corresponding to the (1,2) and (2,3) modes in the disturbance response. This sensor location more accurately reflects the experimental response of the system. The control actuator location does not allow control of these modes as illustrated in the response. So, these modes are excited by the disturbance, but effectively uncontrollable from the control actuator, thus the compensator can exert little influence on this region of the acoustic response.

This design example parallels the experimental setup to be presented, and the results serve as a guideline and benchmark for the implementation.

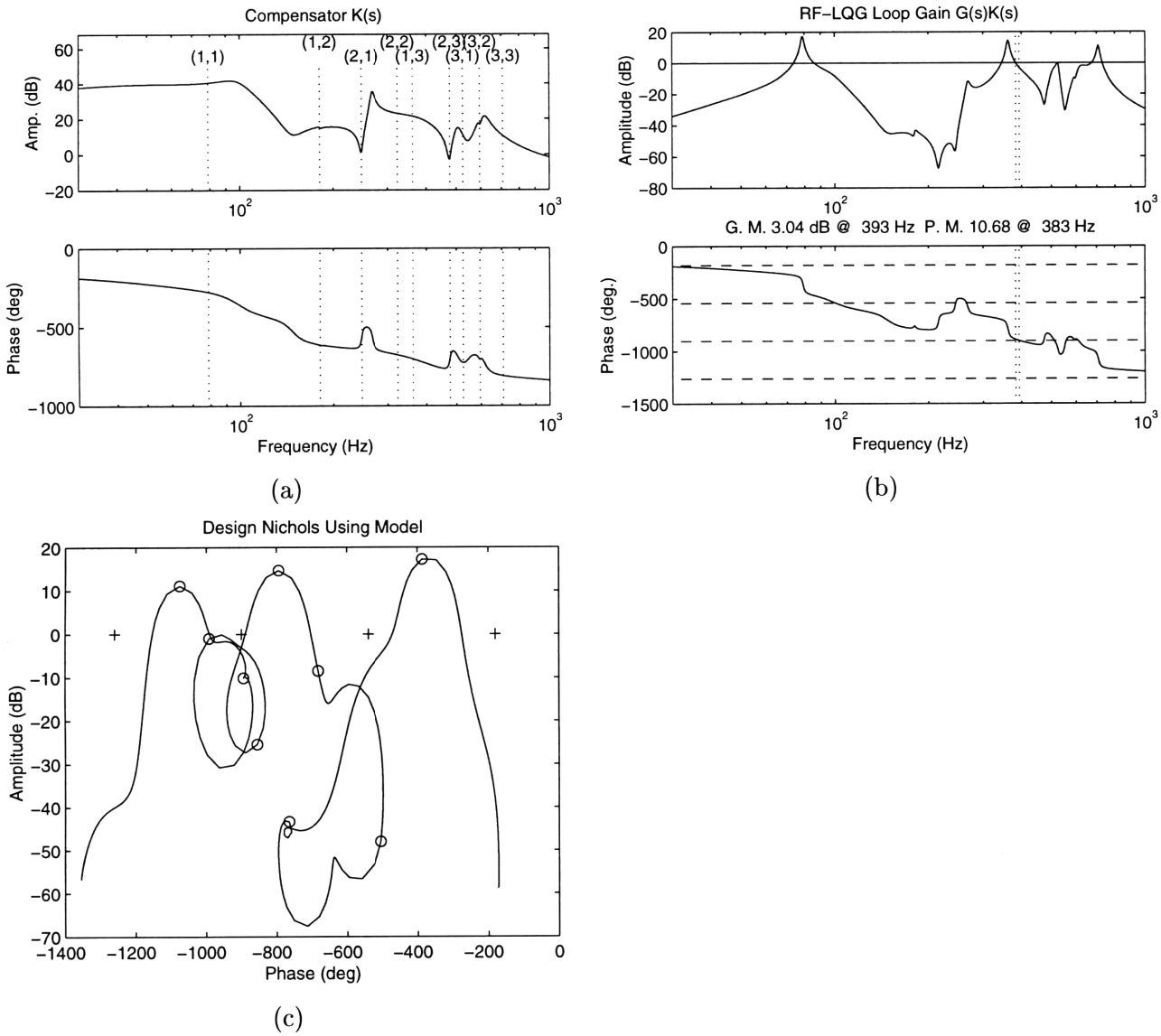

Figure 5.16: RF-LQG Design: a) Compensator, b) Loop Gain, and c) Nichols

5.4 LMS Feedforward Control

In the acoustic control literature, Least Mean Squares (LMS) feedforward control accounts for a large portion of the published results. In comparison to the well defined feedback approaches presented earlier, this adaptive feedforward approach is an *ad hoc* solution, but has been shown to have many implementation advantages over feedback designs. This section will give a brief background on the general LMS algorithm, present an intuitive derivation of the technique, and illustrate the performance and restrictions of this approach with two example problems - a simplified single mode structural example and application to the structural-acoustic model developed previously.

Least Mean Squares adaptive filtering is an estimation technique, but recently it has

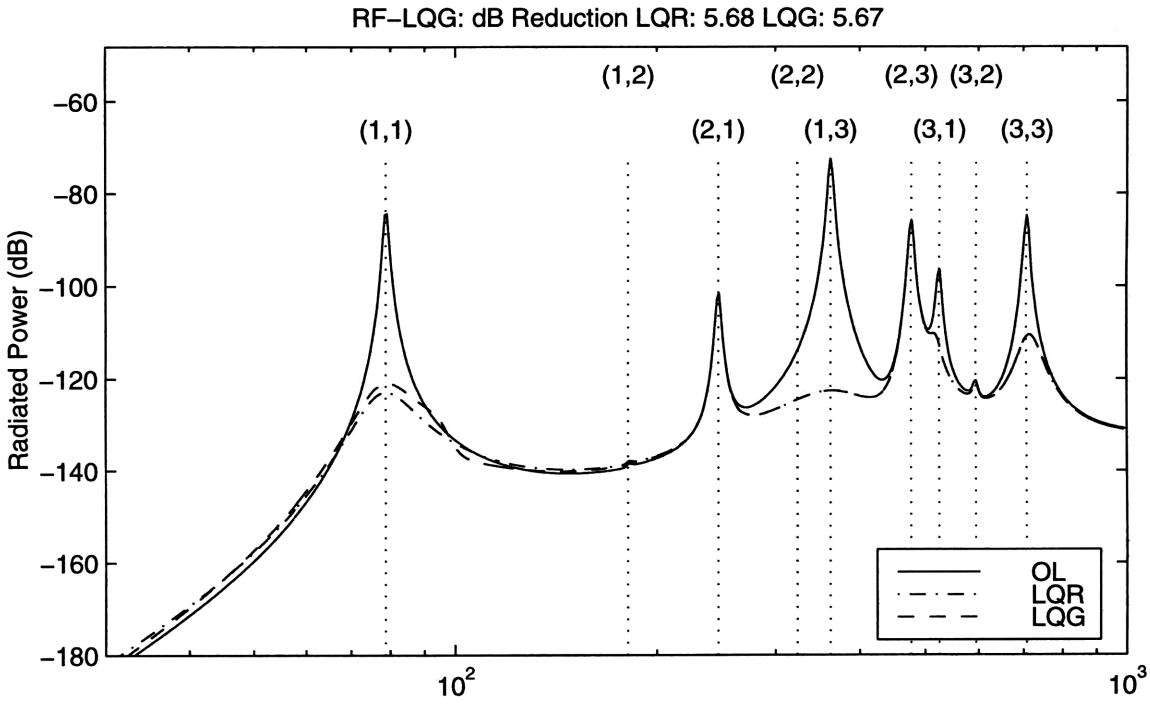

Figure 5.17: RF-LQG Performance

been used to *estimate* the appropriate control signal for noise cancellation. LMS feedforward control was originally presented as a method for noise control from secondary acoustic sources by [Elliot et al., 1987]. This reference develops the particular application of the estimation technique algorithm for acoustic control and analyzes some very specific cases of operation. It is shown that considerable noise cancellation can be achieved for primary and secondary sources separated by less than a half of the wavelength of the acoustic disturbance [Nelson et al., 1986]. As research in acoustic control moved from using secondary sources in the medium to utilizing structural sensing and actuation, the LMS algorithm was carried over to be applied to the problem of active structural-acoustic control. The architecture of the controller is modified slightly for application to structural plants in [Vipperman et al., 1993]. This so-called x-filtered version of the LMS controller (xLMS) implements an infinite impulse response (IIR) filter representation of the control path model to modify the disturbance signal.

5.4.1 Development of the X-Filtered LMS Algorithm

The LMS algorithm is a standard tool of communication theory for signal estimation in the presence of noise and has found a broad range of applications. Recently the simplicity of the technique has been exploited for the acoustic control applications mentioned previously, but many of these examples apply the method in a very *ad hoc* fashion. Although the final

form of the algorithm does not lend itself to the rigorous quantification performed for other estimation techniques (e.g., Recursive Least Squares (RLS) or Kalman filtering), a brief development of the fundamental estimation problem is presented here to add a bit of insight and quantify some of the limitations on the estimation problem. As background, a specific example of the elegant least-square, linear Wiener filter estimator solution is presented first. This optimal solution can be recursively approximated, yielding the standard LMS estimator equation, and finally this formulation is specialized for the structural-acoustic control problem by developing the x-filtered LMS algorithm.

Wiener Filtering

The essence of a signal estimation problem is defining a cost, $J(k)$, which expresses the error in the estimation, and an estimation model. With these two elements, various minimization schemes can be applied to arrive at an optimal estimator minimizing the specified error. Consider the discrete time estimation of an unknown scalar random signal, $x(k)$, based on the observations of a related stochastic process, $y(k)$[12]. In general the Wiener filter is a linear system which operates on the observation sequence to produce an optimal least-square estimate, $\hat{x}(k)$. For this problem the estimator is assumed to take the form of a N^{th}-order finite impulse response (FIR) filter[13].

$$\hat{x}(k) = \sum_{n=0}^{N-1} h(n)y(k-n) = \mathbf{h}(k)^T\mathbf{y}(k) \tag{5.10}$$

$$J(k) = \tfrac{1}{2}E[e^2(k)] = \tfrac{1}{2}E[(x(k) - \hat{x}(k))^2] \tag{5.11}$$

Equation (5.10) expresses this form of the Wiener filter defined by the FIR coefficients, $h(n)$. The convolution sum is equivalent to the inner product of the vector of filter N coefficients with the vector of N past observations[14]. This inner product in the second expression of the equation uses the vector notation where $\mathbf{h}(k)$ is a column vector of length N containing the FIR coefficients at time k and the vector $\mathbf{y}(k)$ contains the last N observations ($y(k-n)$, where $n = 0 \ldots N-1$) at time k. This estimator is, by construction, always causal. The cost function expression of Equation (5.11) is the least-square error or the variance in the

[12]This development is presented in the context of discrete time, scalar, random signals denoted by the discrete sample indices k. However, analogous developments can be achieved in continuous time and for vector random processes without consequence.

[13]As its name implies, a finite impulse response filter considers the outputs as a finite summation of the past and present inputs, in a generalized vector space that is $y =< h, u >$. This is contrasted with infinite impulse response filters where the output is a infinite summation of the inputs, or equivalently a summation of the past and present inputs, and the past outputs. Basically, FIR's represented as transfer functions, only have zeros, while IIR's have both poles and zeros [Oppenheim, 1983]

[14]The vector space development is completely general in that the inner product in discrete time is equivalent to the continuous time convolution.

estimate. Solution for the Wiener filter can be achieved by substitution and setting the gradient of the cost with respect to the filter vector equal to zero.

$$\frac{\partial J(k)}{\partial \mathbf{h}(k)} = E[(x(k) - \hat{x}(k))\mathbf{y}(k)] = E[x(k)\mathbf{y}(k) - (\mathbf{y}(k)\mathbf{y}^T(k))\mathbf{h}(k)] = 0 \tag{5.12}$$

Equation (5.12) expresses the *orthogonality principle* which states that an optimal estimator uncorrelates the observations from the error. Assuming that the signals are jointly wide sense stationary, the processes can be completely described by their second-order statistics - the auto covariance matrix $K_{yy}(k) \equiv E[\mathbf{y}(k)\mathbf{y}^T(k)]$ and the cross covariance vector $K_{xy}(k) \equiv E[x(k)\mathbf{y}(k)]$. Substituting these definitions yields the discrete time *Wiener-Hopf* equation representing the solution for the optimal Wiener filter.

$$K_{yy}(k)\mathbf{h}(k) = K_{xy}(k) \tag{5.13}$$

This expression gives a direct method of determining the optimal filter coefficient values by measuring the statistics of the process at each time step and performing the matrix inversion to solve for the vector $\mathbf{h}(k)$.

LMS Estimation

Many excellent references develop the general concept of the adaptive FIR estimator [Haykin, 1984] and [Kalouptsidis and Theodoridis, 1993]. Here the standard equations are derived as a recursive approximation of the optimal solution. To apply the optimal Wiener filtering technique where large order FIR filters are necessary to estimate the dynamics of the system, a computationally intensive estimation of the correlation terms and matrix inversion must be performed *at each time step.* This may be avoided by recursively solving the equations with each new observation. The LMS algorithm accomplishes this by two simplifications of the Wiener filter. The same error function is defined based on the FIR response, but, instead of solving for the exact coefficient vector to minimize the cost, the FIR coefficients are approximated using gradient descent.

$$\mathbf{h}(k) = \mathbf{h}(k-1) - \mu \left[\frac{\partial J(k)}{\partial \mathbf{h}(k)}\right]$$

Here the update parameter μ must be tuned to speed the convergence of the problem while maintaining stability. The second approximation is made in the evaluation of the gradient. The exact expression for the gradient used in the Wiener filter requires knowledge of the complete second-order characterization, i.e., the autocorrelation and cross correlations for the last N data samples. For this recursive technique, the gradient is approximated by

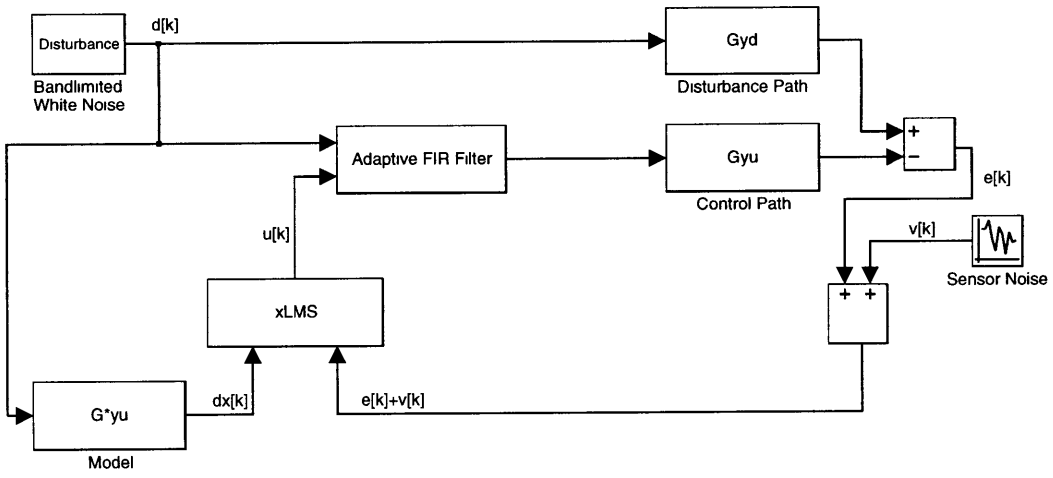

Figure 5.18: Schematic x-filtered LMS algorithm

assuming the expectation is equivalent to the instantaneous value, or that the error signal is deterministic.

$$\left[\frac{\partial J(k)}{\partial \mathbf{h}(k)}\right] = E[(x(k) - \hat{x}(k))\mathbf{y}(k)] \approx [e(k)\mathbf{y}(k)]$$

Using this approximation an simple recursive, or adaptive, updating of the filter values can be implemented using the product of the vector of past observations and the current scalar error signal as the gradient measurement with respect to the FIR weights. Substitution into the gradient decent expression immediately yields the recursive LMS equation.

$$\mathbf{h}(k) = \mathbf{h}(k-1) - \mu[e(k)\mathbf{y}(k)] \tag{5.14}$$

X-Filtered LMS

The LMS algorithm is proven to yield practical performance in a wide variety of estimation problems. To utilize the technique for structural acoustic control, the algorithm must be adjusted slightly for the particular problem yield in the x-filtered LMS (xLMS) feedforward compensator. The concept is to *estimate* a control signal, $u(k)$, that minimizes the error output of the plant. By feeding forward the inverse of this estimate, the estimator is realized as a controller that is capable of cancelling the known disturbance. Figure 5.18 highlights the components of the x-filtered LMS control architecture. The error cost is defined as the square difference between the control and disturbance paths in the plant or the variance of the error sensor. Because structural plants cannot be accurately modeled with FIR filters, it is notationally convenient to express the control signal path in the discrete frequency domain (z-domain), where the discrete convolution sum is transformed to a multiplication.

$$J(k) = E[e^2(k)] = E[(y(k) - \hat{y}(k))^2]$$
$$\hat{Y}(z) = G_{yu}(z)u(z) = G_{yu}(H(z)d(z))$$

The estimation is again expressed as the output of a FIR linear system, $U(z) = H(z)d(z)$, in response to the observed disturbance signal. Defining a new *filtered-x* signal, $d_x(z)$, allows the expression of the gradient of the cost with respect to the filter coefficients to take a form very similar to the previous LMS development.

$$d_x(z) \equiv Gyu(z)d(z)$$

$$\hat{Y}(z) = H(z)d_x(z) \Rightarrow \hat{y}(k) = \mathbf{h}^T(k)\mathbf{d}_x(k) \tag{5.15}$$

$$\frac{\partial J(k)}{\partial \mathbf{h}(k)} = E[e(k)\mathbf{d}_x(k)] \approx [e(k)\mathbf{d}_x(k)] \tag{5.16}$$

Using the same gradient descent algorithm developed for the regular LMS estimation, the adaptation of the FIR filter can be defined based on this filtered-x signal yielding the recursive x-filtered LMS equations.

$$\mathbf{h}(k) = \mathbf{h}(k-1) - \mu[e(k)\mathbf{d}_x(k)] \tag{5.17}$$

For implementation the compensator must have access to this new signal which is not physically measurable. To accomplish this, a model of the control signal path, $\hat{G}yu$, is used to approximate the filtered-x signal necessary for the recursive gradient representation. In Figure ?? this is illustrated by the 'model' block used to pre-filter the disturbance signal input to the LMS adaption algorithm. Intuitively this is equivalent to giving the adaptive filter accurate information on the poles of the system since an FIR filter is not capable of reproducing this resonant behavior. With this information the adaption process attempts to adjust the zeros of the transfer function to approximate an equivalent structural plant that will cancel the error measurement.

In summary the x-filtered LMS algorithm is a specific application of the LMS estimation technique. Implement of the method requires knowledge of the disturbance, an accurate input/output model of the plant, and measurement of the error to be minimized. As a structural-acoustic controller, LMS error cancellation has the following advantages over traditional, feedback methods:

- Tends to reject noisy data due to smoothing action of the small step-size parameter μ.
- Tracks non-stationary, slowly time-varying systems.
- The quadratic error function has a global minimum.
- Implementation is computationally simple with digital signal processing.
- The estimation is more robust to modeling errors than model based feedback compensators (i.e. $\mathcal{H}_2$ and $\mathcal{H}_\infty$).

In the referenced studies these advantages have been used for a variety of experiments. Typically the disturbance signal is considered as a narrowband disturbance or even a single frequency tone. The justification for this simplified analysis is that for many systems a well defined noise source is present, affecting only a narrow frequency band.

Causality is a major concern in most work with xLMS compensators. The feedforward filter is considered to be non-causal if the delay in the control-error path exceeds that of the disturbance-error signal path. This is typically the case in structural control where the disturbance to error delay is effectively zero and the control path has delays introduced by the filtering for control (analog anti-alias filtering and digital computation). One method of accounting for this problem is to introduce a fictitious time delay into the disturbance path. This is a most unrealistic adjustment since it is not physically attainable for in applications. This and other restrictions on the feedforward architecture can be summarized:

- Knowledge of the disturbance signal is required *a priori.*
- Broadband stable implementation is difficult to achieve in practice.
- The convergence is often slow in order to achieve stability.
- Including time-delays in the analysis yield non-causal systems.
- Minimizing of a particular error may not achieve the actual performance specifications, e.g., local sound reduction is achieved near error sensor, where global attenuation is desired.
- Few analytical performance or robustness guarantees offer only an heuristic solution in all but the most simplified cases.

One typical scenario for implementation of feedforward acoustic control includes acoustic actuation and error measurement. While acoustic sensing and actuation are not available for many applications, two advantages are evident for xLMS implementation. First, by directly measuring the performance metric, successful convergence of the algorithm produces a compensator directly targeting the figure of merit. Second, the inherent time delay associated with acoustic propagation ensures the causality of the estimator, requiring less complexity to achieve performance [Burdisso et al., 1993]. This work seeks to analyze the application to structural based acoustic control, where structural sensing and actuation are utilized for acoustic control. This problem is considerable more difficult to implement using a feedforward technique.

To quantify the behavior of the xLMS algorithm for structural (and hence acoustic) control, two simplified examples are included. The first is a simple representation of a structure as a single mode resonant response. This general model can be considered a single residue of a multiple degree of system model, thus lending insight into the application of

xLMS to structural control problems and allowing comparison with the approaches already demonstrated. The second example, in keeping with the previous analyses, applies the algorithm to the nine mode Ritz model of the composite panel in order to extrapolate the broadband, multiple mode performance. In each case the two design parameters, the convergence parameter, μ, and the FIR order, N, are used to optimize the response and generalize the design method for experimental implementation.

The implementation of the xLMS algorithm takes a slightly more complex form. Better performance is gained by implementing a 'normalized' version the LMS algorithm which uses the filtered x signal to normalize the convergence parameter μ. This slight modification of the algorithm exhibits better convergence performance [Kalouptsidis and Theodoridis, 1993].

5.4.2 Example 1: Single Degree of Freedom System

The xLMS feedforward algorithm is typically applied to systems that have a time delay in the disturbance-error path which allows the compensator to effectively *anticipate* the necessary control signal to cancel the disturbance. If the physical system does not include such a delay, often an artificial delay is introduced in the experiment to preserve the causality. For structural control, where the disturbance can not be so well quantified and this delay is not physical, the controller can not rely on such an assumption. Also, typical implementations consider tonal, i.e. single or multiple discrete frequency, disturbances. This greatly simplifies the estimation complexity because can simply be amplified and phase shifted in order to cancel the error.

To address these shortcomings a simple single degree of freedom simulation is presented. The single mode is modeled by a second order resonant response.

$$\frac{y(s)}{d(s)} = \frac{\omega_1^2}{s^2 + 2\zeta\omega_1 + \omega_1^2}$$

Each of the signal paths in Figure 5.19 is considered to have identical response, that is the disturbance and the control enter in the same manner. The simulation is performed on SIMULINK software in order to quantify the performance of the controller. The resonant mode is placed at 600 rad/s, approximately the first mode of the experimental panel setup, while the disturbance is considered to be unit intensity white noise[15]. The simulation was run for each case with time steps of $5\text{x}10^{-4}$ seconds. The simulation contains three main perturbations from ideal conditions that will be present when implementing the controller: variable time delay in the control path, sensor noise at the error, mis-modeled dynamics. Figure 5.20 a) shows the time response for the ideal system with and without these considerations. The disturbance plot shows illustrates broadband nature of the input to the system. The open-loop (OL) the system response is dominated by the single resonant modal

[15]The digital 'white noise' is produced by a random number generator and contains all frequencies up to half the sampling frequency

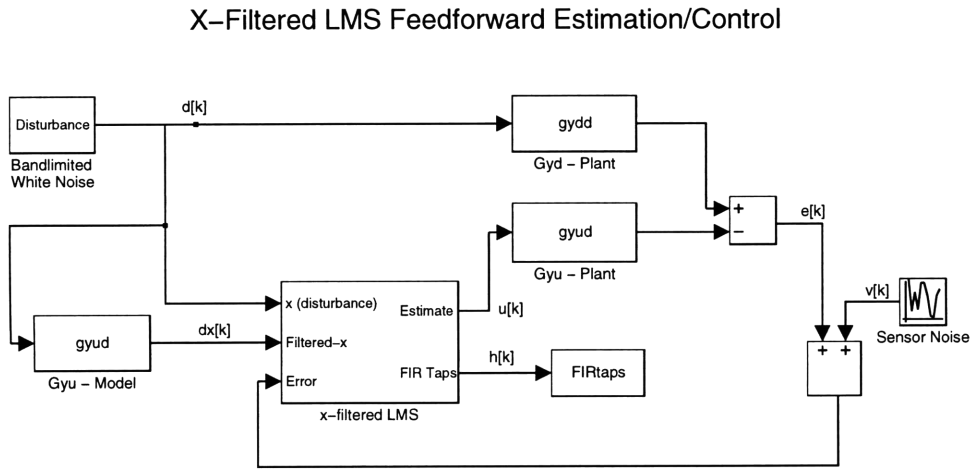

Figure 5.19: xLMS for Structural Control Simulations

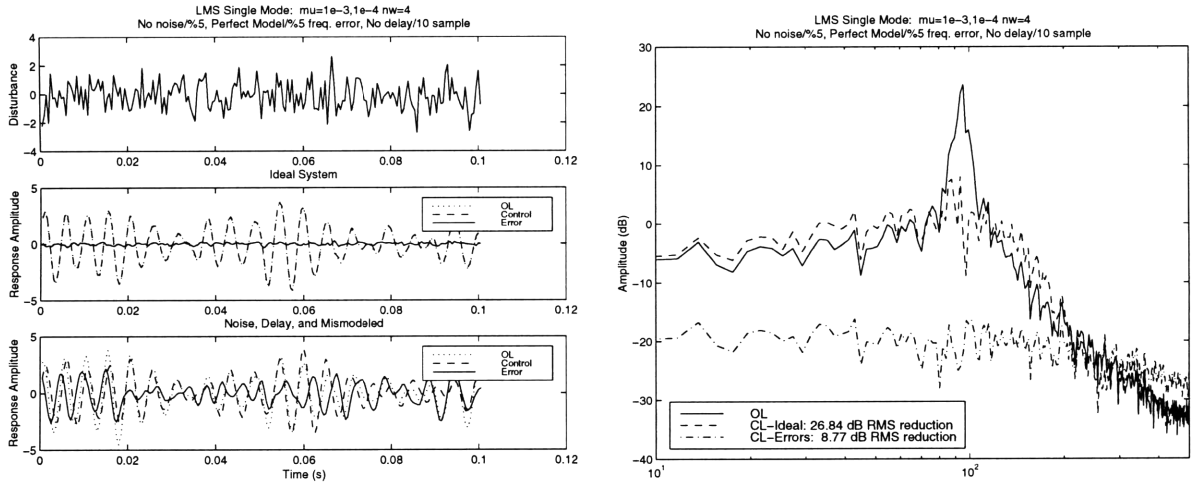

(a) (b)

Figure 5.20: xLMS control for 1-DOF system a) Time response b)Frequency Response

frequency. The slight 'beating' of the response is characteristic of a signal containing closely spaced frequency components. The ideal system time response shows the cancellation of the error signal as the control path output matches the disturbance path output cancelling the resulting error signal. A fourth order FIR was found to be sufficient to estimate the necessary control, with no performance increase for increased order, and the parameter μ was tuned by increasing until the system becomes unstable at a threshold of approximately $5\text{x}10^{-3}$.

In the second case a time delay of 10 samples was added to the control path[16], an uncorrelated sensor noise with variance corresponding to %5 of the sensor variance was added to corrupt the sensor signal, and the resonant frequency was mis-modeled in the control path model by %5 (630 vs. 600 rad/s). The resulting controller performance degradation is quantified in the lower time response of Figure 5.20 a). Direct comparison with the ideal time response shows the result as the control path output no longer matches that of the disturbance path resulting in a substantially larger error signal. Although the fourth order filter was still sufficient, the convergence parameter had to be reduced, to $\mu = 2\text{x}10^{-3}$, in order to maintain the stability of the system. Effectively the presence of these perturbations prevents the estimator from operating as fast as possible in the ideal case, thus achieving less performance. It should also be noted that as reported in [Burdisso et al., 1993] increasing the order of the adaptive FIR, from 4 to 16, did have a small effect on the performance.

The frequency domain comparison is made in Figure 5.20 b) by computing the transfer function from the simulation time-domain data using FFT algorithms in MATLAB. The time data decomposed into and ensemble of 512 point windows that are convolved with a Hanning window to smooth the frequency response. The maximum amount of averages is then taken to further smooth the frequency response estimate. From this analysis the RMS error reduction can be calculated over the shown frequency range. While the 'realistic' case still mitigates the resultant error by 8.8 dB, it does not perform near as well as the 'ideal' experiment which produces 26.8 dB reductions in error.

This result illustrates the viability of xLMS compensation for structural plants. In the presence of modeling errors, time delays, and sensor noise, the approach should yield a stable solution with some, albeit reduced, degree of performance.

5.4.3 Example 2: Ritz Model Simulation

A similar simulation was implemented to demonstrate broadband performance properties of the xLMS on the representative Rayleigh-Ritz panel model. The setup of this example is meant to parallel the experimental results presented shortly. The two signal paths, shown

[16]For $T_s = 5\text{x}10^{-3}$ s sample time and modal period $T = 0.0105$ s this represents approximately 90°of phase loss

in Figure 5.21, define the architecture of the problem. The filtered white noise disturbance enters through the second AFC placed at $(L_x/6, L_y/2)$ (AFC #2) and is labeled G_{yd}, while the control is applied through actuation of the centered AFC pair (AFC #1) and is labeled G_{yu}. The structural error sensor is the same measurement used for the previous feedback examples, the center accelerometer collocated with the control actuator.

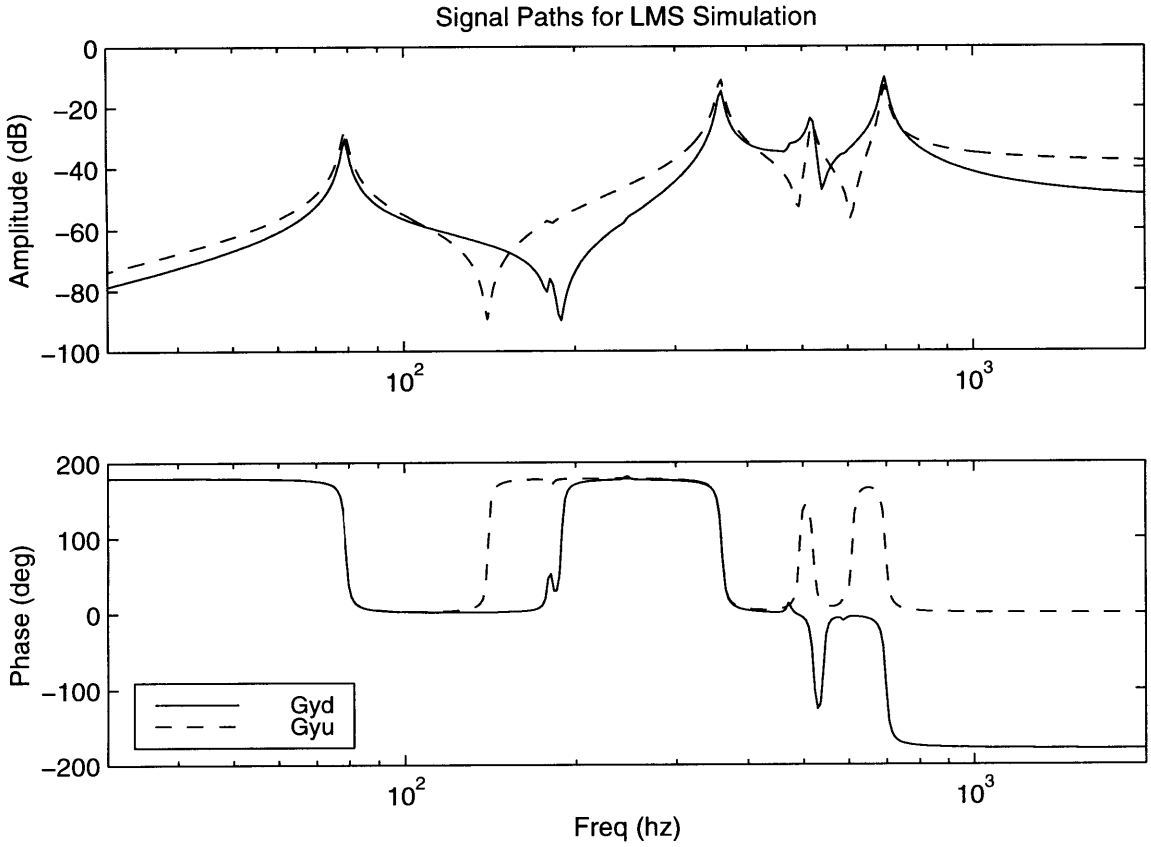

Figure 5.21: Ritz Model Response for xLMS Simulation

A critical design parameter for broadband structural application of this technique is the order of the adaptive FIR filter. Intuitively the system should converge to a representation of the structural plant. Modally dense structures typically have quite complicated frequency response functions for even narrow bandwidths, so it is expected that the xLMS algorithm must be formulated with a sufficient number of filter coefficients, or degrees of freedom, to allow representation of the desired response. To investigate this dimension in the design parameter space, the order of the adaptive filter, N was allowed to vary between values of 8 and 80, and the open-loop and closed-loop time response of the system was measured after the FIR coefficients were observed to converge. The transmission time of the disturbance and control signals was taken to be equivalent and the discrete time simulation was performed at a sampling rate of $1\text{x}10^{-4}$ sec. in order to capture the full dynamic range

of the system. The bandlimited stochastic disturbance was modeled by a unity variance white noise function passed through a low-pass filter with a cutoff frequency of 1,000 Hz. The resulting time data was then used to estimate the steady-state frequency response of

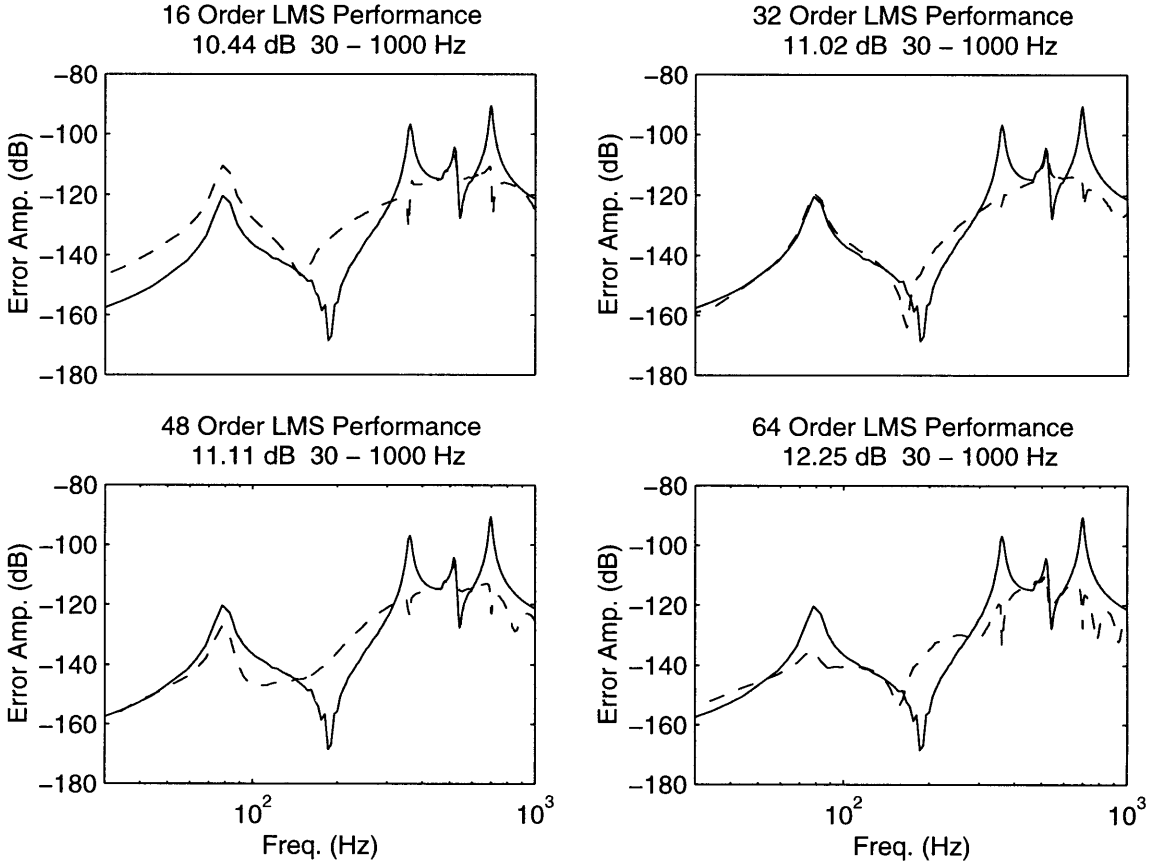

Figure 5.22: Examples of LMS Performance with Increasing Filter Order

the system with and without compensation. The performance is evaluated by integrating the frequency response data over the finite bandwidth from 30 to 1,000 Hz. Figure 5.22 illustrates the necessity of high order filters for broadband compensation. As the order increases the compensator is able to approximate the complex dynamics of the structural system. The positive slope of the dereverberated response causes the error signal to be dominated by the high frequency content. The order of the compensator limits the dynamics which can be represented in the feedforward path, so to achieve performance when limited by insufficient order, the compensator cancels the faster dynamics. As the order increases, more of the dynamics are represented allowing for reduction of the slower dynamics as well. Figure 5.23 expands on these four examples with a broader range of filter sizes. For this particular example, 20 filter coefficients are necessary to cancel the majority of the disturbance response. The performance stays almost constant until the order becomes high enough to represent the first mode at which point the performance is observed to climb

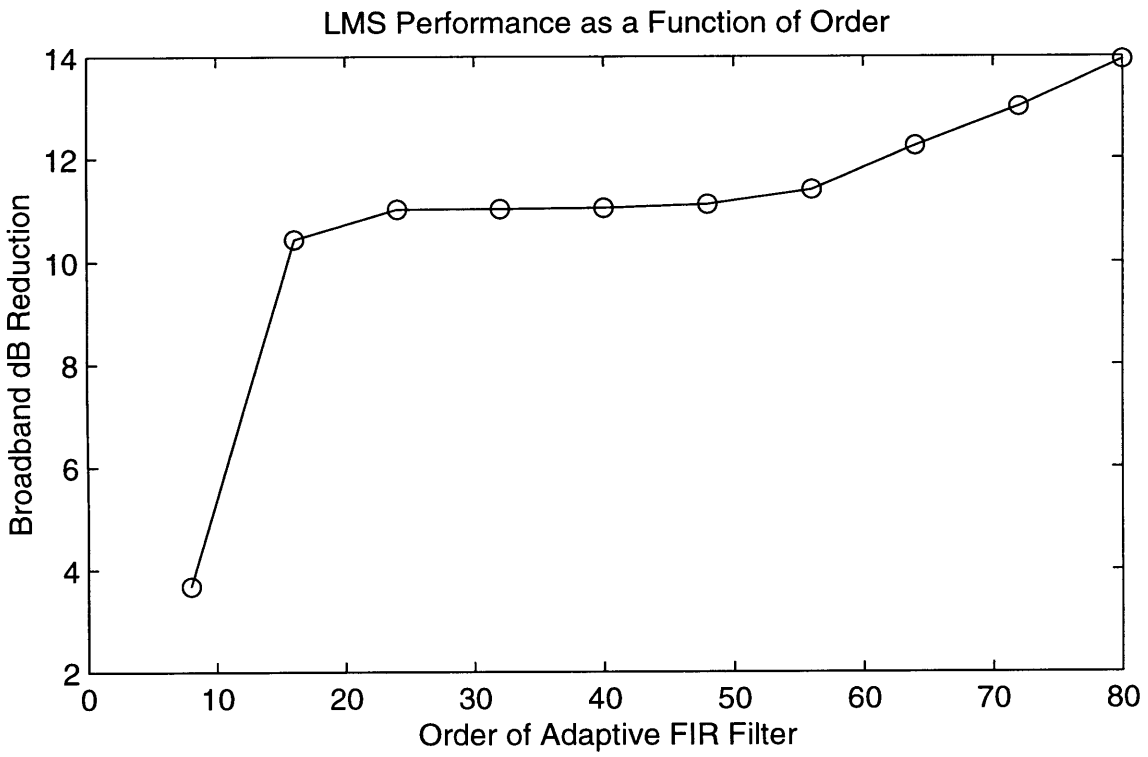

Figure 5.23: LMS Performance with Increasing Filter Order

again with filter size. The important conclusion is that a large order adaptive filter is necessary for broadband structural cancellation and that increasing the order always improves performance as illustrated by the monotonically increasing performance curve.

Another performance issue of interest is the robustness to sensor noise. To characterize the behavior of the xLMS compensator in the presence of uncorrelated additive sensor noise a random signal was injected into the error measurement prior to the adaptation algorithm. The strength of the noise is quantified by the signal to noise ratio (SNR) of the sensor. From the variance of the open-loop response, $4.98\text{x}10^{-12}\ g^2$, the variance of the sensor noise is specified to achieve the desired SNR. Figure 5.24 illustrates the robustness of the algorithm to sensor noise. Three examples are shown with signal to noise ratios of 100, 1, and 0.1 and little degradation in broadband performance is observed. The fourth plot illustrates the sensor noise present in the time data by comparing the uncorrupted error signal and the error measurement with added noise. This corrupted signal is used by the LMS engine for adaptation. This analysis highlights the robustness of the xLMS algorithm to sensor noise, an important consideration when implementing compensators.

The simulations presented serve to highlight some of the characteristics of the xLMS estimator used to cancel stochastic structural disturbances using purely structural actuation. Although the results are based on the structural performance of the technique, the acoustic

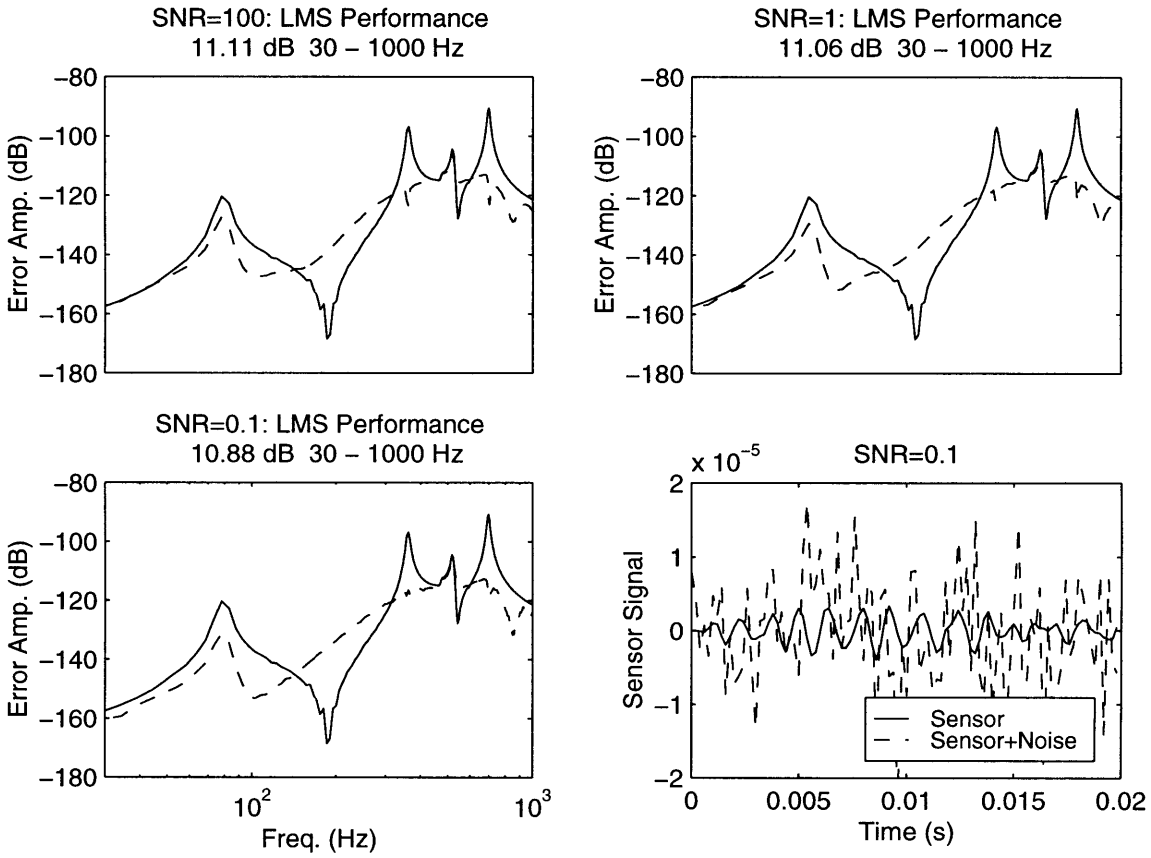

Figure 5.24: xLMS Performance in the Presence of Sensor Noise

performance will be shown through experimental implementation to be directly related.

5.5 Summary

The analytic and simulation results of the preceding discussion are based solely on the structural-acoustic model derived as a part of this work. The examples explore the design and performance of the candidate methods for structural-acoustic control. The analytic model is doomed to be abandoned due to the tight accuracy requirements for performance and robustness of the control design methods, but the utility of the model is in the insight it lends to both the open and closed-loop dynamics.

Three methods of structural-acoustic control have been examined to show the relative merits of each. The simplicity of the classical techniques is evident as are the limitations on performance. Optimal control techniques have been shown to directly incorporate the figure of merit, radiated acoustic power, into the compensator design using the structural-acoustic model. This enables the compensator to reduce the acoustic field directly with accurate knowledge of the structural coupling and the advantages of this approach over

controlling the vibrations are highlighted by the modal restructuring phenomenon. Finally, the application of the adaptive feedforward algorithm to structural control is shown to perform despite the causality and sensor noise issues. The final comparisons between these approaches is withheld until the results of the experimental implementations are presented.

Chapter 6

Closed-Loop Experimental Results

The goal of this chapter is to present a comprehensive comparison between the application of various control techniques for the mitigation of farfield radiated acoustic energy. The chapter records the design process for each of the compensators in order to lend some practical insight into the challenges of implementation. Emphasis is placed on the fundamental limitations of each design to generalize the conclusions. The results from this representative panel structure are connected with the performance capabilities for the target applications.

To achieve a fair comparison between these different approaches a standard experiment, outlined in Chapter 4, is performed to quantify the performance under very specific conditions. The basic scenario considers the broadband disturbance input from the active fiber composite (AFC) located at $(L_x/6, L_y/2)$ in relation to the panel dimensions–AFC #2 from Section 3.5. This disturbance is shown to excite multiple vibration modes in the structure. Control is achieved through the centrally located AFC symmetric pair– AFC #1 from Section 3.5, and the 'collocated' accelerometer is used as the structural sensor. Using the approximation technique outlined in Chapter 4, the performance in terms of reduced farfield radiated power is evaluated for each design along with the vibration performance measured by the sensor. A very important consideration for control design is the bandwidth of interest. Examination of the applications presented in the introduction indicates that active acoustic control of radiation is desired at frequencies below approximately 1 kHz. Passive techniques are typically better suited to reduced the acoustic response above this frequency.

The analytic investigation of these techniques is included in Chapter 5; therefore, the results detailed in the following will strive to compliment this analysis through examples.

6.1 Classical Control

Two classical control techniques are presented first. The great advantage of local, or low authority, techniques is the ease of design and implementation. The only information neces-

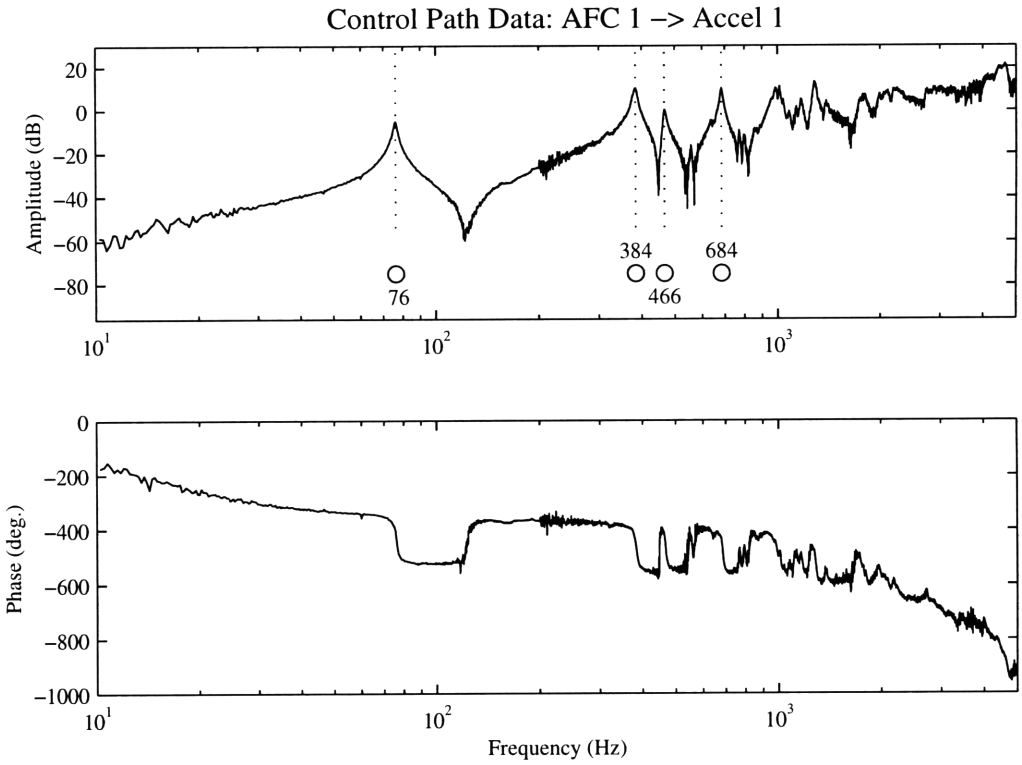

Figure 6.1: Open-Loop Data for Classical Control Design

sary for compensator design is contained in the open-loop data of Figure 6.1. These designs are illustrated to be model-free and low order.

6.1.1 Rate Feedback (RF)

From the analytic discussion on rate feedback for dual, collocated, complementary extreme sensor/actuator pairs, the fundamental idea of a transfer function being positive real is shown to be supremely important to the conclusions of hyperstability of rate feedback control. Two observations should be made from Figure 6.1. First, the sensor/actuator pair behaves in a 'collocated' way throughout the 1 kHz bandwidth of interest despite the fact that a point sensor and a distributed actuator can never be truly collocated. Up through 2 kHz the phase of the transfer function is bounded by 360/440°or equivalently 0/-180°[1], above which the expected *missing zero* causes the phase to drop significantly. The second observation is the slope of the sensor/actuator relation. From the discussion in Chapter 3, the acceleration amplitude is expected to rise linearly with the frequency, for a logarithmic

[1]Recall that this is an acceleration measurement, hence integrating yields the velocity signal which should be bounded by -90/-270°. This is 180°from the expected ±90°bound for *power pairs*, but this discrepancy is simply due to the orientation of the accelerometer in relation to the positive voltage convention on the AFC input.

slope of 20 dB per decade.

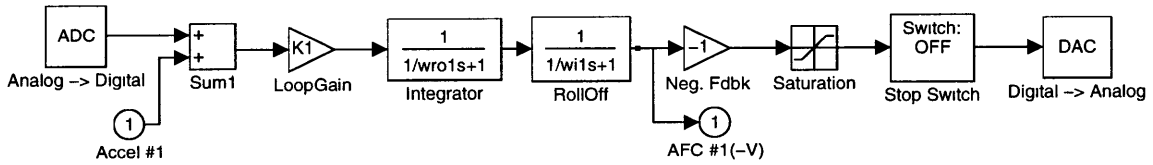

Figure 6.2: SIMULINK Implementation of Rate Feedback Design

Figure 6.2 illustrates the method of implementation using SIMULINK modeling and dSPACE hardware and software to realize the prototype designs. The saturation and stop switch blocks are included to safeguard the actuator voltage which can increase without bound for unstable designs.

Ideally rate feedback for collocated sensor/actuator pairs could be implemented directly, making use of the hyperstability theoretically predicted. Figure 6.3 shows the folly of such a design. To examine the compensator stability the *loop transfer function* is calculated by simply multiplying the complex frequency response with the open-loop data. Both compensators integrate the acceleration with a pole at 10 Hz which integrates the acceleration signal at higher frequencies while maintaining a finite DC gain. In order to realize any appreciable performance the compensator gain must be increased such that the low frequency resonances in the loop gain transfer function exceed unity; however, the zero slope of the dereverberated loop gain causes the bandwidth of the controller to be infinite. This is evident in plots a) and c) where the loop gain exceeds unity at very high frequencies ($\approx 6,000$ Hz). Attempting to implement this design illustrates the limiting nature of the high frequency dynamics. With infinite controller bandwidth, any high frequency dynamics or phase uncertainty destabilize the controller. Experimentally this type of design is not plausible due to it's infinite bandwidth.

The alternative is to incorporate roll-off into the compensator, limiting the bandwidth of the design. The trade-off of adding a low pass filter is that, while it gain stabilizes the high frequency dynamics, it introduces phase lag which tends to destabilize the loop. Typically the designer will attempt to "roll the compensator off" between two modes of the structure using a resonant pole pair because of the localized phase transition and sharp amplitude cutoff. For this example a single pole is introduced at 600 Hz because of the modal density of the structure. Plots b) and d) in Figure 6.3 illustrate the result as the loop gain is gain stabilized above the roll-off frequency.

The performance for this design is shown in Figures 6.4 and ??. The modal density of the plant limits the frequency at which stable roll-off can be realized in the compensator. This high frequency limit is seen to greatly effect both the vibration and acoustic performance of the compensator because of the increased magnitude with frequency, i.e.,

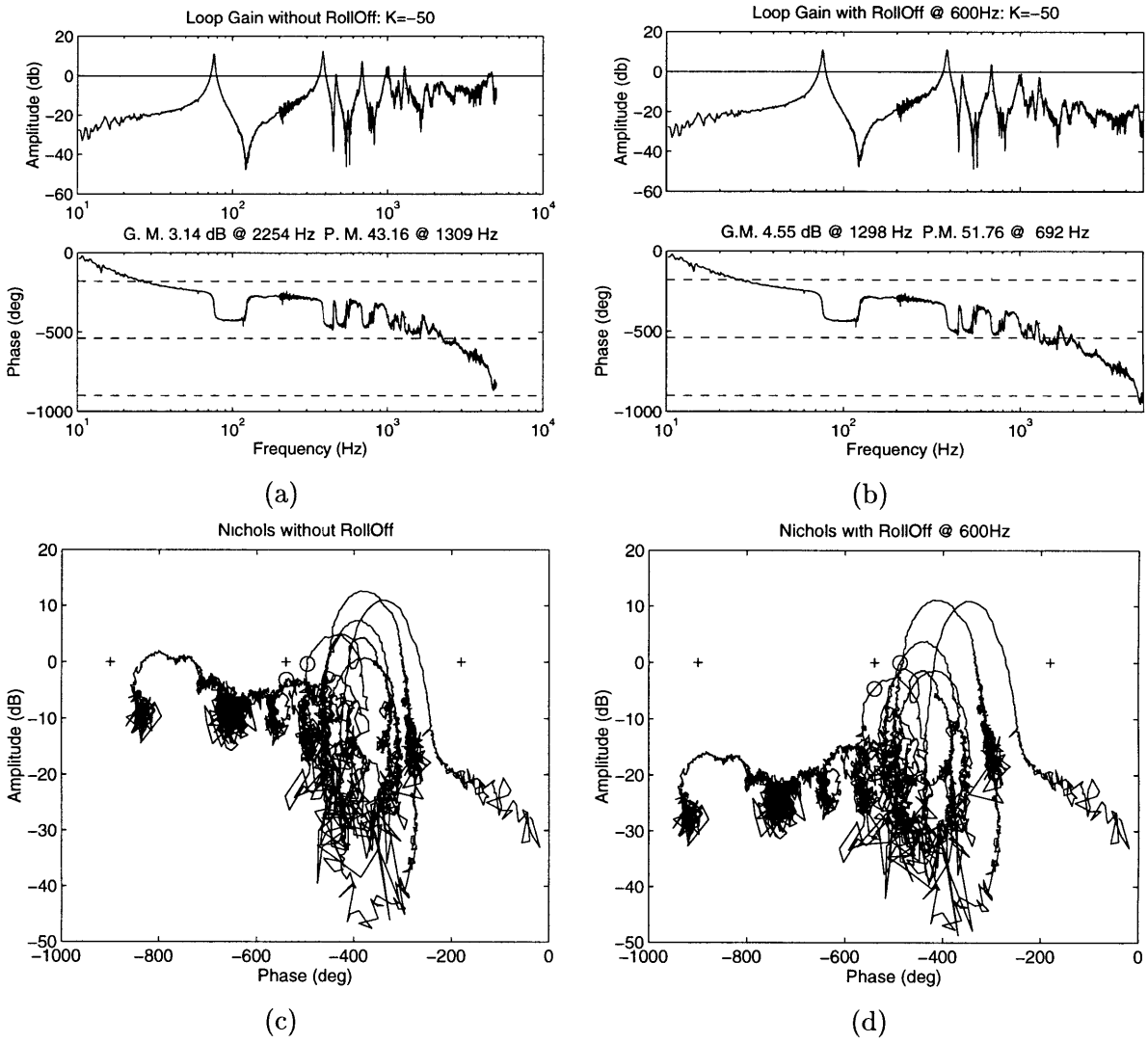

Figure 6.3: Loop Gain Stability Analysis with and without Single Pole Roll-Off

in order to achieve broadband performance the compensator must be capable of controlling the higher frequency modes of the structure.The coherence is included along with the performance data to illustrate the difficulty in making the acoustic measurements in the presence of background noise, but is not shown for future performance plots.

The limitations on this design are derived from the previous discussion on a combination of the dereverberated slope of the sensor/actuator pair and the phase lag of the 'collocated' pair. Alternatively, one might consider different sensors. From the discussion in Chapter 3, the dereverberated slope of various power pairs is given. For conventional piezoelectric actuation, while the velocity sensor (accelerometer) is seen to have zero slope, the alternative of a strain rate sensor (stain gage or piezoelectric) is shown to *roll-up* with a slope of 20 dB per decade. This would require at least a three pole low pass filter to gain stabilize the high frequency loop transfer function and realize a compensator with finite

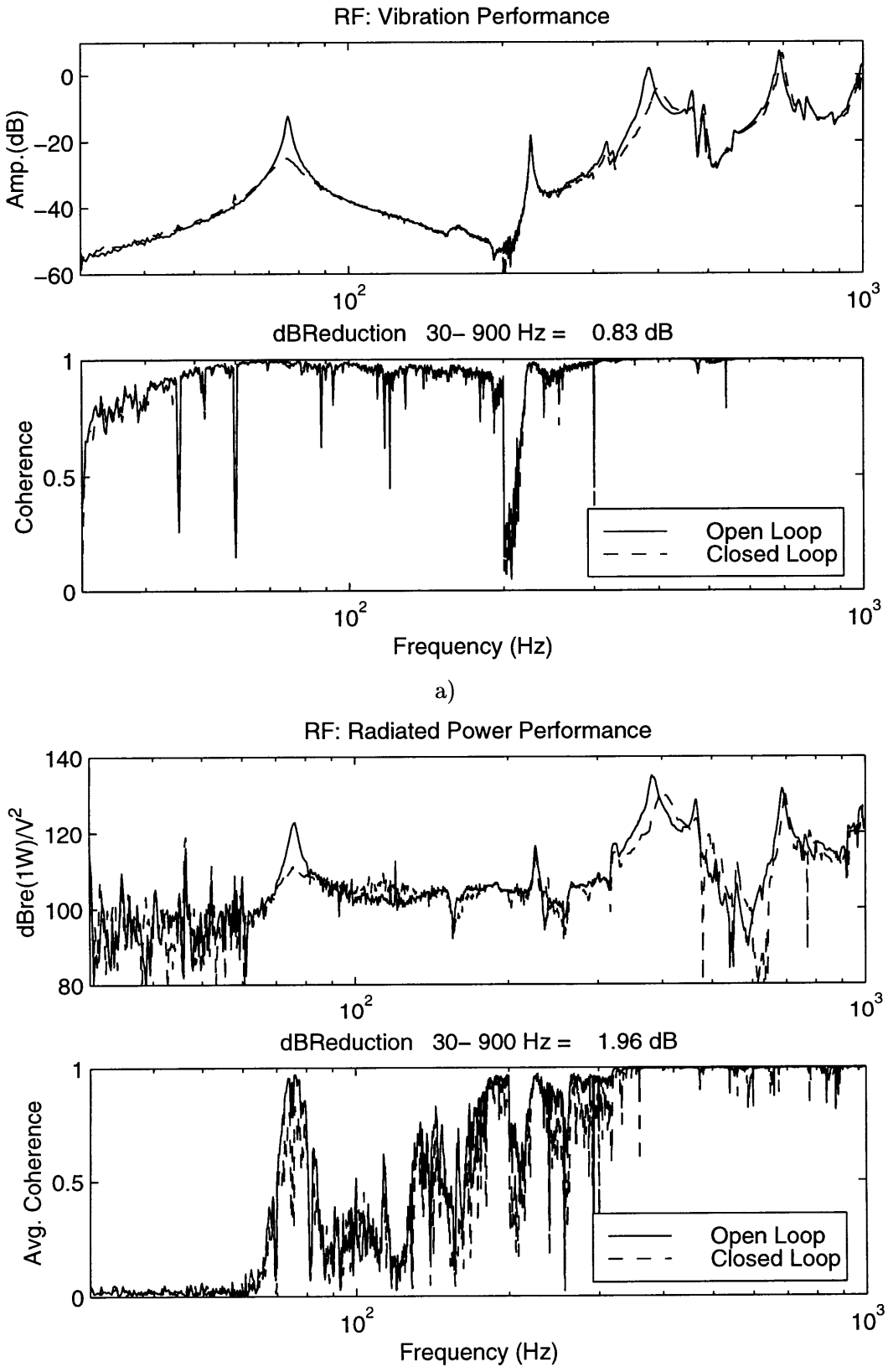

Figure 6.4: Performance of Rate Feedback (RF) Compensator: a) Vibration Performance at Sensor and b) Acoustic Performance

bandwidth. The difficulty is that each added pole compounds the added phase lag which tends to destabilize the loop.

6.1.2 Positive Position Feedback (PPF)

The design of the positive position feedback (PPF) compensator requires only slightly more information about the system than the rate feedback design. For this example a single mode controller is designed based on the modal frequency of the first mode of the structure (76.25 Hz). The compensator consists of a double integrator, realized with two real poles placed at 10 Hz, and a resonance at the the first modal frequency. A damping ratio of 0.3 is used in the compensator design to amplify the compensator gain at the first mode without the 'mode splitting' illustrated in Chapter 5 as the damping ratio is decreased. It should also be mentioned that a high pass filter was implemented in order to reduce the DC gain of the compensator. This filter took the form of a 'lead' compensator with a real zero at 0.01 Hz and a pole at 1 Hz.

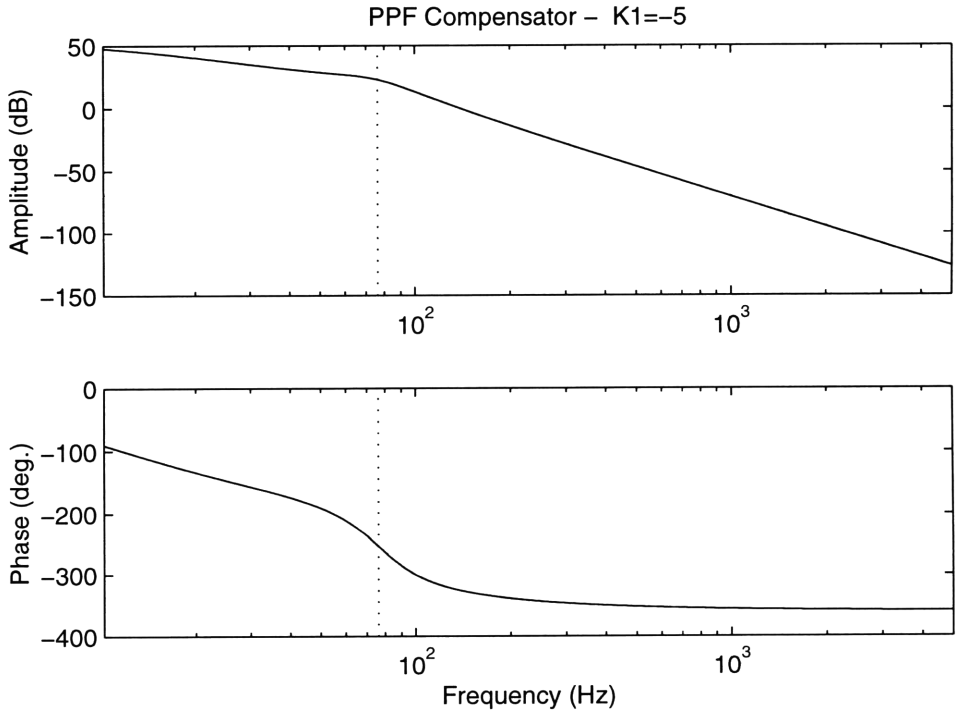

Figure 6.5: PPF Compensator: Resonant Pole at 76 Hz with $\zeta = 0.3$

As discussed in the analytic development of Chapter 5, PPF can be considered as a very localized rate feedback design used to cancel a single mode. This interpretation is bolstered by the loop gain Bode and Nichols plots in Figure 6.6 where the gain at the first resonance is maximized and the phase is approximately 0° at the corresponding frequency. The drastic roll-off of the compensator is obvious in both plots a) and b) of Figure 6.6.

Again the performance limit of this classical design is rooted in the low bandwidth of the compensator. Figure 6.7 illustrates the first mode attenuation from the compensator, but because the performance is calculated over the entire bandwidth, the reduction adds little to the overall performance.

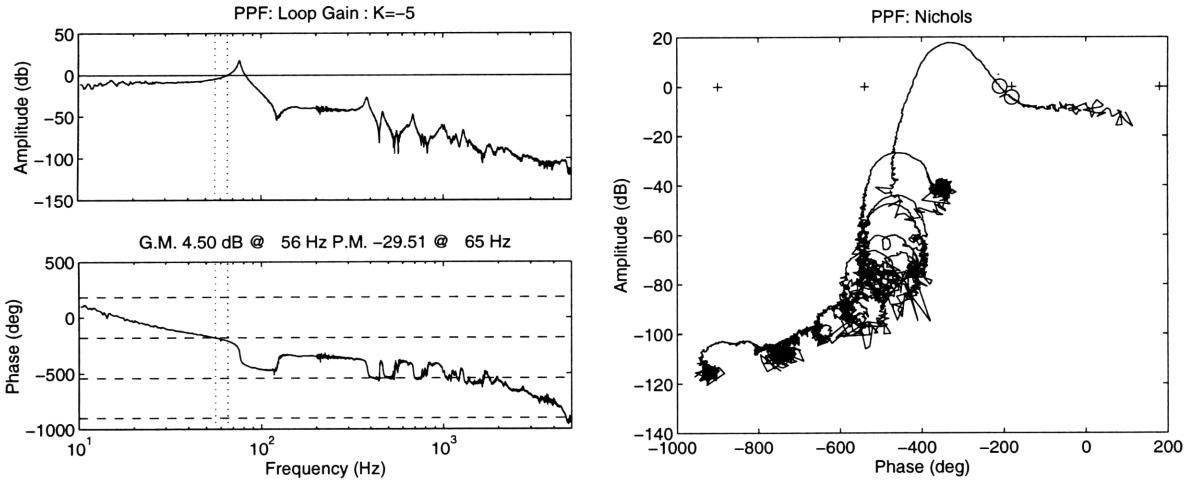

(a) (b)

Figure 6.6: Loop Stability of PPF Design: a) Bode and b) Nichols

6.2 Optimal Control

It is ironic that for all but the most simple systems analytic models are insufficiently accurate for control design. Despite the fact that the Rayleigh-Ritz model correlates well with experimental data presented in Chapter 4, optimal control design can still not be accomplished without more accurate representation of the structural plant. Intuitively one might consider the LQG examples in Chapter 5, where the lightly damped resonant model is directly included in the compensator by the Kalman filter estimator. Errors between the control design model and the actual plant can be disastrous due to the wide range in magnitude for lightly damped plants. Model error can be directly included in the control design, but these robustifying techniques necessarily compromise the available performance of the system.

6.2.1 System Identification

When presented with with an *a priori* model and experimental data, two options are available for arriving at a physical representation appropriate for designing optimal controllers. *Model updating* uses experimental data to adjust the physical parameters in the model, while *system identification* provides a representation of the data that is not necessarily physically relevant.

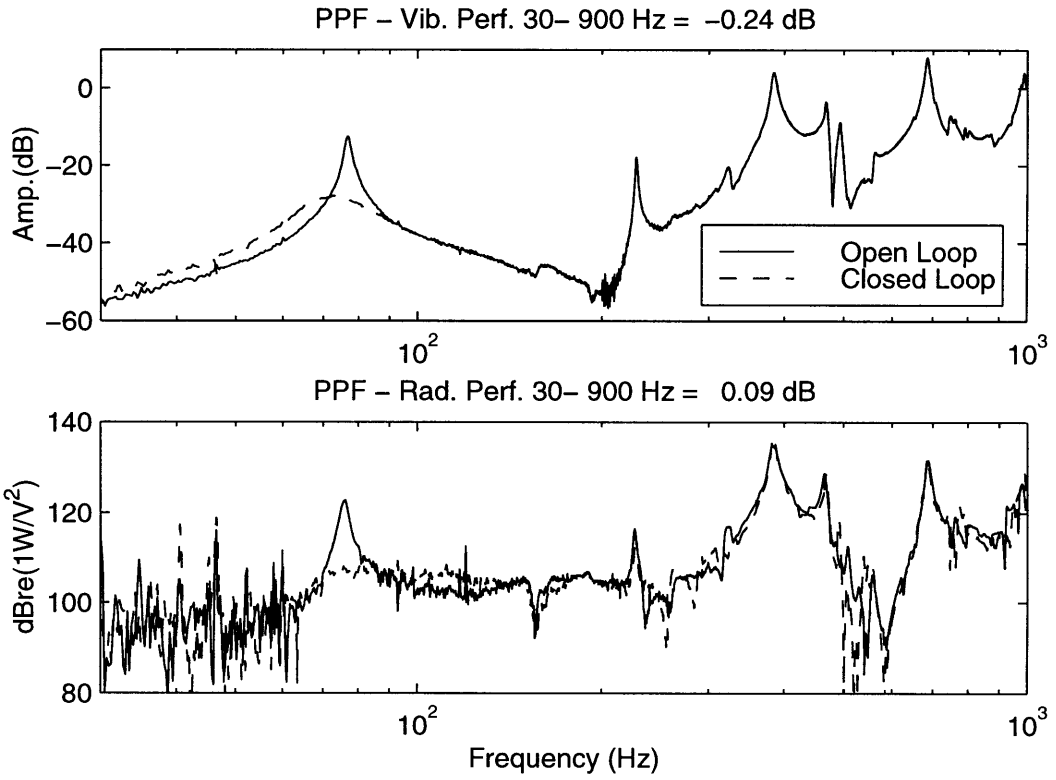

Figure 6.7: Closed Loop Performance for PPF Design

Much work is available on updating Finite Element Models (FEM) using frequency response data. Heuristically the updating process consists of identifying the uncertain parameters in the model synthesis and using an optimization technique to minimize the cost function quantifying the error between the model and the data. As with most optimization problems, the quality of the solution is often dictated by the problem definition - specification of the parameter space (vector of physical constants) and definition of the performance indicator. Minimization of a logarithmic, least-squares, frequency domain error,

$$\hat{\alpha} = \min_{\alpha} [J(\alpha)]$$
$$J(\alpha) = \sum_{i=1}^{n} \left\| \log \left(\frac{G_{data}(j\omega_i)}{G_{model}(j\omega_i, \alpha)} \right) \right\| \tag{6.1}$$

is presented as an appropriate optimization for updating structural models [Balmés, 1993] and implemented by [Glaese, 1994]. Beyond engineering insight typically used to identify the parameters which enable convergence of the model with the experimental data, a vector space approach is presented which uses the orthogonality of parameter perturbations to indicate the capabilities of the updating. The 'engine' of the optimization uses standard minimization algorithms (e.g., gradient descent or quasi-Newtonian schemes) to arrive at the minimum in the multi-dimensional space. Often the gradients necessary are determined

analytically through sensitivity analysis, but for modally dense structures it is advantageous to use reanalysis by iteratively solving the entire model at a given parameterization [Balmés, 1993]. Because the cost function is cast in the frequency domain, the updating process can quickly become computationally challenging for perturbations in a large dimensional parameter space. In order to map the parameter change to it's associated effect on the error, the frequency response must be calculated for each iteration step.

Using the experimental data, a simple updating method was implemented based on cost function in Equation (6.1). The error was minimized over a space of fundamental parameters such as orthotropic stiffness constants (E_{ij}), densities, and modal damping ratios. The error was significantly reduced by the process, but still more accuracy was desired in order to obtain the most performance from the control designs.

The canonical methods of system identification are recounted in [Ljung, 1987] and specific application to structural systems is investigated in [Jacques, 1994]. Parametric identification is typically employed to 'fit' a standard model representation to the experimental data. In contrast to the model updating, system identification does not yield a physically meaningful model. For the most part this eliminates the possibility of extending such a model to parameter changes. This advantage of updating is highlighted in the example of [Glaese, 1994] where a 1-g FEM model of a structural plant is updated using experimental data. Because the process yields a physically reverent model, the representation could be extended to predict the 0-g behavior of the system. With system identification the designer does not have this mapping to physical parameters and therefore cannot implement physically motivated perturbations.

FORSE Data Model

In order to maximize the accuracy of the control design model and hence the closed loop performance of the system, it was necessary to abandon the analytic Rayleigh-Ritz model. This model proved valuable for design and analytic investigation, but the accuracy requirements for optimal control design dictated the need for this step. The method of system identification or model synthesis used here is Frequency domain Observability Range Space Extraction (FORSE) as presented in [Jacques, 1994]. The algorithm is based on the same type of frequency domain logarithmic cost in Equation (6.1) which proves to be a very accurate and robust for lightly damped resonant structures. Multiple input, multiple output (MIMO) models are synthesized from the set of frequency response functions (FRFs) taken up through a bandwidth of 2kHz. The FRFs were obtained through the standard experimental procedures explained in Chapter 4.

For designing the optimal controllers presented in the following section, the model must accurately represent two signal paths through the system, namely from the two inputs, control and disturbance, to the sensor. Figures 6.8 and 6.9 present the correlation between

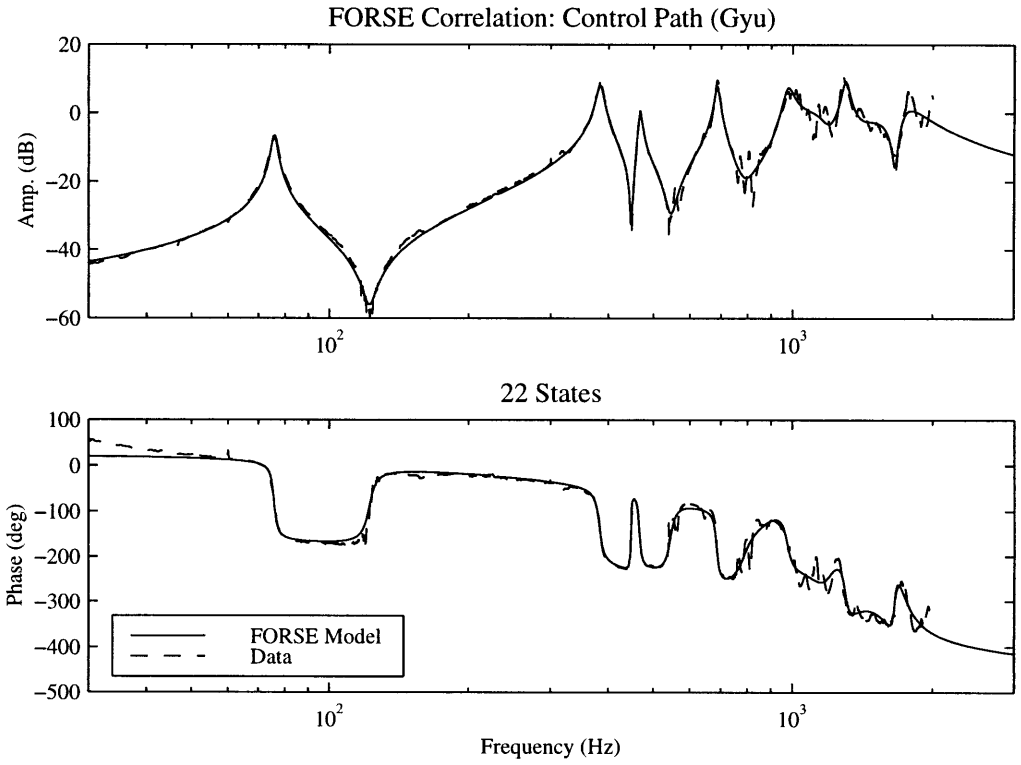

Figure 6.8: FORSE Model Compared with the Experimental Data from Control to Sensor

the experimental data and the 22 state FORSE model. It is interesting to note the slope of the phase in Figure 6.8 due to the anti-aliasing filters[2] and control system delay included in the data loop. The model is shown to closely correlate with the experimental data up through the bandwidth of concern. It should be noted that even though the desired bandwidth of control only extends to 1 kHz, the identification was carried out to create a model with dynamics up through 2kHz. As evident from the figures, the model tends to roll off above the highest frequency content of the data, while previous discussion on rate feedback design and the dereverberated slope indicate that in actuality this is not the case. This discrepancy between the model and data is addressed in the designs which follow. For comparison, modal parameters of the FORSE model and the Rayleigh-Ritz model are compared directly in Table 6.2.1. The reason for the vacancies in the right-hand column is that although the control and disturbance actuators excite all the modes of the structure the sensor placement, approximately in the geometric center of the panel, cause observability of only certain modes. Specifically it is obvious that this location will be on the node lines of any 'even'[3] modes of the panel, thus rendering them unobservable. The reason for the slight observance of the (2,3) mode in the disturbance to sensor transfer function, and hence

[2]For these experiments the filters were set at 1.2 kHz.

[3]Having an even number of half wave lengths in either the x or y direction.

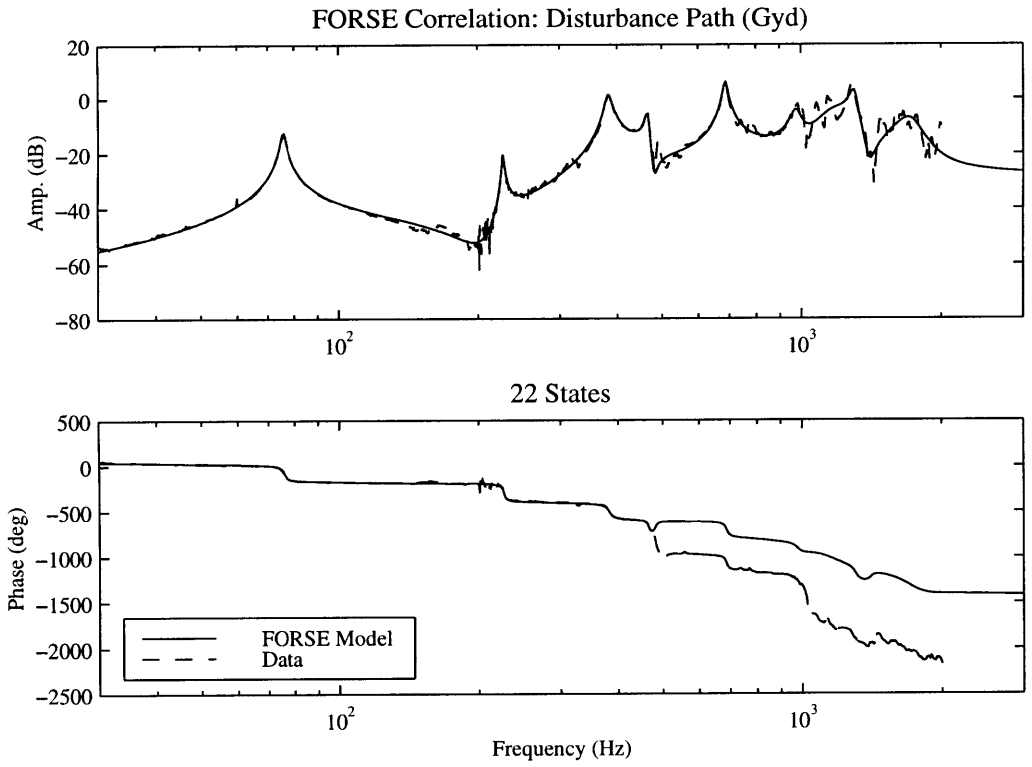

Figure 6.9: FORSE Model Compared with the Experimental Data from Disturbance to Sensor

the necessity of including a resonant pole pair in the FORSE model, is slight misplacement of the accelerometer sensor. This is verified by the Ritz model which predicts this behavior if the sensor location is moved slightly in the frequency response analysis.

Radiation Coupling

From the preceding presentation of the farfield radiated acoustic model in Chapter 2, recall that the acoustic field can be defined by knowledge of the modal velocities, $\dot{\eta}$, corresponding to the panel modes of a simply supported flat plate. In the assumed modes vibration model, these values were directly available as outputs of the state-space representation of the system. From the correlation between this Ritz model and the experimental data and simple investigation using a laser displacement sensor[4], it is assumed that the modes of the experimental system correspond to the panel modes listed in Table 6.2.1. Using a similarity transform, the FORSE state-space model can be configured to have as its states these same modal velocities.

[4]Laser displacement sensors were set up to measure the out-of-plane deflection of the panel operating at various resonant frequencies. Although this data is not presented, it agrees with the predicted panel mode shapes.

Ritz		MODE	FORSE	
ω_i	ζ_i	SHAPE	ω_i	ζ_i
78.8	0.0100	(1,1)	75.7	0.0125
181.1	0.0100	(2,1)		
246.7	0.0100	(1,2)	226.6	0.0064
323.1	0.0100	(2,2)		
361.4	0.0100	(1,3)	382.9	0.0159
475.9	0.0100	(2,3)		
524.8	0.0100	(3,1)	466.8	0.0081
594.9	0.0100	(3,2)		
625.9	0.0100	(1,4)		
707.7	0.0100	(3,3)	687.0	0.0112
728.8	0.0100	(2,4)	706.6	0.4566
918.1	0.0100	(3,4)		
937.6	0.0100	(4,1)		
970.6	0.0100	(1,5)	976.3	0.0236
1003.4	0.0100	(4,2)	1160.1	0.0826

Table 6.1: Correlation Between Ritz and FORSE Modal Parameters

Two typical canonical forms of state-space structural models are the *Jordan form* and *modal form*. Because both forms are decoupled, each modal residue is represented by 2x2 blocks along the diagonal of the system matrix- the A matrix in the state-space [A,B,C,D] convention. Jordan form is typically obtained by eigenvalue decomposition of the state matrix ($[A]$). Damping in the system causes the eigenvalues, λ_i, to occur in complex conjugate pairs with corresponding complex conjugate eigenvector ,ϕ_i, pairs. By separating the real and imaginary portions of the eigenvectors, a transformation is defined which yields the block-diagonal Jordan form-A_j,

$$T = [\mathcal{R}(\phi_1)\mathcal{I}(\phi_1)\ldots\mathcal{R}(\phi_i)\mathcal{I}(\phi_i)\ldots\mathcal{R}(\phi_N)\mathcal{I}(\phi_N)]$$

$$A_j = T^{-1}AT \qquad a_i = \begin{bmatrix} -\zeta_i\omega_i & \omega_i\sqrt{1-\zeta_i^2} \\ -\omega_i\sqrt{1-\zeta_i^2} & -\zeta_i\omega_i \end{bmatrix}$$

$$[A,B,C,D] \Rightarrow [T^{-1}AT, T^{-1}B, CT, D]$$

were a_i are the 2x2 blocks along the diagonal in the Jordan system matrix.

Modal form is what is typically used to transform second order ordinary differential equations (e.g., finite degree of freedom mass, damping, stiffness systems) to state space form (see Equation (2.16)) were the modal displacements and velocities are internal states of the

system. This form also serves to decouple the modal residues, and by correctly ordering the states, a block diagonal form can be deduced. By working with these uncoupled dynamics the eigenvalues and eigenvectors need not be calculated for the full system matrix, and the similarity transform can be defined to relate the Jordan form 2x2 blocks (a_j) to the modal form (a_m).

$$a_m = \begin{bmatrix} 0 & 1 \\ -\omega_i^2 & -2\zeta_i\omega_i \end{bmatrix}$$

$$\lambda_{1,2} = -\zeta_i\omega_i \pm i\,\omega_i\sqrt{1-\zeta_i^2} \qquad \Phi = [\phi_1 \phi_2] = \begin{bmatrix} 1 & 1 \\ \lambda_1 & \lambda_2 \end{bmatrix}$$

$$T = [\mathcal{R}(\phi_1)\mathcal{I}(\phi_1)]$$

$$a_j = T^{-1}a_m T \Rightarrow a_m = T a_j T^{-1} \tag{6.2}$$

Because the FORSE algorithm uses a model that is based on the structural response residues, the Jordan form is easily synthesized. From the similarity transform defined in the last expression of Equation (6.2), this form is easily converted to modal form. In fact, a mapping can be defined by inspection which transforms the modal information of the FORSE model directly to this modal form with the desired modal velocity states. The output of the system can now be set to the modal velocity state vector, and the radiation filter can be appended to the dynamics to predict the radiated power accurately.

The radiation filter used to couple the data-model modal velocities to the radiated power was developed in the modeling chapter. Here the filter takes the form of a 9 input, 9 output, 28 state filter. The eigenvalue decomposition incorporated in the spectral factorization process allows this decoupling which brings the form of the system into a block-diagonal state-space representation. From Figure 6.10 it is evident that the contributing acoustic modes are identified by the radiation filter. Recalling that the purpose of the filter is to weight the modes which radiate effectively, this correlation verifies that capability. As will be shown in the following control design, it is this weighting that gives the compensator the information on the acoustic radiation, the figure of merit for control, using structural sensors. The error in the higher frequency modes (i.e., the (3,1) and (3,3) mode shapes) is most likely due to the fact that at their respective resonant frequencies the farfield assumption used to develop the radiation filter formulation do not hold. Particularly the acoustic wavelength approaches the characteristic length of the panel so that it no longer radiates as a compact source.

6.2.2 Linear Quadratic Gaussian (LQG)

The previous classical designs, RF and PPF, are proven techniques for vibration control or adding active damping to lightly damped structures. Although it is verified that reducing

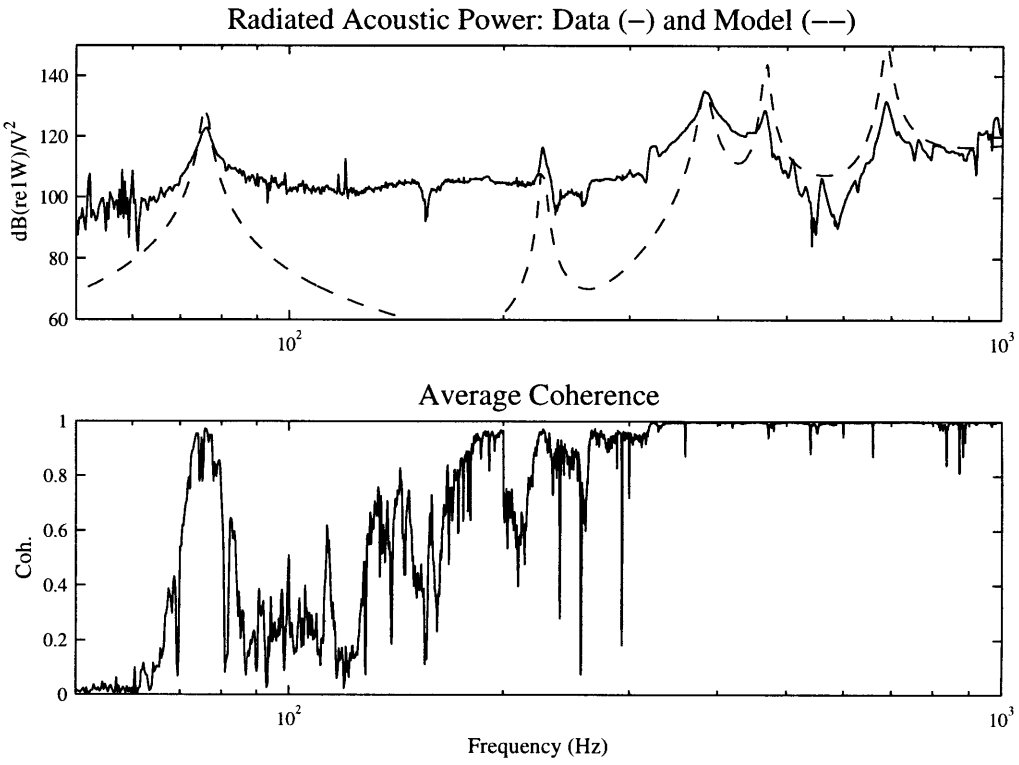

Figure 6.10: Correlation of Radiated Power from FORSE Model and Experimental Approximation

the vibration energy in a structure is an effective method for reducing acoustic radiation, one of the goals of this work is to present a more direct means of formulating the control problem such that the compensator more effectively targets the radiated sound power. As illustrated in Chapter 5, including the radiation filter in the structural-acoustic control design model allows for the optimal solution to directly minimize the acoustic power. The radiation filter weights the contribution of each mode to the cost function used in the control design based on the acoustic coupling of the individual modes. Two design examples are considered in parallel here provide more insight into the problem. Both are based on the frequency weighted linear quadratic Gaussian (FW-LQG) design method presented in Chapter 5. The first example, termed the FW-LQG compensator, is designed based on an *ad hoc* frequency weighting while the second, termed the radiation filter LQG (RF-LQG) compensator, uses the radiation filter to provide this frequency weighting based on the physical model.

The basic design parameters for the optimal compensators presented here are ρ, the control cost; μ, the sensor noise; and the tailored frequency response of the state and control frequency weighting (see Chapter 5 Equation (5.4)). As shown in Chapter 5, the magnitude of the frequency response of weighting filters is tailored by the control designer, selectively weighting regions of the response or control in the frequency domain. For the FW-LQG, a

state-weighting filter is defined based on engineering judgment for the compensator design. The weighting filter response shown in Figure 6.11a concentrates the control effort in the bandwidth of concern (30-900 Hz) by using a two pole resonant bandpass filter concatenated with a two pole resonant roll-off filter to restrict the bandwidth of the final design.

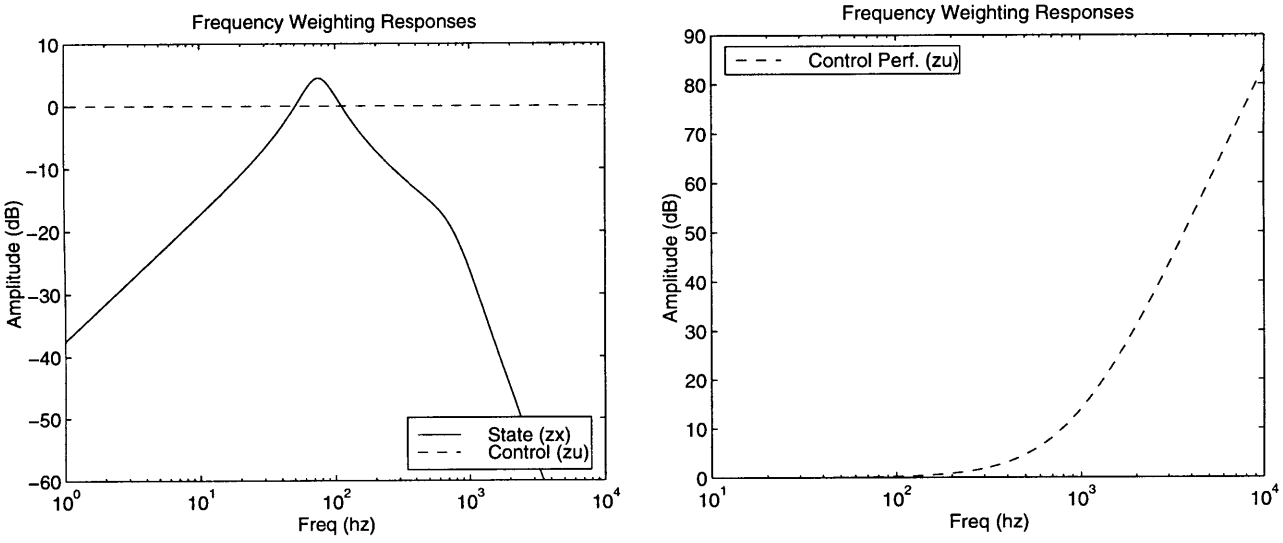

Figure 6.11: Weighting Functions for LQG Designs: a) FW-LQG State and Control Weighting and b) RF-LQG Control Weighting

$$W_3(s) = \left(\frac{\omega_{bp}\, s}{s^2 + 2\zeta_{bp}\omega_{bp}\, s + \omega_{bp}^2}\right)\left(\frac{\omega_{ro}^2}{s^2 + 2\zeta_{ro}\omega_{ro}\, s + \omega_{ro}^2}\right)$$

For this particular design the bandpass filter is centered near the first natural frequency ($\omega_{bp} = 75Hz$, $\zeta_{bp} = 0.3$) and the compensator roll-off is placed near the high frequency end of the bandwidth of concern ($\omega_{ro} = 750Hz$, $\zeta_{ro} = 0.5$). The RF-LQG utilizes the state-weighting provided by the radiation filter and compensator roll-off is achieved by adding a four pole lead filter to frequency weight the control cost.

$$W_4(s) = \left(\frac{(s + \omega_{ro})^4}{(s + (100 * \omega_{ro}))^4}\right)(100)^4$$

As noted in the discussion on the FORSE data model, the finite model obtained by truncation of the infinite data with a finite model does not capture the high frequency amplitude of the actual system. Severely decreasing the state weighting or increasing the control weighting is shown to add equivalent roll-off effects to the compensator design.

Once the weighting functions for the designs is specified, the iterative analysis process is used to choose appropriate values for the remaining design parameters indicating the relative control weighting and sensor noise intensity (ρ and μ respectively). Because the

LQG design process is undertaken in the continuous time domain and the compensator is implemented digitally, the order of the design must be reduced to meet the real-time computation requirements and transformed to a digital system. The actual compensator design is not identical to the implemented controller making it necessary to take extra steps to verify the stability of the system. This is done in two different ways. The product of the frequency response of the reduced, digital compensator with the open-loop data estimates the loop gain transfer function. Additionally, the loop gain transfer function is measured experimentally after the design is loaded onto the digital processor. The following chronicles this process for the implemented designs.

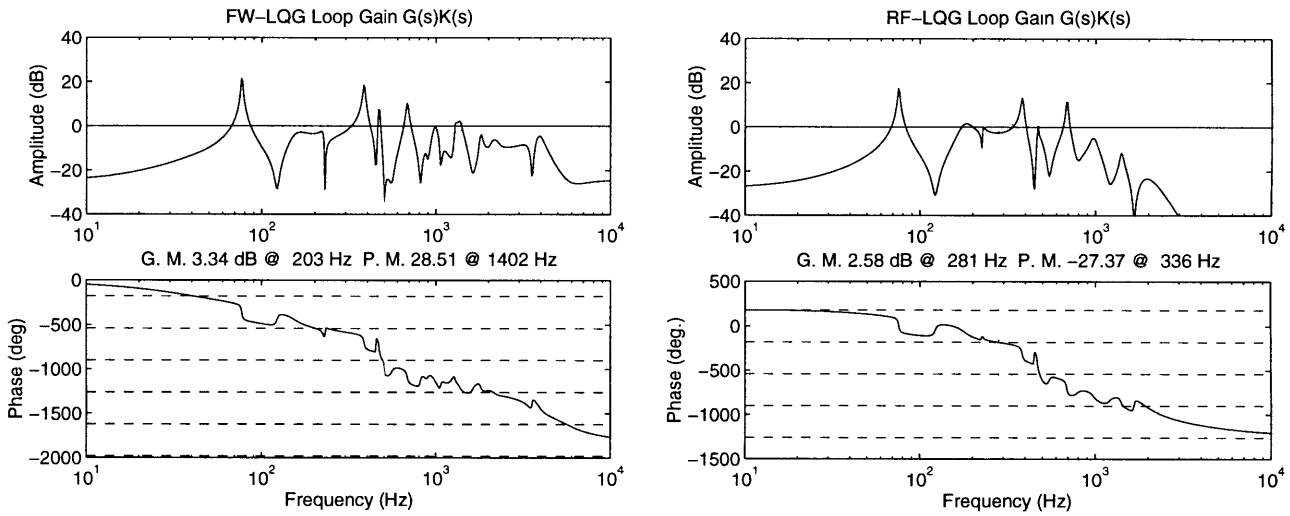

(a) (b)

Figure 6.12: Loop Gain Simulations for a)FW-LQG and b)RF-LQG Designs

Figure 6.12 shows the design loop gain of the full-state, continuous domain, compensator designs based on the control design model. The similarity between the two designs is immediately observable from the bandwidth of the compensators, i.e., the same modes are seen to have loop gain greater than unity while the same high frequency modes are gain stabilized.

The predicted performance of each design is illustrated through the frequency response in Figure 6.13. For the vibration controller, FW-LQG, the performance function is the output of the frequency weighting defined as part of the design and has little physical significance, while the performance of the RF-LQG system is the estimate of the farfield radiated power implicit in the formulation of the radiation filter. For comparison the linear quadratic regulator (LQR) performance is presented along with the LQG results. The LQR results represents an asymptote for the LQG performance in that as the sensor noise becomes small, accurate state estimation is performed by the Kalman filter, approximating full-state feedback.

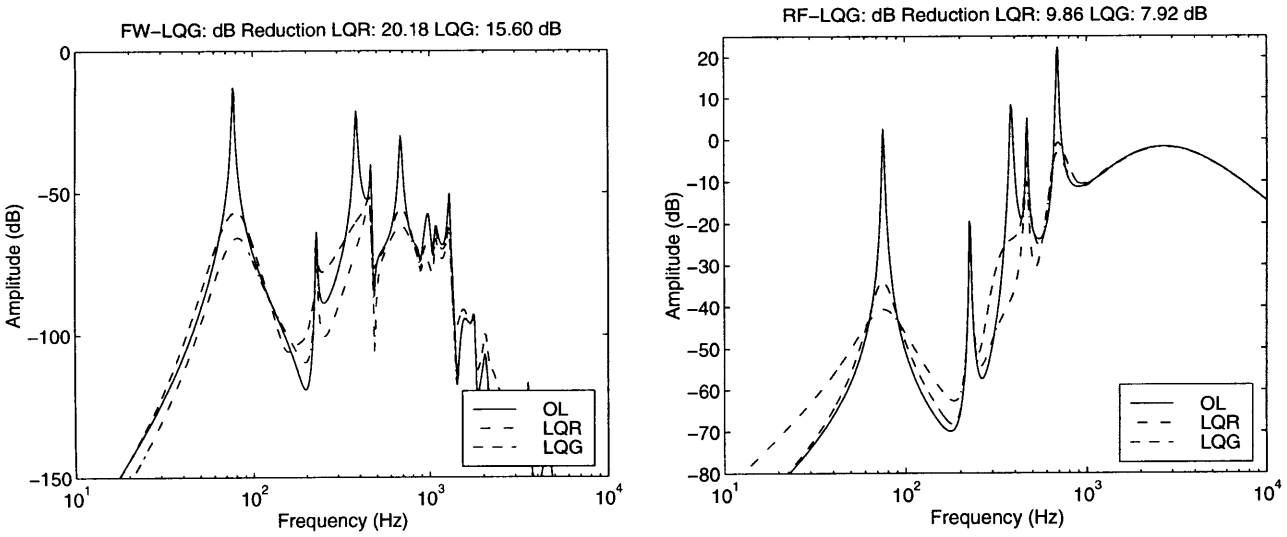

Figure 6.13: Performance Prediction for a)FW-LQG and b)RF-LQG Designs

Realization of the continuous state-space control design is done using the real-time control hardware described in detail in Chapter 4. The discrete sampling and computational capabilities introduce two limitations on the dynamics of the implemented designs: the size of the state-space regulator must be sufficiently small to be implemented on the digital hardware[5] and the magnitude of the largest eigenvalue of the system, indicating the fastest dynamics in the compensator, must be below the Nyquist frequency for the sampling rate used in the continuous to digital conversion[6]. LQG compensators are nominally the size of the state-space design models with the appended dynamics of the weighting systems. For the FW-LQG design, the state-weighting appends 4 states design model thus increasing the full-state compensator to a 36 state state-space continuous time representation. The added complexity of the 28 state radiation filter manifests itself in a compensator design that contains 54 states. The compensator designs are reduced to address both of these limitations. By converting the compensator system to a balanced realization, the controllability and observability grammians are balanced indicating that the states of this balanced realization are equally observable and controllable. *Balanced reduction* truncates the model by directly eliminating the states with corresponding grammian values that are less that some described threshold level. An appropriate number of poorly observable/controllable states

[5]The maximum state-space model size for a given sampling rate is not simply proportional to the number of states; however, empirical results have shown that the current configuration is capable of implementing $\approx$ 25 state filters at 6.67 kHz.

[6]As explained in the experimental setup, the standard sampling period $T_s = 1.5x10^-4$ is typically used for consistency. The hardware/software used in the experiment is capable of implementing continuous designs using a variety of time integration techniques, but to maximize the bandwidth of the implementation 'Tustin' conversion of the continuous state-space system to a digital system is utilized.

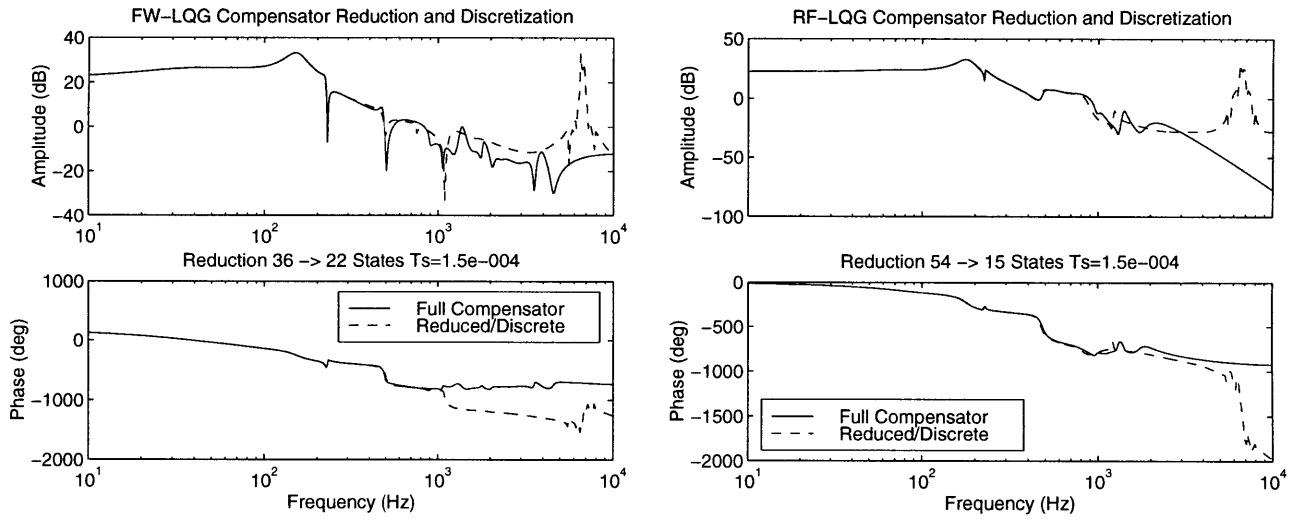

Figure 6.14: Compensator Realization for a)FW-LQG and b)RF-LQG Designs

in the compensator is removed, decreasing both the order of the system and the highest frequency content of the controller dynamics. The results of the controller reduction for the two designs are presented in Figure 6.14. The FW-LQG compensator is reduced from a 36 state model with the fastest pole at 9.47 kHz to a discrete realization containing 22 states and a maximum pole frequency of 2.6 kHz. For the RF-LQG the reduction represents the 54 state design with a fast pole at 3.01 kHz with a 15 state realization with a maximum eigenvalue at1.38 kHz[7]. The large peaks in the amplitude of the compensator responses are artifacts of the digital conversion using a sampling period corresponding to 6.67 kHz. To realize the predicted performance and stability of the designed compensators it is important to perform a reduction which accurately represents the low frequency high gain portion of the compensator where the loop gain exceeds unity and the system is phase stabilized, while capturing the all important roll-off characteristics of the design serving to gain stabilize the high frequency and unmodeled dynamics of the plant.

The limits on the gain of the control design were determined by repeatedly designing a compensator, performing the reduction and discrete conversion, and analyzing the stability of the resulting system through the loop gain of the system. Utilizing the prototyping capabilities of the dSPACE real-time computer hardware and software, designs could be quickly implemented and then the stability assessed directly by measuring the loop gain transfer function. Figure 6.15 presents this data through Bode and Nichols plots for the two designs. The similarity between the two designs is obvious from comparison of this data. It is interesting to note the effect of the (2,3) resonant mode at 477 Hz in the two designs.

[7]Another interesting method of accomplishing the control reduction is to use the frequency response of the full-state compensator to perform FORSE system identification using a constrained model.

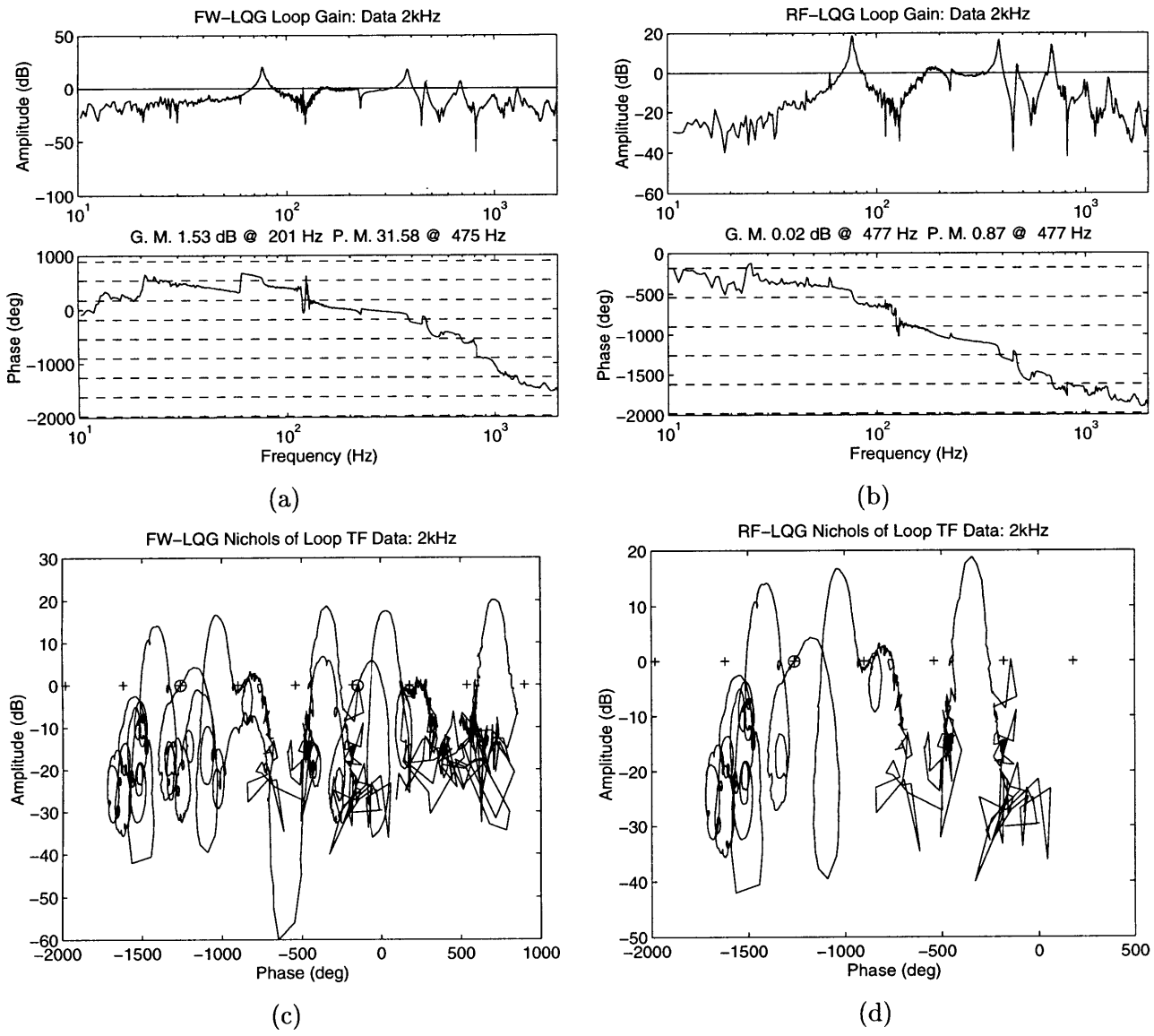

Figure 6.15: Stability Analysis on the Loop Gain Data for a) Bode FW-LQG, b) Bode FW-LQG, c) Nichols FW-LQG, and d) Nichols RF-LQG

For the radiation filter based design this was a severely limited the achievable performance. To increase the the compensator gain and maintain stability of the RF-LQG design, it was necessary to desensitize the compensator to this mode. The reason for this can be gleaned from the loop gain data in plots b) and d) where the gain margin is almost zero at this frequency point. The Nichols plot is particularly illuminating in that the trace almost intersects the critical point indicating that only slight increase in gain would cause this mode to destabilize the design. The design was modified by adding a variable coefficient to the modal velocity output equations used to couple the structural model with the radiation filter. By artificially reducing this parameter the weight assigned to that mode in the

performance function is lowered, effectively 'pushing down' the loop gain at this location adding stability. A final value of 0.7 was used to for this parameter to sufficiently lower the control effort concentrated on this system mode. This technique is directly analogous to the sensitivity weighted LQG design method [Campbell, 1993].

Finally the closed-loop performance of the FW-LQG and RF-LQG designs are presented in Figure 6.16. The scalar performance metric of broadband RMS reduction in decibels is calculated for the standard bandwidth considered in each design for consistency. The vibration performance indicates the reduced acceleration levels at the sensor location while the acoustic performance is based on the farfield radiated power measurement. The similarity between the characteristics of the performance measures is striking, indicating that for this particular setup, the vibration performance gives a direct indication of the acoustic performance. The acoustic performance of the FW-LQG (5.93 dB RMS) is observed to exceed that of the RF-LQG (4.13 dB RMS) by a considerable margin. There are two contributing factors for this. First, it must be recalled that this sensor/actuator structure is designed specifically for this structural-acoustic problem, thus the structural sensor can only observe acoustically radiating modes and the actuator is placed to excite these same modes. Second, because the fixed weighting of the radiation filter, the (2,3) mode contributes to the cost statement in such a way that the compensator attempts to exert considerable control effort at this mode. From the stability discussion, this is seen to detrimentally effect the design. By desensitizing the compensator to this mode, the resulting design exerts little effort at that location resulting in no performance for this mode of the response.

While the RF-LQG design operates as intended, utilizing the model to provide the state weighting to achieve acoustic performance from a purely structural system, it is discouraging that the vibration based compensator design seemed to out perform this design. If the system design had not been optimized for structural-acoustic closed loop performance, all the modes, including those that do not radiate efficiently, would have been observed in the sensor response. The resulting vibration design, without the added information of the radiation filter, would attempt to reduce the vibration in each of these modes, while the RF-LQG design would represent the true figure of merit in the performance function concentrating the control effort on the radiating modes. This example highlights the duality between system design for control and control design. Because the design process placed the sensors and actuators to realize the optimal acoustic performance, the control design is simplified. Considering the observability and controllability of the acoustically radiating indicates that the design has an inherent radiation filtering effect. Since the physics of the radiation coupling have been utilized in choosing the system architecture, the relative performance increase in performance between controlling vibration and acoustic radiation has already been implicitly included.

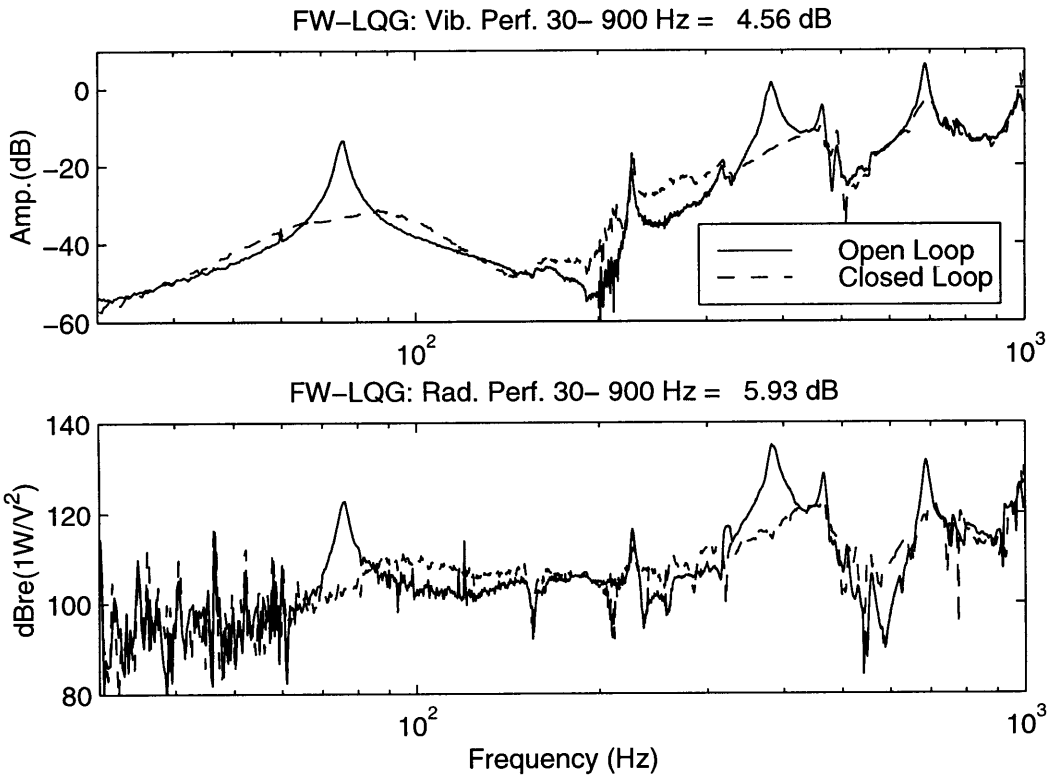

a)

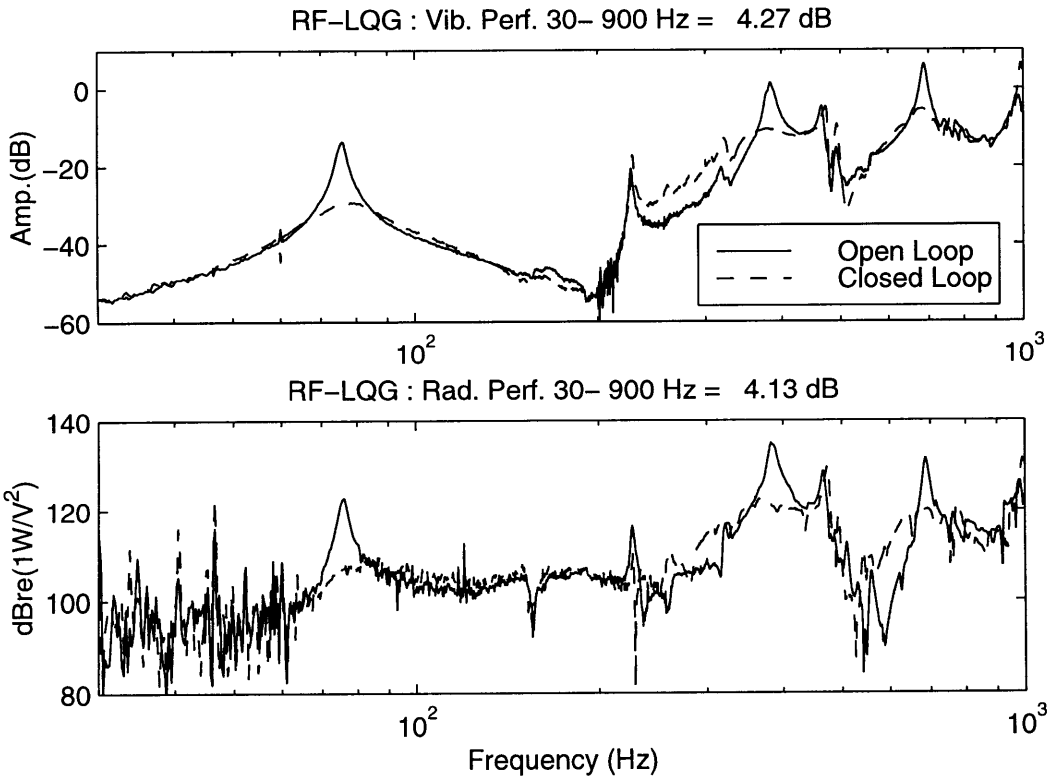

b)

Figure 6.16: Vibration and Acoustic Performance of (a) FW-LQG and (b) RF-LQG Designs

6.3 X-filtered LMS Feedforward Control

Comparisons between feedback control designs illustrated in the preceding discussion and

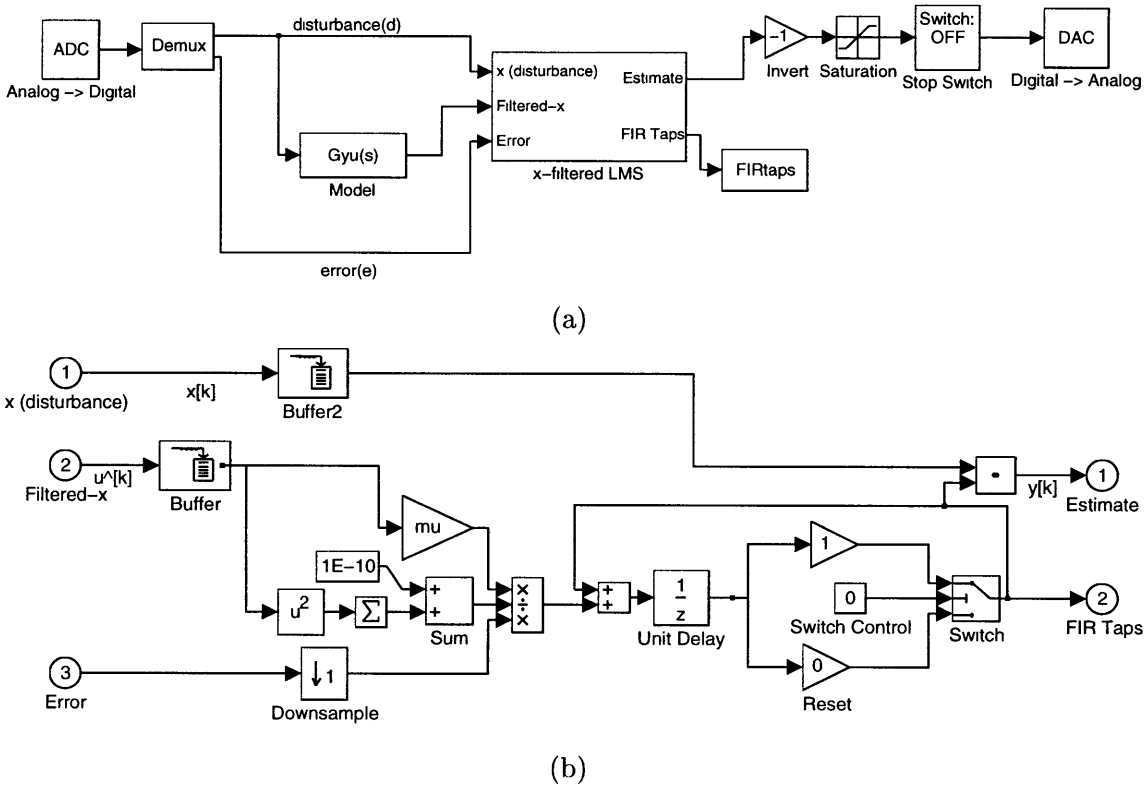

Figure 6.17: SIMULINK Realization of x-filtered LMS Feedforward Compensator

the LMS feedforward application are difficult because the application of each is fundamentally different. In particular, the LMS algorithm assumes knowledge of the disturbance or availability of a signal correlated with the disturbance. Implementation of the algorithm is depicted in Figure 6.17. Diagram 6.17 a) explicitly shows the two inputs to the system, the disturbance and the error sensor. One key element in the compensator is the control path model necessary to do the x-filtering. Because much of the work done with this algorithm is done on narrowband or tonal disturbances, the fact that an accurate system model is required is often overlooked. The results which follow are based on an implementation making use of the same FORSE data model used in the LQG compensator synthesis. Diagram 6.17 b) shows the particulars of the LMS algorithm. Essentially, the product of the scalar error and vector of the delayed filtered-x signal is used to update the FIR coefficients. The magnitude of the filtered-x signal is used to normalize the updating parameter μ, which is analogous to the normalized version of the LMS algorithm [Kalouptsidis and Theodoridis, 1993]. The resulting estimate is the filter response, or the inner product of the delayed disturbance measurements with the adaptive FIR coefficients.

This estimate is inverted and applied to the control actuator. The switch block is included to reset the FIR taps to the initial value of zero during the simulation.

The canonical experiment performed in much of the literature utilizes a tonal disturbance and examines the capabilities of the x-filtered LMS algorithm for adaptively cancelling the error output measured using a structural or acoustic sensor. For such a deterministic response, it is trivial for the algorithm to converge on FIR coefficients representing a compensator that cancels the tonal disturbance. The only limitation on the attenuation is based on the relative control authority and disturbance strength. Typically this analysis yields very attractive directivity plots illustrating the fact that the controller can cancel the tonal disturbance, but it must be emphasized that these results are for a single frequency deterministic disturbance. This capability of the algorithm was verified experimentally, but because the intent is to present a comparative study these results will not be presented here.

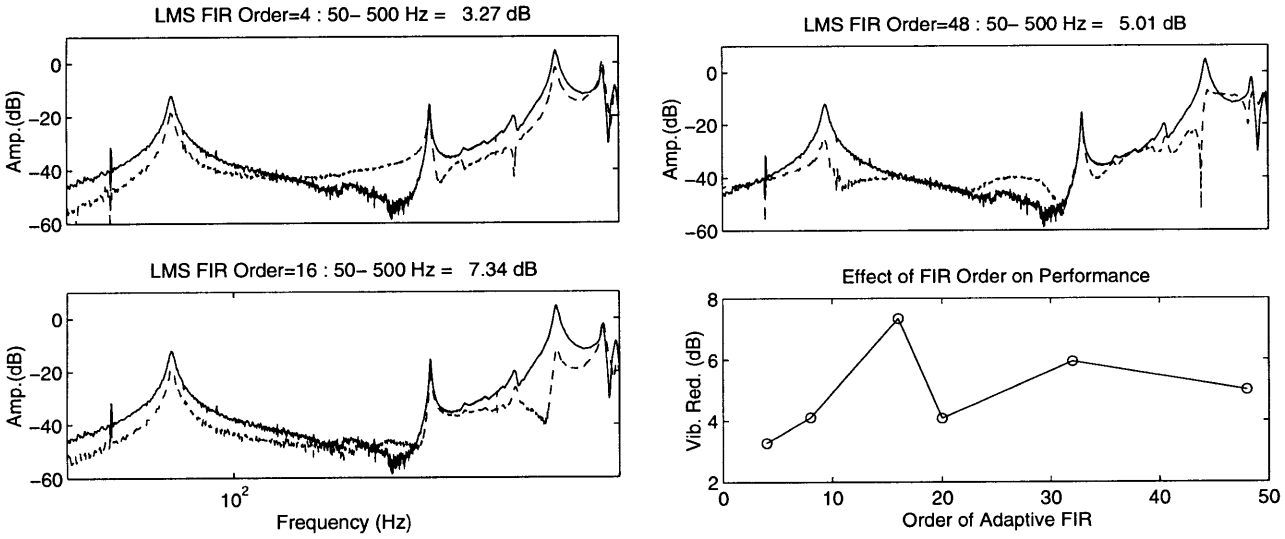

Figure 6.18: x-filtered LMS Performance with Increased Filter Order

To compare this feedforward compensation technique with feedback control the performance of the algorithm on a system subject to stochastic disturbance signals is examined. As shown analytically in Chapter 5, the setup is non-causal due to the digital computation delay in the control path. It has been demonstrated that performance is enhanced by including larger dimension FIR adaptive filters. Figure 6.18 shows the structural performance results for application of adaptive FIR filters with 4, 16, and 48 coefficients to the broadband problem. These results can be compared directly with the simulation results of Section 5.4 (Figure 5.22). A narrower bandwidth was used for this examination because for the full bandwidth, up to 1 kHz, the lower order LMS filters were not effective. For each trial the FIR coefficients were allowed to converge in the presence of a random

disturbance incorporating the entire bandwidth from 0 to 500 Hz. The standard dynamic response measurements were made using these fixed coefficients. As expected, the capability of the algorithm to cancel broadband disturbances is found to be directly related to the size of the compensator. Examination of the three examples in Figure 6.18 show the effect of adding order to the adaptive filter. Intuitively the filter requires a certain order to accurately represent the disturbance path of the plant. As the order is increased, more modes are cancelled in the response and less non-resonant amplification is observed. This is the same behavior predicted in the simulation results. The size of the adaptive filter was limited to 48 coefficients was by the computational load on the processor. For each sampling frequency the processor must not only perform the LMS updating and convolution, but must also simulate the control signal path model, a 22 state state-space model. The final plot in the figure shows the results from applying a variety of LMS adaptive controllers. Although the curve is non monotonically increasing as suggested by the analytic investigation, it does roughly show the increased performance expected with FIR order. These results illustrate the anticipated performance dependence on filter size quantified in the simulations of Section 5.4

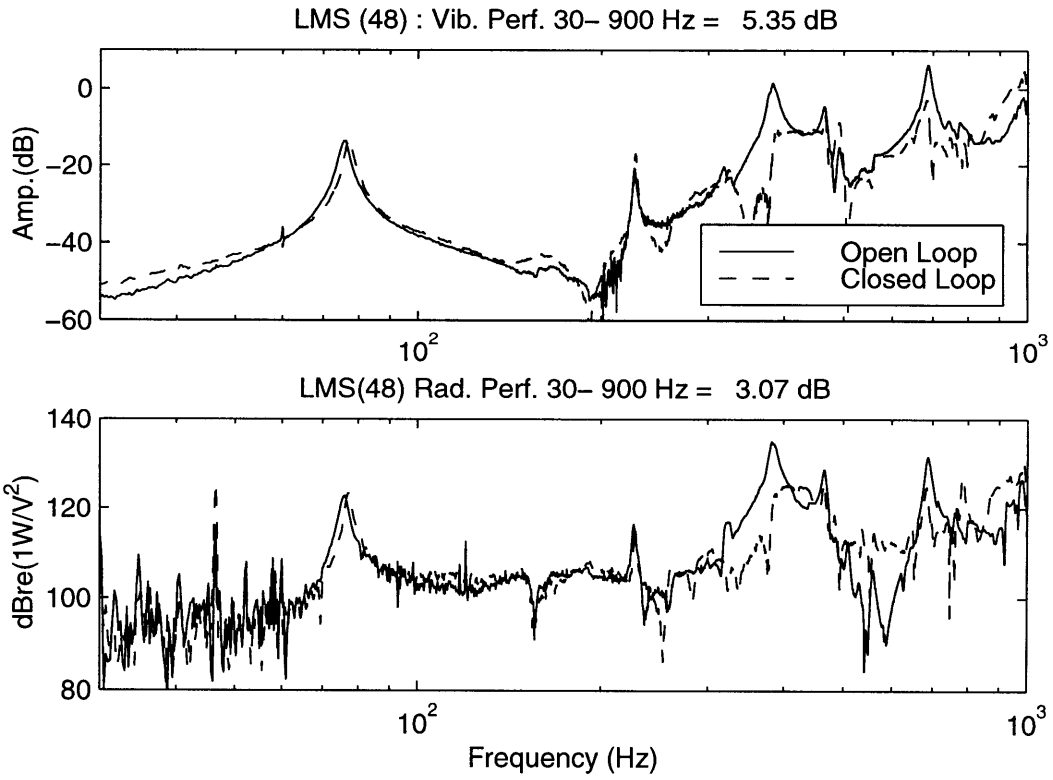

Figure 6.19: Broadband (0-1000Hz) Performance of Structural x-filtered LMS Implementation

To compare the broadband acoustic performance of the x-filtered LMS algorithm to

the previous feedback examples, an equivalent experiment was performed to those used to quantify the feedback control performance. The same random disturbance signal is implemented and the value of the convergence coefficient is increased to a point were the algorithm stability converges to a solution in minimum time. The results shown in Figure 6.19 illustrate the behavior of the 48 coefficient adaptive filter for the same disturbance used in the feedback control experiments. The controller mitigates high frequency vibration and hence the corresponding acoustic radiation. The limited bandwidth of the compensator is illustrated by the lack of authority in region of the first mode.

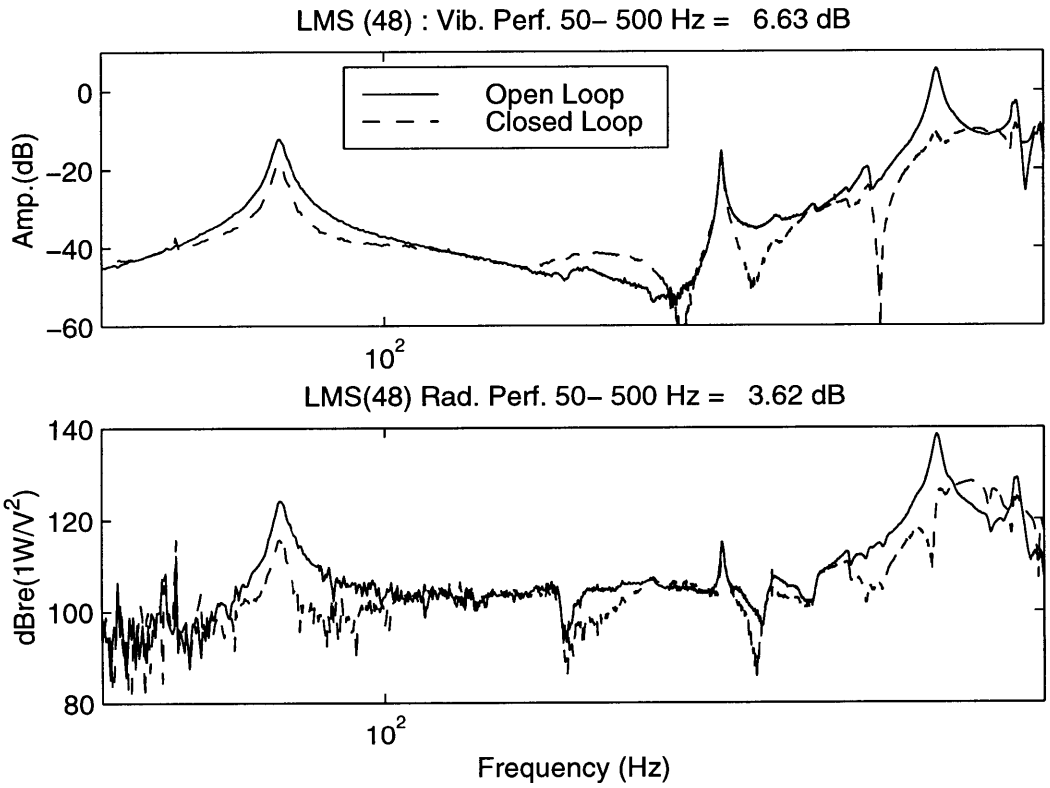

Figure 6.20: Broadband (0-500Hz) Performance of Structural x-filtered LMS Implementation

Figure 6.20 shows the same compensator implemented for a more narrow band disturbance source. Because the computational limit on the FIR size, this example is included to show that the FIR size is limiting the performance of the more broadband application. From this result it may be inferred that increasing the number of FIR coefficients would have an advantageous effect on the broadband response.

6.4 Summary

This chapter has illustrated the capabilities and limitations of the proposed feedback and feedforward compensator designs through implementation on the experimental test panel. Comparisons are made considering the closed-loop performance measured at the accelerometer sensor and by approximating the farfield radiated power with pressure measurements. Table 6.4 summarizes the performance results and the key limiting factors for each design. The "Vib." performance is the measured vibration reduction at the sensor, while the "Rad." performance is the approximated acoustic radiated energy reduction.

Compensator	Performance(dB)		Limitation
	Vib.	Rad.	
RF	0.83	1.96	Modal density limits the roll-off bandwidth.
PPF	-0.24	0.09	Single mode control limits low bandwidth.
FW-LQG	4.56	5.93	Sensitivity to (3,1) mode limits stability.
RF-LQG (Design)	10.96	7.92	"
RF-LQG (Experiment)	4.27	4.13	"
xLMS	5.35	3.07	FIR filter order

Table 6.2: Summary of Experimental Vibration and Radiation Performance and Limitations

The classical designs illustrate the disparity between theoretical predictions and application results. The rate feedback discussion in Chapter 5 highlighted the hyperstability of direct rate feedback, but from the example it is evident that this is not achievable due to the topology of the sensor/actuator architecture. Specifically, the accelerometer and AFC pair cannot be collocated and therefore do not retain the phase bound ($\pm 90°$) of a positive-real transfer function. The necessity to roll-off the compensator degrades the performance and robustness of the implementation.

The optimal designs follow directly from the analytical development of Chapter 5. The analytic example illustrated how the placement of the actuator/sensor pair determined the observability and controllability of the control and disturbance, which in turn limits the achievable performance. This implementation reinforces this insight in two ways. First, the accelerometer placement is shown to observe the radiating modes, allowing for vibration control to achieve acoustic performance. Second, the authority of the control actuator over the (3,1) mode and the observability from the sensor limit the performance of the designs. This is illustrated by the loop gain plots of Section 6.2.2, Figure 6.15 where the frequency region of this resonant response locates the minimum gain and phase stability margins.

The behavior of the x-filtered LMS feedforward compensator is limited by the computational limit of the digital computer processor. Chapter 5 illustrates through simulation how the order of the FIR filter influences the bandwidth of the response, highlighting the need for high order filters for broadband control. For the implementation, the processor power and required sampling period put a practical limit on the size of the adaptive filter which can be implemented. From the similarity between the analytical and experimental results, the performance is anticipated to increase with the ability to realize more complex adaptive filters.

In general the computational load limits the performance of the compensators. For the optimal, dynamic, feedback compensators, the state-space controllers must be of sufficiently low order to be implemented at the sample rate of the system. This requires a controller reduction step which limits the available bandwidth of the design and hence the performance. For the adaptive xLMS compensator, the order of the FIR filter is limited by the computational power. Higher order filters are shown analytically and experimentally to achieve better performance for broadband disturbances.

These comparisons illustrate the necessity of designing the compensators in simulation in order to anticipate the limitations and gain insight into the behavior of the methods. An effort is made to connect these results with the predictions of Chapter 5 demonstrating the power of analytical investigation for choosing the appropriate methodology and showing that implementation can restrict the validity of these predictions. In order to successfully design a controlled structure, the results of both must be considered.

Chapter 7

Conclusions/Further Work

7.1 Conclusions

This work presents a comprehensive view of the structural-acoustic control problem through analytic development and experimental design examples. The theoretical development is meant to lend physical insight into the experimental examples and serve as a basis of approaching the active structural-acoustic control (ASAC) problem for the target applications. Contributions are made at each step in the development and are summarized here.

The coupled structural-acoustic model for a panel structure is presented in Chapter 2. A standard Rayleigh-Ritz model for a laminated plate captures the physics of the vibrating structure. An exact representation of the response of the acoustic medium to this structural vibration is developed, mapping the modal velocities to the acoustic radiated power. The radiation filter is realized by an eigenvalue factorization of the harmonic solutions and a balance reduction of the resulting state-space model. This radiation filter is directly coupled with the structural model. The acoustic model quantifies the radiation efficiency of the contributing modes and allows an explicit statement of the radiated power in terms of structural inputs. The utility of this model is demonstrated in both the system and control designs.

Design of appropriate control algorithms is undertaken analytically, using the structural-acoustic model, and verified experimentally. The theoretical development delineates the limitations of each method and the experimental implementations further the understanding of these restrictions. The direct correlation between the experimental and analytical results verifies that the modeling yields meaningful performance predictions. By understanding these limitations and with an accurate design model, various approaches can be investigated analytically to enhance the final system performance.

By presenting the theoretical and experimental work based on a consistent architecture and experimental setup, a direct comparison between current control techniques is made. Because the disturbance, error sensor, and control signals are each structural based

and broadband, the x-filtered LMS algorithm is applied in a way to allow direct comparison with typical feedback designs. The usual limitations on the method, causality and broadband response, are overcome with increased adaptive filter size; however, the computational load of implementation limits the size of the the experimental compensator.

A representative test article is presented as a design trade-off, balancing the dynamic properties of the target applications. The final design contains four pairs of embedded AFC actuators and collocated strain sensors. Details of the composite manufacturing process are included to make the work repeatable. Dynamic testing is chronicled which illustrates a direct method for comparing the structural-acoustic performance of a particular system.

The culmination of this thesis is the direct comparison of the various control techniques made possible by the parallel development and presentation of each design. To summarize the comparisons in a digestible form, Table 7.1 presents the advantages and disadvantages of each approach to the problem. The statements in the table are the based on both the analytical and experimental results.

To reinforce the conclusions in this table, two points are emphasized. First, the fundamental difference between the feedback and feedforward approaches presented is that the adaptive control assumes direct access to the disturbance signal in order to estimate the error statistics and consequently update the model parameters. This algorithm has more information than the feedback control techniques which just operate on the error sensor signal. This requirement restricts the possible applications of feedforward control and should be a base consideration of any system design.

The second defining issue is how the performance criteria is included in the compensator design. The classical feedback and adaptive feedforward methods presented here do not directly measure the performance of the system. Methods of approximating the acoustic response using structural are currently being researched, [Maillard, 1997], but for the architecture of the experiments presented here, the performance should be similar. Without directly measuring the performance, these approaches rely on the reduced vibration attainable through structural control to indirectly reduce the acoustic energy. This approach is highly dependent on the architecture (sensor and actuator placement) of the system. The optimal control formulation, on the other hand, achieves performance by utilizing the compact form of the radiation filter to express the figure of merit, radiated power, as a function of the states of the vibrating structure. This enables the design to directly optimize the performance of the system.

	CAPABILITIES	*LIMITATIONS*
CLASSICAL FEEDBACK	Compensator design requires no model of the response. (Model Free)	Limited performance due to limited bandwidth of the compensator.
	Simple design process	Implementations cannot achieve theoretical hyperstability of rate feedback.
	Low-order compensator design	Performance objective is not directly included in the design process.
OPTIMAL FEEDBACK	Acoustic performance is directly included in optimal design through the radiation filter.	Accurate model is necessary. (Model Based)
	Closed-loop system is theoretically guaranteed stable.	Compensator reduction and digital conversion eliminate theoretical stability guarantee.
	High bandwidth design	High order compensator design.
	Optimal performance	Non-robust designs may be sensitive to model errors.
	Frequency-domain design.	Iterative design process.
FEEDFORWARD	Adaptively tracks slowly changing plant dynamics.	Error signal must be measurable, i.e., structural sensors do not capture the acoustic performance.
	Simple compensator design - single parameter μ.	Large order FIR filters are necessary for broadband performance.
	Robust to sensor errors.	X-filtered LMS requires similar modeling demand as the model based compensators for optimal feedback control.
		Time-domain design.
		Amplification is observed within the bandwidth - design cannot directly tailor the loop shape.
		Slow filter convergence for broadband disturbance.

Table 7.1: Comparison of Active Structural-Acoustic Control Techniques

7.2 Further Work

As with any project of such a broad nature, this work brings up as many questions as it answers. A few of the many avenues of continued investigation are listed.

A natural extension of this investigation is to apply these techniques to the multiple input, multiple output (MIMO) problem. The experimental article has four actuator/sensor pairs that could be used for control. By studying how the performance scales with actuator and sensor number, a more complete comparison of the technologies may be made.

Another experimental issue of this thesis was the method of adding disturbance noise to the structure. The AFC disturbance source was chosen because it does not change the open-loop dynamics and allows for accurate acoustic measurements. Two other types of disturbances are important in applications and should be investigated experimentally. A point force disturbance can be applied using a dynamic shaker; however, the shaker adds mass to the structure, slightly changing its dynamics. An acoustic disturbance can be implemented, but a good method for channeling the energy through the panel has not been realized. This results in acoustic measurements of the transmission of the panel *and* transmission through the acoustic baffle, making quantifying the transmission loss of the panel impossible.

The x-filtered LMS algorithm was illustrated as a viable alternative to feedback control methods. The *ad hoc* method deserves more consideration. Particularly it should be compared with various other adaptive or feedforward techniques. The solution might be compared with the optimally designed Wiener or Kalman estimators to identify the quality of the convergence method. Another interesting comparison could be made considering neural network approaches to the estimation problem. One limitation of the x-filtered LMS algorithm is that it must contain a model of the control path of the system. An accurate representation of the resonant poles of the structure is necessary because the finite impulse response adaptive filter cannot mimic the modal response. Neural networks or other more general adaptive designs might reduce this dependence on an accurate model.

To compare optimal feedback control with adaptive feedforward it is important to keep everything except for the compensator as similar as possible. Typical application of feedforward techniques do not use *a priori* knowledge of the disturbance, which can be an inherent advantage over feedforward designs. However, to compare the designs it is possible to include disturbance information in the LQG compensator design. An advantage of the optimal designs is that the performance function can be explicitly minimized using the radiation filter. [Maillard, 1997] offers a similar method for including the radiation information in the xLMS formulation by using an array of structural sensors and digital filtering to estimate the radiated acoustic power in real time. These two options for equating the available information in each design may lend to more insight into the fundamental

capabilities and limitations of the methods.

The most important future work that should come about as an extension of this thesis is apply these techniques to a more complex structure and determine how well the predicted performance on a representative structure indicates the capabilities of application.

Bibliography

[Anderson, 1993] Anderson, E. H. (1993). *Robust Placement of Actuators and Dampers for Structural Control.* PhD thesis, MIT.

[Asari, 1998] Asari, K. (1998). Vibroacoustic modeling and control for launch vehicle shrouds. Master's thesis, MIT.

[Athans, 1997] Athans, M. (1997). Multivariable control systems couse notes:6.245. Technical report, MIT.

[Balmés, 1993] Balmés, E. (1993). *Experimental/Analytical Predictive Models of Damped Structural Dynamics.* PhD thesis, MIT.

[Baumann et al., 1992] Baumann, W. T., Ho, F.-S., and Robertshaw, H. H. (1992). Active structural acoustic control of broadband disturbances. *Journal of Acoustical Society of America*, 4:1998–2011.

[Bent, 1997] Bent, A. A. (1997). *Active Fiber Composites for Structural Actuation.* PhD thesis, MIT.

[Bent and Hagood, 1996] Bent, A. A. and Hagood, N. W. (1996). Piezoelectric fiber composites with interdigitated electrodes. *Journal of Intelligent Material Systems and Structures.*

[Bertsekas, 1995] Bertsekas, D. P. (1995). *Dynamic Programming and Optimal Control.* Athena Scientific.

[Bies, 1988] Bies, D. A. (1988). *Engineering Noise Control: Theory and Practice.* Unwin Hyman.

[Blevins, 1979] Blevins, R. D. (1979). *Formulas for Natural Frequency and Mode Shape.* Krieger Publishing Company.

[Burden and Faires, 1989] Burden, R. L. and Faires, J. D. (1989). *Numerical Analysis.* PWS-KENT Pub. Co.

[Burdisso et al., 1993] Burdisso, R. A., Vipperman, J. S., and Fuller, C. R. (1993). Causality analysis of feedforward-controlled systems with broadband inputs. *Journal of Acoustical Society of America*, 94(1):234–242.

[Campbell, 1993] Campbell, M. E. (1993). Neo-classical control of structures. Master's thesis, MIT.

[Clark and Fuller, 1991] Clark, R. L. and Fuller, C. R. (1991). Control of sound radiation with adaptive structures. *J. of Intelligent Material Systems and Structures*, 2:431–452.

[Clark and Fuller, 1992] Clark, R. L. and Fuller, C. R. (1992). Modal sensing of efficient acoustic radiators with pvdf distributed sensors in active structural acoustic control approaches. *J. of Acoustical Society of America*, 91(6):3321–3329.

[Craig, 1981] Craig, Jr., R. R. (1981). *Structural Dynamics: An Introduction to Computer Models.* John Wiley and Sons.

[Crandall, 1968] Crandall, S. H. (1968). *Dynamics of Mechanical and Electromechanical Systems.* Kreiger Publishing Company.

[Crawley and Lazarus, 1989] Crawley, E. F. and Lazarus, K. B. (1989). Induced strain actuation of isotropic and anisotropic plates. *AIAA Journal*, 29(6):944–951.

[Crawley et al., 1995] Crawley, E. F., Masters, B. P., and Hyde, T. T. (1995). Conceptual design methodology for high performance dynamic structures. *AIAA.*

[Dehandschutter et al., 1997] Dehandschutter, W., Henrioulle, K., Swevers, J., and Sas, P. (1997). State space feedback control of sound radiation using structural sensors and structural control inputs. In *EAA International Symposium on Active Control of Sound and Vibration.*

[Elliot et al., 1987] Elliot, S. J., Stothers, I. M., and Nelson, P. A. (1987). A multiple error lms algorithm and its application to the active control of sound and vibration. *IEEE Transactions on Acoustics, Speech, and Signal Processing*, 35(10):1423.

[Fahy, 1985] Fahy, F. (1985). *Sound and Structural Vibration.* Academic Press.

[Fanson and Caughey, 1987] Fanson, J. and Caughey, T. (1987). Positive position feedback control for large space structures. *AIAA Journal.*

[Feynman, 1989] Feynman, R. P. (1989). *The Feynman Lectures on Physics.* Addison-Wesley.

[Fleming, 1990] Fleming, F. M. (1990). The effect of actuator and sensor on the zeros of controlled structures. Master's thesis, MIT.

[Francis, 1987] Francis, F. (1987). *An Introductory Course in $\mathcal{H}_\infty$ Control.* Springer-Verlag.

[Fripp et al., 1997] Fripp, M., O'Sullivan, D. Q., Hall, S. R., Hagood, N. W., and Lilienkamp, K. (1997). Test-bed design and modeling for aircraft interior acoustic control. In *Proceedings of the SPIE - The International Society for Optical Engineering*, volume 3041.

[Fuller et al., 1991] Fuller, C. R., Hansen, C. H., and Snyder, S. D. (1991). Active control of sound radiation from a vibrating rectangular panel by sound sources an vibration inputs: An experimental comparison. *J. of Sound and Vibration*, 145(2):195–215.

[Fuller et al., 1992] Fuller, C. R., Rogers, C. A., and Robertshaw, H. H. (1992). Control of sound radiation with active/adaptive structures. *J. of Sound and Vibration*, 157(1):944–951.

[Fung, 1977] Fung, Y. C. (1977). *A First Course in Continuum Mechanics.* Prentice-Hall.

[Glaese, 1994] Glaese, R. M. (1994). Development of zero-gravity structural control models for analysis and ground experimentation. Master's thesis, MIT.

[Glaese, 1997] Glaese, R. M. (1997). *Impedance Matching for Structural-Acoustic Control.* PhD thesis, MIT.

[Gupta, 1980] Gupta, N. K. (1980). Frequency-shaped cost funtionals: Extension of linear-quadratic-gaussian design models. *Journal of Guidancd and Control*, 3(6):529–535.

[Hagood et al., 1990] Hagood, N., Chung, W. H., and vonFlotow, A. (1990). Modelling of piezoelectric actuator dynamics for active structural control. *Journal of Intelligent Materials Systems and Structures*, 1.

[Haykin, 1984] Haykin, S. (1984). *Introduction to Adaptive Filteres.* MacMillan Publishing Company.

[Jacques, 1994] Jacques, R. N. (1994). *On-Line System Identification and Control Design for Flexible Structures.* PhD thesis, MIT.

[Johnson and Elliot, 1995] Johnson, M. E. and Elliot, S. J. (1995). Active control of sound radiation using volume velocity cancellation. *Journal of Acoustical Society of America*, 98(4):2174–2185.

[Jones, 1975] Jones, R. M. (1975). *Mechanics of Composite Materials.* Hemisphere Publishing Corporation.

[Junger and Feit, 1972] Junger, M. C. and Feit, D. (1972). *Sound, Structures, and Their Interaction.* MIT Press.

[Kalouptsidis and Theodoridis, 1993] Kalouptsidis, N. and Theodoridis, S. (1993). *Adaptive System Identification and Signal Processing Algorithms.* Prentice Hall.

[Lagace, 1988] Lagace, P. A. (1988). Telac manufacturing course class notes. Technical Report 88-4b, Technology Laboratory for Advanced Composites - Massachusetts Institute of Technology.

[Leissa, 1969] Leissa, A. W. (1969). *Vibration of Plates - NASA AP-160.* National Aeronautics and Space Administration.

[Leverton and Pollard, 1979] Leverton, J. W. and Pollard, J. S. (1979). Helicopter internal noise - an overview. *US Army Working Group on Aircraft Noise*, pages A2–7–9.

[Levine, 1996] Levine, W. S. (1996). *The Control Handbook.* CRC Press Inc.

[Ljung, 1987] Ljung, L. (1987). *System Identification: Theory for the User.* Prentic-Hall.

[Lublin et al., 1996] Lublin, L., Grocott, S., and Athans, M. (1996). *$\mathcal{H}_2$ (LQG) and $\mathcal{H}_\infty$ Control: The Control Handbook.* CRC Press Inc.

[Lueg, 1936] Lueg, P. (1936). Process of silencing sound oscillations. US Patent No. 2,043,416.

[MacMartin, 1990] MacMartin, D. G. (1990). *An H_∞ Power Flow Approach to Control of Uncertain Structures.* PhD thesis, MIT.

[MacMartin and Hall, 1992] MacMartin, D. G. and Hall, S. R. (1992). Broadband control of flexible structures using statistical energy analysis concepts. Technical report, MIT.

[Maillard, 1997] Maillard, J. (1997). *Advanced Time Domain Sensing for Active Structural Acoustic Control.* PhD thesis, Virginia Polytechnic Institute and State University.

[Masters, 1998] Masters, B. (1998). Personal correspondence. MIDE Technologies; Cambridge,MA.

[Mattiat et al., 1971] Mattiat, O. E., Belincourt, D., Kikuchi, Y., and Meitzler, A. H. (1971). *Ultrasonic Transducer Materials.* Plenum Press.

[McCain, 1995] McCain, A. J. (1995). Shaped actuators and sensors for local control of intelligent structures. Master's thesis, MIT.

[McDowell, 1998] McDowell, D. (1998). Personal correspondence. NUWC; Newport, RI.

[Moreland, 1979] Moreland, S. (1979). Us army working group on aircraft noise. Technical report, US Army.

[Morris, 1998] Morris, D. (1998). Personal correspondence. Boeing; Seattle, WA.

[Nelson et al., 1986] Nelson, P. A., Curtis, A., and S.J.Elliot (1986). The minimum power output of a pair of free field monopoles. *Journal of Sound and Vibration*, 105:173–178.

[Nelson and Elliot, 1992] Nelson, P. A. and Elliot, S. J. (1992). *Active Control of Sound.* Academic Press.

[Niu, 1988] Niu, M. C. Y. (1988). *Airframe Structural Design.* Conmilit Press LTD.

[Norton, 1989] Norton, M. (1989). *Fundamentals of Noise and Vibration Analysis for Engineers.* Cambridge University Press.

[O'Neil, 1995] O'Neil, P. V. (1995). *Advanced Engineering Mathematics.* Brooks/Cole Publishing Co.

[Oppenheim, 1983] Oppenheim, A. V. (1983). *Signals and Systems.* Prentice-Hall.

[O'Sullivan, 1998] O'Sullivan, D. Q. (1998). Aircraft interior structural-acoustic control design. Master's thesis, MIT.

[Overschee et al., 1997] Overschee, P. V., Moor, B. D., Dehandschutter, W., and Swevers, J. (1997). A subspace algorithm for identification of discrete time frequency domain power spectra. *Automatica*, 33(12):2147–2157.

[Papoulis, 1965] Papoulis, A. (1965). *Probability, Random Variables, and Stochastic Processes.* McGraw-Hill, Inc.

[Pierce, 1981] Pierce, A. D. (1981). *Acoustics: an Introduction to its Physical Principles and Applications.* McGraw-Hill Book Co.

[Pizzochero, 1997] Pizzochero, A. (1997). Residual actuation and stiffness properties for active fiber composites-theory and experiment. Master's thesis, MIT.

[Rayleigh, 1945] Rayleigh, J. W. S. (1945). *The Theory of Sound.* Dover.

[Rodgers, 1995] Rodgers, J. P. (1995). Modeling and manufacturing of adaptive plates incorporating piezoelectric fiber composite plies. Master's thesis, MIT.

[Rodgers et al., 1996] Rodgers, J. P., Bent, A. A., and Hagood, N. W. (1996). High load characterization of interdigitated electrode fiber composites. In *Proceedings of the 1996 North American Conference on Smart Structures and Materials.*

[Snyder and Tanaka, 1995] Snyder, S. D. and Tanaka, N. (1995). Calculating total acoustic power output using modal radiation efficiencies. *Journal of the Acoustical Society of America*, 97(3):1702–1715.

[Strang, 1986] Strang, G. (1986). *Introduction to Applied Mathematics.* Wellesley-Cambridge Press.

[Vipperman et al., 1993] Vipperman, J. S., Burdisso, R. A., and Fuller, C. R. (1993). Active control of broadband structurla vibration using the lms adaptive algorithm. *Journal of Sound and Vibration*, 166(2):283–299.

[Wallace, 1972] Wallace, C. E. (1972). Radiation resistance of a rectangular panel. *The Journal of the Acoustical Society of America*, 51(3).

[Wornell, 1997] Wornell, G. (1997). Stochastic process course notes:16.432. Technical report, MIT.

[Zhou et al., 1995] Zhou, K., Doyle, J. C., and Glove, K. (1995). *Robust and Optimal Control.* Prentice-Hall.

Appendix A

Realization of the Radiation Matrix

As mentioned in Chapter 2, the realization of the contributing terms in the factored radiation matrix are included here for completeness.

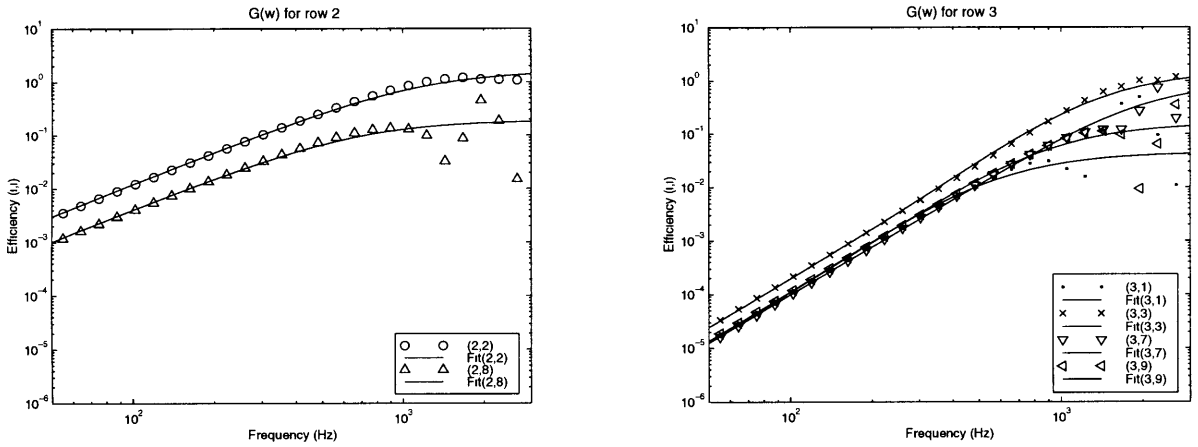

(a) (b)

Figure A.1: Radiation Matrix G(s): a) Row 2 and b) Row 3

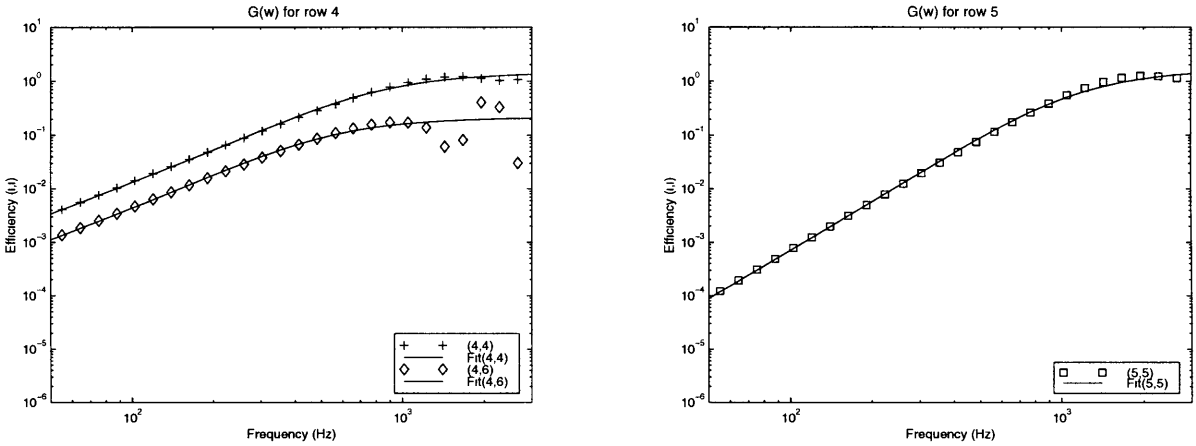

(a) (b)

Figure A.2: Radiation Matrix G(s): a) Row 5 and b) Row 5

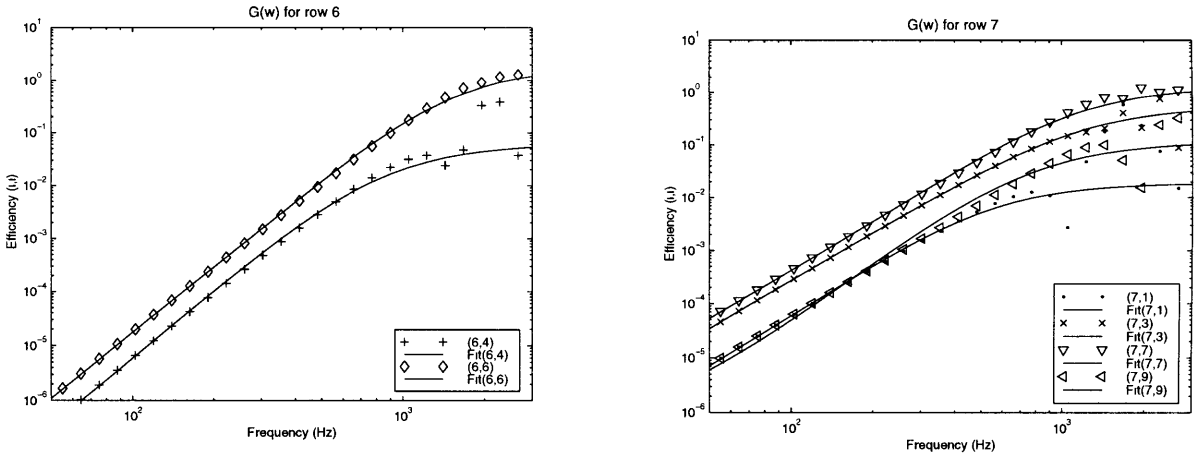

(a) (b)

Figure A.3: Radiation Matrix G(s): a) Row 6 and b) Row 7

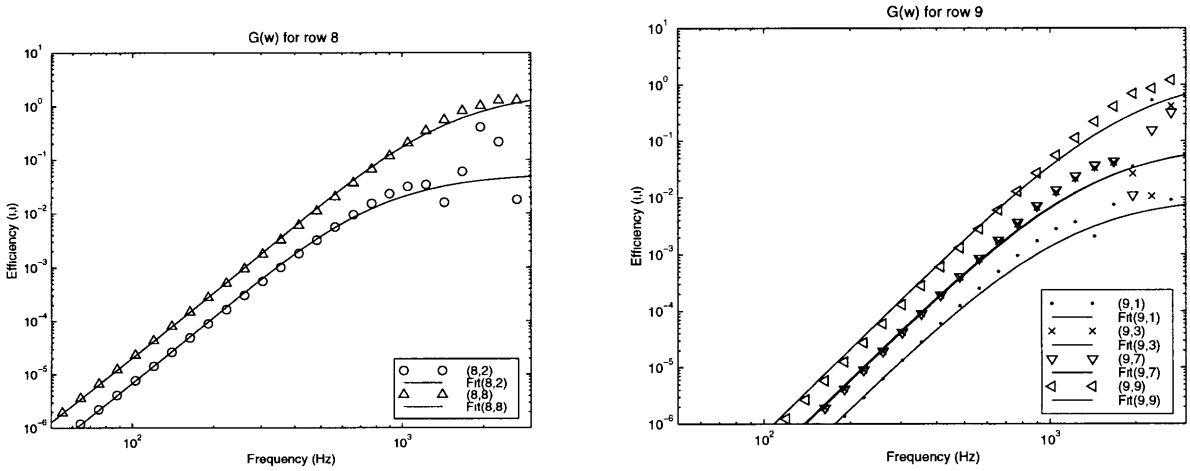

(a) (b)

Figure A.4: Radiation Matrix G(s): a) Row 8 and b) Row 9

Appendix B

Composite Material Properties

B.1 Passive Materials - Orthotropic

	E_{11} (GPa)	E_{22} (GPa)	ν_{12}	G_{12} (Pa)	Density (kg/m^3)	Thickness(mm)
AS4-3501-6	142	9.81	0.3	6.0	1580-1700	0.134
E-glass	19.3	19.3	0.148	4.1	1700	0.1143

Table B.1: Passive Ply Properties

The passive material constants listed in Table ?? are used in the Rayleigh-Ritz model of the composite panel.

B.2 Active Materials

The active material relations labeled "MIDE-AFC" are the properties quoted by the manufacturer, while the specific AFC properties as measured experimentally are included here and in the Rayleigh-Ritz model.

	$S_{11}\ 10^{-12}$ m/N	$S_{22}\ 10^{-12}$ m/N	$S_{66}\ 10^{-12}$ m/N
MIDE-AFC	31	60	-11

Table B.2: Nominal Passive Properties

	d_{31} 10^{-12} m/N	d_{32} 10^{-12} m/N	Density (kg/m^3)	Capacitance (nF)
MIDE-AFC	115	-50	4250	1.5-2.5
AFC 1a	76.6	-33.3	3652	1.61
AFC 1b	76	-33.1	3602	1.54
AFC 2a	60.8	-26.4	3640	1.48
AFC 2b	42.8	-28.3	3602	1.31
AFC 3a	68.1	-29.9	3564	1.60
AFC 3b	60.8	-26.4	3629	1.35
AFC 4a	67	-29.1	3602	1.39
AFC 4b	43.3	-18.8	3677	1.55

Table B.3: Measured Coupling Properties

Appendix C

Panel Transfer Functions

For completeness the input/output relationships for the embedded AFC actuators are recorded here. The numbering convention is consistent with Figure 3.7 for the AFC's and accelerometers. The collocated strain gage measurements are included to illustrate the type of response and noise in the signal.

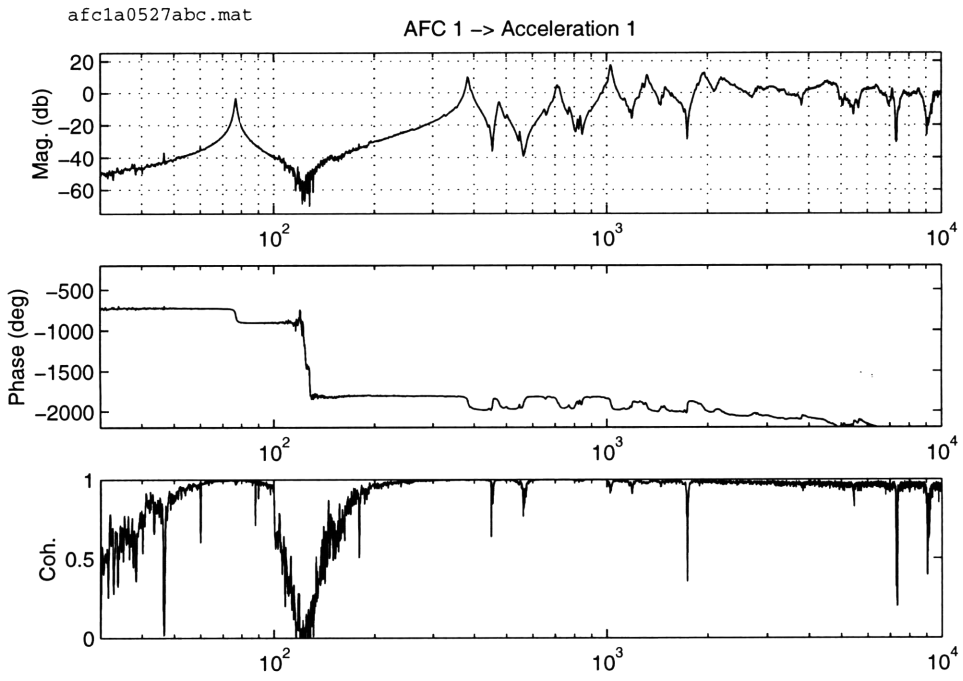

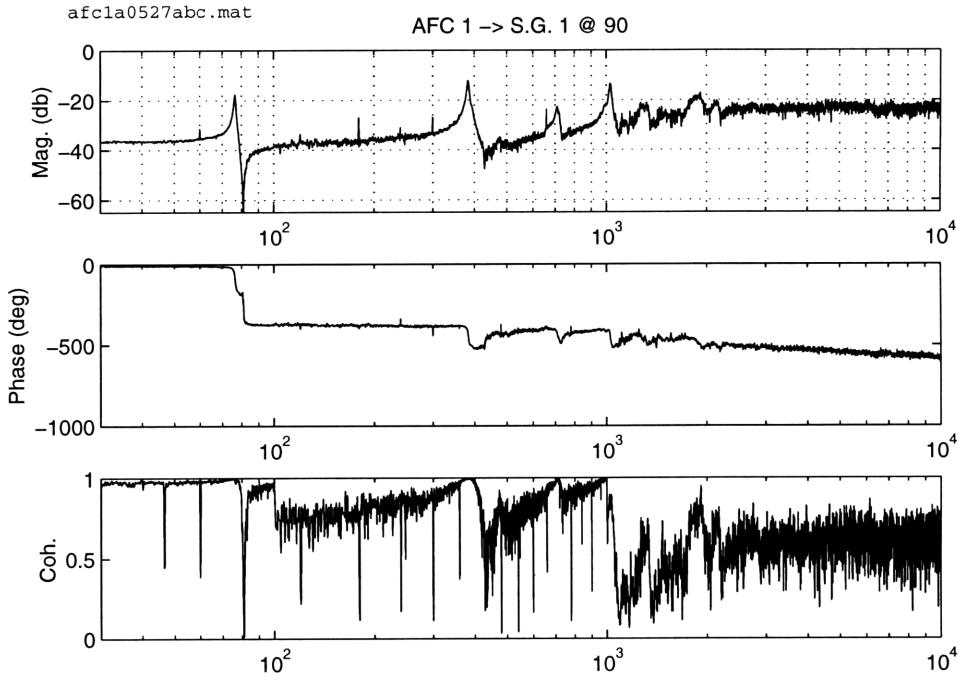
afc1a0527abc.mat
AFC 1 -> S.G. 1 @ 90
Mag. (db)
0
-20
-40
-60
10^2
10^3
10^4
Phase (deg)
0
-500
-1000
Coh.
1
0.5
0

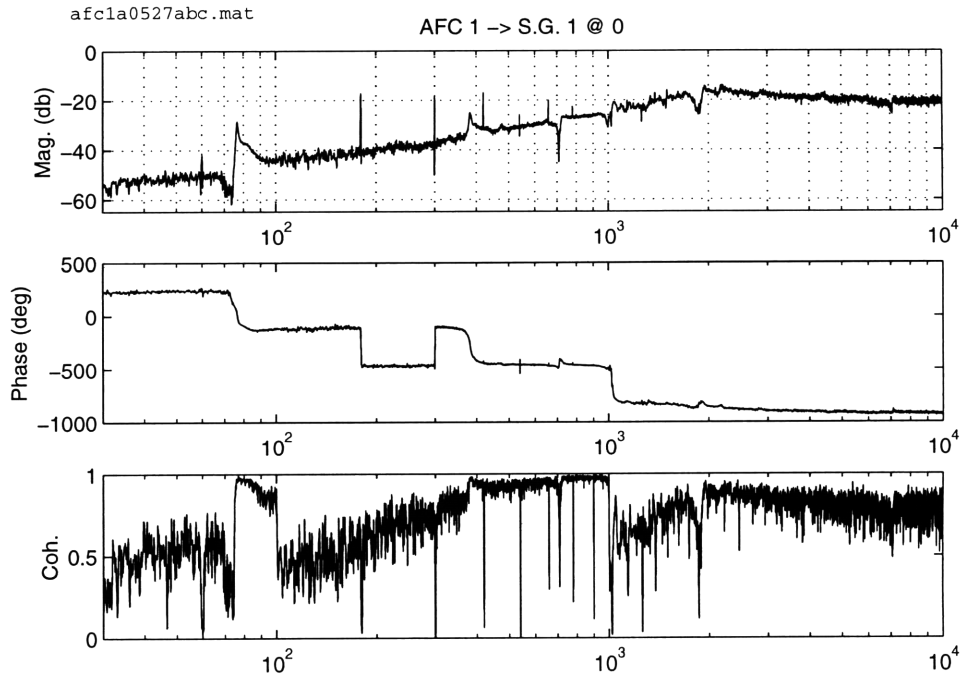
afc1a0527abc.mat
AFC 1 -> S.G. 1 @ 0
Mag. (db)
0
-20
-40
-60
10^2
10^3
10^4
Phase (deg)
500
0
-500
-1000
Coh.
1
0.5
0

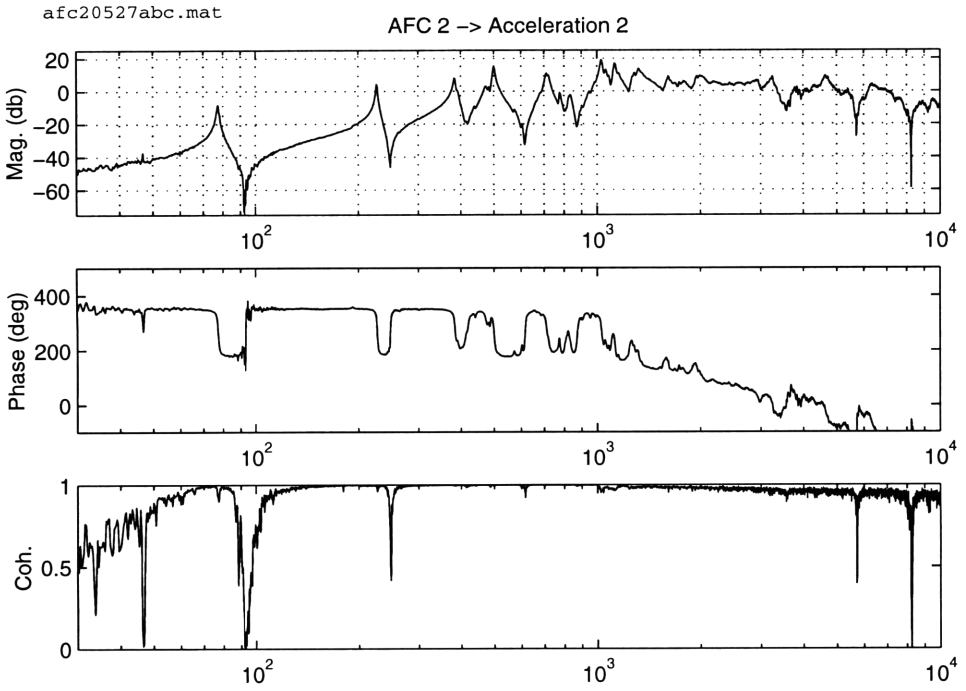
afc20527abc.mat
AFC 2 -> Acceleration 2
Mag. (db)
20
0
-20
-40
-60
10^2
10^3
10^4
Phase (deg)
400
200
0
Coh.
1
0.5
0

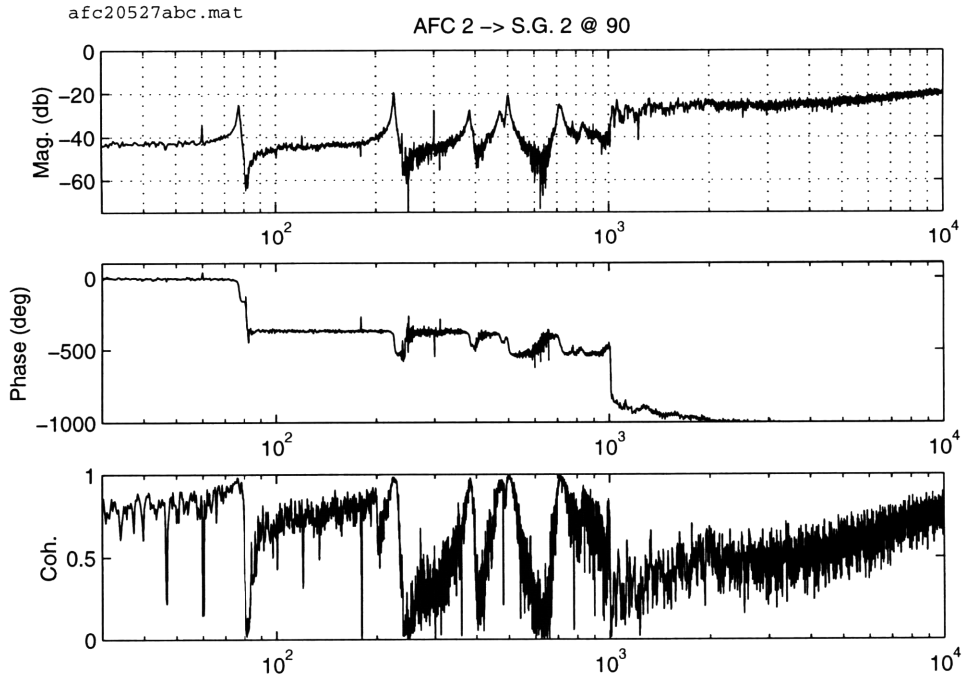
afc20527abc.mat
AFC 2 -> S.G. 2 @ 90
Mag. (db)
0
-20
-40
-60
10^2
10^3
10^4
Phase (deg)
0
-500
-1000
Coh.
1
0.5
0

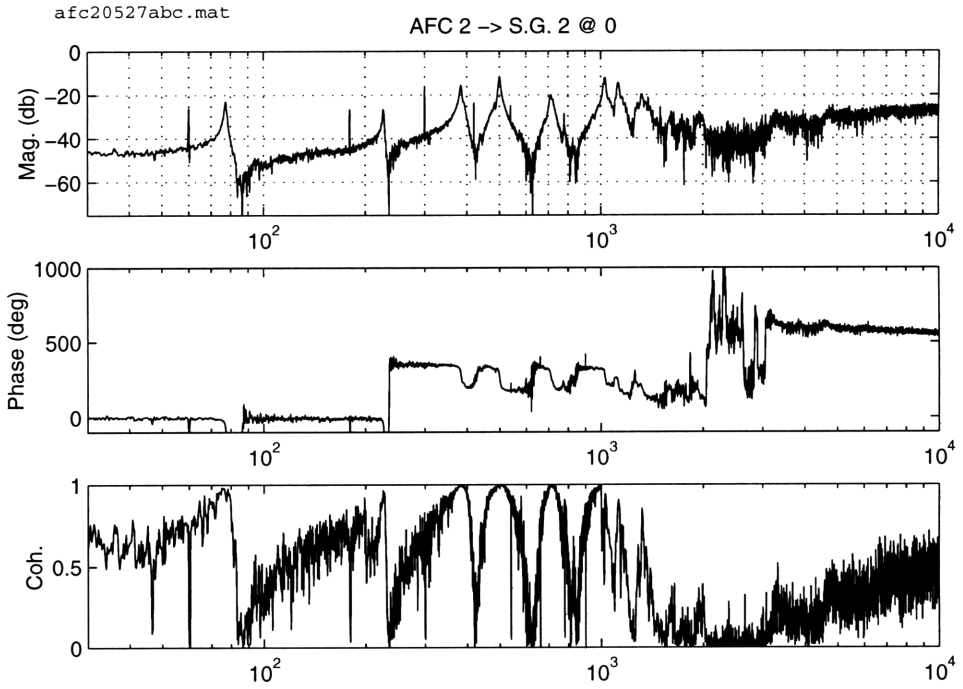
afc20527abc.mat
AFC 2 -> S.G. 2 @ 0
Mag. (db)
0
−20
−40
−60
10^2
10^3
10^4
Phase (deg)
1000
500
0
Coh.
1
0.5
0

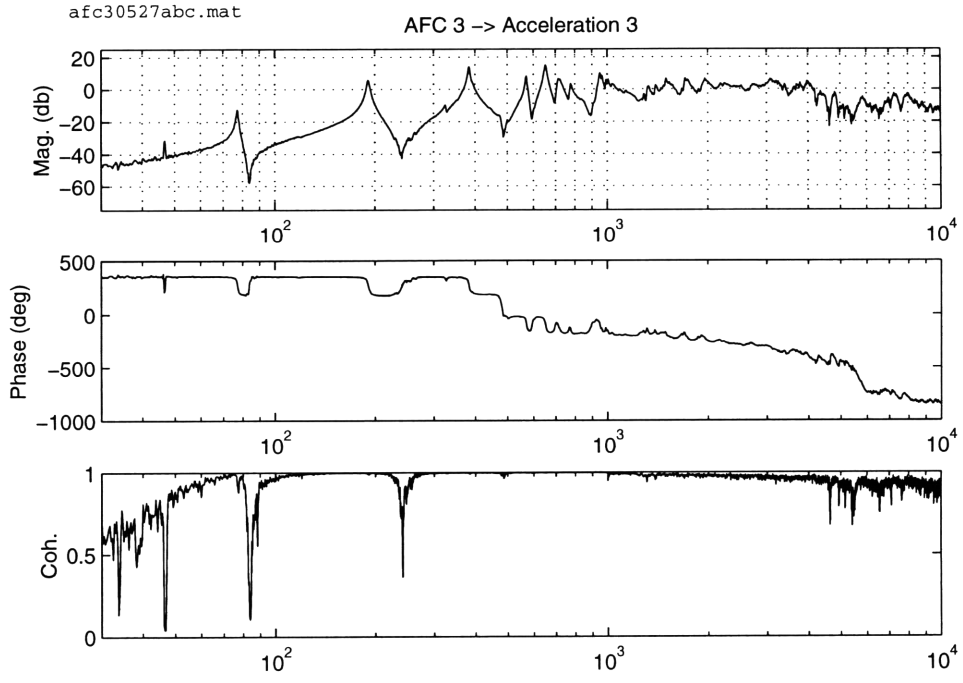
afc30527abc.mat
AFC 3 -> Acceleration 3
Mag. (db)
20
0
−20
−40
−60
10^2
10^3
10^4
Phase (deg)
500
0
−500
−1000
Coh.
1
0.5
0

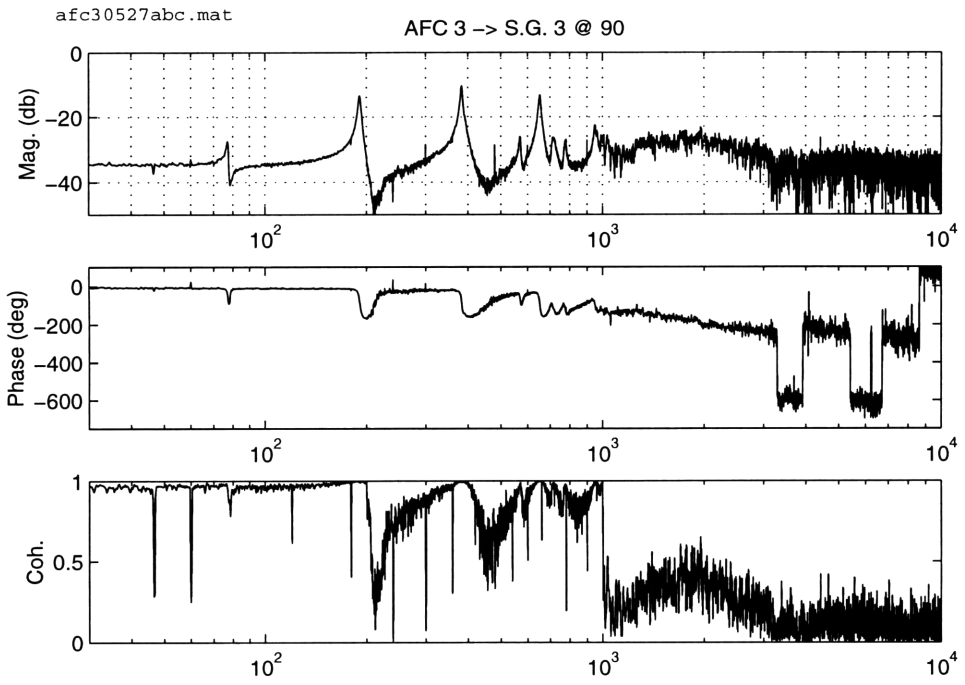
afc30527abc.mat
AFC 3 –> S.G. 3 @ 90
Mag. (db)
0
–20
–40
Phase (deg)
0
–200
–400
–600
Coh.
1
0.5
0
10^2
10^3
10^4

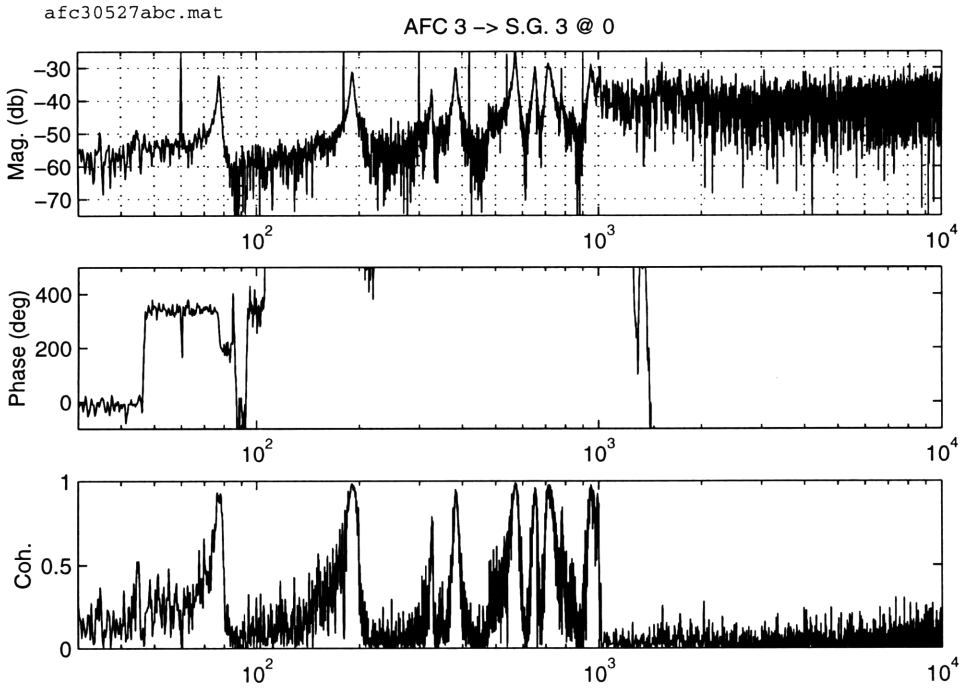
afc30527abc.mat
AFC 3 –> S.G. 3 @ 0
Mag. (db)
–30
–40
–50
–60
–70
Phase (deg)
400
200
0
Coh.
1
0.5
0
10^2
10^3
10^4

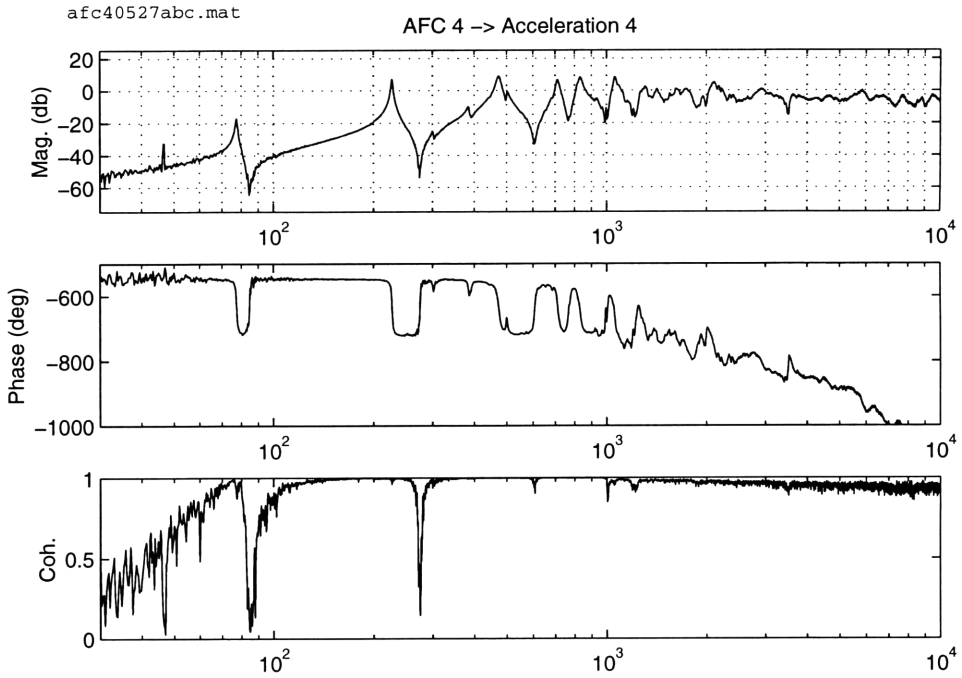
afc40527abc.mat
AFC 4 –> Acceleration 4
Mag. (db)
20
0
−20
−40
−60
Phase (deg)
−600
−800
−1000
Coh.
1
0.5
0
10^2
10^3
10^4

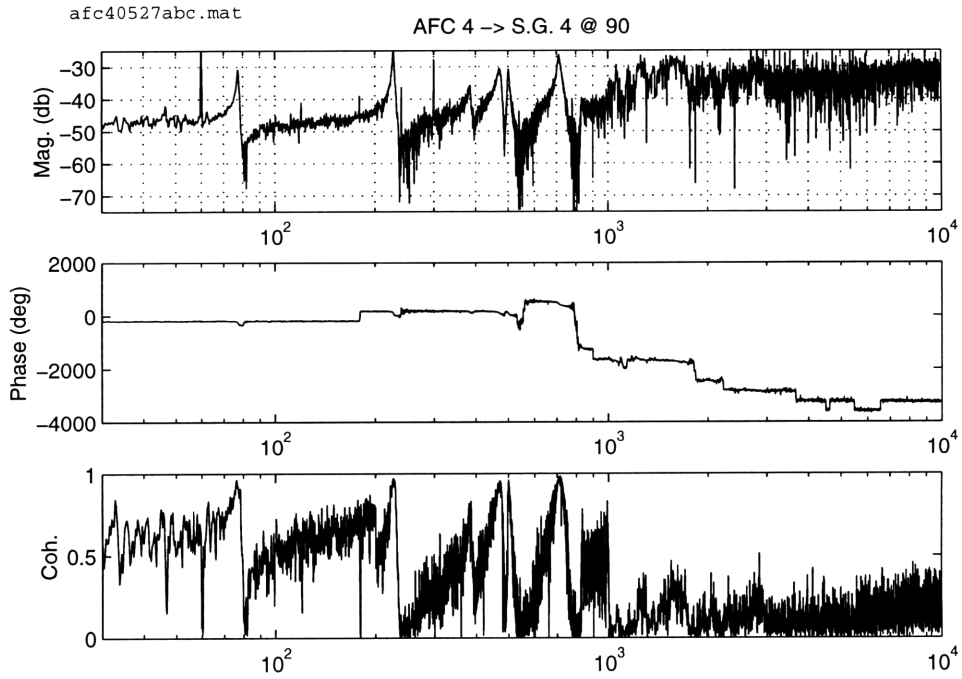
afc40527abc.mat
AFC 4 –> S.G. 4 @ 90
Mag. (db)
−30
−40
−50
−60
−70
Phase (deg)
2000
0
−2000
−4000
Coh.
1
0.5
0
10^2
10^3
10^4

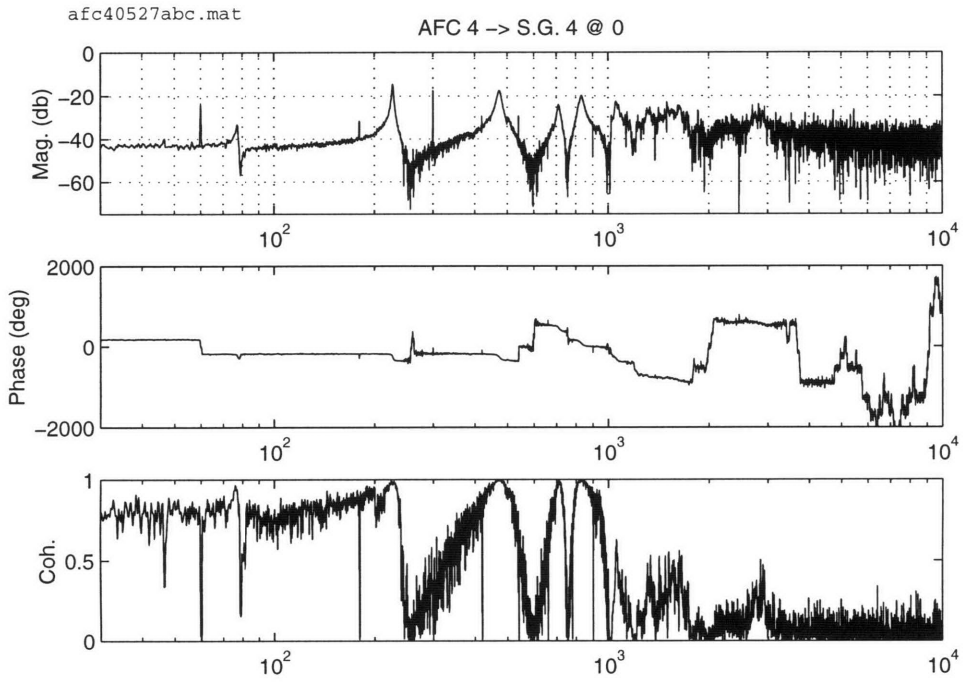
afc40527abc.mat
AFC 4 -> S.G. 4 @ 0
Mag. (db)
0
−20
−40
−60
10^2
10^3
10^4
Phase (deg)
2000
0
−2000
10^2
10^3
10^4
Coh.
1
0.5
0
10^2
10^3
10^4

Appendix D

Acoustic Directivity

The directivity of acoustic radiation from the experimental panel is found by measuring the pressure at discrete locations about the mid-plane of panel at a constant radius of 22 inches. The data is taken as transfer functions from the AFC disturbance input to the microphone outputs. Figure D.1 shows the directivity plots for for particular frequencies.

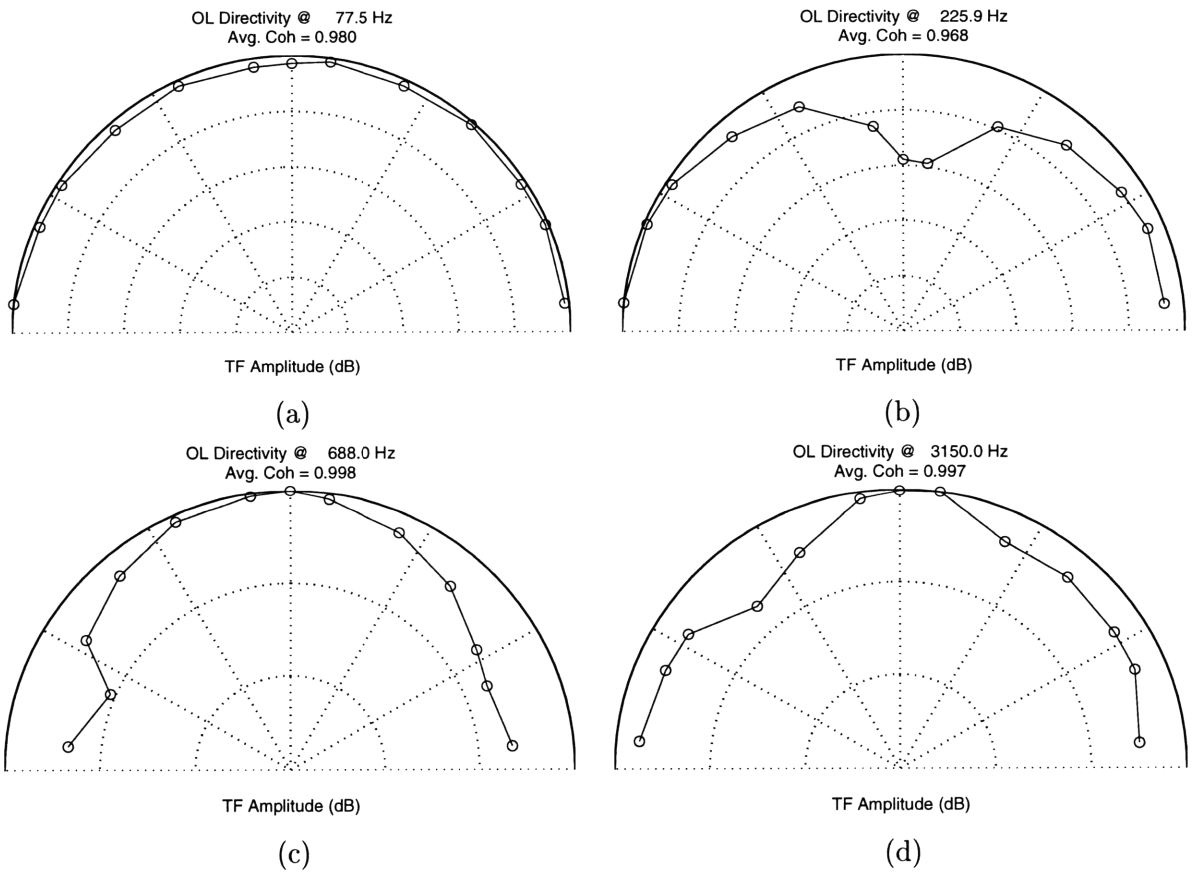

Figure D.1: Directivity Plots (R=22") at a) 77 Hz, b) 225 Hz, c) 688 Hz, and 3150 Hz

The first plot shows the radiation pattern at a frequency corresponding the the first,

(1,1), panel mode. The uniform radiation pattern is indicative of the low-frequency acoustic behavior. Plot b) shows the pattern at the (2,1) mode. Two lobes are observed indicating the directionality of the radiation from this mode shape. Plots c) and d) show how the energy is focused along the z-axis as the frequency increases.

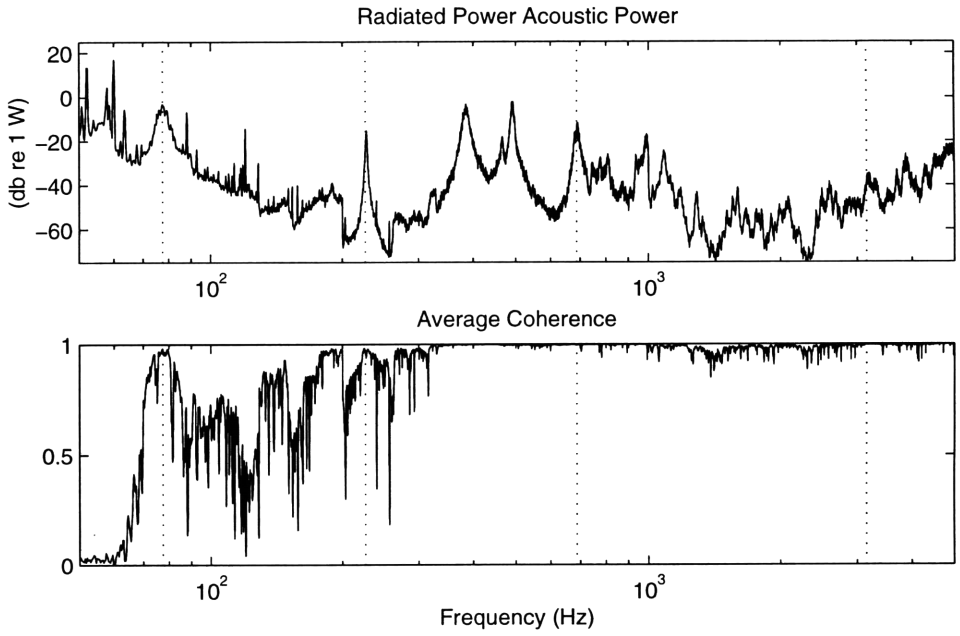

Figure D.2: Acoustic Radiate Power from the Directivity Measurements

Figure D.2 shows the result of integrating this data to obtain the radiated acoustic power. The vertical hashes indicate the frequencies corresponding to the directivity plots presented previously.